

https://dspace.org/

A characterisation of the terrestrial phenology of Bushbuckridge, South Africa, using MISR-HR

De Lemos, Hugo

2021
https://hdl.handle.net/10539/32244

Downloaded from a DSpace repository. https://dspace.org/

UNIVERSITY OF THE WITWATERSRAND, JOHANNESBURG

A CHARACTERISATION OF THE TERRESTRIAL PHENOLOGY OF BUSHBUCKRIDGE, SOUTH AFRICA, USING MISR-HR

Hugo De Lemos

A thesis submitted in fulfilment of the requirements for the degree Doctor of Philosophy: School of Animal, Plant and Environmental Sciences, the Faculty of Science, University of the Witwatersrand, Johannesburg

Supervisor: Prof. Mary Scholes

Co-supervisor: Prof. Michel Verstraete

Braamfontein

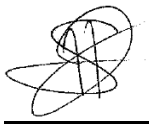
June 2021

WITS University Copyright:

The thesis may not be published either in part (in scholarly, scientific or technical journals), or as a whole (as a monograph), unless permission has been obtained from the University of the Witwatersrand.

DECLARATION

I declare that this thesis is my own, unaided work, unless otherwise specified within the text. It is being submitted for the Degree of Doctor of Philosophy at the University of the Witwatersrand, Johannesburg, South Africa. It has not been submitted before for any other degree or examination at any other university.



Hugo De Lemos

21st day of June 2021 in Johannesburg

ABSTRACT

This study documents (i) the seasonal cycles of vegetation canopies in the Bushbuckridge local municipality (BBR) as well as (ii) their sensitivities to non-seasonal perturbations during the period (2000 to 2018). The Fraction of Absorbed Photosynthetically Active Radiation (FAPAR) product computed by the Multi-angle Imaging SpectroRadiometer-High Resolution (MISR-HR) processing system was used to characterise the phenology of vegetation. This product exploits the measurements collected by NASA's Multi-angle Imaging SpectroRadiometer (MISR) instrument, which has been operational since 24 February 2000. The BBR is predominantly characterised by savanna vegetation, which is critically important in terms of biodiversity and for the sustainable socio-economic development of the region. The performance of parametric double S-shaped models (Gaussian, hyperbolic tangent, logistic and sine) to characterise the vegetation canopy's seasonal cycle in spite of the presence of missing values and noise in the FAPAR data was explored. Simulated FAPAR and *in situ* Gross Primary Productivity (GPP) measurements derived from the Skukuza Eddy Covariance flux tower were integrated over vegetative seasons and compared. The phenology models were all capable of fitting the FAPAR record when the observations were dense enough during the growth and senescence phases of the vegetative season, but some models turned out to be more sensitive than others to the presence of outliers or long data gaps. It was also shown that integrated FAPAR adequately tracks GPP in this environment as long as GPP varies in the range from 0 to 5 gC m^{-2} d^{-1}, beyond which this relation tends to saturate. This study investigated the sensitivity of vegetation productivity and precipitation anomalies, as reported by the Climate Hazards Group InfraRed Precipitations with Stations (CHIRPS), to historical ENSO periods occurring within the last two decades. These teleconnections were found to differ between five sites within the BBR, characterised by different vegetation types, underlying geology and protection status. The sensitivities of vegetation phenology and precipitation were specifically related to varying intensities and sequences of El Niño – Southern Oscillation (ENSO) events (i.e., El Niño and La Niña) at the scale of ecosystems. This study found FAPAR to be better correlated with ENSO than the CHIRPS precipitations. The productivity of vegetation observed in these ecosystems shows that they may be quite sensitive to the particular sequence and relative strengths of the El Niño and La Niña events, but the severity of the impact is related to the physical properties of the site. Regional natural resource management should acknowledge significant differences in the response of vegetation to ENSO events. This, in turn, might inform risk mitigation and adaptation strategies at the level of the BBR municipality.

ACKNOWLEDGEMENTS

This thesis would not be possible without the support of giants whose shoulders I stand on. I would like to thank my primary supervisor Mary Scholes. You took me on in the middle of my studies when I was having some personal challenges, but your caring and hard-working attitude helped me rise above. The commitment and guidance you show to your students is truly admirable.

To my co-supervisor, Michel Verstraete, you inspired me from the very beginning to take the leap and have been with me every step of the way. You possess all the qualities I strive for on my path as an academic and scientist. I am tremendously grateful for your mentorship. Words cannot express how privileged I feel to have had this opportunity to grow under you.

Thank you to Barend Erasmus who initially served as my primary supervisor. You helped kick start this journey and surrounded me with so much support at the Global Change Institute (GCI). Thank you to Bob Scholes who continuously backed my work. You are sorely missed, and I will treasure having had the opportunity to know you and learn from you. I will reflect fondly on my time at the GCI because of the brilliant people I have had the opportunity to befriend and learn from; Kaera Coetzer, Heidi Roberston, Yolandi Ernst, Alacia Armstrong, Ruwa Matsika, Francois Engelbrecht, Yvonne Dube, Ndoni Mcunu, Anita Etale, Khangelani Moyo and Coleen Vogel, thank you for making this journey so worthwhile. I feel very honoured to have been a part of this world class institute.

To my family, thank you for constantly cheering me on. Your support means the world to me. A special thanks to my partner, Calvin. This is largely possible because of your belief in me. Thank you for always being there to push me through the good and the bad.

Last but not least, a word of thanks to the panel of reviewers for their constructive remarks. They have contributed greatly to enhancing this thesis and will help me draft future papers as well.

This study was funded through a grant by Exxaro Limited to the Exxaro Chair in Global Change and Sustainability Research, held at the GCI. The GCI at Wits University currently hosts the MISR-HR processing system, under the supervision of a core team, which includes Michel Verstraete (visiting Professor at Wits and member of the MISR science team since 1995) and Linda Hunt (NASA Langley and Science Systems and Applications, Inc.). The study forms part of the goals of the MISR-HR science team to develop cutting-edge and high impact research on the application of the MISR-HR system in terrestrial environments.

DEDICATION

This body of work is dedicated to:

Gloria Gomes Faria De Lemos

(1932 – 2016)

and

Professor Robert J. Scholes

(1957 – 2021)

'a giant savanna tree providing shade in the heat,
shelter in the rain, and
a point of reference to navigate by'

RESEARCH OUTPUT

Peer reviewed scientific journal paper

Parametric Models to Characterize the Phenology of the Lowveld Savanna at Skukuza, South Africa

by Hugo De Lemos [1], Michel M. Verstraete [1] and Mary Scholes [2]

[1] Global Change Institute, University of the Witwatersrand, Braamfontein-Johannesburg 2050, South Africa

[2] School of Animal, Plant and Environmental Sciences, University of the Witwatersrand, Braamfontein-Johannesburg 2050, South Africa

Author Contributions: This paper is part of the Ph.D. of the first author (H.D.L) who is registered at the University of the Witwatersrand. H.D.L conceptualized and carried out the analysis and interpretation of this work with inputs from the co-authors and supervisors. The second (M.M.V.) and third (M.S.) authors co-directed the first author. M.M.V. wrote the two Appendices.

(This article is published in the Special Issue on Recent Advances in Satellite Derived Global Land Product Validation)

De Lemos, H., Verstraete, M.M. and Scholes, M., 2020. Parametric Models to Characterize the Phenology of the Lowveld Savanna at Skukuza, South Africa. Remote Sensing, 12(23), p.3927. doi: 10.3390/rs12233927

TABLE OF CONTENTS

DECLARATION ii

ABSTRACT iii

ACKNOWLEDGEMENTS iv

DEDICATION v

RESEARCH OUTPUT vi

LIST OF ABBREVIATIONS viii

LIST OF FIGURES xii

LIST OF TABLES xv

CHAPTER 1 INTRODUCTION 1

1.1. Background to the study and rationale 1

1.2. Aim, objectives and key questions of the study 3

1.2.1. Objective one 3

1.2.2. Objective two 3

1.3. Literature review 4

1.3.1. Vegetation dynamics in savannas 4

1.3.2. Land surface phenology 6

1.3.3. Vegetation indices 8

1.3.4. Biogeophysical variables 9

1.3.5. Terrestrial primary productivity 10

1.3.6. Multi-angular measurements 12

1.3.7. Vegetation heterogeneity 16

1.3.8. Aperiodic climatic fluctuations 18

1.3.9. Consequences of climate change 19

1.4. Structure of the dissertation 20

CHAPTER 2 PARAMETRIC MODELS TO CHARACTERIZE THE PHENOLOGY OF THE LOWVELD SAVANNA AT SKUKUZA, SOUTH AFRICA 22

PREFACE 22

ABSTRACT 24

1. Introduction 25

2. Study Area 26

3. Data Collections 26
3.1. Satellite measurements 26
3.1.1. Background 26
3.1.2. Multi-Angular observations 28
3.1.3. MISR-HR FAPAR Product for Skukuza 28
3.2. Flux tower observations 29
4. Data Processing 30
4.1. Measurement uncertainties and missing data 30
4.2. Pre-processing 31
4.2.1. Screening outliers 31
4.2.2. Assembling the FAPAR data cube 34
4.2.3. Identifying individual vegetative seasons 34
4.3. Modeling phenology 36
5. Results and Discussion 38
5.1. Simulation Capability 38
5.2. Ecological effectiveness 39
5.2.1. Comparing daily values 39
5.2.2. Comparing seasonally integrated values 42
5.2.3. Comparison outcome 42
5.3. Numerical efficiency 43
5.3.1. Successful inversions 43
5.3.2. Iterations 43
5.3.3. Computing time 43
5.3.4. Simulation effectiveness 44
5.4. Discussion 45
6. Conclusions 45
APPENDIX A. The MISR Instrument and MISR-HR Products 48
APPENDIX B. Parametric Double S-shaped Functions 50
REFERENCES 56
POSTFACE 63

CHAPTER 3 SEASONAL AND LONG-TERM FLUCTUATIONS AND TRENDS IN LOWVELD VEGETATION 64

1. Introduction 64

2. Materials and Methods 68

2.1. Study Area 68

2.2. Data records 70

2.2.1. Remote sensing vegetation records 70

2.2.2. Climatic records 71

2.2.3. Vegetation types 73

2.3. Study Framework 75

2.3.1. MISR-HR FAPAR pre-processing 77

2.3.2. Temporal aggregations 78

2.3.3. Monthly anomalies 78

2.3.4. Regression analysis 79

3. Results and Discussion 79

3.1. Relationships between FAPAR, precipitation and ENSO 79

3.2. Magnitude and spatial distribution of FAPAR anomalies during peak ENSO conditions 86

3.3. Discussion 91

4. Conclusions 93

CHAPTER 4 OVERALL DISCUSSION AND CONCLUSION 95

1. Evaluating and enhancing historical FAPAR records 98

2. Examining the influence of ENSO on the phenology of Lowveld vegetation 100

3. Overall conclusion 104

COMBINED REFERENCES 106

LIST OF ABBREVIATIONS

AfriGEOSS	African Global Earth Observation System of Systems
ARVI	Atmospherically Resistant Vegetation Index
ASAR	Advanced Synthetic Aperture Radar
ASDC	Atmospheric Science Data Center
ATSR	Along-Track Scanning Radiometer
AVHRR	Advanced Very-High-Resolution Radiometer
BBR	Bushbuckridge
CEOS	Committee on Earth Observation Satellites
CHIRPS	Climate Hazards Group InfraRed Precipitation with Station data archive
CSIR	Council for Scientific and Industrial Research
DGVM	Dynamic Global Vegetation Models
EC	Eddy Covariance
ECMWF	European Centre for Medium-Range Weather Forecasts
ECV	Essential Climate Variable
ENSO	El Niño – Southern Oscillation
EO	Earth Observation
EOS	End Of (vegetative) Season
EPSG	European Petroleum Survey Group
ERA	ECMWF Re-Analysis
FAPAR	Fraction of Absorbed Photosynthetically Active Radiation
FEWS NET	Famine Early Warning Systems Network
GCOS	Global Climate Observing System
GEO	Group on Earth Observations
GEOGLAM	GEO Global Agricultural Monitoring
GPP	Gross Primary Productivity
GSD	Ground Sample Distance
IPCC	Intergovernmental Panel on Climate Change
JRC	Joint Research Centre
JRC-TIP	Joint Research Centre – Two-stream Inversion Package
LAI	Leaf Area Index
LiDAR	Light Detection And Ranging
LOS	Length Of (vegetative) Season
LUE	Light-use Efficiency Model
MISR	Multi-angle Imaging SpectroRadiometer

MISR-HR	Multi-angle Imaging SpectroRadiometer High Resolution
NASA	National Aeronautics and Space Administration
NDVI	Normalized Difference Vegetation Index
NEE	Net Ecosystem CO_2 Exchange
NOAA	National Oceanic and Atmospheric Administration
NPP	Net Primary Productivity
ONI	Oceanic Niño Index
PAR	Photosynthetically Active Radiation
PBL	Protected Basalt Lowveld
PDGF	Parametric Double Gaussian Function
PDHyTgF	Parametric Double Hyperbolic Tangent Function
PDLF	Parametric Double Logistic Function
PDSF	Parametric Double Sine Function
PGL	Protected Granite Lowveld
POLDER	Polarization and Directionality of Earth's Reflectances
RPV	Rahman, Pinty, Verstraete
SANBI	South African National Biodiversity Institute
SAVI	Soil-Adjusted Vegetation Index
SOM	Space Oblique Mercator
SOS	Start Of (vegetative) Season
SPOT	Satellite Pour l'Observation de la Terre
SRES	Special Report on Emissions Scenarios
TIP	Two-stream Inversion Package
UGL	Unprotected Granite Lowveld
UHG	Unprotected Highveld Grassland
USB	Unprotected Sour Bushveld

LIST OF FIGURES

CHAPTER 1

Figure 1. Plot illustrating the sampled bidirectional reflectance function value (along the solid red line) at different MISR (blue) and AVHRR/MODIS observation zenith angles relative to the solar azimuth angle (solid yellow line)……..14

CHAPTER 2

Figure 1. Panel (a): Location of the study site in the Lowveld of South Africa with overlapping footprints of Multi-angle Imaging SpectroRadiometer (MISR) Block 110 for Path 168 (dotted rectangle) and 169 (full rectangle). Panel (b): Detailed map of the environment around Skukuza in the Kruger National Park. Source: South African National Biodiversity Institute (SANBI), acquired from https://www.sanbi.org/link/bgis-biodiversity-gis/. 26
Figure 2. Time series of daily values for the Gross Primary Productivity (GPP) of the unmanaged vegetation around the Skukuza Eddy Covariance (EC) flux tower (in red) and the daily precipitation estimated by the ERA-Interim reanalysis data accompanying the FLUXNET2015 archive. 30
Figure 3. Time series plots showing how a threshold value of the cost function distribution (in this instance 0.1) flags obvious and less apparent cases of problematic values in Fraction of Absorbed Photosynthetically Active Radiation (FAPAR) in the time series at the reference pixel of the Skukuza flux tower and for MISR Paths 168 and 169.. 32
Figure 4. Histogram of FAPAR values for the area surrounding Skukuza and for Paths 168 and 169 (a) before screening outliers and (b) after discarding outliers using a threshold value of the cost function (0.099). 33
Figure 5. Distribution of the availability of the number of valid FAPAR values as a function of month (along the vertical axis) and year (along the horizontal axis), averaged over the target area around the Skukuza flux tower. 33
Figure 6. The pixel reference grids used to co-register the MISR-HR FAPAR variable for Paths 168 and 169 of Block 110 to geographic coordinates for the Skukuza flux tower. 34
Figure 7. Lomb periodogram of the FAPAR time series at the reference pixel of the Skukuza flux tower..... 35
Figure 8. A subset of the FAPAR time series at the reference pixel for the Skukuza flux tower showing the start of the first vegetative season between 2000 and 2001 and the vegetative seasons for 2001–2002, 2002–2003, and 2003–2004. The dotted blue lines delimit the search periods for the start and end of the vegetative seasons, and the solid red lines indicate those boundaries. The dashed green line represents the median value for the record, in this case, 0.25. 36
Figure 9. Boxplots summarizing, for the entire MISR-HR FAPAR record, the number of observations available per year to fit the model during (**a**) entire vegetative seasons, (**b**) the growth phase, and (**c**) the senescence phase. The top and bottom limits of the boxes show the quartiles, the horizontal line in the middle of those boxes and the crosses indicate the median and the average values, respectively, while the 'T' shaped extensions document the range of values (minimum and maximum). 38
Figure 10. Number of successfully simulated vegetative seasons. The four left-most panels report the results for the Parametric Double Gaussian Function (PDGF), Parametric Double Hyperbolic Tangent Function (PDHyTgF), Parametric Double Logistic

Function (PDLF), and Parametric Double Sine Function (PDSF) models, respectively. The fifth panel shows the success rate when the most successful model is selected for each season at the sample and line locations in the target area. 39
Figure 11. Superposition of multiple time series, from September 2000 to August 2013: the FAPAR data (small circles, non-dimensional), averaged over a 3 by 3 pixel area around the Skukuza flux tower, the four model fits (smooth coloured curves, non-dimensional), each adjusted to fit the remote sensing data, and the daily GPP values derived from the *in situ* Eddy Covariance (EC) measurements (jagged grey trace, in gC m^{-2} d^{-1}). 40
Figure 12. Scatterplot of daily FAPAR estimates (when the PDHyTgF model successfully simulates vegetative seasons) versus daily GPP (gC m^{-2} d^{-1}) values when at least half of the expected values are available (i.e., season 2, 3, 4, 9, 10, and 12). 41

CHAPTER 3

Figure 1. Panel (**a**): Location of the study site in the Lowveld of South Africa (solid black line) with overlapping footprints of Multi-Imaging SpectroRadiometer (MISR) Blocks 110 and 111 (dashed and solid line, respectively) for Paths 168 and 169 (blue and red, respectively), and Oct-Apr long-term average rainfall (2000 – 2018, mm, source: IRI, 2020). Panel (**b**): Detailed map of bioregions within the geographic limits of the Bushbuckridge local municipality (source: SANBI, 2006-2012). 70
Figure 2. Savanna vegetation types over the Bushbuckridge local municipality. Source: South African National Biodiversity Institute (SANBI, 2006-2012). 75
Figure 3. Oceanic Niño Index for the period between Sep 2000 and Dec 2018. The ENSO periods included in this study are indicated by the labelled boxes, specifically the ENSO during (1) September 2006 and June 2008, (2) July 2009 and May 2011, and (3) October 2014 and December 2016. 78
Figure 4. FAPAR anomalies for BBR (solid green bars) and sites 1 to 5 (hollow bars) and Niño 3.4 SSTs (grey line) for the ENSO periods (with El Niño and La Niña events indicated in red and blue lines, respectively) during (a) September 2006 and June 2008, (b) July 2009 and May 2011, and (c) October 2014 and December 2016. 80
Figure 5. Precipitation anomalies for BBR (solid blue bars) and sites 1 to 5 (hollow bars) and Niño 3.4 SSTs (grey line) for the ENSO periods (with El Niño and La Niña events indicated in red and blue lines, respectively) during (a) September 2006 and June 2008, (b) July 2009 and May 2011, and (c) October 2014 and December 2016. 81
Figure 6. Accumulated precipitation (x-axis) and integrated FAPAR (y-axis) during ENSO periods one to three (a – c), summed over the growing (Oct – Mar) and senescence months (Apr – Sep) of the El Niño and La Niña events for the vegetation sites (points labelled 1 – 5). 85
Figure 7. Maps of the sum of the FAPAR monthly anomalies, cumulated over the 22 months of ENSO period one (top left) and over the 27 months of ENSO period three (top right). The bottom panels map cumulated FAPAR monthly anomalies over the three-month periods centred on the peak of the El Niño and La Niña events within each of those two ENSO periods, respectively. The site labels include (1) protected granite Lowveld (PGL), (2) protected basalt Lowveld (PBL), (3) unprotected sour bushveld (USB), (4) unprotected granite Lowveld (UGL), and (5) unprotected Highveld grassland (UHG). White pixel regions represent areas with no data values. 87
Figure 8. Site 1 frequency histograms of the FAPAR monthly anomalies, cumulated over the three month periods centred on the peak of the (a) weak El Niño and (b) strong La Niña during period 1, and the (c) strong El Niño and (c) weak La Niña during period 3 (bin width = 1). 89

Figure 9. Site 2 frequency histograms of the FAPAR monthly anomalies, cumulated over the three month periods centred on the peak of the (a) weak El Niño and (b) strong La Niña during period 1, and the (c) strong El Niño and (c) weak La Niña during period 3 (bin width = 1). 89
Figure 10. Site 3 frequency histograms of the FAPAR monthly anomalies, cumulated over the three month periods centred on the peak of the (a) weak El Niño and (b) strong La Niña during period 1, and the (c) strong El Niño and (c) weak La Niña during period 3 (bin width = 1). 90
Figure 11. Site 4 frequency histograms of the FAPAR monthly anomalies, cumulated over the three month periods centred on the peak of the (a) weak El Niño and (b) strong La Niña during period 1, and the (c) strong El Niño and (c) weak La Niña during period 3 (bin width = 1). 90
Figure 12. Site 5 frequency histograms of the FAPAR monthly anomalies, cumulated over the three month periods centred on the peak of the (a) weak El Niño and (b) strong La Niña during period 1, and the (c) strong El Niño and (c) weak La Niña during period 3 (bin width = 1). 90

LIST OF TABLES

CHAPTER 2

Table 1. Relation between the largest allowable cost function value (Threshold), the number of data points identified as outliers, and the number of data points remaining available for further analysis in the time series of Figure 3. 32
Table 2. Correlation coefficients (*r*) between the daily GPP and daily FAPAR estimates from the PDGF, PDHyTgF, PDLF, PDSF, and combined models for each vegetative season and for the area around the Skukuza flux tower. Entry A indicates that fewer than half of the expected GPP values were available, while entry B means that the model could not simulate the available FAPAR data. 41
Table 3. Correlations coefficients (*r*) between the integrated GPP and Cumulated FAPAR (CFAPAR) obtained by integrating the PDGF, PDHyTgF, PDLF, PDSG, and combined models during the indicated vegetative seasons. Computations were skipped whenever fewer than half of the expected GPP observations were available during the season, or when the correlation between the daily GPP and model values dropped below 0.70 in Table 2 (see text for details). 42
Table 4. Number of iterations required, for successful (s) and unsuccessful (u) model inversions. 43
Table 5. Number and proportion of successful model inversions. 43
Table 6. Execution time, relative to the fastest case (successful PDLF model inversion in 0.00299978 second), for successful (s) and unsuccessful (u) model inversions. 44
Table 7. Average χ^2 value at the end of the model inversion step. 44

CHAPTER 3

Table 1. Pearson's correlation coefficients (R) for monthly cumulated CHIRPS data set and in situ daily rainfall measurements recorded at Skukuza (24° 59' 43.44" S and 31° 35' 34.332" E) for the three ENSO periods included in the study……72
Table 2. El Niño and La Niña events over the tropical Pacific Ocean for the period between September 2000 and December 2018. 73
Table 3. Spatially accumulated pixel-to-pixel mean and standard deviation statistics for sites 1 to 5……76
Table 4. Pearson correlation coefficients (R) between integrated monthly FAPAR and Niño 3.4 (first column in each pair) and between cumulated monthly precipitation amounts and Niño 3.4 (second column in each pair), for the entire BBR region as well as for each of the five individual sites, during the ENSO event between Sep 2006 and Jun 2008, and for the time lags indicated in the leftmost column. The density of the green colour in each Table cell is proportional to its R value, and those that are statistically significant ($p < 0.05$) are set in bold face. 82
Table 5. Pearson correlation coefficients (R) between integrated monthly FAPAR and Niño 3.4 (first column in each pair) and between cumulated monthly precipitation amounts and Niño 3.4 (second column in each pair), for the entire BBR region as well as for each of the five individual sites, during the ENSO event between Jul 2009 and May 2011, and for the time lags indicated in the leftmost column. The density of the green colour in each Table cell is proportional to its R value, and those that are statistically significant ($p < 0.05$) are set in bold face. 83
Table 6. Pearson correlation coefficients (R) between integrated monthly FAPAR and Niño 3.4 (first column in each pair) and between cumulated monthly precipitation amounts and

Niño 3.4 (second column in each pair), for the entire BBR region as well as for each of the five individual sites, during the ENSO event between Oct 2014 and Dec 2016, and for the time lags indicated in the leftmost column. The density of the green colour in each Table cell is proportional to its R value, and those that are statistically significant ($p < 0.05$) are set in bold face. 84

CHAPTER 1 INTRODUCTION

1.1. Background to the study and rationale

Vegetation regulates carbon, energy and water fluxes between land and the atmosphere (Scholes et al., 2003; Hoek van Dijke et al., 2020). Plants respond especially to climatic conditions: typically exhibiting annual variations that match seasonal fluctuations of water availability, temperature, solar irradiance, and other critical variables. As a result, plants are also sensitive to fluctuations in climate. Vegetation phenology, the study of recurring events in the life cycle of plants, typically on a seasonal time scale, has gained growing public and scientific attention; the number of peer-reviewed journal articles related to the topic has increased by about 10-fold since the 1980's (Tang et al., 2016).. To the extent fluctuations of those properties can be reliably detected, phenology studies can provide an independent record on climate and global change.

The savanna biome is vital in regulating the global carbon cycle due to its total areal coverage, i.e., about 20% of the global terrestrial surface and 40% of the African continent (Kutsch et al., 2008), and also account for 13% of net primary production on a global scale (Grace et al., 2006). Globally, savannas support a fifth of the world's human population and a majority of its rangeland and livestock biomass (Scholes and Archer, 1997). In the particular context of African ecosystems, savannas provide valuable ecosystem services (Shackleton and Shackleton, 2004; Twine et al., 2003). Effective estimation of these resources is necessary to satisfy commitments to manage and monitor change within them (Main et al., 2016).

Rural livelihoods in the Lowveld, a bioregion of South Africa which is predominantly savanna, depend on fuelwood for energy because gas and other fuels are unaffordable in many households. This socio-economic constraint has led to natural resources being over exploited, well beyond their regenerative capacity, resulting in the progressive deforestation of those environments. Wood scarcity has also resulted in potential conflicts over access to resources (Matsika et al., 2013). Scarcity of resources leads to an exodus from rural settlements to towns and cities, including immigration from neighbouring countries. The expansion of settlements has meant that their environmental footprints have become more severe in time (Erasmus et al., 2011).

The Group on Earth Observations (GEO) coordinates global Earth Observation (EO) efforts, stressing the importance of open access to spatially and temporally detailed information on a global-scale as humanity faces unprecedented social, economic and environmental

challenges. GEO is a is a voluntary partnership of governments and international organizations coordinating efforts to connect the producers of environmental data and decision-support tools with the end users of these products, with the aim of enhancing the relevance of Earth observations to global issues (Fritz, 2014). Currently, major international sustainable development goals (SDGs), such as the UN 2030 Agenda for Sustainable Development, are grounded on regional and global initiatives (e.g., GEO, AfriGEOSS, Blue Planet, GEOGLAM), which prioritise EO technologies for monitoring, measuring, and reporting on progress towards associated targets (Anderson et al., 2017). SDG 15 in particular, stresses the importance of deriving regional and national-scale vegetation status maps from EO technologies to inform efforts to protect, restore and promote the sustainable use of terrestrial ecosystems.

Spaceborne Earth observations have been extensively used to characterise the terrestrial phenology of vegetation in the Northern Hemisphere, but other regions, such as Africa have received far less attention. A systematic review spanning the last decade reveals an increase in the number of phenology studies in Africa based on remote sensing, but suggests that further investigations are needed, particularly to examine the relationship between climate and vegetation (Adole et al., 2016).

The environmental and anthropogenic drivers of vegetation change for the environment within the geographical confines of the Bushbuckridge local municipality (BBR) are well documented in the literature, making it a good choice for studying land surface phenology.

The findings presented here exploit advanced remote sensing products derived from an analysis of the planetary reflectance, acquired by NASA's Multi-angle Imaging SpectroRadiometer (MISR), to deliver a better understanding of the relation between surface properties and the fluxes of matter and energy in vegetation canopies, which until recently was mostly documented using mono-angular spectral instruments and sporadic Light Detection And Ranging (LiDAR) campaigns. The phenology of the vegetation canopy in the Bushbuckridge local municipality is documented over an extended period (2000 to 2018) on the basis of those Earth Observation products. These results may be beneficial to ongoing conservation and resource management efforts in the area in light of expanding settlement footprints and climate change.

Earth Systems (ES) modelling of terrestrial environments using optical satellite observations suffers greatly from noise and missing data attributed mostly to prevailing weather conditions. The results described below document these perturbations and offer the potential to improve the predictions and sensitivities of ES models' through enhanced

characterisations of vegetation dynamics (Alessandri et al., 2017; MacBean et al., 2015; Richardson et al., 2013).

1.2. Aim, objectives and key questions of the study

The aim of the study is to investigate the feasibility of using biogeophysical variables derived from multi-angular satellite observations to provide a holistic long-term characterisation of the phenology of vegetation in the environment of the Bushbuckridge local municipality in support of resource management and conservation efforts. The intrinsic attributes of terrestrial surfaces were analysed through an interpretation of the spatial and temporal variations in the Fraction of Absorbed Photosynthetically Active Radiation (FAPAR), one of the biogeophysical products generated by the MISR-HR processing system.

1.2.1. Objective one

To deliver a methodology for assembling a spatiotemporal record of biogeophysical variables which characterise the nature and properties of the vegetation canopy over Bushbuckridge local municipality over the period 2000 to 2018.

1.2.2. Objective two

To exploit image time series of biogeophysical variables to quantitatively describe interannual and seasonal fluctuations as well as variations in the vegetation of the Bushbuckridge local municipality.

1.3. Literature review

1.3.1. Vegetation dynamics in savannas

Savannas are characterised by a continuous grass layer and a discontinuous stratum of trees (Scholes and Archer, 1997). Wet, hot summer periods and dry, warm winter periods, are typical for savannas, with largely unpredictable and variable rainfall in each year (Hester et al. 2006). Savannas also have distinct dry seasons that range from 2 to 9 months of the year, during which fires are typical (Lloyd et al., 2008; Scholes and Walker, 1993). Savanna ecosystems are strongly influenced by and often reliant on disturbances (Scheiter and Higgins, 2007). The four key variables traditionally viewed as the determinants of savanna structure and function are water availability, fire, soils (geology) and herbivory (Anderson et al., 2016; Archibald, 2016; Colgan et al., 2012; Fisher et al., 2009; Gray and Bond, 2015; Kanniah et al. 2010; Le Roux and Bariac 1998; Scholes and Archer 1997; Wessels et al. 2011; Witkowski and O'Connor 1996). A study of tree cover across multiple savanna sites in Africa shows that after water availability, fires determine much of the variation observed in tree cover, followed by soil properties and herbivory (Sankaran et al., 2008). Additionally, repeat observations of woody plant density and diversity in African savanna suggests that variations in species composition and diversity are greatly influenced by anthropogenic disturbances (Fisher et al., 2009; Higgins et al. 1999; Kalema and Witkowski, 2012). In general, the attributes of the woody flora, such as density, height and biomass have been shown to respond negatively along increasing disturbance gradients (Mograbi et al., 2017; Shackleton et al., 1994; Wessels et al., 2011).

There is a considerable debate amongst ecologists on the forces which explain tree/grass coexistence in savannas. The physiologically based or 'bottom up' view, e.g., root-niche separation model (Walter, 1971), argues that trees and grasses in savannas differentially exploit resources, primarily water availability. In practical terms, grasses which are shallow-rooted exploit the upper soil layer, whereas trees are able to access water from lower down in the soil profile, owing to their deep-rooting ability. Water is regarded as a more dominant control in savannas than soil nutrients since nutrient delivery is tightly coupled to water uptake (van Langevelde et al., 2003; Walker et al., 1981). While the root-niche separation model is consistent in relating water availability to tree cover in arid/semi-arid savannas, they do not empirically support many other savanna environments (Bond, 2008; Higgins et al., 2000; Scholes and Archer, 1997), nor do they account for the seedling stages of trees, when they compete directly with grasses for soil resources (Bond, 2008; Sankaran et al., 2004).

The 'top-down' view emphasises the importance of demographic bottlenecks, rather than physiological mechanisms for regulating savanna structure (Higgins et al., 2000; Sankaran

et al., 2004; van Wijk and Rodriguez-Iturbe, 2002). The nature of the bottleneck varies for each environment. In the Lowveld, demographic mechanisms range from natural phenomena, such as veld fires and invasion by alien species (Archibald et al., 2005; Archibald, 2011; Archibald, 2016; Vilà et al. 2011), to anthropogenic disturbances, such as the harvesting of natural resources and livestock grazing (Dovie et al. 2004; Higgins et al. 1999; Shackleton, 2004; Shackleton et al. 2002; Shackleton et al. 2005; Twine et al. 2003; Twine, 2005; Williams and Shackleton 2002).

In the presence of fire, woody biomass is reduced to give way for an open-savanna state and when fire is absent, savannas transition to a more closed-forest state (Archibald, 2016; Archibald et al. 2005; Higgins and Scheiter, 2012; Moncrieff et al., 2014; Scholes, 2009). Fires are critical for maintaining a positive feedback loop in savannas. Frequent fires maintain an open-savanna state with fire-tolerant grasses, which in turn promote fires and the savanna state (Sankaran and Ratnam, 2013). Savanna distribution is to a large extent predicted by rainfall seasonality (Good and Caylor, 2011). Bush encroachment is more likely to occur when rainfall is high and fire intensity is low whereas low rainfall can lead to more seedling mortalities (Govender et al. 2006; Roques et al. 2001). Fire-climate interactions in southern Africa suggest that the effects of climate in driving fire regime variability between years is limited by anthropogenic impacts, which contrasts to protected areas, where rainfall seasonality influences annual area burnt (Archibald et al., 2010). Fire propagation modelling of grass-fueled savanna and woodland environments on the continent of Africa suggest that the spread of agropastoralism probably had the most significant impact on decreasing burnt area, particularly within the past 4,000 years (Archibald et al., 2011): in many parts of Africa, livestock have overtaken fire and are responsible for fragmented landscapes which reduce area burned (Archibald, 2016).

In the absence of fire, Dynamic Global Vegetation Models (DGVM) predict that forests could almost double their current extent over regions presently characterised by savanna vegetation (Bond et al., 2005). Grazing impacts fire indirectly in savannas, as it reduces biomass to the point where fires become infrequent or absent (Scholes, 1990; Scholes 2009). Similarly, seedlings may benefit from grazing, which reduces grass competition in favour of tree establishment (Sankaran et al., 2004).

Soil properties, such as texture and mineral nutrients play a vital role in regulating savanna structure. Coarse-textured or sandy soils tend to favour tree cover in savannas compared to fine-textured clay soils (Williams et al., 1996). Sandy soils permit more water to percolate to lower soil depths, thus favouring the deep-rooting physiology of woody plants (Walker and Noy-Meir, 1982). The geology of the Lowveld is predominantly composed of granitic and

basaltic formations (Colgan et al. 2012; Helm and Witkowski, 2012; Scholes and Walker, 1993). Two distinguishable vegetation structures are noticeable from the contrasting soil type along the granitic catena sequence (Colgan et al. 2012; Parsons et al. 1997). Vegetation in the hill crests of the catena sequence favour species adapted to the deep sandy soils, which contrasts with the bottomlands which favours species adapted to the sodic clay soil (Colgan et al. 2012; Dzerefos et al. 2003). Broad leaved species, such as *Combretum spp., Diospyros mespiliformis, Peltophorum africanum, Terminalia sericea and Sclerocarya birrea* dominate the hill crests and fine leaved trees, such as *Acacia spp., Dichrostachys cinerea, Albizia harveyi, Euclea spp.,* and *Gymnosporia spp.* characterise the bottomlands (Colgan et al. 2012; Dzerefos et al. 2003; Parsons et al. 1997; Witkowski and O'Connor 1996).

In South Africa and at the turn of the century, nearly 6 million hectares of communal rangelands were home to an estimated 2.4 million rural households (Shackleton et al. 2001). Long-term research in the Lowveld confirms that socio-economic factors are important drivers of vegetation change in the region (Twine et al., 2005), e.g., unsustainable fuelwood extraction (Dovie et al., 2004; Wessels et al., 2013; Matsika et al., 2013). But the differences in the rate of change indicates that patterns are site-specific and influenced by several variables such as, demographics, natural resource availability, and land use (Coetzer et al., 2010; Fisher et al., 2011; Parsons et al., 1997, Matsika et al., 2013). The interdependency of people and the environment shape the savanna ecosystem goods and services upon which many people are dependent, and historical trends indicate that settlements in BBR have been expanding, at least over the first decade since, with an enhanced footprint around each village, where woodland resources get depleted (Erasmus et al., 2011).

Other studies argue that fuelwood extraction may not be as unsustainable as previously thought. For instance, it has been demonstrated that fuelwood shortages occur despite increases in low height vegetation within the sub-canopy, which is purportedly attributable to strong re-sprouting after intensive harvesting (Mograbi et al., 2015; Mograbi et al., 2017; Mograbi et al., 2019). Fine-scale 3D maps of sub-canopy structure using LiDAR suggest that trees more than 3 m in height showed recruitment and gains up to 2.2 times higher in communal rangelands where they are likely protected for cultural reasons (Fischer et al., 2015).

1.3.2. Land surface phenology

Satellite based measurements are advantageous for observing environments in terms of their global spatial coverage and repeat monitoring capabilities. Geographically sparse ground-based observations of plants were used to characterise species specific phenology

prior to satellite remote sensing. Over the last few decades, research on vegetation phenology in terrestrial ecosystems has been stimulated by significant simultaneous developments in Earth Observation and computing technologies, advances in radiation transfer modelling, and growing concerns about the impact of likely climate changes. Shifts in phenological metrics, which quantify the onset and duration of biological cycles bare strong links and feedbacks to variability in climate patterns and environmental conditions (Tang et al., 2016). While early investigations of land surface phenology from space relied on vegetation indices, i.e., simple combinations of satellite observations in a couple of spectral bands, current approaches are based on biophysical variables derived from a physically-based, quantitative analysis of reflectance measurements.

The systematic review of land surface phenology literature published in peer-reviewed scientific journals (Scopus and Web of Science databases) for the period between 1980 and 2018 reveals that the majority of research conducted globally utilises data sets originating from the MODIS and AVHRR sensors, especially for continental or regional scale studies, with only less than 10% of the studies utilising higher spatial resolution data sets from sensors, such as Landsat 8 and Sentinel-1A and -2A for specific areas of individual countries (Caparros-Santiago et al., 2021). While recent instruments such as the European Sentinel series deliver global data at higher spatial and spectral resolutions than earlier generations of sensors, the latter have the undeniable advantage of offering observations over much longer periods of time: since 1979 for AVHRR, 2000 for MODIS and MISR, or 2002 for MERIS, for instance. More recent advances have demonstrated how land surface phenology studies can be complemented by *in situ* measurements captured by spectroradiometers (Wang et al., 2017), carbon flux estimates (Wang et al., 2019), and time-lapse photography (Richardson et al., 2018), to name a few.

Studies using both ground-based and satellite remote sensing observations suggest that in the mid and high latitudes, vegetation phenology is mostly driven by temperature and photoperiod (Piao et al., 2015), whereas water availability is considered the dominant driver in the tropics (Verger et al., 2016; Zhang et al., 2006). In the northern hemisphere, characterisations of land surface phenology suggest that temperature and precipitation are the main drivers responsible for the general advancement of spring and delay in autumn observed in plant phenophases (Richardson et al., 2013). By contrast, few studies quantifying vegetation phenological responses to environmental drivers have been undertaken for the African continent (Adole et al., 2016). A recent systematic analysis aimed at uncovering uncertainties in the relationship between phenological parameters and environmental drivers over the African content reveals that photoperiod is consistently the dominant factor controlling the onset and end of the vegetation growing season, and not one

but a combination of drivers control phenological events (Adole et al., 2019). Despite our current understanding of land surface phenology, there is still a lot of uncertainty about environmental drivers of vegetation seasonal growth and pattern, for instance, deeper inquiries across multiple scales are still needed (Tang et al., 2016).

1.3.3. Vegetation indices

Vegetation indices, combinations of surface reflectance's in two or more wavelengths of the electromagnetic spectrum (primarily the red and near-infrared wavelengths) are among the simplest indicators of the general quantity and vigour of chlorophyll in plants (Myneni et al., 1994; Kaufman and Tanré, 1992; Richardson and Wiegand, 1977; Tucker, 1979). In particular, vegetation indices compare reflectance measurements from the reflectance of vegetation in the near-infrared (NIR) range to another measurement taken in the red range, where chlorophylls strongly absorb photons for photosynthesis in the red region, while plant cell walls strongly scatter photons in the NIR region. Advances in vegetation indices is largely attributed to multispectral measurements collected on-board passive spaceborne platforms, such as the Landsat missions, Advanced Very-High-Resolution Radiometer (AVHRR) and Satellite pour l'Observation de la Terre missions, to name a few.

One of the most widely used vegetation indices, the Normalized Difference Vegetation Index (NDVI), a simplistic ratio of the red and near-infrared bands in the solar spectrum was applied with observations acquired by Earth Resources Technology Satellite (ERTS-1 also known as Landsat 1) to pioneer the land surface phenology of natural vegetation as we understand it today (Rouse et al., 1974). A systematic review of land surface phenology studies reveals that the majority research globally has utilised NDVI derived from AVHRR and MODIS observations (Caparros-Santiago et al., 2021). However, it is well-known that the NDVI saturates at high biomass content making it difficult to differentiate moderately high plant cover from very high plant cover, and is also very sensitive to a host of perturbing factors, such as atmospheric effects, and soil background and surface anisotropy (Dash and Curran, 2004; Liu and Huete, 1995; Huete, 1988; Huete et al., 2002).

Several vegetation indices have emerged since the NDVI. The Soil-Adjusted Vegetation Index (SAVI) is designed to remove the dependency of the NDVI on brightness of background (soil) reflectance, but is more sensitive to atmospheric fluctuations (Huete, 1988). The Atmospherically Resistant Vegetation Index (ARVI) is used to supress the effects of atmospheric aerosols, but it may be more sensitive to soil changes (Kaufman and Tanre, 1992). The Enhanced Vegetation Index (EVI) simultaneously corrects atmospheric and soil effects through a feedback mechanism but ignores the anisotropy of the radiance field (Liu and Huete, 1995). When using vegetation indices, caution should be exercised as they are

indicators which exist solely to exploit spectral differences between channels, despite their attempts to circumvent environmental variations. Vegetation indices propose a universal formula and unique set of coefficients for all environments, which is not grounded in any physical understanding of the properties of those environments.

1.3.4. Biogeophysical variables

In the context of remote sensing, biogeophysical variables refer to physical quantities of vegetation properties, such as chlorophyll pigments, chemical composition or structural variables, which can be related to photosynthesis and productivity. In contrast to vegetation indices, physical-based models are typically developed to derive estimates of the properties of vegetation from the remote sensing measurements, such as the Fraction of Absorbed Photosynthetically Active Radiation (FAPAR) and Leaf Area Index (LAI). The process of generating those biogeophysical variables leverages advances in radiation transfer theory, utilising algorithms which account for processes unrelated to vegetation (such as atmospheric clouds and aerosols, variations in soil moisture, anisotropic effects, etc.) to provide products that deliver a better account of plant processes.

A systematic review of land surface phenology studies globally reveals that only a limited number of studies explored the use of satellite derived biogeophysical variables, the majority of which utilised LAI and FAPAR (Caparros-Santiago et al., 2021). The LAI is a structural parameter defined as the leaf area per unit of ground surface area (Chen and Black, 1992). FAPAR measures the absorption of incoming solar radiation in the plant canopy, within the photosynthetically relevant spectral region (400 to 700 nm) (Pinty et al., 2011c). LAI derived from satellite-based measurements in the solar spectral range can only be used to characterise ecosystems that lie within a certain range of validity. This range varies with the ecosystem and the performance of the sensor. At low LAI values, small variations in vegetation may not be reliably measured as the signal may be dominated by the soil background reflectance. Conversely, dense foliage at the top of the canopy can cause the LAI to saturate obscuring the contribution from lower leaf layers in the canopy. By contrast, the FAPAR suffers less from saturation in dense canopies because the FAPAR accounts for the photosynthetically relevant spectral region, which takes place mostly in the upper layers of the canopy.

This study utilises the MISR-HR FAPAR product generated by the Joint Research Centre Two-stream Inversion Package (JRC-TIP). This algorithm interprets measurements of surface broadband albedos in terms of soil and vegetation properties, using techniques developed to invert a radiation transfer scheme against remote sensing measurements to describe the interaction of solar light with the soil and canopy environment (Pinty et al.,

2007; Clerici et al., 2010; Pinty et al., 2011a; Pinty et al., 2011b). The inversion scheme generates a range of biogeophysical parameters from an analysis of albedo products derived in part from the Rahman-Pinty-Verstraete (RPV) product (Lavergne et al., 2007; Rahman et al., 1993). As will be seen in section 1.3.6 and Chapter 2, remote sensing measurements are generally quite dependent on the particular geometry of illumination and observation, i.e., sensitive to the anisotropy of the radiance field, so that the exploitation of multi-angular measurements tend to deliver more accurate and reliable products than those derived from mono-angular instruments: this is one of the main reasons for basing the current analysis on MISR data.

The MISR-HR FAPAR product has been extensively evaluated (D'Ordorico et al., Kaminski et al., 2014; Pinty et al., 2011c) and offers distinct advantages over traditional vegetation indices. FAPAR is much better grounded in radiative transfer theory and has been identified as an "Essential Climate Variable" by the Global Climate Observing System (CGOS) (Gobron and Verstraete, 2009). The FAPAR plays a central role in quantifying the presence and state of vegetation (Gobron et al., 2006; Gobron et al., 2007) as well as the primary productivity and yield estimates (Fensholt et al., 2004; Martinez et al 2013), and is used to drive carbon cycle models (Pitman, 2003; Knorr et al., 2010; Sellers et al., 1997). A study comparing MISR FAPAR and LAI estimates retrieved using the Earth Observation Land Data Assimilation System (EO-LDAS) radiation transfer model, shows a high correlation with ground measurements recorded at FLUXNET sites (Chernetskiy et al., 2017).

1.3.5. Terrestrial primary productivity

Plants (and phytoplankton) use the sun's energy in photosynthesis and combine CO_2 and water to produce sugar molecules and oxygen. But in order to grow and metabolise, plants respire, breaking down sugar molecules in the presence of oxygen and releasing CO_2 in the process. Atmospheric CO_2 concentrations are tightly tied to pant life, fluctuating seasonally with the gradual growth and decay of plants. The total amount of organic matter produced through photosynthesis is termed gross photosynthesis, but when this is expressed as an integral of the organic matter produced by all the individual plants in a defined area per unit of time, it is termed gross primary productivity (Gitelson et al., 2006). Gross primary productivity (GPP) in ecosystems measures the total amount of carbon removed from the atmosphere by vegetation via photosynthesis and net primary productivity (NPP) accounts for the organic material which is accumulated in excess of ecosystem respiration (R_e) (Gough et al., 2011). The quantification of terrestrial GPP is becoming a major topic in global climate change studies (Anav et al., 2015). Terrestrial GPP plays a major role in the global

carbon balance, driving most carbon sequestration on land, and providing the capacity to partly offset anthropogenic CO_2 emissions (Grace et al., 2006; Janssens et al., 2003).

Inventory based estimates of terrestrial GPP and NPP were originally determined by capturing periodic measurements of plant root, stem, leaf and fruit growth. More recent technological advancements of terrestrial primary production are based on micrometeorological towers, which use the eddy covariance (EC) approach (first published by Swinbank, 1951) to directly measure the exchanges of gas, energy, and momentum between terrestrial ecosystems and the atmosphere (Baldocchi et al., 2003). The EC method has been confirmed to be the most efficient method for measuring the interactions between a terrestrial biosphere and the atmosphere on an ecological scale (Baldocchi, 2008; Friend et al., 2007). Micrometeorological methods estimate GPP and R_e indirectly. The EC method partitions net ecosystem exchange (NEE), a measure of the entire net carbon flux between the land surface and the atmosphere (Gough, 2011), into GPP and R_e (Joiner et al., 2018). However, the NEE and GPP data derived from micrometeorological measurements are representative of only a small footprint area, presenting a challenge when scaling up to entire regions (Gitelson et al., 2006).

Given that photosynthesis is directly related to the interaction of solar radiation in the canopy, remotely sensed irradiance measurements captured by EO satellites are powerful for estimating terrestrial primary productivity at local to global scales. The light-use efficiency concept (LUE) originally pioneered by Monteith (1972) suggested that the GPP of stress-free annual crops, was linearly related to the amount of photosynthetically-active radiation they absorbed, following the general expression:

$$\mathrm{GPP} = \mathrm{LUE} \times \mathrm{APAR} \qquad \text{[Eqn 1]}$$

Where APAR refers to the absorbed photosynthetically active radiation, and the LUE is an empirical factor that converts this absorbed energy to carbon fixed through photosynthesis. Later it was shown that the APAR could be estimated from spectral vegetation indices (Sellers, 1987). Consequently, the fraction of photosynthetically-active radiation absorbed by the canopy could be quantified using radiation transfer models and spectral measurements. Over the past decades, multiple approaches to estimate GPP at a global scale have been developed, but the LUE concept has been widely owing to its simple form and relatively long period of data availability (Zhang et al., 2017). Data-driven approaches have since estimated GPP globally by exploiting space-based estimates of the FAPAR (and other vegetation indices), photosynthetically-active radiation incident at the top of canopy estimated from data assimilation systems or other measurements, and parameterisations of LUE (e.g., Xiao et al., 2004; Yuan et al., 2007; Zhang et al., 2014; Zhang et al., 2017).

1.3.6. Multi-angular measurements

EO technology has been yielding a long-term record for characterising areal changes in the environment, which includes its chemical composition through spectral information, structural properties through spatial and angular measurements, and function through temporal data sets. However, it is still very common practice in the EO community to derive characterisations of terrestrial environments on the basis of observations acquired by mono-angular instruments only. Reflective surfaces are generally not isotropic in nature, reflecting solar light differently when illuminated from different directions. Typical examples include sun glint on water surfaces or the hot spot observable in structured terrestrial surfaces (Verstraete and Pinty, 2001). It is important to be cognisant of the level of uncertainty associated with mono-angular observations.

In the last three decades, the potential benefits of multi-angular observations have been recognised through the operation of innovative EO instruments, such as the Polarization and Directionality of the Earth's Reflectance (POLDER), Along-Track Scanning Radiometer (ATSR-1 and ATSR-2), and the Multi-angle Imaging SpectroRadiometer (MISR) instrument hosted on NASA's Terra platform, which has been continuously operating since February 24, 2000. These instruments provide an improved characterisation of terrestrial and atmospheric environments because multi-angular measurements permit a more accurate, quantitative decoupling of the distinct spectral and directional signatures of those geophysical media than is possible with mono-angular instruments. However, MISR is the only multi-angular spaceborne EO instrument measuring the anisotropy of planetary reflectance at sub-km spatial resolution. The radiative anisotropy of this combined geophysical system, which has long been considered a source of noise when analysing remote sensing data from mono-angular spectral instruments turns out to be a definite advantage when exploiting these more advanced instruments (Diner et al., 1999). In this context, the recent availability of land surface products at the relatively high spatial resolution of 275 m generated by the MISR-HR (for High Resolution, version 2.01-0) processing system (Verstraete et al., 2012), about weekly over a period of 2000-2018, offers new opportunities to deepen our understanding of the relation between surface properties and the fluxes of matter and energy in the environment.

Reflectance anisotropy is a combined property of the system under observation, because it depends as much on the direction of illumination as on the direction of observation. In remote sensing, spectral reflectance measurements obtained from EO instruments are not only specific to the angular conditions at which they are observed, but also the direction of illumination (Meyer et al., 1995). Unlike mono-angular instruments, multi-angular devices

measure the reflectance of targets of interest from various directions, and can therefore document the anisotropy of terrestrial targets in specific solar wavelengths, which can improve the accuracy and reliability of derived products (Pinty et al., 2002). Traditionally, the angular dependency (in zenith and azimuth) of the illumination and observation directions inherent to remote sensing observations were seen as problematic, requiring a correction or normalisation to a standard direction. However, the signatures attainable through multi-angular observations not only improve accuracies relative to single-angle approaches, but also offer unique diagnostic information about the Earth's atmosphere and surface (Diner et al., 1999). The characterisation of surface targets based on both spectral and directional measurements is complementary. The spectral reflectance is a direct measurement of the absorption characteristics of materials, it provides information on the chemical composition of the target. On the other hand, the anisotropy of the targets is largely controlled by their physical structure, hence these approaches are complementary and can help better understand the nature and state of the terrestrial environment. Figure 1 shows a plot of surface anisotropy modelled using the Rahman-Pinty-Verstraete radiative transfer model (Rahman et al., 1993) to illustrate how the MISR instrument (blue) is able to sample the bidirectional reflectance function value (BRF) of the surface at nine observation zenith angles compared to the AVHRR/MODIS instrument's (green) observation zenith angle at nadir, assuming all measurements are taking place in the azimuthal plane that is 30 degrees off the principal plane (which contains the solar zenith angle (yellow line)). The RPV radiative transfer model is discussed further in section 1.3.7 below.

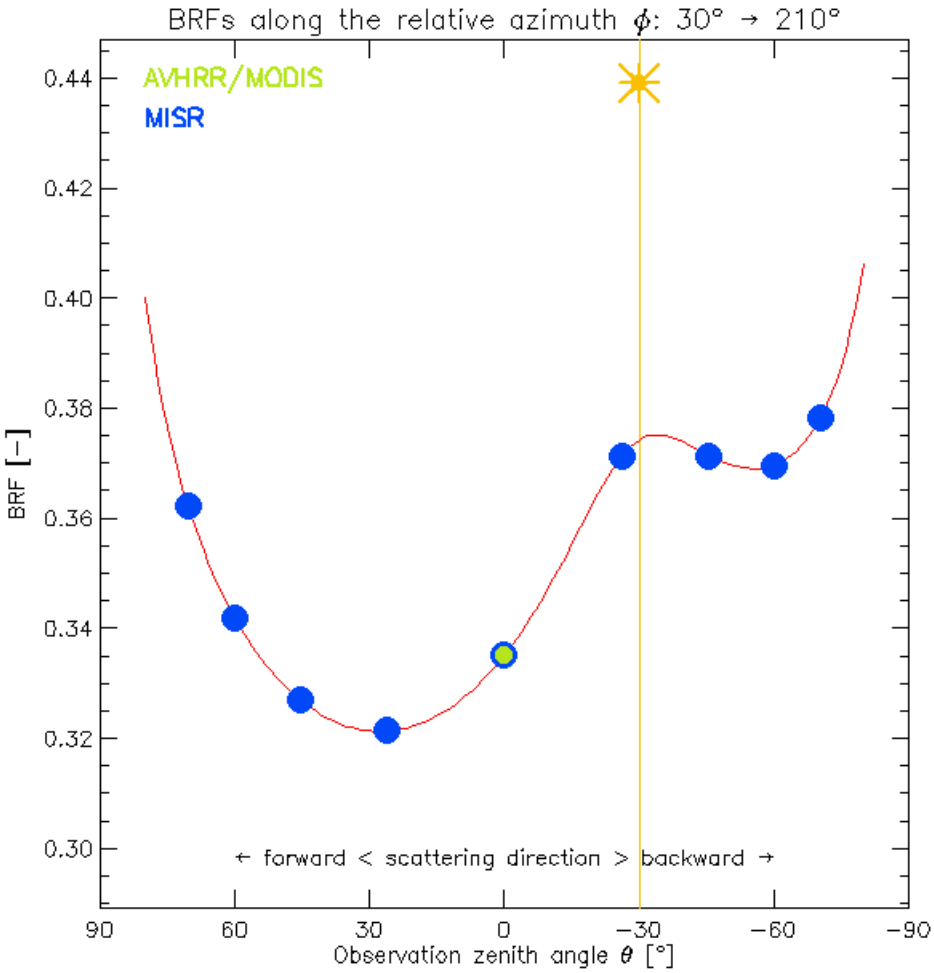


Figure 1. Plot of surface anisotropy modelled using the RPV radiation transfer model (amplitude parameter = 0.25, Minnaert parameter = 0.8 and asymmetry parameter = 0) to illustrate the bidirectional reflectance function value (red line) sampled at different MISR (blue) and AVHRR/MODIS (green point) observation zenith angles assuming the measurements are taking place in the azimuthal plane that is 30 degrees off the principal plane (which contains the solar zenith angle (yellow line))[1].

The first known scientific work observing and describing the anisotropic reflectance of surfaces was probably by Galileo Galilei in 1610, whose astronomical treatise, *Sidereus Nuncius* (The Starry Messenger), first explained why the Moon appears brightest during its opposition phase (Verstraete and Pinty, 2001). In the context of EO, fundamental research in anisotropy of the reflected radiation field can be traced back to the atmospheric scientists who pioneered the exploitation of satellite remote sensing data for meteorological and climate purposes, such as the Earth Radiation Budget Experiment (ERBE) (Barkstrom and

[1] Generated with the AnisView open source software package, provided by Dr. Peter Vogt at the Joint Research Commission, https://ec.europa.eu/jrc/en/scientific-tool/anisview. Last accessed: 25 May 2021.

Smith, 1986). Data collected by the ERBE instrument, on-board the Nimbus platform detected differences between modelled and observed anisotropy for particular scene types and Sun-Earth-satellite viewing geometries (Baldwin and Coackley, 1991; Jacobowits et al., 1984).

Nicodemus et al. (1977) developed the most comprehensive nomenclature for reflectance quantities based on the concept of the bidirectional reflectance distribution function (BRDF). In practical terms, BRDF is a function describing the ratio of the spectral radiance reflected in a given direction to the irradiance received by this target according to a specific illumination geometry; hence it measures reflectance dependency on the illumination and observation geometry (Liang et al., 2000). The reflectance of terrestrial targets varies with wavelength, illumination and sensor viewing geometry, and is determined by the structural and optical characteristics of the surface. The BRDF is often regarded as a source of error rather than information in quantitative estimates of canopy attributes, such as fractional foliage cover (Danaher, 2002). Martonchik et al. (2000) updated and adapted the physically based terminology proposed by Nicodemus et al. (1977) to remote sensing of Earth's planetary surface, and Snyder (2002) extended it to include horizontally heterogeneous surfaces. In any case, the more consistent adoption of reflectance terminology for reflectance products in the wider remote sensing community is arguably in part due to the utilisation of MISR data products (Schaepman-Strub et al., 2006).

In EO, the radiative properties of geophysical systems, such as plant canopies, exert an influence on how they scatter and absorb light. The structural and biochemical properties of vegetation largely control their surface reflectance anisotropy (Asner, 2000; Huber et al., 2010; Widlowski et al., 2004). Recent developments in radiative transfer modelling have led to the generation of better products (improved accuracies relative to mono-angular approaches) as well as new, unique diagnostic information about the Earth's atmosphere and surface that could not be retrieved from spectral measurements alone (Diner et al., 1999). In astrophysics, the Lommel-Seeliger law has long been used in planetary photometry for approximating the diffuse reflection of planetary surfaces (Fairbairn, 2005). Much of planetary photometry is based on the fundamental radiative transfer models (Chandrasekhar, 1960) and bidirectional reflectance spectroscopy theory for planetary remote sensing (Hapke, 1981).

Rayleigh (1903) and Von Helmholtz (1924) were amongst the first to describe how geophysical systems behave as turbid media. Classical turbid media models of radiation transfer provide the conceptual and mathematical framework for adequately describing the scattering of light under a number of assumptions. However, the accurate description of the

transport of photons in geophysical mediums, such as plant canopies, requires more complex models describing the physical properties of the medium (Pinty and Verstraete, 1998). When the size of the scatterers is much smaller than the wavelength of the radiation, the scatterers do not shadow each other, but leaves are much larger than the wavelength of the radiation. Thus, classical turbid media models of radiation transfer are not applicable to plant canopies without further adjustment. One of the first pioneering works on radiative transfer models for vegetation canopies in the optical domain takes into account the spatial distribution of plant leaves (Ross, 1981). Pioneering studies describing the process of radiation transfer through vegetated areas and how the process differs from its atmospheric counterpart, include the works of Gerstl and Simmer (1986), Verstraete (1987), Shultis and Myeni (1988), Verstraete (1988), Pinty et al., (1990), and Verstraete et al., (1990).

Environmental research in the Lowveld using remote sensing technologies has tended to make use of mono-angular spectral measurements from airborne and/or spaceborne sensors, which typically inform on the chemical composition of the targets (Coetzer et al., 2010; Coetzer et al., 2013; Madonsela et al., 2017; Verbesselt et al., 2007). More recently, LiDAR measurements collected during sporadic airborne campaigns have been used to characterise the structural properties of vegetation canopies, e.g., differences in canopy and sub-canopy cover height and distribution (Fisher et al., 2012; Mahlangu et al., 2018; Wessels et al., 2011). A major advantage afforded by LiDAR observations is the ability to quantify sub-canopy structural changes specifically to examine woody bush encroachment, which cannot be achieved using mono-directional spectral measurements alone (Fisher et al., 2015). Hybrid techniques, such as those offered by the Carnegie Airborne Observatory (CAO) which combines LiDAR and spectral measurements to deliver information about the vegetation canopies structure and composition has demonstrated the ability to classify individual tree species (Cho et al., 2012; Naidoo et al., 2012). To a lesser extent, Advanced Synthetic Aperture Radar (ASAR) observations, which measure surface targets irrespective of the cloud cover, have been used to create baseline maps of savanna woody cover in the Lowveld (Main et al., 2016). Research utilising cutting-edge LiDAR and ASAR technologies are novel and promising but the limited spatial coverage and the cost of obtaining the data sets mean these studies infrequent and limited in geographical scope.

1.3.7. Vegetation heterogeneity

Vegetation structure defined here refers to the vertical and spatial distribution, orientation and density of foliage within a plant community (Jupp and Walker, 1997). The structural properties of vegetation determines the pattern of light attenuation and as such also the distribution of photosynthesis, transpiration, respiration, and nutrient cycling (Widlowski et

al., 2004). Characterising vegetation structure is vital to understanding vegetation dynamics; it is indicative of the climatic, ecological and disturbance events that shape a plant community (Specht and Specht, 1999). Vegetation changes can modify local, regional, and global climate at diurnal, seasonal, and long-term scales (Bonan, 1997; Bounoua et al., 2000; Dickinson and Henderson-Seller, 1988; Kauffmann et al., 2003). The clearing of forest and grasslands for crops, for instance results in terrestrial temperature changes attributed to morphological and physiological changes in vegetation that alter its surface albedo and latent heat flux, respectively (Bounoua et al., 2002).

A recent study, using an adaptive DGVM to examine how variations in atmospheric CO_2 and fire regimes influence transient and balanced distributions of grasslands, savannas and forests in Africa, predict that under recent and near-future CO_2 conditions, these systems are more sensitive to changes in CO_2 than was previously thought (Scheiter et al., 2020). It is argued that increases in CO_2 might favour C_3 trees over C_4 grasses (IPCC, 2007). Woody encroachment in South African savannas is consistent with increases in CO_2 concentrations, for instance, but this is contested (Buitenwerf et al., 2012). Understanding the functional and structural properties of woody canopies is crucial to predict encroachment over the next century (Stevens et al., 2017). On the other hand, an increase in temperature would increase rates of C_4 photosynthesis, C_3 photorespiration and evaporative demand, which might directly or indirectly (by promoting fire) favour grasses (Scheiter and Higgins, 2009).

Remote sensing irradiance measurements possess some degree of spatial variability or heterogeneity, irrespective of spatial resolution. The individual pixels of remotely sensed data involve effective averaging over the area of land cover observed, which is further compounded by the adjacency effects of neighbouring pixels, especially in the presence of sharp contrasts in reflectance intensity. Studies using MISR data have demonstrated that using multi-angular measurements can improve estimations of vegetation structural parameters, such as vegetation heterogeneity (Gobron et al., 2002; Widlowski et al., 2001).

The MISR-HR Rahman-Pinty-Verstraete model (RPV), which describes the BRF of a surface using a combination of three parameters, ρ_0, k, and Θ should be appropriate to explore and characterise the structural properties of vegetation canopies (Engelsen et al., 1996; Lavergne et al., 2007; Pinty et al., 2002; Rahman et al., 1993). The ρ_0 parameter is a measure of the mean spectral brightness of the target (Beland and Fournier, 2008; Chopping et al., 2012; Widlowski et al., 2004). The Θ parameter captures the degree of forward or backward scattering. The k parameter, also known as the Minnaert function (Minnaert, 1941), describes the general shape of the anisotropy function, which has been used to study the structure of the environment. Gobron et al. (2002) and Pinty et al. (2002) showed that

relatively homogeneous environments, such as mostly bare soils or densely vegetated areas, exhibited a bowl-shaped anisotropy, characterised by a k<1, while strongly heterogeneous environments exhibited a bell-shaped anisotropy, characterised by k>1. This latter condition is particularly prevailing when the ecosystem is composed of a bright soil and sparse vegetation, and when the geometry of illumination and observation is conducive to such observations. This pattern has been observed at different scales, in laboratory, field, or airborne measurements, and it has also been found that heterogeneous conditions (k>1) are easier to observe and more prevalent at higher spatial resolution (Pinty et al., 2002).

A bell-shaped anisotropy is particularly prevalent when relatively sparse dark vertical structures (such as open woodland) are scattered above a bright background (such as a sandy soil, or snow, for instance). In those cases, the value of k appears to indicate the presence of a heterogeneous canopy, a condition of particular interest to ecosystems which exhibit open bush or woodland vegetation. Simulations of structurally diverse coniferous forest scenes observed that tree canopies with a Minnaert value of k_{red}>1 (i.e., shape of the anisotropy function in the red spectral band) tend to be more open than those with a Minnaert value of k_{red}<1, which implies higher light densities and increased productivity levels in the lower canopy layers, consequently offering opportunities to study the role of canopy heterogeneity on primary productivity (Widlowski et al., 2004).

1.3.8. Aperiodic climatic fluctuations

The Earth's weather and climate are determined by the amount and distribution of radiant solar energy. Seasonal fluctuations are attributed to the Earth's orbit around the Sun and axial tilt relative to the ecliptic plane. The temporally recurring daily and seasonal fluctuations of water availability and temperature regimes impose natural cycles, which constrain vegetation phenology. Radiant solar or shortwave energy also gives rise to a rich variety of weather or turbulent phenomena in the atmosphere and ocean. African savannas can assume different stable states of carbon flux under present day climate and fire regimes, such as tree dominated or C_4 grass dominated depending on the pre-historical vegetation state of the region (Bond et al., 2005). Large-scale non-seasonal atmosphere-ocean climactic fluctuations provide a useful framework to relate carbon fluxes to climate fluctuations (Zhu et al., 2017).

The El Niño – Southern Oscillation (ENSO) is regarded as the dominant coupled ocean-atmosphere phenomenon driving climate variability (Trenberth, 1997; Wolter and Timlin, 2011). The sea surface temperatures (SSTs) of a vast region of the Equatorial Eastern Pacific Ocean fluctuates irregularly with a periodicity of 2 to 5 years or even 7 years. The Niño 3.4 region (5N-5S, 170W-120W) provides a long-term continuous record based on

SSTs averaged across the equatorial tropical Pacific Ocean and is regarded as the key region for monitoring and predicting El Niño and La Niña events (Trenberth, 2001). The occurrence of peaks and troughs in SST indices has been associated with other climatic events worldwide (Lyon and Barnston, 2005; McPhaden et al., 2006). El Niño (warming) events are classified as periods when the consecutive 3-month running mean of Sea Surface Temperature (SST) anomalies in the Niño 3.4 region exceed the +0.5°C threshold, and La Niña (cooling) events qualify as periods when the SST anomalies are below the -0.5°C threshold. This threshold is also used to define weak (with a 0.5 to 0.9 SST anomaly), moderate (1.0 to 1.4), strong (1.5 to 1.9) and very strong (≥ 2.0) events.

Long-term observations since the 1950s show that El Niño usually causes rainfall deficiencies over Indonesia and northern South America, and excess rainfall in the south eastern parts of South America, eastern equatorial Africa, and the southern US (Lyon and Barnston, 2005). Similar connections with climatic events have been established over Southern Africa, where deviations from expected temperature and rainfall patterns have been linked to ENSO events (Dieppois et al., 2015; Lakhraj-Govender and Grab, 2019; Pomposi et al., 2018). However, not every El Niño coincides with the rainfall deficits over the region. The relationship between southern Africa precipitation variability and ENSO is complex, given modulations with other basins and internal atmospheric variations (Pomposi et al., 2018).

ENSO have been studied for decades, but at large spatial scales and over periods ranging from multiple years to few decades (Lyon and Barnston, 2005; Trenberth, 1997). Statistical studies relating vegetation dynamics to ENSO fluctuations have been established for entire biomes, but few detailed investigations, if any, have been conducted at the finer spatial scales of bioregions, especially for African ecosystems (Anyamba et al., 2002; Anyamba et al., 2018; Nicholson and Kim, 1997; Parhi et al., 2016; Philippon et al., 2014).

1.3.9. Consequences of climate change

Vegetation dynamics respond to a range of interacting forces. Climate change is expected to impact ecosystem structure and functioning, as well as possibly modify the spatial distribution of ecosystems and biomes (Archer, et al., 2018; Engelbrecht and Engelbrecht, 2016; Hoegh-Guldberg et al., 2018; Niang et al., 2014). It is argued that changes in environmental drivers are expected to impact savanna vegetation by influencing resource availability and feedback effects arising from changes in top-down controls (Sankaran and Ratnam et al., 2013).

Coupled climate carbon cycle model simulations predict that warming over the African continent may prompt a reduction of net ecosystem productivity, making a 38% contribution

to the global climate-carbon cycle positive feedback by the end of the 21st century (Friedlingstein et al., 2010). In Southern Africa, air temperature near the ground has been increasing rapidly over the last five decades, at about twice the rate of the globally average surface temperature (Archer et al., 2018; Engelbrecht et al., 2015; Jones et al., 2012). This trend is expected to have a significant impact on vegetation cover in savanna biomes, which cover one-third of the country.

In some regions, fewer but more intense rainfall events are projected with longer intervening dry periods (IPCC, 2007), which would result in significant impacts on vegetation dynamics in savannas. Changes in rainfall intensity across sub-Saharan Africa may result in an increase in trees and shrubs in previously open grasslands and rangelands, and limit tree growth in wetter savannas (D'Onofrio et al., 2018; D'Onofrio et al., 2019). In many regions, savannas are projected to shift toward more wooded states as C_3 trees gain a competitive advantage over C_4 grasses under increased atmospheric CO_2 concentrations (Midgley and Bond, 2015; Osborne et al., 2018; Sage and Kubien, 2003; Wigely et al., 2010). Woody encroachment is also likely to reduce the strength of fire-imposed bottlenecks (Bond and Midgely, 2012).

Whilst the projected effects of climate change in savannas is well documented, large uncertainties between models mean that adaptation strategies will need to be highly flexible (Martens et al., 2020). Also, the literature concerning vegetation productivity in terrestrial environments is vast, but as previously noted, mostly documented for developed regions in temperate latitudes (Adole et al., 2016). These studies also tend to rely on traditional vegetation indices, such as the NDVI despite major scientific and technological advances, which provide more accurate estimations of vegetation productivity (e.g., FAPAR). Studies utilising MISR observations which are available at the nominal Top of the Atmosphere globally in 36 spectro-directional channels since late February 2000 are very rare particularly over developing regions.

1.4. Structure of the dissertation

Chapter one covers the rationale, aim and objectives, and literature review of the research. Chapter two includes the bulk of the methodology and addresses objective 1 of the study. The chapter was accepted for publication on 24 November 2020 (De Lemos et al., 2020). It discusses the use of parametric double S-shaped functions (Gaussian, hyperbolic tangent, logistic and sine) to model the phenology of vegetation as observed by the MISR-HR instrument despite missing data and irregular temporal coverage, predominantly due to obscuration by clouds. The chapter is appended to the document with a preface and

postface, which introduce the purpose of the work and how the findings link to the research presented in Chapter three.

Chapter three addresses objective 2; discusses the seasonal and long-term impacts of vegetation in the Lowveld region in response to aperiodic fluctuations in sea surface temperatures over a wide region of the eastern tropical Pacific Ocean. The chapter is structured as a standalone article as the intention is to submit it to a peer refereed journal.

Chapter four provides a detailed discussion of how the problems identified, which drove this research, resulted in the development of new knowledge and was innovative at:

i. Presenting a methodology for characterising the phenology of the natural, unmanaged vegetation in the Lowveld despite the presence of spatio-temporal gaps in the satellite observations.
ii. Finding linkages between between the behaviour of vegetation phenology in the Lowveld region to the influence of coupled ocean atmosphere phenomena.

The combined references include the references for chapters 1, 3 and 4. Chapter 2 includes an appended published article with its own referencing style and reference list.

CHAPTER 2 PARAMETRIC MODELS TO CHARACTERIZE THE PHENOLOGY OF THE LOWVELD SAVANNA AT SKUKUZA, SOUTH AFRICA

PREFACE

One of the biggest challenges confronting terrestrial observations from remotely sensed imagery observed from optical-based instruments on-board space-borne platforms is the obscuration of the surface by atmospheric constituents during acquisition. This manifests spatially as regions of missing values (depending on the distribution of clouds and aerosols) and gaps in time series. To a lesser extent, some observations may be unavailable because of systematic errors at the receiving station and/or technical problems with the platform.

The vast majority of published studies use the Gaussian and logistic functions to model the phenology of vegetation and fill these gaps. Most also focus on agricultural areas, which follow regular seasons and are often accompanied by phenological calendars of key events, such as first full leaf burst. The Normalized Difference Vegetation Index (NDVI) derived from satellite-based observations is often used for characterising land surface phenology, even though better suited variables are available for this purpose, such as the Fraction of Absorbed Photosynthetically Active Radiation (FAPAR). This chapter presents a methodology for testing the capacity of four parametric double S-shaped functions (Gaussian, hyperbolic tangent, logistic and sine) to characterise the phenology of natural, unmanaged vegetation in the Lowveld despite the presence of missing data values in MISR-HR FAPAR. The results of the modelled inversions were subjected to accuracy, precision and efficiency testing.

The accuracy (or representativeness) of the modelled results were confronted to daily *in situ* measurements of Gross Primary Productivity (GPP) as measured by the Skukuza Eddy covariance (EC) flux tower for the period between 2000 and 2013 when the GPP data are available. Using a discrete integral approach, the modelled FAPAR were aggregated by vegetative seasons to represent biomass accumulation, a proxy for terrestrial GPP. The integrated results were then compared to GPP estimates at the Skukuza EC flux tower as they currently represent the only publicly available and relevant records for that region. Terrestrial GPP is not measured directly either at the ground or by satellites. EC flux towers estimate GPP by partitioning NEE and R_e (Anav et al., 2015), whereas satellite-based approaches estimate GPP using spectral measurements in combination with models and various assumptions, such as the LUE concept (Monteith, 1972 and 1977). The evaluation between GPP estimated from tower-based carbon flux measurements and satellite data is novel but complementary (Wang et al., 2019).

The adequacy of these models to account for the observed variability was evaluated using the cost function, a measure of how well the original MISR-HR FAPAR data values fit the modelled results. Efficiency was evaluated through an examination of the relative computational time taken by the models to succeed or fail at converging.

The results show that all functions were capable of simulating the phenology of the vegetation canopy over the study area, provided the FAPAR values were well distributed in time. But the models do differ in their efficiency and effectiveness with respect to the presence of missing data values. The hyperbolic tangent appears to be the least sensitive (i.e., the most tolerant) to the particular distribution of input data although it is somewhat more computationally expensive. The sine model fits the FAPAR data with the smallest cost function value, but is the most sensitive to the presence of gaps in the FAPAR data. The comparisons of modelled FAPAR with *in situ* GPP suggests that FAPAR may be appropriate to monitor GPP in the range from 0 to 5 gC m^{-2} d^{-1}, but that it loses sensitivity at larger values, due to the saturation of the non-linear asymptotic relation.

The study suggests that appropriate techniques to reduce the impact of gaps in the data (through either spatial or temporal interpolation) may significantly improve the capacity of those models to represent the phenology of vegetation canopies. Future work should also consider the inclusion of GPP from the Malopeni, Vuwani and Agincourt Eddy covariance flux towers to confirm the sensitivity between large GPP and FAPAR values in the vegetation canopy of the Lowveld region.

remote sensing

MDPI

Article

Parametric Models to Characterize the Phenology of the Lowveld Savanna at Skukuza, South Africa

Hugo De Lemos [1,*], Michel M. Verstraete [1] and Mary Scholes [2]

[1] Global Change Institute, University of the Witwatersrand, Braamfontein-Johannesburg 2050, South Africa; Michel.Verstraete@wits.ac.za or MMVerstraete@gmail.com

[2] School of Animal, Plant and Environmental Sciences, University of the Witwatersrand, Braamfontein-Johannesburg 2050, South Africa; Mary.Scholes@wits.ac.za

* Correspondence: 0402879V@students.wits.ac.za or HDeLemos@gmail.com

Received: 4 November 2020; Accepted: 24 November 2020; Published: 30 November 2020



Abstract: Mathematical models, such as the logistic curve, have been extensively used to model the temporal evolution of biological processes, though other similarly shaped functions could be (and sometimes have been) used for this purpose. Most previous studies focused on agricultural regions in the Northern Hemisphere and were based on the Normalized Difference Vegetation Index (NDVI). This paper compares the capacity of four parametric double S-shaped models (Gaussian, Hyperbolic Tangent, Logistic, and Sine) to represent the seasonal phenology of an unmanaged, protected savanna biome in South Africa's Lowveld, using the Fraction of Absorbed Photosynthetically Active Radiation (FAPAR) generated by the Multi-angle Imaging SpectroRadiometer-High Resolution (MISR-HR) processing system on the basis of data originally collected by National Aeronautics and Space Administration (NASA)'s Multi-angle Imaging SpectroRadiometer (MISR) instrument since 24 February 2000. FAPAR time series are automatically split into successive vegetative seasons, and the models are inverted against those irregularly spaced data to provide a description of the seasonal fluctuations despite the presence of noise and missing values. The performance of these models is assessed by quantifying their ability to account for the variability of remote sensing data and to evaluate the Gross Primary Productivity (GPP) of vegetation, as well as by evaluating their numerical efficiency. Simulated results retrieved from remote sensing are compared to GPP estimates derived from field measurements acquired at Skukuza's flux tower in the Kruger National Park, which has also been operational since 2000. Preliminary results indicate that (1) all four models considered can be adjusted to fit an FAPAR time series when the temporal distribution of the data is sufficiently dense in both the growing and the senescence phases of the vegetative season, (2) the Gaussian and especially the Sine models are more sensitive than the Hyperbolic Tangent and Logistic to the temporal distribution of FAPAR values during the vegetative season, and, in particular, to the presence of long temporal gaps in the observational data, and (3) the performance of these models to simulate the phenology of plants is generally quite sensitive to the presence of unexpectedly low FAPAR values during the peak period of activity and to the presence of long gaps in the observational data. Consequently, efforts to screen out outliers and to minimize those gaps, especially during the rainy season (vegetation's growth phase), would go a long way to improve the capacity of the models to adequately account for the evolution of the canopy cover and to better assess the relation between FAPAR and GPP.

Keywords: FAPAR; Lowveld; MISR; MISR-HR; modeling; phenology; savanna; seasonality

1. Introduction

Vegetation regulates the carbon, energy, and water fluxes between the land and the atmosphere. Plants affect and respond to environmental and especially climatic conditions: they typically exhibit annual variations that match the seasonal evolution of temperature, water availability, solar irradiance, and other critical variables. Hence, they are also sensitive to climate fluctuations and changes. Phenology, the study of the seasonal evolution of plants, documents these variations and therefore provides evidence of the impact of climate change on the environment.

The Special Report on Emissions Scenarios (SRES) socio-economic CO_2 emission scenario A2 of the Intergovernmental Panel on Climate Change (IPCC) provides a suitable context to evaluate conditions appropriate for the African continent. Under this scenario, Friedlingstein et al. [1] estimate that climate warming during the 21st century may reduce the net ecosystem productivity of the African continent and contribute up to 38% of the global climate-carbon cycle feedback. Properly characterizing vegetation's phenology is crucial to document this evolution and to accurately parameterize the global land-atmosphere models [2]. In Southern Africa, air temperature near the ground has been increasing rapidly over the last five decades, at about twice the rate of the globally average surface temperature [3–5]. These changes, and associated fluctuations in the water cycle, are expected to have a significant impact on vegetation cover in the savanna biome, which occupies about 20% of the global land surface and 40% of Africa, according to Kutsch et al. [6].

Phenology, may have notable economic implications, as plant growth and development depend on the occurrence of essential weather events. Natural hazards, such as drought, flood, or fire, can jeopardize agricultural yield in a given year, or sometimes the sustainability of that economic activity. Phenology also informs on the land use and land cover type, providing useful information to manage societies, their economic systems, as well as to monitor the evolution of unmanaged areas, such as nature reserves. In the particular context of African ecosystems, savanna woody vegetation provides valuable ecosystem services [7,8], and the effective estimation of those resources is required to satisfy commitments to monitor and manage change within them [9].

Repeated observations of the density and diversity of woody plant species in African savanna regions suggest that variations in species composition and diversity are to a great extent also influenced by land use and anthropogenic disturbances [10]. In South Africa, and in the Lowveld in particular, rural households critically depend on fuelwood as a source of energy because of the prohibitive cost of gas and fuels. This socio-economic constraint has resulted in the exploitation of natural resources well beyond their capacity to regenerate, and therefore in the progressive deforestation of those environments. That situation leads to wood scarcity, as well as potential, and, in many cases, actual, conflicts over access to resources [11]; it is further exacerbated by a continuous exodus from rural areas to towns and cities, as well as by immigration from neighboring countries. As a result, settlements have been expanding and their environmental footprints have become more severe over time [12].

This paper leverages two resources to bear on this problem: remote sensing and field measurements to provide empirical evidence, and modeling to provide a rational framework for the interpretation of the data, despite the uncertainties inherent to all measurements, the irregular distribution of observations in time and missing data for various reasons. The aims of this methodological study were (i) to assess the suitability of four parametric double S-shaped functions (the Gaussian, Hyperbolic Tangent, or Logistic and Sine) to describe the phenology of savanna vegetation in the Lowveld, and (ii) to evaluate the capability of these data and models to account for the Gross Primary Productivity (GPP) of the vegetation around the Skukuza flux tower in South Africa's Kruger National Park. This is of particular interest insofar as GPP is one of the contributing factors to estimate biomass accumulation or yield (in an agricultural context).

2. Study Area

The study site is centered on the Skukuza Eddy Covariance (EC) flux tower, which falls within the Lowveld in the north eastern part of Mpumalanga Province of South Africa (Figure 1). The Lowveld predominantly belongs to the large savanna biome, which covers one-third of the country. It is characterized by hot humid summers and mild dry winters. Summer rains occur between October and May across a west to east precipitation gradient, with a mean annual precipitation of 633 mm and mean annual temperature of 21 C [13]. The Lowveld's dominant geology includes granite and gneiss with local gabbro intrusions [14]. The slopes and crests are characterized by a mixture of tall shrubland with few trees to moderately dense low woodland, and valleys dominated by dense thicket and open savanna. Vegetation distribution and density in the region are influenced by the rainfall gradient, geology, fire events, mega-herbivore browsing, cattle grazing, and the anthropogenic harvesting of wood [14,15]. Coppicing is prominent in areas which experience high levels of anthropogenic utilization [9]. Granite lowveld is the main vegetation unit in the area, with dominant tree species, including *Terminalia sericea*, *Combretum zeyheri*, *Combretum apiculatum*, *Acacia nigrescens*, dominant shrub species, including *Dichrostachys cinerea* and *Grewia bicolor*, and dominant grass species, including *Pogonarthria squarrosa*, *Tricholaena monachne*, *Eragrostis rigidior*, *Panicum maximum*, *Aristida congesta*, *Digitaria eriantha*, and *Urochloa mossambicensis* [13].

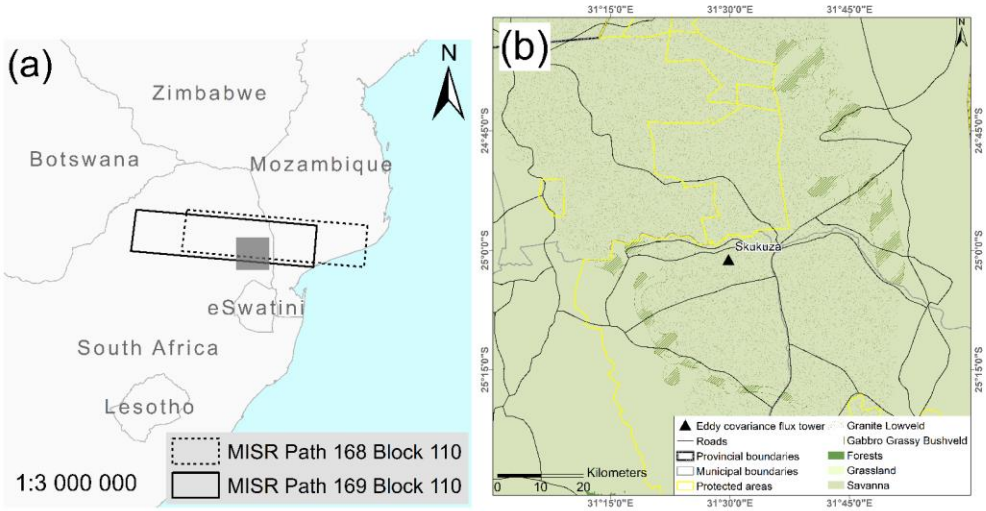


Figure 1. Panel (**a**): Location of the study site in the Lowveld of South Africa with overlapping footprints of Multi-angle Imaging SpectroRadiometer (MISR) Block 110 for Path 168 (dotted rectangle) and 169 (full rectangle). Panel (**b**): Detailed map of the environment around Skukuza in the Kruger National Park. Source: South African National Biodiversity Institute (SANBI), acquired from https://www.sanbi.org/link/bgis-biodiversity-gis/.

3. Data Collections

3.1. Satellite Measurements

3.1.1. Background

Observations of land surfaces from spaceborne platforms started in earnest in the early 1970s with the launch of the Earth Resources Technology Satellite (ERTS-1), subsequently renamed Landsat 1. In turn, the availability of multispectral measurements stimulated the development of methods to explore the significance and implications of those observations in practical applications. Rouse Jr. et al. [16] and [17]

suggested that the ratio subsequently known as the Normalized Difference Vegetation Index (NDVI) was adequate to monitor "the vernal advancement and retrogradation (Green wave effect) of natural vegetation", i.e., to monitor plant phenology as we understand it today. These events mark the start of a sustained effort to monitor the biosphere on the basis of space observations [18].

Over the past 50 years, significant progress has been achieved, and thousands of publications have been published [19], to characterize the state and evolution of plant canopies using observations of the reflectance of the planet in the solar spectral range. A full review of the literature dealing with the documentation of plant phenology on the basis of remote sensing measurements is outside the scope of this paper, but it is worth noting that progress has been achieved on multiple fronts:

1. Major advances in understanding the processes of radiation transfer in complex environments resulted in the design and implementation of much improved algorithms. These aimed to effectively account for processes unrelated to vegetation (such as atmospheric clouds and aerosols, anisotropic effects, contributions to the measured signals due to variations in soil moisture, etc.) and to deliver reliable and accurate products to describe plant processes. The Fraction of Absorbed Photosynthetically Active Radiation (FAPAR) is a case in point, since it has been identified as one of the *Essential Climate Variables* (ECV) by the Global Climate Observing System (GCOS) [20]. These developments, in turn, led to a more quantitative representation of plant phenology (in [21–23]).
2. The technology of measuring reflected radiation on spaceborne platforms has improved drastically, and is currently able to deliver up to hundreds of spectral bands at spatial resolutions of the order of tens of meters or less, sometimes on a daily basis, or to acquire data from multiple directions or in multiple polarizations. Data fusion with observations obtained with different instruments (e.g., LiDARs: see [24–26]) or in entirely different spectral regions (e.g., microwaves: see [27–29]) have also been explored, though much remains to be done in order to provide a holistic description of the environment, or of plant phenology in particular.
3. Progress in the field of information technology delivered computing, networking and data archiving resources and capabilities orders of magnitude faster and more performant than even a few decades ago, and permitted the investigation of complex issues. Although the drive to acquire more and better observations continues unabated, the major bottleneck today concerns the actual analysis of those data and the extraction of useful information from the immense archives that have already been accumulated.

As a result, Earth observing satellites have yielded a long-term record of changes in vegetation photosynthetic activity, while ground-based eddy covariance measurements are providing automated, continuous and spatially averaged measures of carbon exchanges between the surface and the atmosphere. A global increase in 'greening' has been evidenced through remotely sensed indices, such as the Leaf Area Index (LAI) and Normalized Difference Vegetation Index (NDVI), suggesting an increase in the seasonally-integrated LAI of up to 25–50%, while less than 4% of the terrestrial areas exhibit a decrease of LAI [30]. Key drivers of phenology include temperature and photoperiod in the mid- and high-latitudes [2,31–33], while precipitation is regarded as the dominant driver in the tropics [34,35]. Satellite-based observations have been widely used to characterize the evolution of vegetation in the Northern Hemisphere, but other regions have received far less attention: A systematic review of phenology in Africa over the last decade reveals a recent increase in the number of phenological studies based on remote sensing but suggests that further investigations are needed across this continent, especially to focus on the relationship between climate and vegetation phenological changes [36].

Remote sensing research in the Lowveld has tended to focus on the use of mono-directional spectral measurements (from airborne and/or spaceborne sensors) which typically inform on the chemical composition of the targets (in [37–40]). More recently, sporadic airborne campaigns collecting Light

Detection And Ranging (LiDAR) measurements have been used to document the structural properties of the vegetation canopies, e.g., to map the differences in canopy and sub-canopy cover height and distribution [26,41,42]. One of the main advantages of using LiDAR observations is the ability to capture sub-canopy structural changes specifically to examine bush encroachment, otherwise unattainable in mono-directional spectral measurements which only account for the aerial extent of the vegetation canopy [43]. Hybrid techniques combining structural observations from LiDAR and spectral measurements from hyperspectral and multispectral data sets demonstrate the ability to classify individual tree species [25,44]. To a lesser extent, Advanced Synthetic Aperture Radar (ASAR) measurements, which can observe the surface irrespective of the cloud cover, have been used to create regional scale baseline maps of savanna woody cover in the Lowveld [9]. Cutting-edge approaches utilizing LiDAR, ASAR, and hybrid-techniques are very interesting but infrequent and limited in geographical scope, constrained in part by the limited spatial coverage and the cost of obtaining the data sets.

3.1.2. Multi-Angular Observations

Anisotropy is typically considered a source of noise when analyzing remote sensing data from mono-angular spectral instruments but constitutes a definite advantage when analyzing measurement from multi-angular instruments [45]. Over the last three decades, the potential benefits of multi-angular observations have been recognized through the operation of innovative Earth Observation (EO) instruments, such as the Along-Track Scanning Radiometer (ATSR-1 and ATSR-2), the Polarization and Directionality of the Earth's Reflectance (POLDER), and the Multi-angle Imaging SpectroRadiometer (MISR) instrument on-board National Aeronautics and Space Administration (NASA)'s Terra platform, which has been continuously operating since 24 February 2000. These instruments generate an improved characterization of the atmospheric and terrestrial environments because multi-angular measurements permit an accurate, quantitative decoupling of the distinct spectral and directional signatures of those geophysical media.

In this context, the recent availability of land surface products at the relatively high spatial resolution of 275 m generated by the MISR-HR (for High Resolution; version 2.01-0) processing system [46], about weekly over the period 2000–2018, offers new opportunities to explore the relation between surface properties and the fluxes of matter and energy in the environment. Appendix A summarizes the specifications of the MISR instrument and outlines the products generated by the MISR-HR processing system. Specifically, the Joint Research Centre-Two-stream Inversion Package (JRC-TIP) algorithm [47,48] derives the Fraction of Absorbed Photosynthetically Active Radiation (FAPAR) product from an analysis of albedo values obtained by integrating the Rahman-Pinty-Verstraete (RPV) model [49,50]. FAPAR is a measure of the absorption of incoming solar radiation in the canopy, within the photosynthetically relevant spectral region (400 to 700 nm) (in [51,52]). The JRC-TIP inversion process returns the final value of the cost function, as well as estimates of the variance, associated with each product: the former is a measure of the distance between the model and the data, while the latter measures the uncertainty associated with the retrieved product.

3.1.3. MISR-HR FAPAR Product for Skukuza

This MISR-HR FAPAR product has been extensively evaluated [53–56] and serves as a benchmark in various contexts, as noted earlier. It also offers three advantages over the traditional NDVI used in many phenological studies: (1) FAPAR is much better grounded in radiation transfer theory and has been identified as an "Essential Climate Variable" by the GCOS, which is not the case for NDVI, (2) this particular product is derived using the JRC-TIP algorithm, a state of the art inversion procedure that has been extensively validated (see, e.g., https://fapar.jrc.ec.europa.eu/Home.php, last visited on

21 November 2020), and routinely used by the Committee on Earth Observation Satellites (CEOS) Working Group on Calibration and Validation (WGCV) and the European Commission Quality Assurance for Essential Climate Variables (QA4ECV) project, for instance, and (3) this product is made available at a higher spatial resolution (275 m) than any of the traditional global vegetation index products (500 m at best, and often 1 km or more) available over the last 20 years.

The Skukuza flux tower site falls within Block 110 of MISR Paths 168 and 169 (Figure 1, panel (a)). The repeat period of this instrument for a single Path is exactly 16 days, but the study area is located within the overlap of those Paths, giving a staggered revisit period of seven and nine days between those two Paths. A total of 859 combined Orbits for both Paths (i.e., 429 and 430, respectively) were acquired between 15 March 2000 and 30 December 2018; 17 of them were irretrievable from NASA's Atmospheric Science Data Center (see https://asdc.larc.nasa.gov/project/MISR/, last accessed on 14 October 2020.), due to technical issues with the platform. As a result, the longest period between successive acquisitions is 32 days. However, cloudiness further reduces the availability of usable surface observations, so the time gaps between successive observations is typically 7 or 9 days during the dry season, but may reach up to 100 days or more during the wet season.

The MISR-HR FAPAR product is made available on the Space Oblique Mercator (SOM) map projection, like all standard MISR data products. This projection minimizes shape distortion and scale errors throughout the length of the Orbit near the satellite ground track. However, each Path possesses its own unique SOM map projection parameters, so assembling data sets involving two or more Paths imply re-projecting the data onto a common grid, in this case, the geographic spatial reference system, i.e., European Petroleum Survey Group (EPSG) code: 4326, as explained below in Section 4.2.2.

3.2. Flux Tower Observations

Flux towers use micrometeorological measurements and the Eddy Covariance (EC) method (first published by [57]) to directly observe air motion and gas concentrations at two or more heights, and to estimate the exchanges of gas, energy, and momentum between the terrestrial biosphere and the overlying atmosphere on an ecological scale from the covariance between fluctuations in those variables [58–60]. GPP (expressed in units of $g_C\,m^{-2}\,d^{-1}$) is derived from an analysis of those data. Figure 2 shows the relation between the GPP and precipitations, in this case, estimated as part of the European Centre for Medium-Range Weather Forecasts (ECMWF) Re-Analysis (ERA)-Interim reanalysis project.

It is important to note, from the outset, that unmanaged, protected areas in a National Park are not monitored or used like an agricultural field: there is no planting or harvesting date, and nobody observes the emergence of leaves or flowers. This would be difficult in any case, given the diversity of species involved. Hence, the characterization of the phenology of the canopy must be derived from remote sensing measurements and access to local observations from an EC flux tower provides a unique opportunity to establish possible relations between remote and in situ measurements, even though these address quite different biogeophysical variables.

The Skukuza EC flux tower is located at 25°1′10.54″S, 31°29′48.6″E within the Kruger National Park, near the Skukuza camp, at an altitude of 365 m above sea level. It has been in continuous operation since 2000, and stands on the ecotone between broad-leafed *Combretum* savanna on sandy soil and fine-leafed *Acacia* savanna on clayey soil [61]. Woody vegetation height ranges between eight and ten m, and the flux sensors on the tower are 17 m above ground, implying a sensor footprint of about 500 m [62]. The Skukuza flux tower currently makes use of the LiCor 7500 open-path infrared gas analyzer to measure carbon dioxide (CO_2, μmol mol^{-1}) and water vapor (H_2O, mmol mol^{-1}) concentrations, as well as ultrasonic anemometers (Gill Wind Master Pro and Campbell Scientific CSAT3), to measure horizontal and vertical fluctuations in wind speed (m s^{-1}) and air temperature (K).

NASA erected this flux tower as part of the Southern African Regional Science Initiative (SAFARI–2000), an international field campaign investigating emissions, transport, transformation and deposition of trace gases and aerosols over southern Africa between 1999 and 2001 [61,63–65]. The tower was subsequently donated to the Council for Scientific and Industrial Research (CSIR).

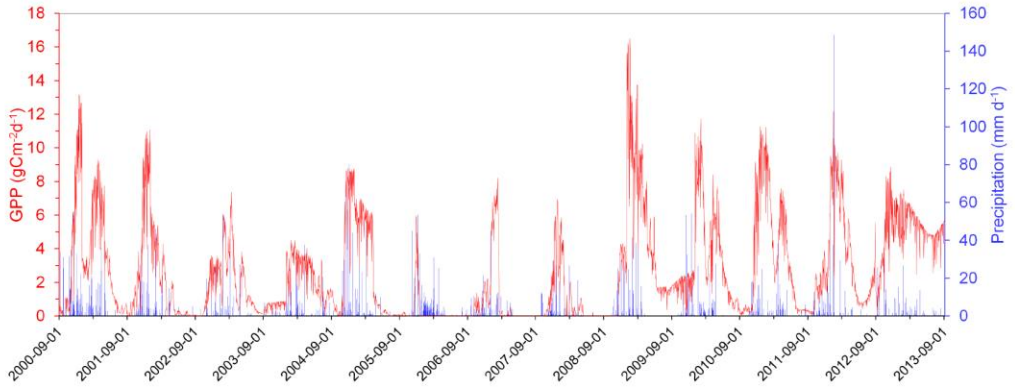


Figure 2. Time series of daily values for the Gross Primary Productivity (GPP) of the unmanaged vegetation around the Skukuza Eddy Covariance (EC) flux tower (in red) and the daily precipitation estimated by the ERA-Interim reanalysis data accompanying the FLUXNET2015 archive.

The Skukuza EC flux tower measurements confirm the close inter-connection between the water and carbon fluxes: ecosystem respiration is highest at the onset of the wet season, continuously decreasing during the transition towards the dry season [6]. Variations in precipitation between years, which influence variations in the amount of green leaf area, seasonal patterns, and soil water availability are the main drivers of Net Ecosystem Exchange [62]. This approach has been used to estimate GPP [66], as well as to partition the energy fluxes, at the surface [67].

For the purpose of this study, the Skukuza flux tower data set processed by the FLUXNET organization (Site Id: ZA-Kru) was downloaded from the FLUXNET2015 data archive (Available from the portal https://doi.org/10.18140/FLX/1440188, last accessed on 14 October 2020.). This organization coordinates regional and national networks to harmonize the compilation, archival and distribution of data to the scientific community. It comprises over 900 flux tower sites globally (See https://fluxnet.fluxdata.org/, last accessed on 14 October 2020.). Data were originally released in December 2015 and subsequently updated in July 2016 and November 2016, following the procedures and quality controls described in [68,69]. The ERA-Interim global reanalysis data set of the European Centre for Medium-Range Weather Forecasts (ECMWF) is used to fill extended gaps of micrometeorological variable records. These data are distributed under the CC-BY-4.0-based data policy (See https://creativecommons.org/licenses/by/4.0/, last accessed on 14 October 2020.).

The reliability of phenological information derived from satellite remote sensing observations is evaluated by confronting them to flux tower results [70,71]. The availability of both remote sensing and field measurements at the Skukuza site thus offers a unique opportunity to characterize the phenology of that biome.

4. Data Processing

4.1. Measurement Uncertainties and Missing Data

Each plant species typically follows its own phenological development, itself dependent on the locally prevailing conditions. For their part, spaceborne EO instruments acquire measurements (usually over

areas large with respect to the dimensions of plants, hence containing many plant species), over periods of time which may or may not coincide with the specific observational needs at any given location. Individual observations are associated with measurement uncertainties, which result from systematic, as well as random, errors, due to incorrect or biased calibration, and intrinsic limitations on the precision of the instrument, respectively. In addition, optical instruments measure the combined contributions of the planetary surface and the overlying atmosphere: clouds and aerosols can perturb or prevent observations of the surface. Measurements actually useful to characterize the phenology of plant canopies are therefore scattered in space and time, especially during rainy seasons [72].

Models, such as the ones described below, are required to provide a reliable representation of the phenology of plant canopies despite these challenges. Once they have been adjusted to optimally fit the available empirical evidence, they can be used to provide a simplified stable characterization of the evolution of plant canopies. The combined empirical evidence on phenology derived from remote sensing and ground-based observations has been shown to improve the accuracy of models simulating surface-atmosphere interactions (in [73–75]).

4.2. Pre-Processing

4.2.1. Screening Outliers

The reliability of an analysis based on measurements clearly depends on the accuracy of the inputs, so outliers and doubtful items should be culled out of the data. As explained above and in Appendix A.2, FAPAR values are themselves obtained through a model inversion procedure, and their accuracy and reliability can be quantitatively assessed by inspecting two pieces of information: the variance associated with the reported values, and the value of the cost function at the end of the inversion process. Whenever the latter exceeds a given threshold (in this case, set to the 90th percentile of its distribution), the mismatch between the model and the empirical evidence is deemed excessive and the corresponding data items are discarded, following the approach described in Liu et al. [76]. This is preferable to traditional statistical methods (such as box-and-whisker statistics) because it eliminates not only obvious outliers but also data values that may look reasonable but are probably questionable: a high cost function value betrays a mismatch between the JRC-TIP model and the input data and often results in one or more of the model parameters taking on unusual or obviously unbelievable values. This process, thus, tends to discard more data points than would be eliminated on the basis of extreme values only but yields a time series of high quality.

The threshold of acceptability can be fine-tuned by inspecting the histogram of cost function values, which typically exhibits a long tail of occasional large values, so the selection of a particular value within that tail is not very crucial, as it screens out a small number of points. Figure 3 shows that keeping data points associated with slightly higher cost function values (for instance 0.12 instead of 0.10) would add a few more data points to the time series, though most of them cluster in late 2016 and early 2017, at a time when they would not provide much additional constraint on the model inversion. Selecting much smaller values does have a significant impact on the number of remaining data points, as documented in Table 1. In practice, the choice should be driven by the requirements of the user of the information: is it better to have very reliable data on a smaller number of cases, or more approximate and potentially less reliable information more frequently? The interesting feature of this approach is that there is no need to impose a single solution for all possible problems: the process can be customized to meet the specific requirements of the user.

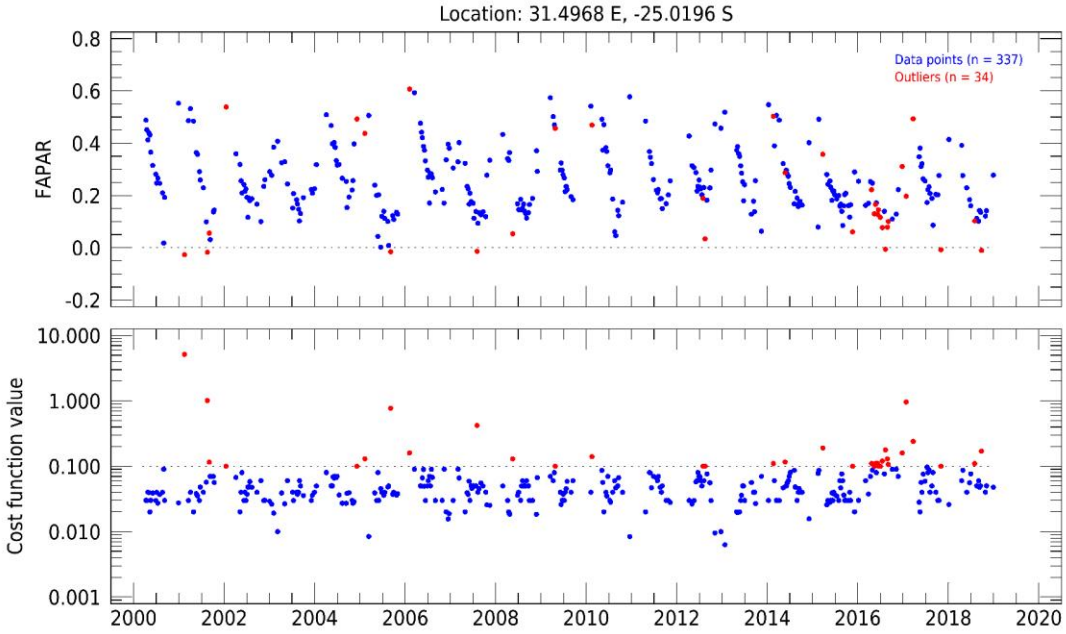


Figure 3. Time series plots showing how a threshold value of the cost function distribution (in this instance 0.1) flags obvious and less apparent cases of problematic values in Fraction of Absorbed Photosynthetically Active Radiation (FAPAR) in the time series at the reference pixel of the Skukuza flux tower and for MISR Paths 168 and 169.

Figure 3 shows the outcome of this process in a particular case: The top panel exhibits the time series of FAPAR values for the Skukuza flux tower for Paths 168 and 169, while the bottom panel shows the associated JRC-TIP cost function values. In this case, the threshold of acceptable cost function values is set to 0.1. All cost values larger than this threshold and the corresponding FAPAR values in the top panel, are marked in red. This process eliminates the occasional slightly negative FAPAR values, but also other values that might otherwise appear to be reasonable at face value. Of course, a lower threshold would prune even more data points and jeopardize the feasibility of characterizing the vegetative season, while a larger threshold would retain more data but possibly lead to an incorrect interpretation because of the presence of dubious values.

Table 1 shows how selecting progressively stricter threshold values for the cost function increases the number of data points considered outliers or potentially suspicious and decreases the number of data points remaining available for further analysis.

Table 1. Relation between the largest allowable cost function value (Threshold), the number of data points identified as outliers, and the number of data points remaining available for further analysis in the time series of Figure 3.

Threshold	**0.1**	**0.08**	**0.06**	**0.04**
Outliers	34	59	110	211
Remaining	303	278	227	126

Figure 4 exhibits the histogram of the FAPAR values in the five-by-five pixel area around Skukuza for Paths 168 and 169 (a) before screening outliers (indicated in red), and (b) after discarding values associated with an excessive cost function value for those pixels (depicted in blue). The average cost

function threshold for all pixel locations in the FAPAR record was 0.099, which resulted in about 10.7% of the values in the image time series being discarded.

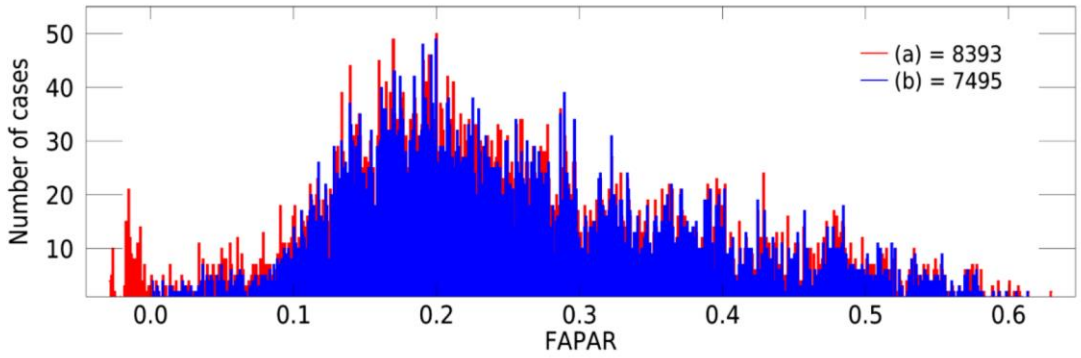


Figure 4. Histogram of FAPAR values for the area surrounding Skukuza and for Paths 168 and 169 (a) before screening outliers and (b) after discarding outliers using a threshold value of the cost function (0.099).

Figure 5 summarizes the number of valid FAPAR values available per month, for each year in the record, averaged over the target area around the Skukuza flux tower. It can be seen that remote sensing observations are most often lacking during the wet season (December to March), due to the prevailing cloudiness. The longest continuous period without any observations in this particular case can last up to four months, as happened between October 2009 and January 2010, and between December 2011 and March 2012, inclusive. This situation would be even worse close to the Equator, both because of the prevailing cloudiness and because of the minimal overlap between consecutive MISR Paths. Contrariwise, at higher latitudes, in both hemispheres, a larger overlap between Paths provides more frequent opportunities to observe the surface.

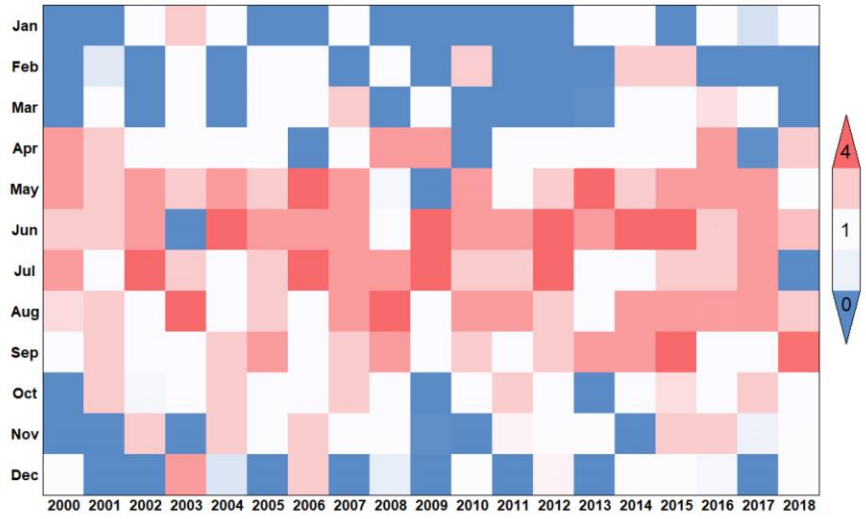


Figure 5. Distribution of the availability of the number of valid FAPAR values as a function of month (along the vertical axis) and year (along the horizontal axis), averaged over the target area around the Skukuza flux tower.

4.2.2. Assembling the FAPAR Data Cube

The next step consists in merging data from the two relevant MISR Paths. Raster images of five samples by five lines, centered on the geographic location of the flux tower, were extracted from the FAPAR product for each of the 842 available Orbits and reprojected onto a common geographical grid, since both the MISR data and the MISR-HR products are provided in the SOM projection specific to each Path. Figure 6 explains this process graphically: Three grids are superimposed on a background map of the area around Skukuza, symbolized by the black triangle at the center of the display: the yellow and blue grids show idealized representations of the locations of the areas observed by MISR in Path 168 and 169 acquisitions, respectively. The red grid is the common geographical projection used as the target, and all grid squares are 275 m on the side, the ground sampling distance of MISR-HR products. This process roughly doubles the number of observations at each location, and helps constrain the phenology.

4.2.3. Identifying Individual Vegetative Seasons

The successive vegetative seasons must be identified before attempting to fit a double S-shaped model through the data, accounting for the fact that their growth and senescence phases can start and last differently in different years, mostly as a result of climatic fluctuations. This process is implemented as follows. A power spectrum for the entire time series is computed first, using the Lomb-Scargle algorithm [77,78] since the remote sensing data are provided on irregular dates. The resulting periodogram indicates whether the record exhibits primarily an annual variation (as is the case in Skukuza), or a biannual cycle, as would occur in agricultural regions where two crops can be grown per year. Figure 7 shows the Lomb periodogram for the FAPAR time series at the pixel location of the Skukuza Flux tower. This area exhibits a strong annual cycle (peak power: 71.72, frequency: 0.0027 day^{-1}, and period: 364.75 days) and a minor semi-annual fluctuation (peak power: 16.63, frequency: 0.00548 day^{-1}, and period: 182.37 days).

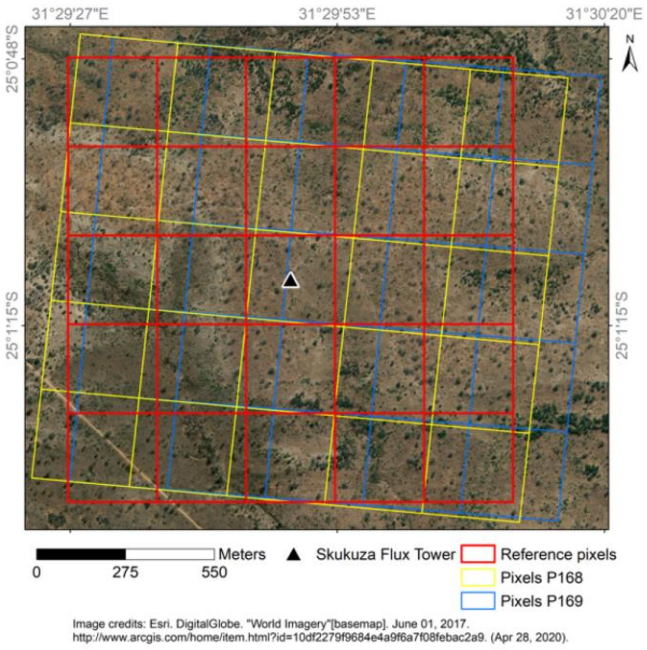


Figure 6. The pixel reference grids used to co-register the MISR-HR FAPAR variable for Paths 168 and 169 of Block 110 to geographic coordinates for the Skukuza flux tower.

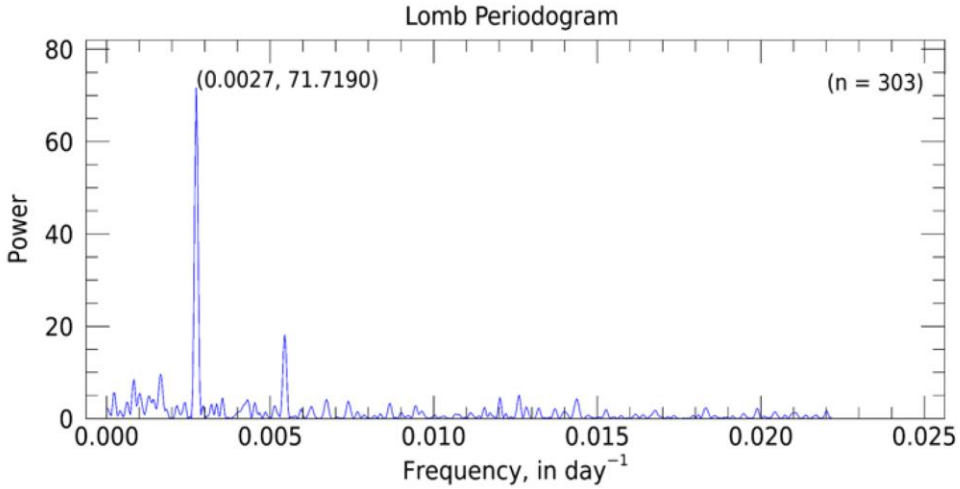


Figure 7. Lomb periodogram of the FAPAR time series at the reference pixel of the Skukuza flux tower.

Since satellite records may start and end at arbitrary times relative to climatic or ecological cycles, the second step consists in identifying the start of the first complete vegetative season that can be documented on the basis of the data record. This is achieved as follows:

- compute the median of the entire FAPAR record,
- search, from the start of the record, the date of the first observation whose value is lower than this threshold,
- define a time interval equal to 1/3 of the expected length of the vegetative period (as determined from the Lomb-Scargle algorithm), starting on this date, and
- set the start date of the first vegetative season to the date of acquisition of the minimum FAPAR value within this limited time period.

From that point onwards, the end date of each vegetative season is automatically considered the start of the next one. The end of each season date is determined as follows:

- add the expected average length of the vegetative season to the starting date just identified to estimate a nominal end date,
- define a new limited time window located around that nominal end date, extending 1/6 of the expected length of the vegetative season on either side of that nominal date, and
- set the end date of the vegetative season to the date of acquisition of the minimum FAPAR value within this limited time period.

This process is repeated until the nominal date of the end of the nth vegetative season exceeds the length of the remote sensing record. As a result, some data may be discarded at the start and end of the entire record, since they only document parts of vegetative seasons.

Figure 8 plots a subset of the FAPAR time series at the pixel location of the Skukuza flux tower, showing the first few years of the MISR-HR FAPAR time series: the vegetative season ending in August 2000 is ignored because it is incomplete, and the next three are properly identified. The successive search periods are indicated by the blue dotted lines, and the red lines mark the start and end dates of the vegetative seasons.

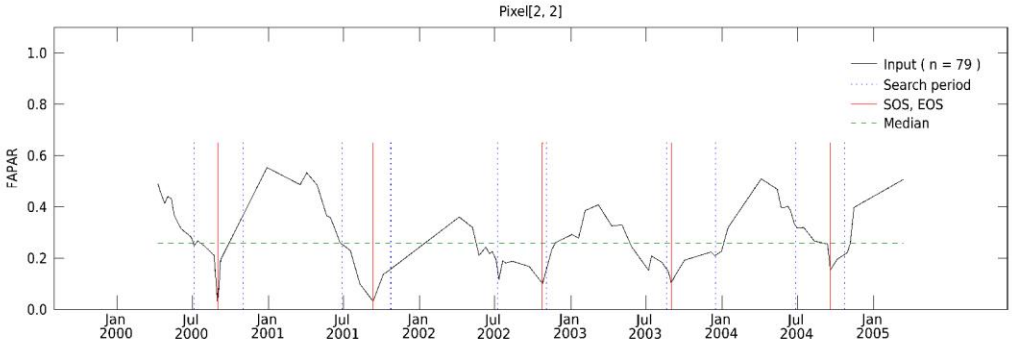


Figure 8. A subset of the FAPAR time series at the reference pixel for the Skukuza flux tower showing the start of the first vegetative season between 2000 and 2001 and the vegetative seasons for 2001–2002, 2002–2003, and 2003–2004. The dotted blue lines delimit the search periods for the start and end of the vegetative seasons, and the solid red lines indicate those boundaries. The dashed green line represents the median value for the record, in this case, 0.25.

4.3. Modeling Phenology

Once each individual vegetative season has been identified, the evolution of the plant canopy properties during that period can be modeled. This is beneficial (i) to estimate the timing of events, such as the start, end, and length of the season (SOS, EOS, and LOS, respectively), (ii) to document the probable value of biogeophysical variables, such as FAPAR, when direct observations are missing, and (iii) to characterize the long-term evolution of the environment, in this case, for the environment around the Skukuza flux tower, in the Lowveld savanna of north-eastern South Africa, during the period 2000–2018, despite the presence of noise in the data.

Global and local methods have been used in the literature for similar purposes. Local approaches take existing data at face value and generate estimates of missing observations on the basis of the values of neighboring measurements [79]. They include rank based filters, e.g., minimum, median, and maximum filters [80], linear/polynomial filters, such as moving average and adaptive Savitzky-Golay filters [81–83], locally weighted scatterplot smoothing (in [79,84]), and Whittaker smoother (in [85]) to name a few. Advantages include the applicability to any time series, irrespective of their semantic or thematic context, and an ability to match arbitrary fluctuations, but at the risk of simulating fluctuations that may be suggested by noisy or erroneous data.

Global models, by contrast, impose a functional shape that is intended to represent the likely evolution of the variable of interest, in this case, the phenology of vegetation, which is expected to exhibit a growth phase, followed by a senescence phase. They include function-fitting approaches, e.g., polynomial, double logistic, asymmetric Gaussian [86–89], and signal smoothing or decomposition techniques, e.g., wavelet transform, Fourier analysis, Lomb-Scargle [90–95]; see [79]. Signal decomposition techniques provide forecasts over a season by decomposing the time series into noise, seasonal variability and trend [96]. The Lomb-Scargle algorithm, initially developed by Lomb [97] and subsequently elaborated by [98], implements an approach similar to Fourier analysis [99], adapted to estimate the power spectral density of unevenly sampled data [77,78].

Local and global phenology models both have advantages and drawbacks: The selection of a global versus a local model must depend on the intended usage of the resulting information. Global models are deemed particularly suited to represent the temporal evolution of vegetation when the empirical evidence exhibits unusual or unexpected fluctuations (as is the case here): they are used as low-pass filters to screen out the influence of extraneous or uncontrolled processes, such as biomass burning, random browsing, the possible contamination due to thin clouds or aerosols, or simply noise in the data. A local modeling

approach would definitely be more appropriate if the objective were to specifically monitor biomass burning events, for instance.

This study explores the suitability of four different global models, each constructed as a pair of S-shaped functions (one to simulate the growth phase and the other to represent the senescence phase): Gaussian, hyperbolic tangent, logistic (these two functions are mathematically equivalent, but they exhibit differences in terms of numerical efficiency, as will be shown below), and sine. Of those four models, the logistic function has been used most frequently in phenology (and other ecological) studies (in [21, 34,88]). A smaller number of investigations explored the suitability of the hyperbolic tangent [100–102], probably because of its similarity with the logistic function. Rather fewer researchers seem to have considered the Gaussian [103,104] or the sine functions. This paper aimed in part to explore which of those formulations might be more appropriate or more advantageous for this purpose.

These four mathematical models are described in detail in Appendix B. The shape of each elementary S-shaped function is determined by four independently adjustable parameters, typically to specify the (Julian) date and value of the start and of the end of the simulated fluctuation. Imposing a continuity condition between the two functions of each pair reduces the number of parameters to be adjusted to seven. The process of fitting a double S-shaped model to the data reduces to an inversion procedure, where the goal is to optimize a goodness of fit criterion: it is typically implemented as an iterative algorithm to minimize a figure of merit function, such as the root mean square difference between the model and the observed values (χ^2). When this condition is realized, the values of the model parameters are deemed to optimally describe the seasonal evolution of the simulated geophysical variable, and the model, together with these newly established parameters, can be used to generate a complete time series, at whatever frequency is required.

Data points can be assigned weights during this inversion process, to allow those with smaller uncertainties to have more influence on the outcome than points with larger uncertainties. The inverse of the estimated standard deviation provided by the JRC-TIP algorithm for each FAPAR value was used as the weight in this investigation. The iterative inversion process is terminated when the value of χ^2 changes by less than 10^{-3} between successive iterations, i.e., when there is little benefit to be gained by searching for another minimum in the current neighborhood.

This approach requires at least four FAPAR values within each of the growing and decay phases, and more than seven values over the entire vegetative season to ensure that the number of measurements exceeds the number of model parameters to be determined [105]. The average number of valid FAPAR observations across all pixel locations in the FAPAR record is 288, which, over a period of 18 years, yields around 16 observations per season. However, those are very unevenly distributed, with many more data points during the dry season (under clear skies) than during the rainy season, as was shown in Section 4.2.1. In fact, the process of inverting the models against those data can fail or lead to unrealistic results whenever there are fewer than four observations during the growing phase, which is always the most cloudy.

In addition to systematically fitting each of these double S-shaped models to each vegetative season, a combined approach was also explored, whereby the best model for each individual season is selected, to increase the number of successful model inversions and decrease the average χ^2 statistic.

Once a parametric double S-shaped model has been successfully fitted to the remote sensing measurements, classical techniques based on an inspection of the first and second derivative of this model can be used to determine the start, end, and length of the growing season (in [22,106], among many others).

5. Results and Discussion

This section documents the results obtained from the application of the methods described in Section 4 to the data sets identified in Section 3. Section 5.1 discusses to what extent the parametric double S-shaped models are capable of representing the phenology of vegetation as reported by MISR-HR FAPAR time series. Section 5.2 explores the effectiveness of this joint approach to document the ecological evolution of the target area by comparing those results with the Gross Primary Productivity (GPP) estimates derived from in situ measurements at the Skukuza flux tower. Section 5.3 reports on the numerical efficiency of these algorithms, while Section 5.4 summarizes the results.

5.1. Simulation Capability

All four parametric double S-shaped models are capable of simulating a seasonal signal when the number of data points is large enough to individually document the growth and senescence phases. Each of those models relies on seven adjustable parameters to match the empirical evidence, so eight measurements are required at a minimum before attempting to invert the model against the data for a particular season. It is generally easy to document the evolution of the phenology during the dry season, i.e., when the vegetation senesces or becomes dormant. The difficulty arises when persistent cloudiness generates long gaps in the remote sensing measurements during the rainy season, precisely when the vegetation grows. Figure 9 exhibits the number of FAPAR values available per year over the target of interest for the entire record available.

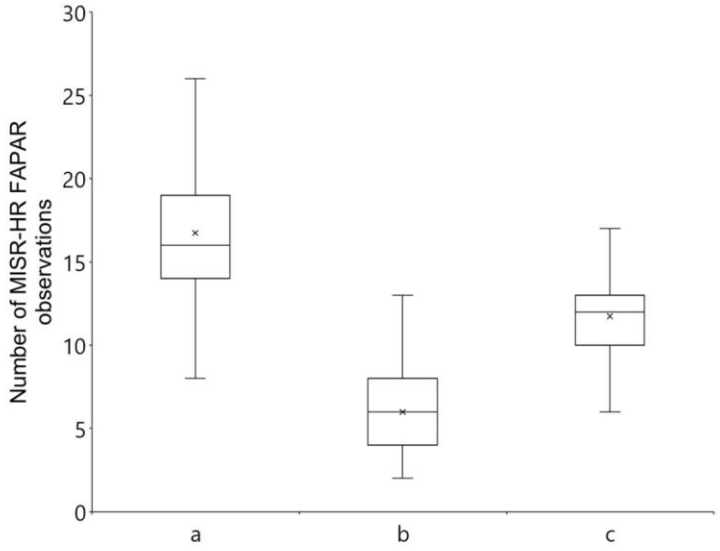


Figure 9. Boxplots summarizing, for the entire MISR-HR FAPAR record, the number of observations available per year to fit the model during (**a**) entire vegetative seasons, (**b**) the growth phase, and (**c**) the senescence phase. The top and bottom limits of the boxes show the quartiles, the horizontal line in the middle of those boxes and the crosses indicate the median and the average values, respectively, while the 'T' shaped extensions document the range of values (minimum and maximum).

As expected, there are fewer observations during the rainy season (growth phase). Whenever too few FAPAR values are present during the growth (more rarely senescence) phases, the inversion process fails. It is interesting to note that the various models exhibit different sensitivities to the presence of those

data gaps. Figure 10 summarizes the number of successful inversions for each of the four models in the target area.

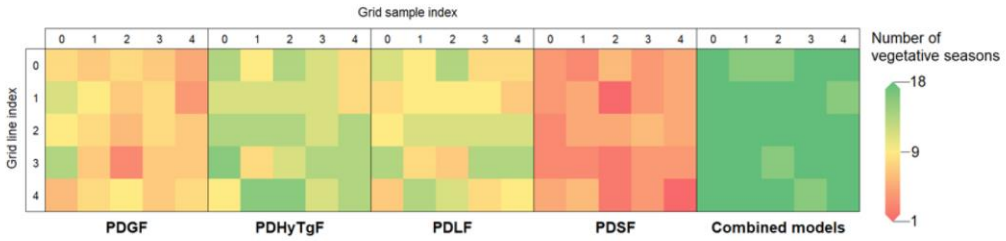


Figure 10. Number of successfully simulated vegetative seasons. The four left-most panels report the results for the Parametric Double Gaussian Function (PDGF), Parametric Double Hyperbolic Tangent Function (PDHyTgF), Parametric Double Logistic Function (PDLF), and Parametric Double Sine Function (PDSF) models, respectively. The fifth panel shows the success rate when the most successful model is selected for each season at the sample and line locations in the target area.

It can be seen that the hyperbolic tangent model offers the most frequent opportunities to successfully simulate a vegetative season, as well as that the sine model is the most sensitive to the presence of gaps in the data, i.e., to the temporal distribution of empirical data throughout the season.

5.2. Ecological Effectiveness

Comparisons between models adjusted to fit remote sensing data and in situ field measurements must take place over approximately similar areas. Since the Gross Primary Productivity (GPP) estimates derived from flux tower Eddy Covariance (EC) measurements are deemed to be representative of an area of approximately 500 m around the tower (an area of 53.5 ha), the FAPAR product is averaged over the subset of 3 by 3 pixels centered on the Skukuza flux tower (an area of 68.1 ha). The corresponding average standard deviation for each date in the remote sensing time series is computed as the square root of the average variance of the nine pixel values. The four models described earlier are then adjusted to this spatially averaged time series, and the results are described in the following subsections.

5.2.1. Comparing Daily Values

Figure 11 exhibits multiple time series at once, over the period September 2000 to August 2013, when the GPP data are available: the little circles represent the 215 average FAPAR values available for that period, estimated as explained above. The four sets of smooth colored dashed curves represent the model fits, and the highly variable grey trace shows the daily values of GPP, derived from the Skukuza flux tower EC measurements. The traces of the four models largely overlap each other when the temporal distribution of the FAPAR data is adequate and when all models exhibit a very similar performance in simulating the phenology (for seasons peaking in early 2002, 2003, 2004, 2006, 2009, and 2013). By contrast, during the seasons peaking in early 2001, 2005, 2007, 2008, 2010, 2011, and 2012, the Parametric Double Sine Function (PDSF) model did not converge to a useful solution, so its trace is absent from the Figure. In these latter cases, it can be seen that the traces of Parametric Double Hyperbolic Tangent Function (PDHyTgF) and Parametric Double Logistic Function (PDLF) coincide, as well as that the Parametric Double Gaussian Function (PDGF) model delivered a different simulation, clearly distinguished from the other two.

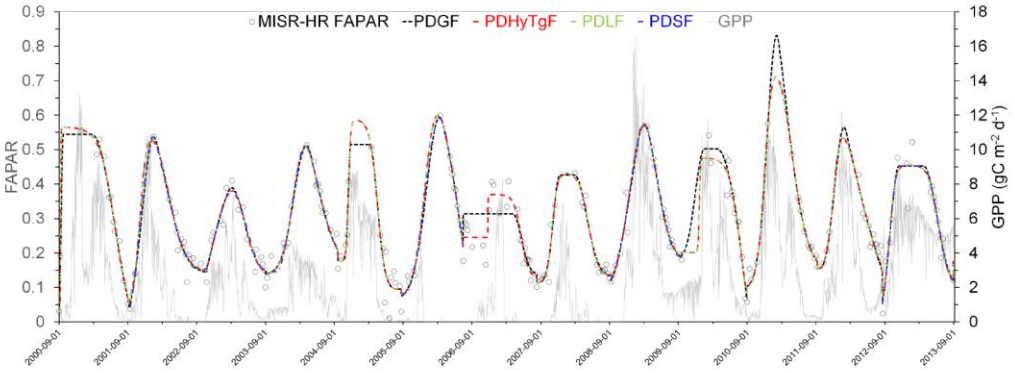


Figure 11. Superposition of multiple time series, from September 2000 to August 2013: the FAPAR data (small circles, non-dimensional), averaged over a 3 by 3 pixel area around the Skukuza flux tower, the four model fits (smooth colored curves, non-dimensional), each adjusted to fit the remote sensing data, and the daily GPP values derived from the in situ Eddy Covariance (EC) measurements (jagged grey trace, in gC m^{-2} d^{-1}).

Table 2 quantifies the correlation between daily FAPAR estimates generated by the four models (PDGF, PDHyTgF, PDLF, and PDSF) and the corresponding daily GPP record retrieved from an analysis of the EC flux tower, for each of the 13 vegetative seasons available. The first column reports the dates of the start and end of those seasons and the second refers to the season number. The third and fourth columns indicate the number and the proportion (in%) of days in the corresponding seasons for which GPP measurements were available, respectively. The next four columns report the Pearson correlation coefficient between model-generated daily estimates of FAPAR and the daily GPP values derived from in situ measurements for the same days. The last column shows the same statistics for the combined model, i.e., when the best (smallest χ^2) model is chosen for each year. Label `A` in the four model columns flags cases where fewer than half of the daily GPP values were available for the concerned season (as shown in the fourth column, and also in Figure 11). Label `B` in those columns flags cases where the model values are unavailable, typically because the temporal distribution of the FAPAR data did not permit the model inversion. Vegetative season numbers set in bold face within the second column point to cases where the number of daily GPP was sufficient (more than 50% of the days) and where all four parametric double S-shaped functions could be successfully inverted against the FAPAR data.

Correlation coefficients between the daily GPP and daily estimates derived from the PDGF, PDHyTgF, PDLF and combined model approaches are always equal to or larger than 0.69 in seasons 2 to 5 and 9 to 12. This coefficient is much lower in the case of season 1 because (1) a long gap in the remote sensing data, due to persistent cloudiness, hampers the model inversion procedure and (2) the GPP data suggest a noticeable but unexpected double vegetative season during that period, unconfirmed by the remote sensing record. The number of daily GPP measurements available in seasons 6, 7, and 8 was too low to compute that statistic. Season 13 was also exceptional in two other ways: (1) the FAPAR data includes an anomalously low value near the peak of the growing phase (possibly due to incomplete or insufficient cloud screening), while the GPP data suggests a sustained activity throughout the period. The PDSF model, for its part and in its current implementation, appears to be more sensitive to the distribution of data points during the season than other models. However, when the model inversion does work, it tends to yield very good results.

Figure 12 shows the non-linear relation between daily simulated FAPAR and daily GPP measurements across all seasons, as represented by each of the indicated models: remote sensing measurements (in this case, of FAPAR) appear quite sensitive to small variations of GPP when the latter is itself low (i.e., at the

start an end of the vegetative seasons), as well as tends to saturate during the peak of the growing phase. This finding may need to be confirmed in other locations but suggests that FAPAR is a sensitive indicator of GPP in the range of 0 to 5 $g_C\,m^{-2}\,d^{-1}$ but then saturates and is not usable to estimate larger carbon exchanges.

Table 2. Correlation coefficients (*r*) between the daily GPP and daily FAPAR estimates from the PDGF, PDHyTgF, PDLF, PDSF, and combined models for each vegetative season and for the area around the Skukuza flux tower. Entry A indicates that fewer than half of the expected GPP values were available, while entry B means that the model could not simulate the available FAPAR data.

SOS/EOS	Vegetative Season	Season Length	GPP %	PDGF *r*	PDHyTgF *r*	PDLF *r*	PDSF *r*	Combined *r*
2000–08–31								
2001–09–10	1	375	99.2	0.56	0.52	0.52	B	0.56
2002–10–24	**2**	409	86.8	0.72	0.78	0.78	0.74	0.72
2003–08–31	**3**	311	100	0.71	0.70	0.70	0.70	0.71
2004–09–18	**4**	384	100	0.81	0.82	0.82	0.82	0.81
2005–08–20	5	336	94.6	0.92	0.93	0.93	B	0.93
2006–07–15	6	329	24.9	A	A	A	A	A
2007–08–10	7	391	41.4	A	A	AB	AB	A
2008–09–06	8	393	45.3	A	A	A	AB	A
2009–09–16	**9**	375	82.1	0.79	0.80	0.80	0.80	0.79
2010–08–27	10	345	100	0.69	0.72	0.72	B	0.69
2011–09–06	11	375	100	0.80	0.82	0.82	B	0.80
2012–09–01	12	361	100	0.82	0.80	0.80	B	0.82
2013–08–26	**13**	359	100	0.56	0.56	0.56	0.55	0.56

However, Figure 11 also shows why that relation is complex: daily model values for seasons 4 and 5 are very similar, while daily GPP values in season 5 are almost double the values in season 4.

The impact of lacking remote sensing evidence on the shape of the model can also be highlighted by comparing seasons 10 and 11: In those cases, the GPP daily values are comparable but the absence of observational constraint near the peak of the season probably resulted in substantial overestimations by the model in season 11.

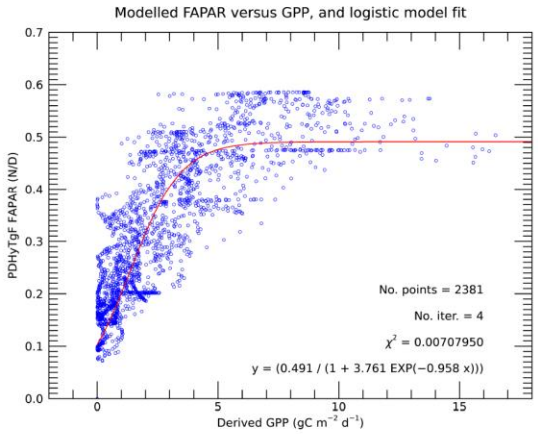


Figure 12. Scatterplot of daily FAPAR estimates (when the PDHyTgF model successfully simulates vegetative seasons) versus daily GPP ($g_C\,m^{-2}\,d^{-1}$) values when at least half of the expected values are available (i.e., season 2, 3, 4, 9, 10, and 12).

5.2.2. Comparing Seasonally Integrated Values

A high correlation between daily FAPAR values (retrieved from remote sensing or simulated) and daily GPP estimates (derived from flux tower measurements) is not expected because the former correspond to instantaneous assessments of the reflectance of the canopy, while the latter accounts for the evolution of that canopy throughout the day. In situ observations are also sensitive to a wide range of local perturbing factors that do not affect the observations gathered from space, such as wind speed and direction, for instance. On the other hand, it is customary to integrate these time series over the lengths of vegetative seasons. This approach tends to reduce the inherent variability of those signals (mainly the GPP in this case) and to focus on the seasonal environmental properties rather than the daily fluctuations. Table 3 shows the result of this process: The first two columns are the same as for Table 2; the third one shows the integrated GPP value for the specified seasons, and the next four columns provide the integral of the four models over these same seasons, again using the results obtained for the spatially averaged 3 by 3 pixel area around the Skukuza flux tower.

Table 3. Correlations coefficients (r) between the integrated GPP and Cumulated FAPAR (CFAPAR) obtained by integrating the PDGF, PDHyTgF, PDLF, PDSG, and combined models during the indicated vegetative seasons. Computations were skipped whenever fewer than half of the expected GPP observations were available during the season, or when the correlation between the daily GPP and model values dropped below 0.70 in Table 2 (see text for details).

SOS/EOS	Vegetative Season	Integrated GPP	CFAPAR				
			PDGF	PDHyTgF	PDLF	PDSF	Combined
2001–09–10							
2002-10-24	2	815.25	117.72	122.26	122.26	118.50	117.72
2003–08–31	3	656.65	84.19	84.14	84.14	84.40	84.19
2004–09–18	4	682.33	119.50	119.91	119.91	119.24	119.50
2005–08–20	5	1043.88	105.95	111.70	111.70		111.70
2009–09–16	9	1522.03	130.12	130.87	130.87	130.44	130.12
2010–08–27	10	1185.21	129.29	117.07	117.07		129.29
2011–09–06	11	1314.19	155.09	148.36	148.36		155.09
2012–09–01	12	1178.08	116.34	115.56	115.56		116.34
	r		0.65	0.62	0.62	0.65	0.65
	p-value		0.35	0.38	0.38	0.35	0.35

5.2.3. Comparison Outcome

These results call for various comments:

- The GPP estimates derived from the flux tower measurements exhibit a very high day-to-day variability, as a result of fluctuations in local conditions, including turbulence. While progressively larger values are expected during the vegetation growth phase than during senescence, there is no expectation that successive values generate a smooth sequence.
- By contrast, vegetation growth and senescence occurs as a generally slow, smooth process, with more branches and leaves occurring during the rainy season, and the plants wilting progressively during the dry season. Hence, it makes sense to fit a smooth model through the FAPAR data, while this would not be appropriate for the GPP data, at least on a daily time scale.
- Inspecting again Figure 11, it is seen that FAPAR and GPP both increase quickly and together at the start of the rainy seasons, but that the decrease in FAPAR tends to lag behind the decline in GPP: plants continue to appear photosynthetically active from space longer than the in situ measurements of CO_2 indicate.

- GPP values measured at the Skukuza flux tower range from 0.0 to about 16 gC m^{-2} d^{-1}, while FAPAR rarely drops below 0.1 or raises above 0.6 at this site: these variables experience quite different ranges of variability.
- As expected, the PDHyTgF (Hyperbolic Tangent) and the PDLF (Logistic) models generate essentially the same traces, since their parameters can be adjusted to generate the same values; however, they exhibit somewhat different levels of numerical efficiency, as will be seen shortly in Section 5.3.

5.3. Numerical Efficiency

The numerical performance of the four parametric double S-shaped models described above can be assessed using four criteria.

5.3.1. Successful Inversions

This first criterion explores how often the selected model is actually able to fit the empirical evidence provided by remote sensing, or, equivalently, the sensitivity of the models to the temporal distribution of the input data. For this purpose, the entire record of 18 years of FAPAR data is used, over the 5 by 5 pixel target area around the Skukuza EC flux tower, so there are 450 possible cases. Table 4 provides the statistics, and it can be seen that the PDHyTgF (Hyperbolic Tangent) model provides the greatest proportion of successful model inversions for the 450 possible cases in the 5 by 5 pixel target area.

Table 4. Number and proportion of successful model inversions.

Successes	**PDGF**	**PDHyTgF**	**PDLF**	**PDSF**
Number	309	382	355	224
Proportion (%)	68.6	84.8	78.8	49.7

5.3.2. Iterations

A second performance criterion is the number of iterations required to reach a solution. This depends strongly on the algorithm used to conduct the inversion process. In this case, the IDL `CURVEFIT` function is used in all cases, and analytic versions of the partial derivatives of the model with respect to the model parameters were explicitly provided (see Appendix B).

Table 5 shows the results, and it is clear that the PDSF model converged to a solution in fewer iterations than the other models, although it achieved a successful inversion much less often than other models, as has been shown above.

Table 5. Number of iterations required, for successful (s) and unsuccessful (u) model inversions.

Iterations	**PDGF**		**PDHyTgF**		**PDLF**		**PDSF**	
Cases	**s**	**u**	**s**	**u**	**s**	**u**	**s**	**u**
Minimum	2	1	1	1	1	1	2	1
25th percentile	7	1	8	2	8	1	7	1
Median	10	2	12	2	12	3	9	2
Mean	20.8	3	18.6	7.2	18.7	7.2	10.8	4
25th percentile	14	3	19	4	19.5	4	11	3
Maximum	71	8	53	27	53	27	25	13

5.3.3. Computing Time

The third relevant criterion is the time required to achieve the inversion process. Again, this depends largely on the power of the computer, its clock frequency, the number of cores available, the ability of the

software to take advantage of multithreading, etc. All results described in this paper were generated on the same computer, and the results are normalized by the fastest time achieved for each category (successful and unsuccessful), to provide a rating independent of the particular hardware and software available.

Table 6 reports the average amount of time spent inverting each of the four models against the FAPAR data for each of the 25 locations in the target area and for each of the 18 seasons in the input data set. All four models can be inverted against the seasonal data in about the same amount of time when presented with an optimal data distribution. However, as the pattern of FAPAR data starts to diverge from expectations or to feature longer gaps of missing data, the inversion process takes more time to reach a solution. Interestingly, the PDLF and the PDGF models take less time to conclude in the worst cases than the PDSF and the PDHyTgF. On the other hand, inverting the PDHyTgF model is the fastest process to conclude with an unsuccessful fit, followed by the PDSF; the PDLF and especially the PDGF models appear to require more time before deciding to quit in unsuccessful cases.

Table 6. Execution time, relative to the fastest case (successful PDLF model inversion in 0.00299978 second), for successful (s) and unsuccessful (u) model inversions.

Iterations	**PDGF**		**PDHyTgF**		**PDLF**		**PDSF**	
Cases	**s**	**u**	**s**	**u**	**s**	**u**	**s**	**u**
Minimum	1.00008	1.00008	1.00008	1.33341	1.00000	1.00008	1.00008	1.00008
25th percentile	1.66675	1.66675	1.66683	1.66675	1.66675	1.66675	1.66683	1.33341
Median	2.00008	2.00008	2.00016	2.00016	2.00016	1.66683	2.00016	1.66683
Mean	2.26680	2.53349	2.66686	2.13346	2.26680	2.06678	2.46685	1.93348
75th percentile	2.00016	2.33349	2.33357	2.33349	2.33349	2.00016	2.33349	2.00016
Maximum	4.66708	5.66708	6.33383	3.33357	4.33365	4.00023	5.33372	3.66700

5.3.4. Simulation Effectiveness

Last but not least, simulation models can be compared in terms of how well they are able to represent the variability present in the empirical evidence, in this case, in the MISR-HR FAPAR records. This is done by contrasting the χ^2 values at the end of the inversion.

Table 7 summarizes the results and shows that the PDSF actually best matches the available remote sensing data, when they are available. However, as was shown above, it is also the model that achieved the smallest number of successful inversions.

Table 7. Average χ^2 value at the end of the model inversion step.

PDGF	**PDHyTgF**	**PDLF**	**PDSF**
0.022	0.020	0.018	0.015

As noted above, the PDHyTgF and PDLF models yield very similar results: This was expected because they can be made to match each other exactly by manipulating the model coefficients. However, these functions are not identical: both are defined on the domain $\mathbb{R}$ of real numbers, or in the context of this application, on the subdomain $\mathbb{R}_J$ of real numbers suitable to represent Julian days, but their co-domains are the intervals $[-1.0, 1.0]$ and $[0.0, 1.0]$, respectively. More importantly, they do differ from each other in terms of their numerical efficiency: the PDLF model achieves, on average, a slightly better fit than the PDHyTgF, though the latter did manage to achieve a successful inversion in more cases than the former.

Again, these last results depend on the availability of a floating-point coprocessor, or on the implementation of the algorithms to compute transcendental functions, such as exponential and trigonometric functions. However, since all results were obtained on the same computer, the results

exhibited here may be indicative of the relative performance of these models. These findings may need to be confirmed over a larger number of cases to provide general guidance about the selection of such models.

5.4. Discussion

Comparing FAPAR values retrieved from an analysis of remote sensing data to GPP values derived from field measurements acquired at a flux tower is a complex endeavor.

One difficulty arises from the fact that remote sensing measurements correspond to instantaneous snapshots of the radiative state of the surface at the time of the satellite overpass (around 10:36 AM in the case of the MISR instrument), while in situ observations are taking place over the entire day and generate daily-averaged GPP values.

Another drawback is the irregular availability of FAPAR data, as prevailing cloudiness prevents the observation of land surfaces during the rainy season, which is the period of intense growth for vegetation. This issue could be alleviated in at least four different ways:

- Spatial analysis: Terrestrial ecosystems exhibit a high degree of spatial variability, due to the large number of plant species (especially in protected environments, such as the Kruger National Park), combined with a potentially similar variability in soil properties. These spatial fluctuations may be further enhanced by patchy precipitations, in particular in convective systems. However, spatial patterns may subsist over periods of weeks or more, because plants remain in place. Hence, if relevant spatial correlations can be established (e.g., by kriging), it may be possible to infer the likely value of FAPAR at one location where it is missing on the basis of its value at another location, provided both places share a common evolution.
- Temporal analysis: When excessively long gaps arise in the remote sensing data, it may be sufficient to interpolate the missing values on the basis of the last value available before and the first value after the gap. This approach tends to underestimate the actual variability of the variable (FAPAR in this case), as it will never generate higher (or lower) values than those effectively observed.
- Other sources: It may also be possible to ingest other data products. Indeed, FAPAR products are available from other instruments, such as NASA's MODIS instrument (over the period of interest here). However, that approach carries its own set of complexities, as the algorithms used to generate these products (including to implement atmospheric corrections) are different so that the products may not match, or may introduce systematic biases or shifts.
- As far as the future is concerned, a particularly promising approach consists in operating constellations of identical instruments, in order to expand the number of opportunities to observe the surface despite the cloud coverage.

Another lesson learned from this study is that it is difficult to fit a parametric double S-shaped model to a seasonal phenology where one or a few data points with an anomalously low value occurs right in the middle of the peak period of photosynthetic activity. These events can occur as a result of multiple causes, including instrumental or environmental noise (e.g., a lingering cloud or aerosol contamination effect), or a legitimate process, such as biomass burning, for example. Additional external data sources are needed to reliably attribute definite causes to these events. If those are unavailable, it may be necessary to sift those points from the data set, so that the analysis can proceed.

6. Conclusions

The state and evolution of plant canopies has been monitored from space for decades because the phenology of vegetation foreshadows the yield of crops and therefore serves as a useful indicator of economic output and impacts. The crucial role of vegetation in the carbon cycle has also stimulated a strong interest in the assessment of the net primary productivity of the biosphere. However, the bulk of

published studies (1) are mostly concerned about agricultural productivity in monocultures over large areas in the Northern Hemisphere, where phenology follows a regular, highly predictable seasonal evolution, (2) are based on an analysis of the Normalized Difference Vegetation Index (NDVI), mostly using the logistic or hyperbolic tangent models, and (3) rely on globally available data products at a spatial resolution of 500 m or coarser.

This paper explored the feasibility of modeling natural, unmanaged vegetation canopy in the protected Kruger National Park in South Africa, where the vegetation features significant biodiversity and exhibits much larger spatial and temporal fluctuations than crops (in particular, from year-to-year and within-seasons). This study relied on a state of the art FAPAR data product available since March 2000, derived from NASA's MISR instrument, using the MISR-HR processing system, and generated at a spatial resolution of 275 m.

This paper compared the suitability of four different parametric double S-shaped models to simulate the phenology of plant canopies: the Gaussian (PDGF), the Hyperbolic Tangent (PDHyTgF), the logistic (PDLF), and the Sine (PDSF) models, and it showed that they are all capable of explaining the bulk of the variability present in the FAPAR record when constrained with ample empirical data, well distributed in time. These models do differ, though, in their efficiency and effectiveness with respect to the presence of gaps in the data, an issue that is intrinsic to the use of remote sensing observations in the solar spectral range. Specifically, PDHyTgF appears to be the least sensitive to the particular distribution of input data during the vegetative season, though it is somewhat more computationally expensive. The PDSF model fits the FAPAR data with the smallest χ^2 but is also the most sensitive to the presence of gaps in the input data. The PDLF model is functionally equivalent to PDHyTgF, in the sense that both models can be made to match each other perfectly, though they do differ somewhat in terms of their sensitivity and computational efficiency.

It has also been shown that the presence of gaps in the empirical evidence over extended periods, especially during the growing phase (rainy season), is detrimental to the successful inversion of global models over the vegetative season. This suggests that further efforts to reduce the gaps in the input data will go a long way to improve the benefits to be derived from this modeling approach.

FAPAR values simulated by those models were compared to Gross Primary Productivity (GPP) estimates derived from an analysis of the Eddy Covariance flux tower at Skukuza, as this environmental variable is useful to investigate biomass accumulation, agricultural yield, or elements of the carbon cycle over land, for instance. A general non-linear relation between FAPAR and GPP has been confirmed when all data sets are adequate for the purpose, and a useful relation exists between FAPAR and GPP when the latter varies in the range from 0 to 5 gC m^{-2} d^{-1}. That relation saturates at larger values of GPP, so FAPAR may no be appropriate to monitor large values of GPP. However, long gaps were also occurring in this GPP data set, and the uneven distribution or even absence of FAPAR data during the vegetation growth phase in multiple seasons prevented meaningful comparisons, or resulted in unrealistic assessments in those seasons. Further efforts should examine the potential for improving the association between GPP with model fits by applying spatial or temporal interpolation techniques to provide best estimates during excessively long gaps in the FAPAR record.

Author Contributions: This paper is part of the Ph.D. thesis of the first author (H.D.L.). The second (M.M.V.) and third (M.S.) authors co-directed the first author. M.M.V. wrote the two Appendices. All authors have read and agreed to the published version of the manuscript.

Funding: Hugo De Lemos is financially supported through a grant by Exxaro Limited to the Exxaro Chair in Global Change and Sustainability Research, held at the Global Change Institute.

Acknowledgments: The Authors are most thankful to the three anonymous Reviewers who have provided numerous and substantial constructive comments to improve this manuscript. The first author (HDG) is very grateful to Prof. Barend Erasmus, who originally hosted him at the GCI and funded his research position. The authors also gratefully

acknowledge Dr. Gregor Feig at the South African Environmental Observation Network (SAEON) and Ms. Humbelani Thenga at the Council for Scientific and Industrial Research (CSIR), South Africa, for providing access to the open source Skukuza EC flux tower data (2000–2013), as well as the principal investigators and the wider FLUXNET scientific community involved in processing the FLUXNET2015 data set (Site ID: Za-Kru) used in the study. The authors are most thankful to Linda Hunt (NASA/SSAI) for her continuing support to the MISR-HR project over the last 15+ years. The second author (MMV) gratefully acknowledges the logistic support of the Global Change Institute (GCI) at the University of the Witwatersrand during periodic visits from 2016 to 2019.

Conflicts of Interest: The authors declare no conflict of interest.

Data Availability: MISR data are freely available from NASA's Atmospheric Science Data Center (ASDC) in Hampton, VA, USA. GPP data for the Skukuza EC flux tower are obtainable under the CC-BY-4.0 license from the FLUXNET2015 web site (https://fluxnet.org/data/fluxnet2015-dataset/), as noted in the main text. Intermediary and final results described in this paper are available upon request from the first author (HDL). Software codes to evaluate the four models used above are distributed under the MIT license from the GitHub web site https://github.com/mmverstraete.

Abbreviations

The following abbreviations are used in this manuscript:

ASAR	Advanced Synthetic Aperture Radar
ASDC	Atmospheric Science Data Center
ATSR	Along-Track Scanning Radiometer
CEOS	Committee on Earth Observation Satellites
CSIR	Council for Scientific and Industrial Research
EC	Eddy Covariance
ECMWF	European Centre for Medium-Range Weather Forecasts
ECV	Essential Climate Variable
EOS	End Of (vegetative) Season
EO	Earth Observation
EPSG	European Petroleum Survey Group
ERA	ECMWF Re-Analysis
FAPAR	Fraction of Absorbed Photosynthetically Active Radiation
GCOS	Global Climate Observing System
IPCC	Intergovernmental Panel on Climate Change
JRC	Joint Research Centre
JRC-TIP	Joint Research Centre Two-stream Inversion Package
LAI	Leaf Area Index
LiDAR	Light Detection And Ranging
LOS	Length Of (vegetative) Season
MISR	Multi-angle Imaging SpectroRadiometer
MISR-HR	Multi-angle Imaging SpectroRadiometer High Resolution
NASA	National Aeronautics and Space Administration
NDVI	Normalized Difference Vegetation Index
PDGF	Parametric Double Gaussian Function
PDHyTgF	Parametric Double Hyperbolic Tangent Function
PDLF	Parametric Double Logistic Function
PDSF	Parametric Double Sine Function
POLDER	Polarization and Directionality of Earth's Reflectances
RPV	Rahman, Pinty, Verstraete
SOM	Space Oblique Mercator
SOS	Start Of (vegetative) Season
SRES	Special Report on Emissions Scenarios

Appendix A. The MISR Instrument and MISR-HR Products

This Appendix serves as a quick introduction to the MISR instrument and MISR-HR products and provides pointers to further resources on these topics.

NASA's Terra mission (See https://terra.nasa.gov/, last accessed on 14 October 2020.), launched into space on 18 December 1999, embarked five Earth Observing (EO) instruments: Advanced Spaceborne Thermal Emission and Reflection Radiometer (See https://asterweb.jpl.nasa.gov/, last accessed on 14 October 2020.) (ASTER), Clouds and the Earth's Radiant Energy System (See https://ceres.larc.nasa.gov/, last accessed on 14 October 2020.) (CERES), Multi-angle Imaging SpectroRadiometer (See https://www-misr.jpl.nasa.gov/, last accessed on 14 October 2020.) (MISR), Moderate Resolution Imaging Spectroradiometer (See https://modis.gsfc.nasa.gov/, last accessed on 14 October 2020.) (MODIS), and Measurement of Pollution in the Troposphere (See https://mopitt.physics.utoronto.ca/, last accessed on 14 October 2020.) (MOPITT). Terra's sun-synchronous orbit is tightly maintained to avoid drifting and completes 233 revolutions around the planet during its 16-day repeat cycle, crossing the Equator within less than a minute of 10:30 A.M. (local time).

Appendix A.1. The MISR Instrument

MISR became operational on 24 February 2000 and is still working as of this writing. This instrument measures the amount of solar radiation reflected by the Earth, providing a unique opportunity to monitor climate and environmental changes with the same, carefully calibrated instrument over this period.

Remote sensing from space traditionally relies on the analysis of spectral, spatial and temporal variations to characterize the state and evolution of the environment. MISR enhances this approach by also collecting quasi-simultaneous multi-angular observations through its nine separate cameras, each acquiring spectral measurements in four spectral bands (blue: 446 nm, green: 558 nm, red: 672 nm, and near-infrared (NIR): 867 nm): Four cameras are pointing forward (Df: 70.3°, Cf: 60.2°, Bf: 45.7°, Af: 26.2°), one camera is pointing at nadir (An: 0.1°), and the last four cameras are pointing aft (Aa: 26.2°, Ba: 45.7°, Ca: 60.2°, Da: 70.6°) of the platform. MISR, therefore, measures the intensity of the solar radiation reflected by the planet in 36 data channels ([45,107–110], as well as a recent issue of the MDPI journal *Remote Sensing* dedicated to that instrument (See https://www.mdpi.com/journal/remotesensing/special_issues/misr_rs, last accessed on 14 October 2020.)).

The native spatial resolution (technically the ground sampling distance) of MISR is 275 m in all 36 data channels (actually 250 m at nadir, before the resampling implemented at Level 1). However, the resulting data rate exceeds the download bandwidth assigned to that instrument. To meet that constraint, 12 of those data channels are actually downloaded at the full spatial resolution (the 4 spectral bands of the nadir-pointing camera, and the red spectral channels of the 8 off-nadir-pointing cameras). The remaining 24 data channels, i.e., the non-red spectral channels from the off-nadir-pointing cameras, are averaged on-board the satellite and downloaded at the spatial resolution of 1100 m, achieving a 16:1 compression ratio in those channels. This is known as the MISR Global Mode (GM) of operation. MISR can also occasionally be operated in Local Mode (LM), whereby all 36 data channels are acquired at the full spatial resolution of 275 m but only over a limited region of about 300 km along the track of the platform.

As a result, all standard MISR Level-2 data products available from NASA are also provided at the spatial resolution of 1100 m (or coarser). They are openly accessible and permanently archived at the NASA Atmospheric Science Data Center (ASDC) in Hampton, VA, USA.

Each location on Earth is successively observed by all nine cameras in less than seven minutes. To combine and analyze the data from multiple cameras, these observations must be projected onto a common geographical grid, in this case, the orbit-specific Space Oblique Mercator (SOM) projection. This projection minimizes the distortion resulting from assigning raw data (from the detectors) into a

common grid to co-register the outputs of the various cameras. All MISR data products at Level 1B2 and Level 2 are geo-referenced to the SOM appropriate for the orbit.

Since the Terra platform repeats its orbital sequence every 16 days, the instruments observe the same locations from the same angular position every 233 orbits. These repeating orbital patterns are called Paths in MISR parlance. An Orbit refers to one Terra satellite revolution around the planet, numbered sequentially since launch. The elementary MISR data granule is a full Orbit (from pole to pole), but data are logically assigned to successive Blocks to ease the ordering and processing. Some 180 Blocks have been defined for each Path, and their geographical locations are fixed with respect to the planetary surface. At any one time, about 140 of those Blocks contain useful data: they correspond to the areas actually illuminated by the Sun on the selected day. The set of Blocks extends beyond both terminators to account for the seasonal variation in latitudinal illumination associated with the inclination of the Earth's rotational axis with respect to the ecliptic. Each Block covers an area of 563.2 km across-track by 140.8 km along-track, though only about 380 km of the data across-track contain usable data [111]. This width is somewhat larger for the more inclined cameras than for the nadir-pointing camera.

Appendix A.2. The MISR-HR Processing System

Land surfaces often exhibit significant heterogeneity at scales finer than the spatial resolution of standard MISR products (1100 m). Other instruments operating during the same period, such as the NASA Landsat program or the CNES SPOT instrument, deliver imagery at finer spatial resolutions but offer a lower revisit frequency because of their narrow swath width; they also lack the ability of systematically acquiring multi-angular observations. Recently, the trend towards finer and finer spatial resolutions has led to ever more limited spatial coverage (for engineering reasons), and stimulated the operation of constellations of satellites to remedy this problem. However, the interpretation of data products generated by very high spatial resolution instruments (e.g., at sampling distances commensurate with the size of the objects in the scene, such as trees) is very complex, as it requires radiation transfer models that represent the scene with that amount of detail.

The MISR-HR (for High Resolution) processing system [46] is designed to deliver a suite of land surface products at the native spatial resolution of 275 m, which is finer than the standard MISR products but nevertheless coarse enough to allow the use of classical (e.g., two-stream) radiation transfer models. This processing system requires four standard MISR data products as input:

1. The Ancillary Geographic Product (Earth Science Data Type or ESDT identifier: MIANCAGP) contains information on the latitude, longitude, and altitude distribution of each Block within the corresponding Path, as well as a scene classifier, for each 1100 m pixel, on the SOM map projection grid.
2. The Geometric Parameters Product (ESDT identifier: MI1B2GEOP) contains information on the applicable illumination and observation geometry (zenith and azimuth angles), as well as the scatter (angular distance between the Sun and camera directions) and glitter (angular distance to specular reflection) angles for each of the 9 cameras.
3. The L1B2 Terrain-projected Product (ESDT identifier: MI1B2T), in either Global or Local Mode, contains the calibrated Georectified Radiance Product (GRP) values measured by the MISR instrument, i.e., at the nominal 'Top of the Atmosphere' (ToA).
4. The Level 2 Land Product (ESDT identifier: MIL2ASL) contains the standard MISR Level 2 Land products, at the nominal 'Bottom of the Atmosphere' (BoA), i.e., after taking into account the contribution of the atmosphere to the observed radiance.

The MISR-HR processing system (currently at Version 2.01) proceeds through six steps to generate four sets of output products:

1. The first step consists in replacing missing values in the MISR L1B2 GRP, as well as in the Radiometric Camera-by-Camera Cloud Mask (RCCM) data sets, as described in [112,113]. These intermediary products are currently not saved but used directly in the subsequent steps.
2. A sharpening algorithm is then applied to this updated L1B2 GRP product to generate the L1B3 product, i.e., the 36 bidirectional spectral reflectance data channels at the nominal Top of the Atmosphere (ToA), at the full spatial resolution of the instrument (275 m). This product resembles the MISR Local Mode product, except that (1) it can be generated everywhere (and does not depend on Local Mode acquisitions), (2) the data values in the 24 non-red, off-nadir data channels are obviously reconstructed (since the only available observations are at the spatial resolution of 1100 m), and (3) the swath width of the L1B3 product does not exceed that of the nadir camera since the latter is used in this reconstruction.
3. An algorithm is then applied to the L1B3 product to estimate the bidirectional spectral reflectance factor (BRF) of the surface, sometimes also called Bottom of the Atmosphere (BoA) reflectance. This process takes into account the contribution of the atmosphere itself to the original measurements and yields 36 data channels at the native spatial resolution of the instrument.
4. The parametric bidirectional reflectance model of Rahman et al. [49] is subsequently inverted against the nine surface directional measurements available for each location, in the four spectral bands, to document the spectral anisotropy of the surface. Three model parameters are retrieved in each band, together with estimates of their associated uncertainties: a base reflectance ρ, which determines the brightness level of the reflectance, the Minnaert parameter k, which defines the bowl or bell shape of the reflectance as a function of the geometry of illumination and observation, and the asymmetry parameter Θ, which controls whether the reflectance is predominantly due to forward or backward scattering (also see [114]).
5. Those RPV results are spectrally and directionally integrated to generate the broadband albedos in the visible (VIS) and near-infrared (NIR) broadband regions required by the next step. These intermediary results are physically contained in the output files of the last processing step.
6. Finally, the Joint Research Centre (JRC) Two-stream Inversion Package (TIP) is inverted against the albedos just computed to offer a complete description of the radiation fluxes at the surface, specifically through estimates of the reflectance, transmittance and absorptance of the plant canopy, in addition to estimates of the Leaf Area Index (LAI), the Fraction of Absorbed Photosynthetically Active Radiation (FAPAR), and optical properties of the leaves, as well as the implied albedo of the underlying surface. This inversion procedure also delivers estimates of the variance associated with each output variable, and the final value of the goodness of fit criterion, which can be used to cull data items that are obviously wrong or of doubtful reliability [76].

These products have been found useful in a variety of applications, including to describe the heterogeneity of plant canopies [115,116], the foliage projective cover of plant canopies [117], the structural parameters of forests [26], or the response of grasslands to rainfall regimes [118].

Appendix B. Parametric Double S-Shaped Functions

Each of the four models mentioned in this paper is constructed as a superposition of an initial free parameter p_0 and two elementary S-shaped functions, representing the growing and the senescence phases, respectively (see Equations (A1), (A12), (A23), and (A34)).

This Appendix documents the mathematical representation of each of the four Parametric Double S-Shaped Functions, namely the Gaussian, Hyperbolic Tangent, Logistic, and Sine models. It also provides the analytic derivatives of those functions, which are used to accelerate the process of inverting those models against time series data.

The software to compute model values, written in the IDL (IDL is a Trademark of Harris Geospatial Solutions, Inc.) language, is available under the MIT license from the GitHub web site https://github.com/mmverstraete. This Appendix is a summary of the more exhaustive User Manual for those routines, available from the same source. In each of these four models, the independent variable is named x and the dependent variable is $y = f(x)$.

Appendix B.1. Parametric Double Gaussian Function

The Parametric Double Gaussian Function (PD_Gaus_F) is composed of 2 half Gaussian (or normal) distributions, each characterized by its own set of parameters:

$$f(x) = p_0 + f_1(x) + f_2(x), \tag{A1}$$

$$f_1(x) = \begin{cases} p_1 \exp\left[-0.5\left((p_2 - x)/p_3\right)^2\right] & \text{if } x \le p_2 \\ p_1 & \text{if } x > p_2, \end{cases} \tag{A2}$$

$$f_2(x) = \begin{cases} 0.0 & \text{if } x < p_5 \\ p_4\left[1.0 - \exp\left[-0.5\left((x - p_5)/p_6\right)^2\right]\right] & \text{if } x \ge p_5, \end{cases} \tag{A3}$$

where

- $f(x)$ is the value of the Parametric Double Gaussian Function at argument x, returned by the IDL function `pd_gaus_f`,
- $f_1(x)$ is the value of the first Parametric Gaussian Function at argument x, using parameters p_1 to p_3 and provided as the output positional parameter `pgf1`, and
- $f_2(x)$ is the value of the second Parametric Gaussian Function at argument x, using parameters p_4 to p_6 and provided as the output positional parameter `pgf2`.

The 7 PD_Gaus_F model parameters have the following meanings:

- p_0 = Base value of $f(x)$, i.e., asymptotic value when $x \to -\infty$.
- p_1 = Amplitude of $f_1(x)$ (positive for an increase, negative for a decrease), independently from the base value.
- p_2 = Phase shift along the x axis for the maximum of $f_1(x)$: a positive (negative) value shifts the function to the right (left) of $x = 0$.
- p_3 = Standard deviation of $f_1(x)$.
- p_4 = Amplitude of $f_2(x)$ (positive for an increase, negative for a decrease), independently from the base value.
- p_5 = Phase shift along the x axis for the maximum of $f_2(x)$: a positive (negative) value shifts the function to the right (left) of $x = 0$.
- p_6 = Standard deviation of $f_2(x)$.

The partial derivatives of the PD_Gaus_F model with respect to the 7 parameters are as follows:

$$\partial f(x)/\partial p_i = \partial p_0/\partial p_i + \partial f_1(x)/\partial p_i + \partial f_2(x)/\partial p_i, \tag{A4}$$

$$\partial p_0/\partial p_i = \begin{cases} 1.0 & \text{if } i = 0 \\ 0.0 & \text{if } i > 0 \end{cases}, \tag{A5}$$

$$\partial f_1(x)/\partial p_{1,} = \begin{cases} \exp\left[-0.5\left((p_2 - x)/p_3\right)^2\right] & \text{if } x \le p_2 \\ 1.0 & \text{if } x > p_2 \end{cases}, \tag{A6}$$

$$\partial f_1(x)/\partial p_2 = \begin{cases} -\left[p_1\left(p_2 - x\right)/p_3^2\right]\, \exp\left[-0.5\left((p_2 - x)/p_3\right)^2\right] & \text{if } x \le p_2 \\ 0.0 & \text{if } x > p_2 \end{cases}, \tag{A7}$$

$$\partial f_1(x)/\partial p_3 = \begin{cases} \left[p_1\left(p_2 - x\right)^2/p_3^3\right]\, \exp\left[-0.5\left((p_2 - x)/p_3\right)^2\right] & \text{if } x \le p_2 \\ 0.0 & \text{if } x > p_2 \end{cases}, \tag{A8}$$

$$\partial f_2(x)/\partial p_4 = \begin{cases} 0.0 & \text{if } x < p_5 \\ 1.0 - \exp\left[-0.5\left((p_5 - x)/p_6\right)^2\right] & \text{if } x \ge p_5 \end{cases}, \tag{A9}$$

$$\partial f_2(x)/\partial p_5 = \begin{cases} 0.0 & \text{if } x < p_5 \\ \left[p_4\left(p_5 - x\right)/p_6^2\right]\, \exp\left[-0.5\left((p_5 - x)/p_6\right)^2\right] & \text{if } x \ge p_5 \end{cases}, \tag{A10}$$

$$\partial f_2(x)/\partial p_6 = \begin{cases} 0.0 & \text{if } x < p_5 \\ -\left[p_4\left(p_5 - x\right)^2/p_6^3\right]\, \exp\left[-0.5\left((p_5 - x)/p_6\right)^2\right] & \text{if } x \ge p_5 \end{cases}, \tag{A11}$$

and all other partial derivatives (e.g., $\partial f_1(x)/\partial p_0$, $\partial f_1(x)/\partial p_5$ or $\partial f_2(x)/\partial p_3$) are null.

Appendix B.2. Hyperbolic Tangent Functions

The Parametric Double Hyperbolic Tangent Function (PD_HyTg_F) is composed of 2 Parametric Hyperbolic Tangent functions, each characterized by its own set of parameters:

$$f(x) = p_0 + f_1(x) + f_2(x), \tag{A12}$$

$$f_1(x) = p_1\left(\left(\tanh\left(\left(x - p_2\right)p_3\right) + 1.0\right)/2.0\right), \tag{A13}$$

$$f_2(x) = p_4\left(\left(\tanh\left(\left(x - p_5\right)p_6\right) + 1.0\right)/2.0\right), \tag{A14}$$

where

- $f(x)$ is the value of the Parametric Double Hyperbolic Tangent Function at argument x, returned by the IDL function `pd_hytg_f`,
- $f_1(x)$ is the value of the first Parametric Hyperbolic Tangent Function at argument x, using parameters p_1 to p_3 and provided as the output positional parameter `phtf1`, and
- $f_2(x)$ is the value of the second Parametric Hyperbolic Tangent Function at argument x, using parameters p_4 to p_6 and provided as the output positional parameter `phtf2`.

The 7 PD_HyTg_F model parameters have the following meanings:

- p_0 = Base value of $f(x)$, i.e., asymptotic value when $x \to -\infty$.
- p_1 = Amplitude of $f_1(x)$ (positive for an increase, negative for a decrease), independently from the base value.
- p_2 = Phase shift along the x axis for the inflection point of $f_1(x)$: a positive (negative) value shifts the function to the right (left) of $x = 0$.
- p_3 = Slope of $f_1(x)$ at the inflection point.

- p_4 = Amplitude of $f_2(x)$ (positive for an increase, negative for a decrease), independently from the base value.
- p_5 = Phase shift along the x axis for the inflection point of $f_2(x)$: a positive (negative) value shifts the function to the right (left) of $x = 0$.
- p_6 = Slope of $f_2(x)$ at the inflection point.

Note that the current codes expand upon and supersede the model description contained in [102]. The partial derivatives of the PD_HyTg_F model with respect to the 7 parameters are as follows:

$$\partial f(x)/\partial p_i = \partial p_0/\partial p_i + \partial f_1(x)/\partial p_i + \partial f_2(x)/\partial p_i, \tag{A15}$$

$$\partial p_0/\partial p_i = \begin{cases} 1.0 & \text{if } i = 0 \\ 0.0 & \text{if } i > 0 \end{cases}, \tag{A16}$$

$$\partial f_1(x)/\partial p_1 = (\tanh((x - p_2)\, p_3) + 1.0)/2.0, \tag{A17}$$

$$\partial f_1(x)/\partial p_2 = -(p_1\, p_3)/(2.0\, \cosh^2((x - p_2)\, p_3)), \tag{A18}$$

$$\partial f_1(x)/\partial p_3 = (p_1\, (x - p_2))/(2.0\, \cosh^2((x - p_2)\, p_3)), \tag{A19}$$

$$\partial f_2(x)/\partial p_4 = (\tanh((x - p_5)\, p_6) + 1.0)/2.0, \tag{A20}$$

$$\partial f_2(x)/\partial p_5 = -(p_4\, p_6)/(2.0\, \cosh^2((x - p_5)\, p_6)), \tag{A21}$$

$$\partial f_2(x)/\partial p_6 = (p_4\, (x - p_5))/(2.0\, \cosh^2((x - p_5)\, p_6)), \tag{A22}$$

and all other partial derivatives (e.g., $\partial f_1(x)/\partial p_0$, $\partial f_1(x)/\partial p_5$ or $\partial f_2(x)/\partial p_3$) are null.

Appendix B.3. Logistic Functions

The Parametric Double Logistic Function (PD_Logi_F) is composed of 2 Logistic functions, each characterized by its own set of parameters:

$$f(x) = p_0 + f_1(x) + f_2(x), \tag{A23}$$

$$f_1(x) = p_1 / \left(1.0 + \exp(-(x - p_2)\, p_3)\right), \tag{A24}$$

$$f_2(x) = p_4 / \left(1.0 + \exp(-(x - p_5)\, p_6)\right), \tag{A25}$$

where

- $f(x)$ is the value of the Parametric Double Logistic Function at argument x, returned by the IDL function `pd_logi_f`,
- $f_1(x)$ is the value of the first Parametric Logistic Function at argument x, using parameters p_1 to p_3 and provided as the output positional parameter `plf1`, and
- $f_2(x)$ is the value of the second Parametric Logistic Function at argument x, using parameters p_4 to p_6 and provided as the output positional parameter `plf2`.

The 7 parameters have the following meanings:

- p_0 = Base value of $f(x)$, i.e., asymptotic value when $x \to -\infty$.
- p_1 = Amplitude of $f_1(x)$ (positive for an increase, negative for a decrease), independently from the base value.
- p_2 = Phase shift along the x axis for the inflection point of $f_1(x)$: a positive (negative) value shifts the function to the right (left) of $x = 0$.
- p_3 = Slope of $f_1(x)$ at the inflection point.

- p_4 = Amplitude of $f_2(x)$ (positive for an increase, negative for a decrease), independently from the base value.
- p_5 = Phase shift along the x axis for the inflection point of $f_2(x)$: a positive (negative) value shifts the function to the right (left) of $x = 0$.
- p_6 = Slope of $f_2(x)$ at the inflection point.

The partial derivatives of the PD_Logi_F model with respect to the 7 parameters are as follows:

$$\partial f(x)/\partial p_i = \partial p_0/\partial p_i + \partial f_1(x)/\partial p_i + \partial f_2(x)/\partial p_i, \tag{A26}$$

$$\partial p_0/\partial p_i = \begin{cases} 1.0 & \text{if } i = 0 \\ 0.0 & \text{if } i > 0 \end{cases}, \tag{A27}$$

$$\partial f_1(x)/\partial p_1 = 1.0/(1.0 + \exp(-(x - p_2)\, p_3)), \tag{A28}$$

$$\partial f_1(x)/\partial p_2 = -(p_1\, \exp(-(x - p_2])\, p_3))/(1.0 + \exp(-(x - p_2)\, p_3))^2, \tag{A29}$$

$$\partial f_1(x)/\partial p_3 = -(p_1\, \exp(-(x - p_2)))/(1.0 + \exp(-(x - p_2)\, p_3))^2, \tag{A30}$$

$$\partial f_2(x)/\partial p_4 = 1.0/(1.0 + \exp(-(x - p_5)\, p_6)), \tag{A31}$$

$$\partial f_2(x)/\partial p_5 = -(p_4\, \exp(-(x - p_5)\, p_6))/(1.0 + \exp(-(x - p_5)\, p_6))^2, \tag{A32}$$

$$\partial f_2(x)/\partial p_6 = -(p_4\, \exp(-(x - p_5)))/(1.0 + \exp(-(x - p_5)\, p_6))^2, \tag{A33}$$

and all other partial derivatives (e.g., $\partial f_1(x)/\partial p_0$, $\partial f_1(x)/\partial p_5$ or $\partial f_2(x)/\partial p_3$) are null.

Appendix B.4. Sine Functions

The Parametric Double Sine Function (PD_Sine_F) is composed of 2 sine functions, each characterized by its own set pf parameters:

$$f(x) = p_0 + f_1(x) + f_2(x), \tag{A34}$$

$$f_1(x) = \begin{cases} 0.0 & \text{if } x < p_2 \\ p_1\,(1.0 + \sin(-(\pi/2.0) + ((x - p_2)/(p_3 - p_2))\,\pi))/2.0 & \text{if } p_2 \le x \le p_3 \\ p_1 & \text{if } p_3 < x \end{cases}, \tag{A35}$$

$$f_2(x) = \begin{cases} 0.0 & \text{if } x < p_5 \\ -p_4\,(\sin((\pi/2.0) + ((x - p_5)/(p_6 - p_5)\,\pi)) - 1.0)/2.0 & \text{if } p_5 \le x \le p_6 \\ -p_4 & \text{if } p_6 < x \end{cases}, \tag{A36}$$

where

- $f(x)$ is the value of the Parametric Double Sine Function at argument x, returned by the IDL function `pd_sine_f`,
- $f_1(x)$ is the value of the first Parametric Sine Function at argument x, using parameters p_1 to p_3 and provided as the output positional parameter `psf1`, and
- $f_2(x)$ is the value of the second Parametric Sine Function at argument x, using parameters p_4 to p_6 and provided as the output positional parameter `psf2`.

The 7 parameters have the following meanings:

- p_0 = Base value of $f(x)$, i.e., asymptotic value when $x \to -\infty$.
- p_1 = Amplitude of $f_1(x)$ (positive for an increase, negative for a decrease), independently from the base value.

- p_2 = Phase shift along the x axis for the start of $f_1(x)$: a positive (negative) value shifts the function to the right (left) of $x = 0$.
- p_3 = Phase shift along the x axis for the end of $f_1(x)$: a positive (negative) value shifts the function to the right (left) of $x = 0$.
- p_4 = Amplitude of $f_2(x)$, independently from the base value.
- p_5 = Phase shift along the x axis for the start of $f_2(x)$: a positive (negative) value shifts the function to the right (left) of $x = 0$.
- p_6 = Phase shift along the x axis for the end of $f_2(x)$: a positive (negative) value shifts the function to the right (left) of $x = 0$.

The partial derivatives of the PD_Sine_F model with respect to the 7 parameters are as follows:

$$\partial f(x)/\partial p_i = \partial p_0/\partial p_i + \partial f_1(x)/\partial p_i + \partial f_2(x)/\partial p_i, \tag{A37}$$

$$\partial p_0/\partial p_i = \begin{cases} 1.0 & \text{if } i = 0 \\ 0.0 & \text{if } i > 0 \end{cases}, \tag{A38}$$

$$\partial f_1(x)/\partial p_1 = \left[1 - \cos\left(\frac{\pi\,(x - p_2)}{p_3 - p_2}\right)\right]/2, \tag{A39}$$

$$\partial f_1(x)/\partial p_2 = \left[\pi p_1\,(x - p_3)\sin\left(\frac{\pi\,(x - p_2)}{p_3 - p_2}\right)\right] / \left(2\,(p_2 - p_3)^2\right), \tag{A40}$$

$$\partial f_1(x)/\partial p_3 = -\left[\pi p_1\,(x - p_2)\sin\left(\frac{\pi\,(x - p_2)}{p_3 - p_2}\right)\right] / \left(2\,(p_3 - p_2)^2\right), \tag{A41}$$

$$\partial f_1(x)/\partial p_4 = \left[1 - \cos\left(\frac{\pi\,(x - p_5)}{p_6 - p_5}\right)\right]/2, \tag{A42}$$

$$\partial f_1(x)/\partial p_5 = \left[\pi p_4\,(x - p_6)\sin\left(\frac{\pi\,(x - p_5)}{p_6 - p_5}\right)\right] / \left(2\,(p_5 - p_6)^2\right), \tag{A43}$$

$$\partial f_1(x)/\partial p_6 = -\left[\pi p_4\,(x - p_5)\sin\left(\frac{\pi\,(x - p_5)}{p_6 - p_5}\right)\right] / \left(2\,(p_6 - p_5)^2\right), \tag{A44}$$

and all other partial derivatives (e.g., $\partial f_1(x)/\partial p_0$, $\partial f_1(x)/\partial p_5$ or $\partial f_2(x)/\partial p_3$) are null.

Appendix B.5. Prior Values

The numerical inversion of anyone of those models against a particular data set requires the specification of some starting state of the system, specifically be providing initial values to the model parameters. These are known as the *prior values*. This subsection describes how those values are determined for each of those models.

The IDL function `set_prior_dsf.pro` determines the most appropriate prior values for the model parameters. This function can handle seasonal signals that fluctuate from low to high and back to low values, as is the case for FAPAR or LAI, or signals that evolve from high to low and back to high values (like albedo), during a typical vegetative season. The algorithm used in the former case proceeds through the following steps, where the `identifiers` set in typewriter face correspond to the names of the variables in the associated software code:

1. Compute the mean value `mid_y` of the biogeophysical variable across the entire season.
2. Identify the start `fst_x_during` and end `lst_x_during` of the period during which the input signal is higher than `mid_y`.
3. Locate the largest value `x_fst_max_y_during` of this biogeophysical variable within this restricted period. The function also handles cases where there may be more than one instance of such a large value.

4. Identify the start and end of the initial and final periods when the biogeophysical variable is lower than the mean value: `fst_x_before`, `lst_x_before`, `fst_x_after` and `lst_x_after`, respectively.
5. Compute the mean values `mean_before`, `mean_during` and `mean_after` of the biogeophysical variable during the initial, peak and final periods characterized above.
6. For all four models, set the prior value of parameter p_0 to `mean_before`, the prior value of parameter p_1 to (`mean_during` − `mean_before`), and the prior value of parameter p_4 to (`mean_after` − `mean_during`).
7. For the PDGF model, set the prior values of parameter p_2 to `fst_x_during`, parameter p_3 to ((`x_fst_max_y_during` − `lst_x_before`) / 3.0), parameter p_5 to `lst_x_during`, and parameter p_6 to ((`fst_x_after` − `x_lst_max_y_during`) / 3.0).
8. For the PDHyTgF model, set the prior values of parameter p_2 to (`lst_x_before` + ((`fst_x_during` - `lst_x_before`) / 2.0)), parameter p_3 to ((`fst_y_during` − `lst_y_before`) / `delta_x`), where `delta_x` is (`fst_x_during` − `lst_x_before`), parameter p_5 to (`lst_x_during` + ((`fst_x_after` − `lst_x_during`) / 2.0)), and parameter p_6 to (ABS(`fst_y_after` − `lst_y_during`) / `delta_x`).
9. For the PDLS model, set the prior values of parameter p_2 to (`lst_x_before` + ((`fst_x_during` - `lst_x_before`) / 2.0)), parameter p_3 to (2.0 × (`fst_y_during` − `lst_y_before`) / `delta_x`), where `delta_x` is (`fst_x_during` − `lst_x_before`), parameter p_5 to (`lst_x_during` + ((`fst_x_after` − `lst_x_during`) / 2.0)), and parameter p_6 to (2.0 × ABS(`fst_y_after` − `lst_y_during`) / `delta_x`).
10. For the PDSF model, set the prior values of parameter p_2 to `fst_x_before`, parameter p_3 to `x_fst_max_y_during`, parameter p_5 to `x_lst_max_y_during`, parameter p_6 to `lst_x_after`.

References

1. Friedlingstein, P.; Cadule, P.; Piao, S.; Ciais, P.; Sitch, S. The African contribution to the global climate-carbon cycle feedback of the 21st century. *Biogeosciences* **2010**, *7*, 513–519. [CrossRef]
2. Adole, T.; Dash, J.; Rodriguez-Galiano, V.; Atkinson, P.M. Photoperiod controls vegetation phenology across Africa. *Commun. Biol.* **2019**, *2*, 1–13. [CrossRef] [PubMed]
3. Jones, P.D.; Lister, D.H.; Osborn, T.J.; Harpham, C.; Salmon, M.; Morice, C.P. Hemispheric and large-scale land-surface air temperature variations: An extensive revision and an update to 2010. *J. Geophys. Res. Atmos.* **2012**, *117*, 1–29. [CrossRef]
4. Engelbrecht, F.; Adegoke, J.; Bopape, M.J.; Naidoo, M.; Garland, R.; Thatcher, M.; McGregor, J.; Katzfey, J.; Werner, M.; Ichoku, C.; et al. Projections of rapidly rising surface temperatures over Africa under low mitigation. *Environ. Res. Lett.* **2015**, *10*, 085004. [CrossRef]
5. Archer, E.R.M.; Engelbrecht, F.A.; Hänsler, A.; Landman, W.; Tadross, M.; Helmschrot, J. Seasonal prediction and regional climate projections for southern Africa. In *Climate Change and Adaptive Land Management in Southern Africa—Assessments, Changes, Challenges, and Solutions*; Revermann, R., Krewenka, K.M., Schmiedel, U., Olwoch, J.M., Jörg, H., Jürgens, N., Eds.; Klaus Hess Publishers: Göttingen, Germany; Windhoek, Namibia, 2018; Volume 6, pp. 14–21. [CrossRef]
6. Kutsch, W.L.; Hanan, N.; Scholes, R.J.; McHugh, I.; Kubheka, W.; Eckhardt, H.; Williams, C. Response of carbon fluxes to water relations in a savanna ecosystem in South Africa. *Biogeosciences* **2008**, *5*, 1797–1808. [CrossRef]
7. Twine, W.C.; Moshe, D.; Netshiluvhi, T.; Siphugu, V. Consumption and direct-use values of savanna bio-resources used by rural households in Mametja, a semi-arid area of Limpopo province, South Africa. *S. Afr. J. Sci.* **2003**, *99*, 467–473.
8. Shackleton, C.M.; Shackleton, S.E. The importance of non-timber forest products in rural livelihood security and as safety nets: A review of evidence from South Africa. *S. Afr. J. Sci.* **2004**, *100*, 658–664.
9. Main, R.; Mathieu, R.; Kleynhans, W.; Wessels, K.; Naidoo, L.; Asner, G.P. Hyper-Temporal C-Band SAR for Baseline Woody Structural Assessments in Deciduous Savannas. *Remote Sens.* **2016**, *8*, 661. [CrossRef]

10. Kalema, V.N.; Witkowski, E.T.F. Land-use impacts on woody plant density and diversity in an African savanna charcoal production region. *Int. J. Biodivers. Sci. Ecosyst. Serv. Manag.* **2012**, *8*, 231–247. [CrossRef]
11. Matsika, R.; Erasmus, B.F.N.; Twine, W.C. Double jeopardy: The dichotomy of fuelwood use in rural South Africa. *Energy Policy* **2013**, *52*, 716–725. [CrossRef]
12. Erasmus, B.F.N.; Coetzer, K.; Mambo, J.; Archer, E.R.M.; Fisher, J.T.; Asner, G.P. Environmental change in Bushbuckridge. In *Observation on Environmental Change in South Africa*; Sun Media Publishing: Stellenbosch, South Africa, 2011; pp. 1–5. Available online: https://researchspace.csir.co.za/dspace/handle/10204/6742 (accessed on 14 October 2020).
13. Mucina, L.; Rutherford, M.C. (Eds.) *The Vegetation of South Africa, Lesotho and Swaziland*; Number 19 in Strelitzia; South African National Biodiversity Institute: Pretoria, South Africa, 2006.
14. Venter, F.J.; Scholes, R.J.; Eckhardt, H.C. The Abiotic Template and Its Associated Vegetation Pattern. In *The Kruger Experience: Ecology and Management of Savanna Heterogeneity*; du Toit, J.T., Rogers, K.H., Biggs, H.C., Eds.; Island Press: Washington, DC, USA, 2003; pp. 83–129.
15. Sankaran, M.; Ratnam, J.; Hanan, N. Woody cover in African savannas: The role of resources, fire and herbivory. *Glob. Ecol. Biogeogr.* **2008**, *17*, 236–245. [CrossRef]
16. Rouse, J.W., Jr.; Haas, R.H.; Schell, J.A.; Deering, D.W. *Monitoring the Vernal Advancement and Retrogradation (Green Wave Effect) of Natural Vegetation*; Technical report; Texas A&M University, Remote Sensing Center: College Station, TX, USA, 1973.
17. Rouse, J.W., Jr.; Haas, R.H.; Schell, J.A.; Deering, D.W. Monitoring Vegetation Systems in the Great Plains with ERTS. In Proceedings of the Third Earth Resources Technology Satellite-1 Symposium, Washington, DC, USA, 1 January 1974; Volume 1, pp. 309–317.
18. Committee on Planetary Biology; Space Science Board; Commission on Physical Sciences, Mathematics, and Resources; National Research Council. *Remote Sensing of the Biosphere*; Number 12344; National Academy Press: Washington, DC, USA, 1986; p. 148.
19. Tang, J.; Körner, C.; Muraoka, H.; Piao, S.; Shen, M.; Thackeray, S.J.; Yang, X. Emerging opportunities and challenges in phenology: A review. *Ecosphere* **2016**, *7*, 1–17. [CrossRef]
20. Gobron, N.; Verstraete, M.M. *FAPAR—Fraction of Absorbed Photosynthetically Active Radiation (FAPAR)*; Technical Report T10–GTOS 65; Global Terrestrial Observing System (GTOS): Rome, Italy, 2009.
21. Zhang, X.; Friedl, M.A.; Schaaf, C.B.; Strahler, A.H.; Hodges, J.C.F.; Gao, F.; Reed, B.C.; Huete, A. Monitoring vegetation phenology using MODIS. *Remote Sens. Environ.* **2003**, *84*, 471–475. [CrossRef]
22. Butt, B.; Turner, M.D.; Singh, A.; Brottem, L. Use of MODIS NDVI to evaluate changing latitudinal gradients of rangeland phenology in Sudano-Sahelian West Africa. *Remote Sens. Environ.* **2011**, *115*, 3367–3376. [CrossRef]
23. Buitenwerf, R.; Rose, L.; Higgins, S.I. Three decades of multi-dimensional change in global leaf phenology. *Nat. Clim. Chang.* **2015**, *5*, 364–368. [CrossRef]
24. Kellndorfer, J.M.; Walker, W.S.; LaPoint, E.; Kirsch, K.; Bishop, J.; Fiske, G. Statistical fusion of lidar, InSAR, and optical remote sensing data for forest stand height characterization: A regional-scale method based on LVIS, SRTM, Landsat ETM+, and ancillary data sets. *J. Geophys. Res.* **2010**, *115*, 1–10. [CrossRef]
25. Naidoo, L.; Cho, M.A.; Mathieu, R.; Asner, G. Classification of savanna tree species, in the Greater Kruger National Park region, by integrating hyperspectral and LiDAR data in a Random Forest data mining environment. *Isprs J. Photogramm. Remote Sens.* **2012**, *69*, 167–179. [CrossRef]
26. Mahlangu, P.; Mathieu, R.; Wessels, K.; Naidoo, L.; Verstraete, M.M.; Asner, G.; Main, R. Indirect Estimation of Structural Parameters in South African Forests Using MISR-HR and LiDAR Remote Sensing Data. *Remote Sens.* **2018**, *10*, 1537. [CrossRef]
27. Haack, B.N.; Herold, N.D.; Bechdol, M.A. Radar and Optical Data Integration for Land-Use/Land-Cover Mapping. *Photogramm. Eng. Remote Sens.* **2000**, *66*, 709–716.
28. Joshi, N.; Baumann, M.; Ehammer, A.; Fensholt, R.; Grogan, K.; Hostert, P.; Jepsen, M.R.; Kuemmerle, T.; Meyfroidt, P.; Mitchard, E.T.A.; et al. A Review of the Application of Optical and Radar Remote Sensing Data Fusion to Land Use Mapping and Monitoring. *Remote Sens.* **2016**, *8*, 70. [CrossRef]

29. Lopes, M.; Frison, P.L.; Durant, S.M.; Schulte to Bühne, H.; Ipavec, A.; Lapeyre, V.; Pettorelli, N. Combining optical and radar satellite image time series to map natural vegetation: Savannas as an example. *Remote Sens. Ecol. Conserv.* **2020**, *6*, 316–326. [CrossRef]
30. Zhu, Z.; Piao, S.; Myneni, R.B.; Huang, M.; Zeng, Z.; Canadell, J.G.; Ciais, P.; Sitch, S.; Friedlingstein, P. Greening of the Earth and its drivers. *Nat. Clim. Chang.* **2016**, *6*, 791–795. [CrossRef]
31. Jolly, W.M.; Nemani, R.; Running, S.W. A generalized, bioclimatic index to predict foliar phenology in response to climate. *Glob. Chang. Biol.* **2005**, *11*, 619–632. [CrossRef]
32. Piao, S.; Tan, J.; Chen, A.; Fu, Y.H.; Ciais, P.; Liu, Q.; Janssens, I.A.; Vicca, S.; Zeng, Z.; Jeong, S.J.; et al. Leaf onset in the northern hemisphere triggered by daytime temperature. *Nat. Commun.* **2015**, *6*, 1–8. [CrossRef]
33. Workie, T.G.; Debella, H.J. Climate change and its effects on vegetation phenology across ecoregions of Ethiopia. *Glob. Ecol. Conserv.* **2018**, *13*, e00366. [CrossRef]
34. Zhang, X.; Friedl, M.A.; Schaaf, C.B. Global vegetation phenology from Moderate Resolution Imaging Spectroradiometer (MODIS): Evaluation of global patterns and comparison with in situ measurements. *J. Geophys. Res. Biogeosci.* **2006**, *111*, G04017. [CrossRef]
35. Verger, A.; Filella, I.; Baret, F.; Peñuelas, J. Vegetation baseline phenology from kilometric global LAI satellite products. *Remote Sens. Environ.* **2016**, *178*, 1–14. [CrossRef]
36. Adole, T.; Dash, J.; Atkinson, P.M. A systematic review of vegetation phenology in Africa. *Ecol. Inform.* **2016**, *34*, 117–128. [CrossRef]
37. Verbesselt, J.; Somers, B.; Lhermitte, S.; Jonckheere, I.; Van Aardt, J.; Coppin, P. Monitoring herbaceous fuel moisture content with SPOT VEGETATION time-series for fire risk prediction in savanna ecosystems. *Remote Sens. Environ.* **2007**, *108*, 357–368. [CrossRef]
38. Coetzer, K.L.; Erasmus, B.F.N.; Witkowski, E.T.F.; Bachoo, A.K. Land-cover change in the Kruger to Canyons Biosphere Reserve (1993–2006): A first step towards creating a conservation plan for the subregion. *S. Afr. J. Sci.* **2010**, *106*, 1–10. [CrossRef]
39. Coetzer, K.L.; Erasmus, B.F.N.; Witkowski, E.T.F.; Reyers, B. The Race for Space: Tracking Land-Cover Transformation in a Socio-ecological Landscape, South Africa. *Environ. Manag.* **2013**, *52*, 595–611. [CrossRef] [PubMed]
40. Madonsela, S.; Cho, M.A.; Ramoelo, A.; Mutanga, O. Remote sensing of species diversity using Landsat 8 spectral variables. *ISPRS J. Photogramm. Remote Sens.* **2017**, *133*, 116–127. [CrossRef]
41. Wessels, K.J.; Mathieu, R.; Erasmus, B.F.N.; Asner, G.P.; Smit, I.P.J.; Van Aardt, J.A.N.; Main, R.; Fisher, J.; Marais, W.; Kennedy-Bowdoin, T.; et al. Impact of communal land use and conservation on woody vegetation structure in the Lowveld savannas of South Africa. *For. Ecol. Manag.* **2011**, *261*, 19–29. [CrossRef]
42. Fisher, J.T.; Witkowski, E.T.F.; Erasmus, B.F.N.; van Aardt, J.A.N.; Asner, G.P.; Wessels, K.J.; Mathieu, R. Human-modified landscapes: Patterns of fine-scale woody vegetation structure in communal savannah rangelands. *Environ. Conserv.* **2012**, *39*, 72–82. [CrossRef]
43. Fisher, J.T.; Witkowski, E.T.F.; Erasmus, B.F.N.; Mograbi, P.J.; Asner, G.P.; van Aardt, J.A.N.; Wessels, K.J.; Mathieu, R. What lies beneath: Detecting sub-canopy changes in savanna woodlands using a three-dimensional classification method. *Appl. Veg. Sci.* **2015**, *18*, 528–540. [CrossRef]
44. Cho, M.A.; Mathieu, R.; Asner, G.P.; Naidoo, L.; van Aardt, J.; Ramoelo, A.; Debba, P.; Wessels, K.; Main, R.; Smit, I.P.J.; et al. Mapping tree species composition in South African savannas using an integrated airborne spectral and LiDAR system. *Remote Sens. Environ.* **2012**, *125*, 214–226. [CrossRef]
45. Diner, D.J.; Asner, G.P.; Davies, R.; Knyazikhin, Y.; Muller, J.P.; Nolin, A.W.; Pinty, B.; Schaaf, C.B.; Stroeve, J. New Directions in Earth Observing: Scientific Applications of Multiangle Remote Sensing. *Bull. Am. Meteorol. Soc.* **1999**, *80*, 2209–2228. [CrossRef]
46. Verstraete, M.M.; Hunt, L.A.; Scholes, R.J.; Clerici, M.; Pinty, B.; Nelson, D.L. Generating 275 m Resolution Land Surface Products From the Multi-Angle Imaging SpectroRadiometer data. *IEEE Trans. Geosci. Remote Sens.* **2012**, *50*, 3980–3990. [CrossRef]

47. Pinty, B.; Andredakis, I.; Clerici, M.; Kaminski, T.; Taberner, M.; Verstraete, M.M.; Gobron, N.; Widlowski, J.L. Exploiting the MODIS albedos with the Two-stream Inversion Package (JRC–TIP): 1. Effective Leaf Area Index, Vegetation, and Soil Properties. *J. Geophys. Res.* **2011**, *116*, D09105. [CrossRef]
48. Pinty, B.; Clerici, M.; Andredakis, I.; Kaminski, T.; Taberner, M.; Verstraete, M.M.; Gobron, N.; Widlowski, J.L. Exploiting the MODIS albedos with the Two-stream Inversion Package (JRC–TIP): 2. Fractions of Transmitted and Absorbed Fluxes in the Vegetation and Soil Layers. *J. Geophys. Res.* **2011**, *116*, D09106. [CrossRef]
49. Rahman, H.; Pinty, B.; Verstraete, M.M. Coupled Surface-Atmosphere Reflectance (CSAR) Model. 2. Semiempirical Surface Model Usable With NOAA Advanced Very High Resolution Radiometer Data. *J. Geophys. Res.* **1993**, *98*, 20791–20801. [CrossRef]
50. Lavergne, T.; Kaminski, T.; Pinty, B.; Taberner, M.; Gobron, N.; Verstraete, M.M.; Vossbeck, M.; Widlowski, J.L.; Giering, R. Application to MISR land products of an RPV model inversion package using adjoint and Hessian codes. *Remote Sens. Environ.* **2007**, *107*, 362–375. [CrossRef]
51. Clerici, M.; Vossbeck, M.; Pinty, B.; Kaminski, T.; Taberner, M.; Lavergne, T.; Andredakis, I. Consolidating the Two-Stream Inversion Package (JRC-TIP) to Retrieve Land Surface Parameters From Albedo Products. *IEEE J. Sel. Top. Appl. Earth Obs. Remote Sens.* **2010**, *3*, 286–295. [CrossRef]
52. Chernetskiy, M.; Gómez-Dans, J.; Gobron, N.; Morgan, O.; Lewis, P.; Truckenbrodt, S.; Schmullius, C. Estimation of FAPAR over Croplands Using MISR Data and the Earth Observation Land Data Assimilation System (EO-LDAS). *Remote Sens.* **2017**, *9*, 656. [CrossRef]
53. Pinty, B.; Jung, M.; Kaminski, T.; Lavergne, T.; Mund, M.; Plummer, S.; Thomas, E.; Widlowski, J.L. Evaluation of the JRC-TIP 0.01° products over a mid-latitude deciduous forest site. *Remote Sens. Environ.* **2011**, *115*, 3567–3581. [CrossRef]
54. D'Odorico, P.; Gonsamo, A.; Pinty, B.; Gobron, N.; Coops, N.; Mendez, E.; Schaepman, M.E. Intercomparison of fraction of absorbed photosynthetically active radiation products derived from satellite data over Europe. *Remote Sens. Environ.* **2014**, *142*, 142–154. [CrossRef]
55. Kaminski, T.; Pinty, B.; Voßbeck, M.; Lopatka, M.; Gobron, N.; Robustelli, M. Consistent retrieval of land surface radiation products from EO, including traceable uncertainty estimates. *Biogeosciences* **2017**, *14*, 2527–2541. [CrossRef]
56. Gobron, N.; Marioni, M.; Robustelli, M.; Vermote, E. Can We Use the QA4ECV Black-sky Fraction of Absorbed Photosynthetically Active Radiation (FAPAR) using AVHRR Surface Reflectance to Assess Terrestrial Global Change? *Remote Sens.* **2019**, *11*, 3055. [CrossRef]
57. Swinbank, W.C. The measurement of vertical transfer of heat and water vapor by eddies in the lower atmosphere. *J. Meteorol.* **1951**, *8*, 135–145. [CrossRef]
58. Friend, A.D.; Arneth, A.; Kiang, N.Y.; Lomas, M.; Ogée, J.; Rödenbeck, C.; Running, S.W.; Santaren, J.D.; Sitch, S.; Viovy, N.; et al. FLUXNET and modelling the global carbon cycle. *Glob. Chang. Biol.* **2007**, *13*, 610–633. [CrossRef]
59. Baldocchi, D.D. 'Breathing' of the terrestrial biosphere: Lessons learned from a global network of carbon dioxide flux measurement systems. *Aust. J. Bot.* **2008**, *56*, 1–26. [CrossRef]
60. Baldocchi, D.D. Assessing the eddy covariance technique for evaluating carbon dioxide exchange rates of ecosystems: Past, present and future. *Glob. Chang. Biol.* **2003**, *9*, 479–492. [CrossRef]
61. Scholes, R.J.; Gureja, N.; Giannecchinni, M.; Dovie, D.; Wilson, B.; Davidson, N.; Piggott, K.; McLoughlin, C.; Van der Velde, K.; Freeman, A.; et al. The environment and vegetation of the flux measurement site near Skukuza, Kruger National Park. *Koedoe* **2001**, *44*, 73–83. [CrossRef]
62. Archibald, S.A.; Kirton, A.; van der Merwe, M.R.; Scholes, R.J.; Williams, C.A.; Hanan, N. Drivers of inter-annual variability in Net Ecosystem Exchange in a semi-arid savanna ecosystem, South Africa. *Biogeosciences* **2009**, *6*, 251–266. [CrossRef]
63. Annegarn, H.J.; Otter, L.; Swap, R.J.; Scholes, R.J. Southern Africa's ecosystem in a test-tube: A perspective on the Southern African Regional Science Initiative (SAFARI 2000). *S. Afr. J. Sci.* **2002**, *98*, 111–113.
64. Otter, L.B.; Scholes, R.J.; Dowty, P.; Privette, J.; Caylor, K.; Ringrose, S.; Mukelabai, M.; Frost, P.; Hanan, N.; Totolo, O.; et al. The Southern African Regional Science Initiative (SAFARI 2000): Wet season campaigns. *S. Afr. J. Sci.* **2002**, *98*, 131–137.

65. Shugart, H.H.; Macko, S.A.; Lesolle, P.; Szuba, T.A.; Mukelabai, M.M.; Dowty, P.; Swap, R.J. The SAFARI 2000—Kalahari Transect Wet Season Campaign of year 2000. *Glob. Chang. Biol.* **2004**, *10*, 273–280. [CrossRef]
66. Nickless, A.; Archibald, S.A.; Van der Merwe, M.R.; Scholes, R.J.; Williams, C.A.; Hanan, N. Estimation of net ecosystem exchange at the Skukuza flux site, Kruger National Park, South Africa. In Proceedings of the Open Science Conference on "Africa and Carbon Cycle: The CarboAfrica Project, Accra, Ghana, 25–27 November 2008; pp. 23–32.
67. Majozi, N.P.; Mannaerts, C.M.; Ramoelo, A.; Mathieu, R.; Nickless, A.; Verhoef, W. Analysing surface energy balance closure and partitioning over a semi-arid savanna FLUXNET site in Skukuza, Kruger National Park, South Africa. *Hydrol. Earth Syst. Sci.* **2017**, *21*, 3401–3415. [CrossRef]
68. Pastorello, G.Z.; Papale, D.; Chu, H.; Trotta, C.; Agarwal, D.A.; Canfora, E.; Baldocchi, D.D.; Torn, M.S. A New Data Set to Keep a Sharper Eye on Land-Air Exchanges. *EOS* **2017**, *98*. [CrossRef]
69. Pastorello, G.; Trotta, C.; Canfora, E.; Chu, H.; Christianson, D.; Cheah, Y.W.; Poindexter, C.; Chen, J.; Elbashandy, A.; Humphrey, M.; et al. The FLUXNET2015 dataset and the ONEFlux processing pipeline for eddy covariance data. *Sci. Data* **2020**, *7*, 225. [CrossRef]
70. Reed, B.C.; Schwartz, M.D.; Xiao, X. Remote Sensing Phenology. In *Phenology of Ecosystem Processes*; Springer: New York, NY, USA, 2009; pp. 231–246. [CrossRef]
71. Xiao, X.; Zhang, J.; Yan, H.; Wu, W.; Biradar, C. Land Surface Phenology: Convergence of Satellite and CO2 Eddy Flux Observations. In *Phenology of Ecosystem Processes: Applications in Global Change Research*; Noormets, A., Ed.; Springer Science + Business Media, LLC: Berlin, Germany, 2009; pp. 247–270. [CrossRef]
72. McCloy, K.R. Development and Evaluation of Phenological Change Indices Derived from Time Series of Image Data. *Remote Sens.* **2010**, *2*, 2442. [CrossRef]
73. Richardson, A.D.; Keenan, T.F.; Migliavacca, M.; Ryu, Y.; Sonnentag, O.; Toomey, M. Climate change, phenology, and phenological control of vegetation feedbacks to the climate system. *Agric. For. Meteorol.* **2013**, *169*, 156–173. [CrossRef]
74. MacBean, N.; Maignan, F.; Peylin, P.; Bacour, C.; Bréon, F.M.; Ciais, P. Using satellite data to improve the leaf phenology of a global terrestrial biosphere model. *Biogeosciences* **2015**, *12*, 7185–7208. [CrossRef]
75. Alessandri, A.; Catalano, F.; De Felice, M.; Van Den Hurk, B.; Reyes, F.D.; Boussetta, S.; Balsamo, G.; Miller, P. A. Multi-scale enhancement of climate prediction over land by increasing the model sensitivity to vegetation variability in EC-Earth. *Clim. Dyn.* **2017**, *49*, 1215–1237. [CrossRef]
76. Liu, Z.; Verstraete, M.M.; de Jager, G. Handling outliers in model inversion studies: A remote sensing case study using MISR-HR data in South Africa. *S. Afr. Geogr. J.* **2018**, *100*, 122–139. [CrossRef]
77. Press, W.H.; Flannery, B.P.; Teukolsky, S.A.; Vetterling, W.T. *Numerical Recipes in FORTRAN 77: The Art of Scientific Computing*; Cambridge University Press: Cambridge, UK, 1993.
78. Hocke, K.; Kämpfer, N. Gap filling and noise reduction of unevenly sampled data by means of the Lomb-Scargle periodogram. *Atmos. Chem. Phys.* **2009**, *9*, 4197–4206. [CrossRef]
79. Moreno, Á.; García-Haro, F.J.; Martínez, B.; Gilabert, M.A. Noise Reduction and Gap Filling of fAPAR Time Series Using an Adapted Local Regression Filter. *Remote Sens.* **2014**, *6*, 8238–8260. [CrossRef]
80. Ma, M.; Veroustraete, F. Reconstructing pathfinder AVHRR land NDVI time-series data for the Northwest of China. *Adv. Space Res.* **2006**, *37*, 835–840. [CrossRef]
81. Chen, J.; Jönsson, P.; Tamura, M.; Gu, Z.; Matsushita, B.; Eklundh, L. A simple method for reconstructing a high-quality NDVI time-series data set based on the Savitzky–Golay filter. *Remote Sens. Environ.* **2004**, *91*, 332–344. [CrossRef]
82. Verger, A.; Baret, F.; Weiss, M. A multisensor fusion approach to improve LAI time series. *Remote Sens. Environ.* **2011**, *115*, 2460–2470. [CrossRef]
83. Pan, Z.; Hu, Y.; Cao, B. Construction of smooth daily remote sensing time series data: A higher spatiotemporal resolution perspective. *Open Geospat. Data Softw. Stand.* **2017**, *2*, 1–11. [CrossRef]
84. Cleveland, W.S.; Devlin, S.J. Locally Weighted Regression: An Approach to Regression Analysis by Local Fitting. *J. Am. Stat. Assoc.* **1988**, *83*, 596–610. [CrossRef]
85. Eilers, P.H.C. A Perfect Smoother. *Anal. Chem.* **2003**, *75*, 3631–3636. [CrossRef]

86. Jönsson, P.; Eklundh, L. Seasonality extraction by function fitting to time-series of satellite sensor data. *IEEE Trans. Geosci. Remote Sens.* **2002**, *40*, 1824–1832. [CrossRef]
87. Jönsson, P.; Eklundh, L. TIMESAT—A program for analyzing time-series of satellite sensor data. *Comput. Geosci.* **2004**, *30*, 833–845. [CrossRef]
88. Beck, P.S.A.; Atzberger, C.; Høgda, K.A.; Johansen, B.; Skidmore, A.K. Improved monitoring of vegetation dynamics at very high latitudes: A new method using MODIS NDVI. *Remote Sens. Environ.* **2006**, *100*, 321–334. [CrossRef]
89. Eklundh, L.; Jönsson, P. TIMESAT: A Software Package for Time-Series Processing and Assessment of Vegetation Dynamics. In *Remote Sensing Time Series*; Kuenzer, C., Dech, S., Wagner, W., Eds.; Number 22 in Remote Sensing and Digital Image Processing; Springer: Cham, Switherland, 2015; pp. 141–158. [CrossRef]
90. Azzali, S.; Menenti, M. Mapping vegetation-soil-climate complexes in southern Africa using temporal Fourier analysis of NOAA-AVHRR NDVI data. *Int. J. Remote Sens.* **2000**, *21*, 973–996. [CrossRef]
91. Bradley, B.A.; Jacob, R.W.; Hermance, J.F.; Mustard, J.F. A curve fitting procedure to derive inter-annual phenologies from time series of noisy satellite NDVI data. *Remote Sens. Environ.* **2007**, *106*, 137–145. [CrossRef]
92. Martínez, B.; Gilabert, M.A. Vegetation dynamics from NDVI time series analysis using the wavelet transform. *Remote Sens. Environ.* **2009**, *113*, 1823–1842. [CrossRef]
93. Sakamoto, T.; Wardlow, B.D.; Gitelson, A.A.; Verma, S.B.; Suyker, A.E.; Arkebauer, T.J. A Two-Step Filtering approach for detecting maize and soybean phenology with time-series MODIS data. *Remote Sens. Environ.* **2010**, *114*, 2146–2159. [CrossRef]
94. Atkinson, P.M.; Jeganathan, C.; Dash, J.; Atzberger, C. Inter-comparison of four models for smoothing satellite sensor time-series data to estimate vegetation phenology. *Remote Sens. Environ.* **2012**, *123*, 400–417. [CrossRef]
95. Gerard, F.F.; George, C.T.; Hayman, G.; Chavana-Bryant, C.; Weedon, G.P. Leaf phenology amplitude derived from MODIS NDVI and EVI: Maps of leaf phenology synchrony for Meso- and South America. *Geosci. Data J.* **2020**, *7*, 13–26. [CrossRef]
96. Kandasamy, S.; Baret, F.; Verger, A.; Neveux, P.; Weiss, M. A comparison of methods for smoothing and gap filling time series of remote sensing observations–application to MODIS LAI products. *Biogeosciences* **2013**, *10*, 4055–4071. [CrossRef]
97. Lomb, N.R. Least-squares frequency analysis of unequally spaced data. *Astrophys. Space Sci.* **1976**, *39*, 447–462. [CrossRef]
98. Scargle, J.D. Studies in astronomical time series analysis. III-Fourier transforms, autocorrelation functions, and cross-correlation functions of unevenly spaced data. *Astrophys. J.* **1989**, *343*, 874–887. [CrossRef]
99. Fourier, J. *Théorie Analytique de la Chaleur*; Firmin Didot, Père et Fils: Paris, France, 1822; p. 639.
100. Hmimina, G.; Dufrêne, E.; Pontailler, J.Y.; Delpierre, N.; Aubinet, M.; Caquet, B.; de Grandcourt, A.; Burban, B.; Flechard, C.; Granier, A.; et al. Evaluation of the potential of MODIS satellite data to predict vegetation phenology indifferent biomes: An investigation using ground-based NDVI measurements. *Remote Sens. Environ.* **2013**, *132*, 145–158. [CrossRef]
101. Meroni, M.; Marinho, E.; Sghaier, N.; Verstraete, M.M.; Léo, O. Remote Sensing Based Yield Estimation in a Stochastic Framework – Case Study of Durum Wheat in Tunisia. *Remote Sens.* **2013**, *5*, 539–557. [CrossRef]
102. Meroni, M.; Verstraete, M.M.; Rembold, F.; Urbano, F.; Kayitakire, F. A phenology-based method to derive biomass production anomalies for food security monitoring in the Horn of Africa. *Int. J. Remote Sens.* **2014**, *35*, 2472–2492. [CrossRef]
103. Tan, B.; Morisette, J.T.; Wolfe, R.E.; Gao, F.; Ederer, G.A.; Nightingale, J.; Pedelty, J.A. An Enhanced TIMESAT Algorithm for Estimating Vegetation Phenology Metrics From MODIS Data. *J. Sel. Top. Appl. Earth Obs. Remote Sens.* **2011**, *4*, 361–371. [CrossRef]
104. Cho, M.A.; Ramoelo, A.; Dziba, L. Response of Land Surface Phenology to Variation in Tree Cover during Green-Up and Senescence Periods in the Semi-Arid Savanna of Southern Africa. *Remote Sens.* **2017**, *9*, 689. [CrossRef]
105. Verstraete, M.M.; Pinty, B.; Myneni, R.B. Potential and Limitations of Information Extraction on the Terrestrial Biosphere From Satellite Remote Sensing. *Remote Sens. Environ.* **1996**, *58*, 201–214. [CrossRef]

106. Gong, Z.; Kawamura, K.; Ishikawa, N.; Goto, M.; Wulan, T.; Alateng, D.; Yin, T.; Ito, Y. MODIS normalized difference vegetation index (NDVI) and vegetation phenology dynamics in the Inner Mongolia grassland. *Solid Earth* **2015**, *6*, 1185–1194. [CrossRef]
107. Diner, D.J.; Bruegge, C.J.; Martonchik, J.V.; Ackerman, T.P.; Davies, R.; Gerstl, S.A.W.; Gordon, H.R.; Sellers, P.J.; Clark, J.; Daniels, J.A.; et al. MISR: A Multiangle Imaging SpectroRadiometer for Geophysical and Climatological Research from EOS. *IEEE Trans. Geosci. Remote Sens.* **1989**, *27*, 200–214. [CrossRef]
108. Diner, D.J.; Beckert, J.C.; Reilly, T.H.; Ackerman, T.P.; Bruegge, C.J.; Conel, J.E.; Davies, R.; Gerstl, S.A.W.; Gordon, H.R.; Kahn, R.A.; et al. Multi-angle Imaging SpectroRadiometer (MISR) Instrument Description and Experiment Overview. *IEEE Trans. Geosci. Remote Sens.* **1998**, *36*, 1072–1087. [CrossRef]
109. Diner, D.J.; Verstraete, M.M.; Martonchik, J.V. Foreword to Special Section on MISR. *IEEE Trans. Geosci. Remote Sens.* **2002**, *40*, 1447–1448. [CrossRef]
110. Diner, D.J.; Braswell, B.H.; Davies, R.; Gobron, N.; Hu, J.; Jin, Y.; Kahn, R.A.; Knyazikhin, Y.; Loeb, N.; Muller, J.P.; et al. The value of multiangle measurements for retrieving structurally and radiatively consistent properties of clouds, aerosols, and surfaces. *Remote Sens. Environ.* **2005**, *97*, 495–518. [CrossRef]
111. Bull, M.; Matthews, J.; McDonald, D.; Menzies, A.; Moroney, C.; Mueller, K.; Paradise, S.; Smyth, M. *Data Products Specifications*; Technical Report JPL D-13963, Revision S; Jet Propulsion Laboratory, California Institute of Technology: Pasadena, CA, USA, 2011.
112. Verstraete, M.M.; Hunt, L.A.; De Lemos, H.; Di Girolamo, L. Replacing Missing Values in the Standard MISR Radiometric Camera-by-Camera Cloud Mask (RCCM) Data Product. *Earth Syst. Sci. Data* **2020**, *12*, 611–628. [CrossRef]
113. Verstraete, M.M.; Hunt, L.A.; Jovanovic, V.M. Improving the usability of the Multi-angle Imaging SpectroRadiometer (MISR) L1B2 Georectified Radiance Product (2000–present) in land surface applications. *Earth Syst. Sci. Data* **2020**, *12*, 1321–1346. [CrossRef]
114. Engelsen, O.; Pinty, B.; Verstraete, M.M.; Martonchik, J.V. *Parametric Bidirectional Reflectance Factor Models: Evaluation, Improvements and Applications*; Technical Report EUR 16426 EN; EC Joint Research Centre: Ispra, Italy, 1996.
115. Pinty, B.; Widlowski, J.L.; Gobron, N.; Verstraete, M.M.; Diner, D.J. Uniqueness of Multiangular Measurements—Part I: An Indicator of Subpixel Surface Heterogeneity From MISR. *IEEE Trans. Geosci. Remote Sens.* **2002**, *40*, 1560–1573. [CrossRef]
116. Gobron, N.; Pinty, B.; Verstraete, M.M.; Widlowski, J.L.; Diner, D.J. Uniqueness of Multiangular Measurements—Part II: Joint Retrieval of Vegetation Structure and Photosynthetic Activity From MISR. *IEEE Trans. Geosci. Remote Sens.* **2002**, *40*, 1574–1592. [CrossRef]
117. Armston, J.D.; Scarth, P.F.; Phinn, S.R.; Danaher, T.J. Analysis of multi-date MISR measurements for forest and woodland communities, Queensland, Australia. *Remote Sens. Environ.* **2007**, *107*, 287–298. [CrossRef]
118. Van den Hoof, C.; Verstraete, M.M.; Scholes, R.J. Differing Responses to Rainfall Suggest More Than One Functional Type of Grassland in South Africa. *Remote Sens.* **2018**, *10*, 2055. [CrossRef]

Publisher's Note: MDPI stays neutral with regard to jurisdictional claims in published maps and institutional affiliations.



© 2020 by the authors. Licensee MDPI, Basel, Switzerland. This article is an open access article distributed under the terms and conditions of the Creative Commons Attribution (CC BY) license (http://creativecommons.org/licenses/by/4.0/).

POSTFACE

Chapter 3 utilised a dekadal temporally spaced image time series of MISR-HR FAPAR over the Bushbuckridge local municipality for the period between 2000 and 2018. A dekad refers to a period of 10 days. Each month contains three dekads. The first dekad includes day 1 to 10, the second includes day 11 to 20 and the third day 21 to the last day of the particular month. The dekadal sampling procedure was selected to archive the modelled phenology on days 1, 11, and 21 of each month to ensure that the calendar dates between years in the time series are in sync and thus comparable. The parametric double S-shaped models used in chapter 2 were extended to select the inversion model producing the lowest cost function (smallest mismatch between the model and the input FAPAR values), and in doing so ensuring the greatest number of model inversions for the vegetative seasons.

Chapter 3 is focused on addressing objective two of this study:

- Objective two:
  To exploit image time series of biogeophysical variables to quantitatively describe interannual and seasonal fluctuations as well as variations in the vegetation of the Bushbuckridge local municipality.

While the literature on the drivers of savanna phenology in the Lowveld region of South Africa is well established (see chapters 1 and 2), studies characterising the response of vegetation phenology to non-seasonal or aperiodic perturbations, such as ENSO at the spatial scale of ecosystems are virtually non-existent.

CHAPTER 3 SEASONAL AND LONG-TERM FLUCTUATIONS AND TRENDS IN LOWVELD VEGETATION

1. Introduction

The savanna terrestrial biome is home to over a fifth of the world's human population (Scholes and Archer, 1997) and diverse endemic floras and faunas. They cover about 20% of the global land surface and 40% of Africa (Kutsch et al., 2008). Savannas store a significant amount of carbon in terrestrial ecosystems and are responsible for 13% of net primary production on a global scale (Grace et al., 2006). In southern Africa, growing evidence shows that the recorded expansion of woody plant species in savannas may be linked to rising CO_2 emissions (Buitenwerf et al., 2012). Savannas over the southern African region have noted significant increases of woody plants, with a mean increase of about 6.2% per decade (O'Connor et al., 2014). The four key variables traditionally viewed as the drivers of savanna structure and function include water availability, fire, soils and herbivory (Anderson et al., 2016; Archibald, 2016; Colgan et al. 2012; Fisher et al., 2009; Gray and Bond, 2015; Kanniah et al. 2010; Le Roux and Bariac 1998; Scholes and Archer 1997; Wessels et al. 2011; Witkowski and O'Connor 1996). In the Lowveld, a bioregion of South Africa which is predominantly savanna, rural households critically depend on woody species for fuelwood as a source of energy. Dependence on natural resources and expanding human settlements have altered vegetation structure in the Lowveld (Coetzer et al. 2010; Coetzer 2013). Over-grazing/browsing and human-induced fire regimes have also altered the structure of vegetation in this biome (Archibald et al., 2016; Scholes and Archer 1997).These processes have been of increasing concern (United Nations, 2017) because population density is projected to double (or triple) by 2050 across most savannas on the African continent.

One of the expected consequences of accelerated climate change in sub-Saharan Africa is that the region may experience fewer but more intense rainfall events with longer intervening dry periods (IPCC, 2007). Changes in rainfall intensity across sub-Saharan Africa may result in an increase in tree and shrub density in previously more open savannas, while limiting tree growth in wetter savannas (D'Onofrio et al., 2018; D'Onofrio et al., 2019). In southern Africa, water availability is the main constraint on plant productivity in savannas. Dynamic Vegetation Models (DVMs) predict that impacts of future climate change over southern Africa show an expansion of woody plants and a contraction of grasses in response to increased CO_2 emissions (Higgins and Scheiter 2012; Moncrieff et al., 2015). Woody plant encroachment in savannas contrasts with deforestation noted in forest ecosystems. The

proliferation of woody plants in savannas threatens the biodiversity endemic to these ecosystems, and the livelihoods of communities who depend on them (Archer et al., 2017). Understanding environmental changes in the past is always evolving and likely to change in the future in response to changes in local and global drivers (Stevens et al., 2015).

The timing of phenological phases in plants has gained increasing interest as a consequence of climate change; phenology variables are some of the most sensitive data to differences in climate conditions (Menzel, 2006). In the context of remote sensing, land surface phenology refers to the study of seasonal patterns in the biological life cycle of plants based on time series of vegetation indices or biophysical variables derived from satellite observations (Caparros-Santiago et al., 2021). A systematic review of vegetation phenology studies over the African continent reveals that while there is a significant increase in the number of studies adopting satellite-based remote sensing, few of them focus on the relationship between climate change and vegetation phenology (Adole et al., 2016). Non-seasonal or aperiodic perturbations like the El Niño–Southern Oscillation (ENSO) have been studied for decades, but at large spatial scales and over periods ranging from multiple years to few decades (Lyon and Barnston, 2005; Trenberth, 1997). Also, statistical studies relating land surface phenology and other vegetation dynamics to ENSO climatic fluctuations have been established for entire biomes, but few detailed investigations, if any, have been conducted at the finer spatial scales of bioregions, especially for African ecosystems (Anyamba et al., 2002; Anyamba et al., 2018; Nicholson and Kim, 1997; Parhi et al., 2016; Philippon et al., 2014), even though it has been shown to be the major driver of precipitation variability over the sub-continent on an interannual timescale (Janowiak, 1988, Jury et al., 2004; Philippon et al., 2014).

The El Niño – Southern Oscillation (ENSO) is a large-scale coupled ocean-atmosphere teleconnection, which strongly influences global climate variability (Trenberth, 1997; Wolter and Timlin, 2011). The sea surface temperature of a vast region of the Equatorial Eastern Pacific Ocean fluctuates irregularly with a periodicity of 2 to 5 years, and the occurrence of peaks and troughs in that index has been associated with other climatic events worldwide (Lyon and Barnston, 2005; McPhaden et al., 2006). In particular, El Niño events (sea surface temperature warmer than usual in that region) lead to more convection, which increases latent heating in the upper atmosphere. Warm moist air can then branch away from the equator to higher latitudes, modifying circulation patterns globally. A weakening of the Walker circulation, coupled with a strengthening of the Hadley circulation, generates an El Niño event that can lead to noticeable changes in rainfall patterns in faraway places, for instance. Long-term observations since the 1950s show that El Niño usually causes rainfall deficiencies over Indonesia and northern South America, and excess rainfall in the south

eastern parts of South America, eastern equatorial Africa, and the southern US (Lyon and Barnston, 2005). Similar connections with climatic events have been established over Southern Africa, where deviations from expected temperature and rainfall patterns have been linked to ENSO events (Lakhraj-Govender and Grab, 2019; Dieppois et al., 2015; Pomposi et al., 2018). However, not every El Niño coincides with the rainfall deficits over the region. The relationship between southern Africa precipitation variability and ENSO is complex, given modulations with other basins and internal atmospheric variations (Pomposi et al., 2018). During the 1997 – 1998 El Niño, moderately dry and wetter conditions were observed over different locations in southern Africa.

In South Africa, ENSO events after the late 1970s have been observed to have a stronger warming effect during austral summer, particularly over the northern and central interior regions of the country (Lakhraj-Govender and Grab, 2019). The high rainfall of the 1970s has been associated with much of the increases observed in woody plant cover over the region (O'Connor et al., 2014). Hence, quantifying changes and trends in the productivity of these systems is both ecologically and economically important because the affected ecosystems provide multiple services (carbon sequestration, filtration and storage of freshwater, soil retention), grazing for livestock, energy, forestry products and ecotourism, especially in developing countries. The relationship between precipitation in austral summer and ENSO is important for seasonal forecasting efforts in southern Africa (Goddard and Dilley 2005). Crops in the region depend on the availability of water, which is largely (but not only) controlled by precipitations. The severe drought conditions over parts of southern Africa have been partially attributed to the historic 2015 – 2016 El Niño event. Documenting trends and other statistical relations between vegetation productivity and ENSO may provide evidence to improve operational decision-making about land-use and water management in these regions.

Over the last two decades, the availability of spatially and temporally consistent biogeophysical variables derived from Earth Observation (EO) satellite measurements has afforded the scientific community the ability to assess local to global changes and trends in vegetation productivity (Beck et al., 2011; Fensholt et al., 2012; Wessels et al., 2004). Early on, this study examined whether or not significant linear trends could be observed in vegetation phenology in response to progressive climate change. This investigation was inconclusive, likely because two decades worth of satellite observations may still be insufficient to document the presence of definite trends, but also because large inter-annual fluctuations may mask such trends. The Multi-angle Imaging SpectroRadiometer (MISR) instrument, hosted on the National Aeronautics and Space Administration (NASA) platform, has been collecting planetary reflectance data globally since 24 February 2000. Multi-

angular remote sensing measurements from MISR document the spectral anisotropy of the surface reflectance and deliver a better empirical basis to understand the relation between surface properties and the fluxes of matter and energy in the environment, compared to what can be achieved on the basis of mono-angular instruments. These data have been analysed with the MISR High Resolution (MISR-HR) processing system (Verstraete et al., 2012) to generate the Fraction of Absorbed Photosynthetically Active Radiation (FAPAR) product, used here as a proxy for vegetation productivity.

The FAPAR, a key variable in the assessment of vegetation productivity and yield estimates (Monteith 1977) is the culmination of advances and understanding in the processes of radiation transfer in plant canopies. In practical terms, the FAPAR is a measure of the fraction of sunlight absorbed by leaves in the 0.4 – 0.7 μm solar spectrum (Fensholt et al., 2004). The MISR-HR FAPAR product is retrieved through an inversion process involving state of the art models of radiation transfer in the environment that takes full advantage of the anisotropy data, as well as cutting edge optimisation techniques (Pinty et al., 2011a and b).

The stages of vegetation growth from establishment to senescence respond to seasonal fluctuations of water availability, temperature, solar irradiance, and other critical climatic and environmental variables. This study examines to what extent vegetation productivity over the Bushbuckridge local municipality (which is predominantly savanna) may be related to decadal changes in water availability, as reported by the Climate Hazards Group InfraRed Precipitations with Stations (CHIRPS), or shorter-term climatic phenomena, specifically the aperiodic changes of sea surface temperatures (SSTs) in a region of the eastern tropical Pacific Ocean as represented by the ENSO during the first two decades of this century. The MISR-HR FAPAR record was used as a proxy for vegetation productivity and scrutinised alongside the climatic observations to gauge immediate and delayed impacts of peak ENSO events in the study region. ENSO events occur every 2 to 5 or even 7 years and have been shown to amplify or damp the more regular seasonal or annual variability in environmental constraints mentioned above. This paper addresses the following questions concerning the land surface phenology and productivity of vegetation as evidenced by the MISR-HR FAPAR product:

i. Does this empirical record suggest the presence of trends or fluctuations in plant productivity during the period 2000 to 2018? And if a trend is discernible,
    a. how large and significant is it?
    b. does it differ between protected and unprotected areas, or between different types of vegetation in the Lowveld?

2. Materials and Methods

2.1. Study Area

The study area contains the Bushbuckridge local municipality (BBR) and is defined by the boundaries 23°58’52.46” S to 25°11’14.63” S and 30°47’42.14” E to 32°02’00.92” E. It is located between the north eastern part of Mpumalanga Province and south eastern part of Limpopo Province of South Africa (Figure 1, panel (b)), covering an area of about 16,757 km^2, which is predominantly Lowveld. The Lowveld region lies typically between 150 m and 600 m above sea level, extending between the South African provinces of Mpumalanga, KwaZulu-Natal, to parts of Swaziland and south-eastern Zimbabwe. The Savanna Biome, the largest Biome in South Africa, occupying one third of the total land area, is well developed in the Lowveld (Low and Rebelo, 1996).

The climate of the Lowveld region is characterised by hot humid summers and mild dry winters. Rainfall occurs predominantly in the summer months (October to April) across an east to west regional precipitation gradient, with the mean annual rainfall ranging between 500 mm in the east and 800 mm in the west. A topographic and temperature gradient is noted for the area, with higher altitudes and lower temperatures to the south west, which include the boundary between the northern escarpment and the Lowveld. This differs from the general rainfall gradient across Southern Africa, from deserts and arid zones in the west (along the Atlantic Ocean coastline) to wetter areas in the east, on shores of the Indian Ocean. The mean annual temperature is 21°C with the mean daily minimum temperature during the coldest months seldom falling below 10°C, which suggests the irrelevance of a chilling period for breaking dormancy in most savanna plants (Mucina and Rutherford, 2006).

Granite and basalt are the two major geological formations in the Lowveld (Colgan et al., 2012). The granites are predominantly composed of granite gneiss with local gabbro intrusions (Venter et al., 2003). The granite soils have a higher sandy content and are usually nutrient poor, while the basalt soils are black or red clay soils associated with higher nutrient contents (Colgan et al., 2012, Mucina and Rutherford, 2006). Topographic contrasts in the soils of the Lowland granite formation result in two distinct sequences (catena sequence), namely uplands dominated by broad leafed tree species adapted to deep sandy soils and lowlands dominated by fine leaved tree species adapted to sodic clay soils (Colgan et al. 2012; Dzerefos et al. 2003).

Water availability, fire-regime, soils (geology), grazing by herbivores, and the anthropogenic harvesting of wood are seen as the main environmental determinants shaping vegetation distribution and density in the region (Venter et al., 2003; Sankaran et al., 2008; Sankaran et al., 2013). Dominant tree species include *Terminalia sericea, Combretum zeyheri,*

Combretum apiculatum, Acacia nigrescens, dominant shrub species include, *Dichrostachys cinerea and Grewia bicolor*, and dominant grass species include *Pogonarthria squarrosa, Tricholaena monachne, Eragrostis rigidior, Panicum maximum, Aristida congesta, Digitaria eriantha, and Urochloa mossambicensis* (Mucina and Rutherford, 2006).

The Bushbuckridge municipal region consists of a mix of mostly designated protected areas (under National parks management and private nature reserves), rural settlements and communal rangelands. The larger protected areas include Klaserie Private Nature Reserve, Manyeleti Game Reserve, Sabie Sands Private Nature Reserve, Timbavati Private Nature Reserve and the Kruger National Park (KNP). The areas adjacent to protected areas (unprotected areas) include mainly human settlements and communal rangelands that were formerly Apartheid homelands, e.g., Gazankulu and Lebowa (Thornton, 2002), which in 1994 were rezoned by Traditional leaders into residential, arable and communal areas for grazing and harvesting (Shackleton and Shackleton, 2000). There exists a great deal of literature devoted to both social and ecological topics in the region. In addition, the region hosts the Wits Rural Facility and several ground-based sensors, such as eddy covariance (EC) flux towers. The Wits Rural Facility is a unique campus of the University of the Witwatersrand established in 1989 for the purpose of stimulating the application of academic knowledge to development challenges created by the Apartheid homeland system. The region hosts several EC flux towers. The Skukuza flux tower, in particular, was erected by NASA as part of the Southern African Regional Science Initiative (SAFARI–2000). The SAFARI–2000 initiative was an international field campaign investigating emissions, transport, transformation and deposition of trace gases and aerosols over southern Africa between 1999 and 2001 (Annegarn et al., 2002; Otter et al., 2002; Scholes et al., 2001).

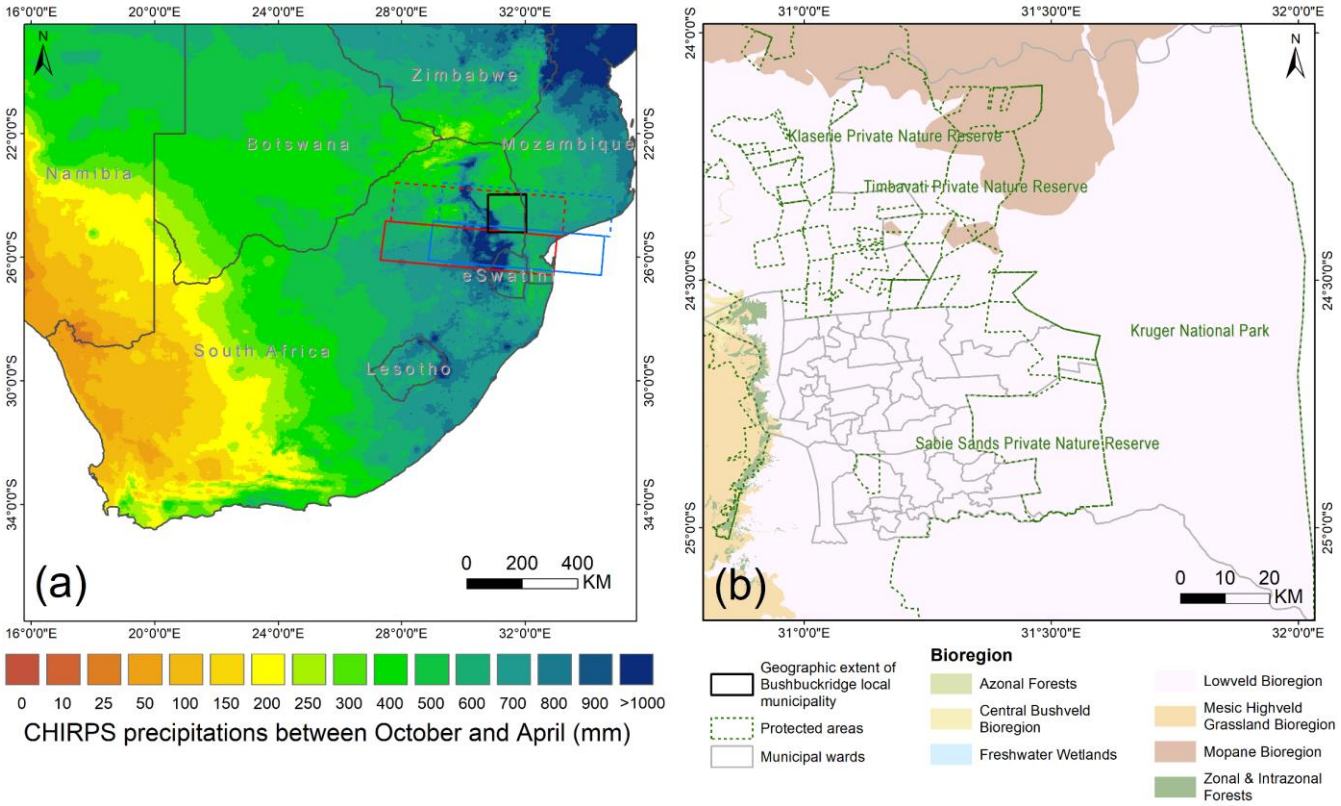


Figure 1. Panel (**a**): Location of the study site in the Lowveld of South Africa (solid black line) with overlapping footprints of Multi-Imaging SpectroRadiometer (MISR) Blocks 110 and 111 (dashed and solid line, respectively) for Paths 168 and 169 (blue and red, respectively), and Oct-Apr long-term average rainfall (2000 – 2018, mm, source: IRI, 2020). Panel (**b**): Detailed map of bioregions within the geographic limits of the Bushbuckridge local municipality (source: SANBI, 2006-2012).

2.2. Data records

2.2.1. Remote sensing vegetation records

MISR radiance observations at the nominal Top of the Atmosphere have been available globally in 36 spectro-directional channels since late February 2000[2]. These data were further analysed over the BBR region with the MISR-HR processing system (Verstraete et al., 2012), which delivers the FAPAR product as well as several other biogeophysical products at the spatial resolution of 275 m. This processing system uses the Joint Research Centre Two-stream Inversion Package (JRC-TIP) algorithm (Pinty et al., 2011a; Pinty et al., 2011b) to analyse broadband albedo values obtained by spectrally and directionally integrating the Rahman-Pinty-Verstraete (RPV) model (Lavergne et al., 2007; Rahman et al., 1993). This product has been extensively evaluated and is routinely included in international

[2] https://asdc.larc.nasa.gov/project/MISR/, last accessed on 14 October 2020.

benchmarking exercises (Pinty et al., 2011c; Gobron et al., 2019). Its spatial and temporal resolution make it particularly suitable to document the phenology of vegetation over an area such as the BBR.

The BBR study area falls within Blocks 110 and 111 of MISR Paths 168 and 169 (Fig. 1, panel (a)). The repeat period of MISR for a single Path is exactly 16 days, but the study area falls within the overlap of Paths 168 and 169, giving a staggered revisit period of seven and nine days between those two Paths. A combined total of 859 Orbits were acquired for Paths 168 and 169 (i.e., 429 and 430, respectively) between 15 March 2000 and 30 December 2018. However, 17 Orbits were irretrievable from NASA's Atmospheric Science Data Center, due to technical issues with the platform.

2.2.2. Climatic records

Precipitation

Data on the spatial and temporal distribution of precipitation over the study region were downloaded from the Famine Early Warning Systems Network (FEWS) for the period between 2000 and 2018 (FEWS NET, 2020). This data portal provides access to the Climate Hazards Group InfraRed Precipitation with Station (CHIRPS) data archive (version 2.0), a gridded precipitation record of continental areas between 50°S–50°N and 180°E–180°W, at a spatial resolution of 0.05° (i.e., available on a lat/lon grid, where the longitudinal cell side is 5% of a degree), spanning 1981 to near-present. This archive was explicitly developed for monitoring environmental extremes, such as drought (Funk et al., 2014; Funk et al., 2015).

The CHIRPS data set is available at a pentadal temporal resolution (i.e., every 5-days), and is derived through an interpolation process which includes (1) the Climate Hazards group Precipitation climatology (CHPClim), describing the expected annual sequence of rainfall at each location; (2) quasi-global geostationary thermal infrared (IR) satellite observations from the Climate Prediction Center (CPC) IR and the National Climatic Data Center (NCDC) B1 IR (Janowiak et al., 2001; Knapp et al., 2011); (3) the Tropical Rainfall Measuring Mission (TRMM) 3B42 product from NASA, (Huffman et al., 2007; Huffman et al., 2011); (4) atmospheric model rainfall fields from the National Oceanic and Atmospheric Administration (NOAA) Climate Forecast System, version 2 (CFSv2) (Saha et al., 2014); and (5) *in situ* precipitation observations from a variety of national and regional meteorological services.

While the CHIRPS record is a suitable source of spatial and temporal information on precipitation on a continental scale, it is based on a limited number of weather stations available in the region and is known to underestimate precipitations due to orographic effects. An independent study by Belay et al. (2019), showed that the reliability of the CHIRPS data set depends on the duration of the integration time and varies with the altitude

of the terrain. Table 1 shows the correlation between daily rainfall measurements (mm d^{-1}) recorded at the Kruger National Park's Skukuza camp[3] and the CHIRPS time series corresponding to geographic location of that's weather station (24° 59' 43.44" S and 31° 35' 34.332" E), both of which were cumulated to monthly values for direct comparison with the three ENSO periods investigated in the study (see section 2.3 below for the ENSO periods). The correlation between the Skukuza *in situ* rainfall measurements and CHIRPS record is significantly lower for ENSO periods 2 and 3 owing to many instances where gaps were observed in the daily rainfall measurements from April 2009.

Table 1. Pearson's correlation coefficients (R) for monthly cumulated CHIRPS data set and *in situ* daily rainfall measurements recorded at Skukuza (24° 59' 43.44" S and 31° 35' 34.332" E) for the three ENSO periods included in the study.

ENSO Periods	R
Period 1: Sep 2006 to Jun 2008	0.89
Period 2: Jul 2009 to May 2011	0.66
Period 3: Oct 2014 to Dec 2016	0.68

El Niño–Southern Oscillation (ENSO) Indices

This study includes monthly Niño 3.4 and Oceanic Niño Index (ONI) climatic records downloaded from the National Oceanic and Atmospheric Administration's (NOAA) Climate Prediction Center (NOAA, 2020a) for the period between September 2000 and December 2018. NOAA CPC monitors SSTs in the tropical Pacific Ocean for the purpose of forecasting the onset and tracking the life cycle of ENSO events. The Niño 3.4 region (5N-5S, 170W-120W) provides a long-term continuous record based on SSTs averaged across the equatorial tropical Pacific Ocean and is regarded as the key region for monitoring and predicting El Niño and La Niña events (Trenberth, 2001). The Oceanic Niño Index (ONI) is used by NOAA as the standard metric for identifying ENSO events in the tropical Pacific Ocean (NOAA, 2020b). The ONI is calculated using Extended Reconstructed Sea Surface Temperature data (ERSSTv5) anomalies, relative to a 30-year base period (1971-2000) from the Niño 3.4 region (Huang et al., 2017).

El Niño (warming) events are classified as periods when the consecutive 3-month running mean of Sea Surface Temperature (SST) anomalies in the Niño 3.4 region exceed the +0.5°C threshold, and La Niña (cooling) events qualify as periods when the SST anomalies are below the -0.5°C threshold. This threshold is also used to define weak (with a 0.5 to 0.9

[3] Daily rainfall measurements provided by South African National Parks Scientific Services, KNP, http://dataknp.sanparks.org/sanparks/, Last accessed 14 June 2021.

SST anomaly), moderate (1.0 to 1.4), strong (1.5 to 1.9) and very strong (≥ 2.0) El Niño/La Niña events. Correlations with MISR-HR FAPAR were based on the original SST anomalies in the Niño 3.4 index while the ONI (standardised Niño 3.4 SSTs) was used to identify values in the Niño 3.4 index associated with El Niño and La Niña events, i.e., positive and negative standardised SST anomalies, respectively. Table 2 provides a summary of historical El Niño and La Niña events in the ONI for the period between September 2000 and December 2018.

Table 2. El Niño and La Niña events over the tropical Pacific Ocean for the period between September 2000 and December 2018.

ENSO event	Period	SST anomalies (°C)
El Niño	Sep 2002 - Feb 2003	0.6 to 1.3
	Jul 2004 - Feb 2005	0.5 to 0.7
	Sep 2006 - Jan 2007	0.5 to 0.9
	Jul 2009 - Mar 2010	0.5 to 1.6
	Oct 2014 - Apr 2016	0.5 to 2.6
	Sep 2018 - Dec 2018	0.5 to 0.9
La Niña	Sep 2000 - Feb 2001	-0.5 to -0.7
	Nov 2005 - Mar 2006	-0.6 to -0.9
	Jun 2007 - Jun 2008	-0.5 to -1.6
	Nov 2008 - Mar 2009	-0.6 to -0.8
	Jun 2010 - May 2011	-0.6 to -1.6
	Jul 2011 - Apr 2012	-0.5 to -1.1
	Aug 2016 - Dec 2016	-0.5 to -0.7
	Oct 2017 - Apr 2018	-0.5 to -0.7

2.2.3. Vegetation types

The 2012 Vegetation Map of South Africa (Version 2, last updated in March 2016 and published by the South African National Biodiversity Institute (SANBI)) was used here to establish the spatial distribution of vegetation types across the BBR study region (SANBI, 2006-2012). This spatial data set is one of several products generated by the National Vegetation Map Project (VEGMAP), which was established to classify, map and sample the vegetation of South Africa, Lesotho and Swaziland. Predominant vegetation types in the BBR study region includes the granite Lowveld, Legogote sour bushveld, and Tshokwane-Hlane basalt Lowveld vegetation types. The northern escarpment dolomite grassland to the extreme south western part of the region belongs to the mesic Highveld grassland bioregion.

The vegetation units in the study were sampled in protected (private nature reserves and the Kruger National Park (KNP)) and unprotected areas (communal rangelands, human settlements and plantations). Figure 2 shows the locations of the five sample sites with respect to their vegetation unit in the BBR study region. The five sample sites and their respective upper-left and lower right latitude and longitude boundary coordinates include:

- site 1: protected granite Lowveld (PGL),
  24°55'23.221" S to 25°10'44.033" S and 31°29'42.317" E to 31°45'3.132" E,
- site 2: protected basalt Lowveld (PBL),
  24°9'4.626" S to 24°19'56.197" S and 31°41'11.58" E to 31°52'3.151" E,
- site 3: unprotected sour bushveld (USB),
  24°50'0.128" S to 24°57'10.919" S and 30°57'29.149" E to 31°4'39.936" E,
- site 4: unprotected granite Lowveld (UGL),
  24°34'23.16" S to 24°45'41.656" S and 31°7'43.025" E to 31°19'1.517" E,
- site 5: unprotected Highveld grassland (UHG),
  24°45'36.623" S to 24°50'28.5" S and 30°47'45.564" E to 30°52'37.441" E,

Sites 1 and 4 are dominated by tall shrubland with few trees to moderately dense low woodland on deep sandy soils in the hillcrests to dense thicket and open savanna on more nutrient poor sandy soils in the lowlands (Witkowski and O'Connor, 1996). Site 2 occurs in the KNP over fairly flat plains consisting of shallow (usually not more than 1 m deep), but nutrient rich clay soils dominated by open tree savanna (Mucina and Rutherford, 2006). Vegetation structure is less pronounced in the catenal sequence of basaltic landscapes in South Africa, due to the small change in the topographic gradient (Colgan et al. 2012). Site 3 occurs on a gently to moderately sloping topography consisting of shallow to deep sandy soils dominated by dense woodland and medium to large shrubs (Acocks, 1988).

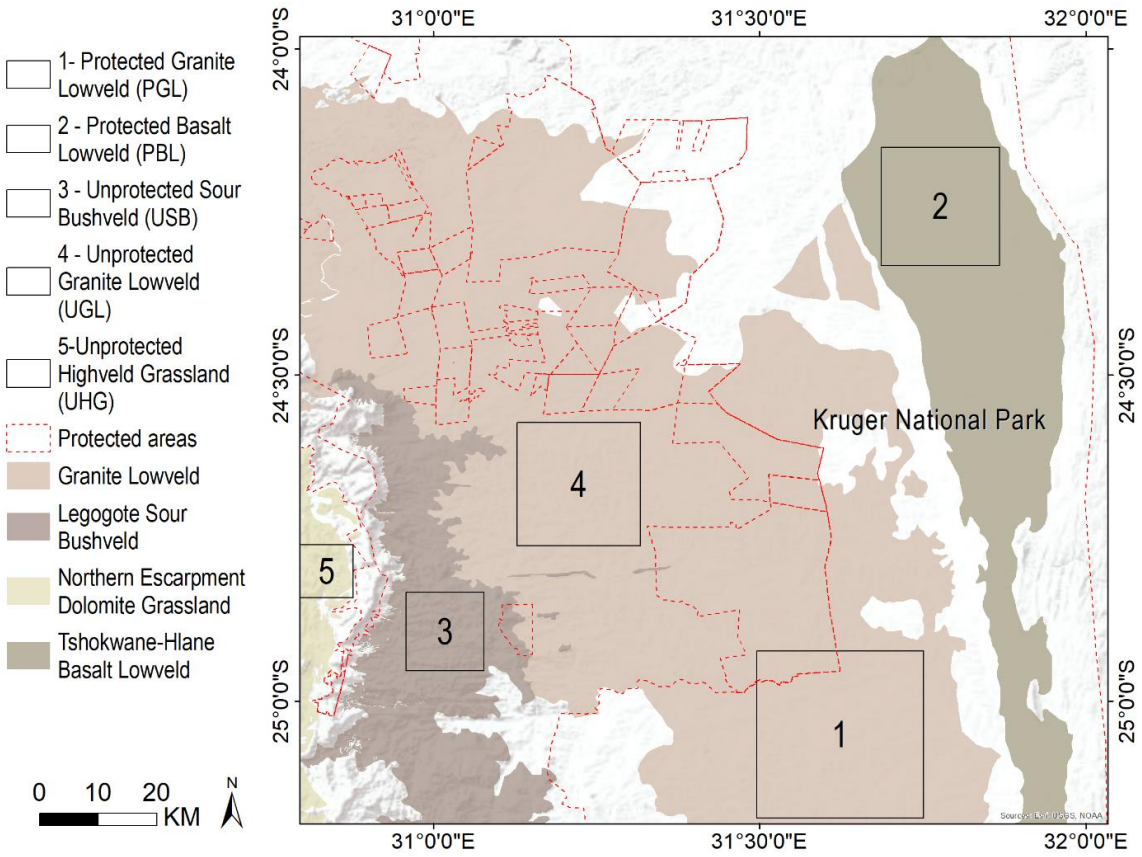


Figure 2. Savanna vegetation types over the Bushbuckridge local municipality. Source: South African National Biodiversity Institute (SANBI, 2006-2012).

2.3. Study Framework

This study analyses the phenological response of four vegetation units to historical ENSO periods occurring within the last two decades. The ENSO periods indicated by the labelled boxes in figure 3 were selected using the ONI classification and annual phase locking of ENSO events (Rasmusson and Carpenter, 1982). They include the ENSO between (1) September 2006 and June 2008, (2) July 2009 and May 2011, and (3) October 2014 and December 2016. The historic El Niño experienced during the third ENSO period actually began developing in late 2014, cancelled for a brief period and then strengthened in the spring and summer of 2015, lasting 19 months. By contrast, the El Niño during the first and second ENSO periods lasted five and nine months, respectively.

To facilitate comparisons with the monthly ENSO SST anomalies, the MISR-HR FAPAR and CHIRPS precipitation records were temporally aggregated to monthly observations. Anomalies for the monthly FAPAR and precipitation records were used throughout the analysis to isolate inter-annual variability associated with the seasonal cycle. A regression between the Niño 3.4 SSTs and FAPAR and precipitation anomalies was performed for the ENSO periods at multiple time lags to characterise whether deviations from the seasonal

patterns of precipitation and vegetation phenology at the five sites may have been associated with fluctuations in ENSO. The monthly FAPAR and precipitation anomalies used in the regression analysis and discussed in section 3.1 were based on temporal profiles that represent the pixel-to-pixel mean for each monthly observation of the individual sites, i.e., for each monthly image, the pixels falling within the geographic bounds of the site were spatially aggregated using the mean statistic. By contrast, section 3.2 reports on the spatial distribution of the immediate impacts of El Niño and La Niña at the sites during the varying intensities of the ENSO periods using three-monthly cumulated rasters of the FAPAR anomalies.

Vegetation exhibits spatial variability at all scales from microscopic to continental. The same is true in the context of remote sensing, irradiance measurements always result from the observation of finite areas that exhibit some degree of spatial variability or heterogeneity, irrespective of the spatial resolution of the sensor. To demonstrate, table 3 lists the spatially accumulated pixel-to-pixel mean and standard deviation for each of the five sites for the MISR-HR FAPAR acquired on 2014-06-26. The standard deviation for each of the five sites is lower than the variability between sites, i.e., the inter-site variability is much larger than the intra-site variability within any one of the sites. This does not indicate a lack of heterogeneity, but rather that a similar level of heterogeneity is present in neighbouring pixels within each site, and that the remote sensing instrument may not be able to report on that aspect.

Table 3. Spatially accumulated pixel-to-pixel mean and standard deviation statistics for sites 1 to 5.

Site	Pixel count	Mean	Standard deviation
1	10,609	0.258	0.023
2	5,309	0.169	0.067
3	2,352	0.473	0.075
4	5,852	0.281	0.045
5	1,050	0.390	0.028

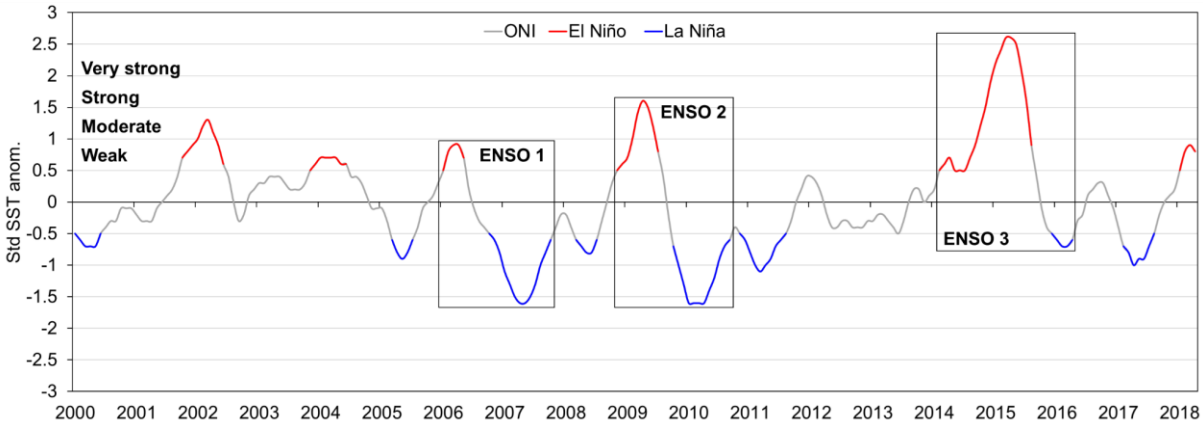


Figure 3. Oceanic Niño Index for the period between Sep 2000 and Dec 2018. The ENSO periods included in this study are indicated by the labelled boxes, specifically the ENSO during (1) September 2006 and June 2008, (2) July 2009 and May 2011, and (3) October 2014 and December 2016.

2.3.1. MISR-HR FAPAR pre-processing

As previously discussed in section 2.2.1, the MISR-HR FAPAR available over the BBR study region are provided with a staggered revisit period of seven and nine days. A model inversion procedure to adjust four parametric double S-shaped functions (the Gaussian, Hyperbolic Tangent, or Logistic and Sine) was used to describe the phenology of the vegetation despite the presence of noise and missing values in the MISR-HR FAPAR record, an issue that mostly affects observations during the summer months when clouds are more prevalent. The inversion procedure selects, for successive vegetative seasons, the parametric double S-shaped function which yields the smallest mismatch between the model inversion and the observed data. The procedure is documented at length in chapter two (De Lemos et al., 2020). The model inversion procedure was performed at pixel locations whose time series met the following four criteria:

i. The vegetative seasons in the time series possess a dominant annual fluctuation (in this instance 18 seasons for 18 years' worth of FAPAR observations).

ii. More than two-thirds of the observed FAPAR values in the entire time series are available.

iii. The FAPAR of the entire time series exhibits sufficient amplitude as measured by the difference of the 95th and 5th percentile threshold values. If this difference was below 0.1, the data for that pixel were discarded.

iv. In addition to the requirements imposed on each individual time series, only vegetative seasons within a time series that contained eight or more usable FAPAR

values per season were considered, a requirement imposed by the curve fitting procedure.

A dekadal sampling procedure was selected to archive the modelled phenology on days 1, 11, and 21 of each month to ensure that the calendar dates between years in the time series are in sync and thus comparable. The fitted MISR-HR FAPAR imagery were generated at a spatial resolution of 275 m ground sampling distance (GSD) and include 502 pixel samples by 489 pixel lines over the BBR study region. The samples for sites 1 – 5 contain the following pixel dimensions:

- Site 1: 103 samples by 103 lines (10,609 pixels)
- Site 2: 73 samples by 73 lines (5,329 pixels)
- Site 3: 48 samples by 48 lines (2,304 pixels)
- Site 4: 76 samples by 76 lines (5,776 pixels)
- Site 5: 33 samples by 33 lines (1,089 pixels)

2.3.2. Temporal aggregations

The dekadal MISR-HR FAPAR records simulated using the parametric double S-shaped functions were temporally cumulated to monthly values. Integrated (accumulated) monthly values derived from the simulated FAPAR values are expected to be more reliable than estimates that would be based on the original data alone because the phenology models act as low-pass filters for the noise component and as interpolating tools to provide reasonable estimates when measurements may not have been acquired. The monthly integrated FAPAR were calculated by accumulating over the month the product of the FAPAR for each dekad multiplied by the number of days within that dekad.

Contrary to plant properties, precipitation is essentially discontinuous in space and time. However, that geophysical variable is provided as amounts of water (as opposed to a density of productivity, as is the case for FAPAR), so the temporal integration consists simply in accumulating the precipitation totals for the month. The CHIRPS precipitation records were aggregated to monthly observations by accumulating the pentads for each month.

2.3.3. Monthly anomalies

The removal of the long-term average from biophysical time series which exhibit a seasonal cycle is required for examining deviations from a long-term pattern. The results can convey the intensity of the departures relative to the normal range of variability, such as early or late starts in a season, or whether particular seasons were more or less productive than the long-term average. Anomalies of the monthly integrated FAPAR and cumulated precipitation

records were calculated by subtracting the climatology, or long-term monthly average of each month from the original values.

2.3.4. Regression analysis

The regression analysis was performed on the monthly FAPAR anomalies and Niño 3.4 SST anomalies (predictor variable), and precipitation and Niño 3.4 SST anomalies (predictor variable) at time lags between 1 and 24 months for the three ENSO periods defined in section 2.3. The correlation coefficients at the various time lags convey the time at which ENSO exerts maximum influence on rainfall and vegetation phenology, i.e., equivalent to cross-correlation, a measure of similarity of two series as a function of the displacement of one relative to the other. Some studies have proposed that terrestrial productivity could be correlated to multi-year lags in the response of ecosystems to fluctuations in precipitation (Sala et al., 2012; Reichmann et al., 2014). It has been demonstrated that the MISR-HR FAPAR is appropriate for revealing spatial variability in grassland productivity, and that mean annual precipitation is a good predictor for the mean annual FAPAR, a proxy for primary productivity (Van den Hoof et al., 2018).

3. Results and Discussion

This section documents the results obtained from the study framework discussed in section 2.3. Section 3.1 presents the results of the regression analysis which were performed on temporal profiles of the monthly FAPAR and precipitation anomalies, spatially accumulated using the mean statistic, with temporal profiles of Niño 3.4 SSTs. The results of the spatial distribution and impact on vegetation during peak El Niño and La Niña events are discussed in section 3.2. Section 3.3 summarises the results, comparing them to earlier findings in the region.

3.1. Relationships between FAPAR, precipitation and ENSO

Figures 4 and 5 show the monthly FAPAR and precipitation anomalies for the entire BBR (solid bars) and sites 1 to 5 (hollow bars) and Niño 3.4 SSTs (dashed grey line) for the three ENSO periods. Tables 4, 5, and 6 present the lagged correlation coefficients for monthly FAPAR anomalies and Niño 3.4 SSTs, and monthly precipitation anomalies and Niño 3.4 SSTs for those same ENSO periods. The linear regressions were based on subsets of the temporal profiles of monthly FAPAR and precipitation anomalies (response variable), and Niño 3.4 SSTs (predictor variable) for the length of each ENSO period:

- Period one: 22 months
- Period two: 23 months
- Period three: 27 months

The temporal profiles of the monthly FAPAR and precipitation anomalies for sites 1 – 5 and the entire BBR study region were computed by spatially accumulating the pixels within each monthly observation using the mean statistic (see section 2.3). A total of 25 correlations were found for each period, which includes no lag and lags of up to 24 months. The correlations at each of the various lags were used to examine the response of the vegetation and precipitation to the various ENSO fluctuations for each of the sites. The F-test for the null hypothesis was used to test the overall significance of the correlation results.

The El Niño during the third period presented the strongest response with departures in the FAPAR and precipitation anomalies; as many as 10 consecutive months at sites 1 and 2. Departures in FAPAR anomalies during the same event were lowest at sites 3 and 5.

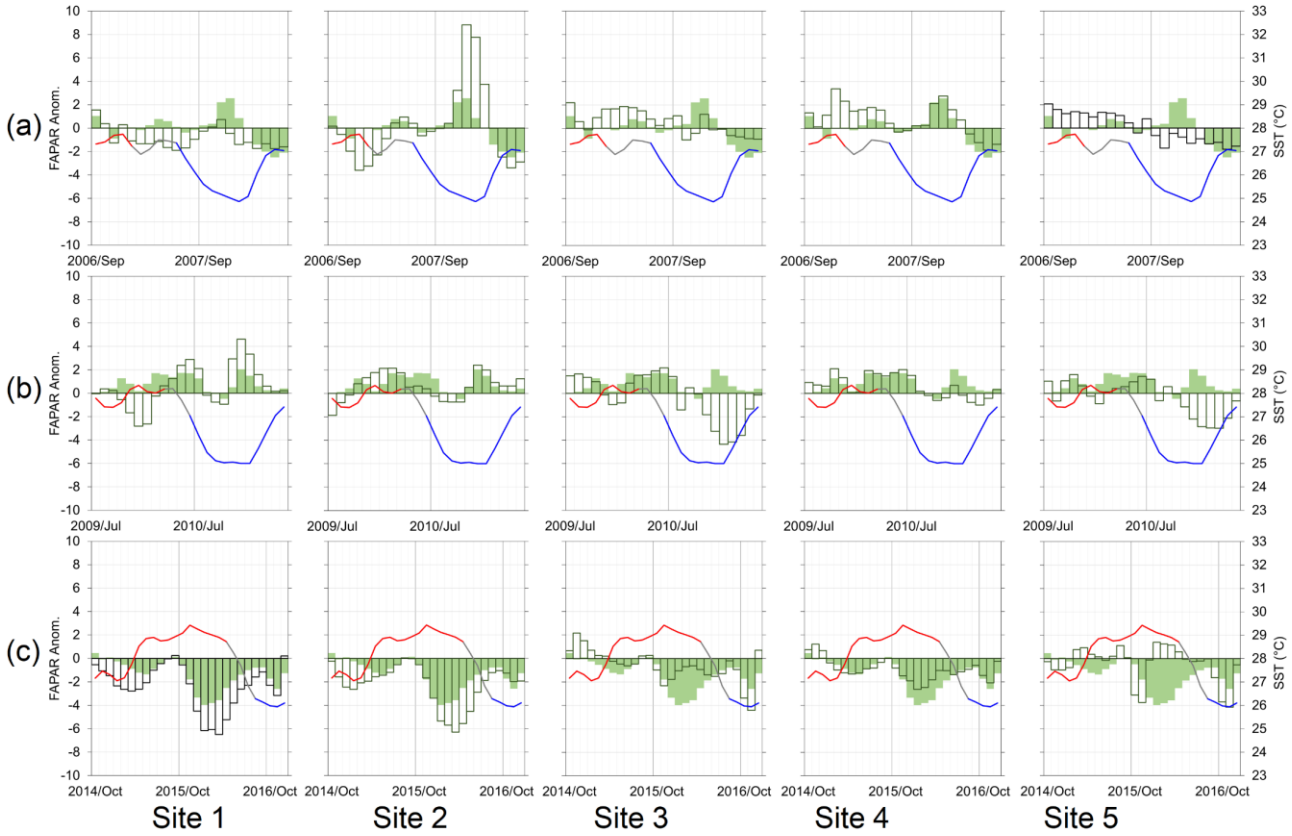


Figure 4. FAPAR anomalies for BBR (solid green bars) and sites 1 to 5 (hollow bars) and Niño 3.4 SSTs (grey line) for the ENSO periods (with El Niño and La Niña events indicated in red and blue lines, respectively) during (a) September 2006 and June 2008, (b) July 2009 and May 2011, and (c) October 2014 and December 2016.

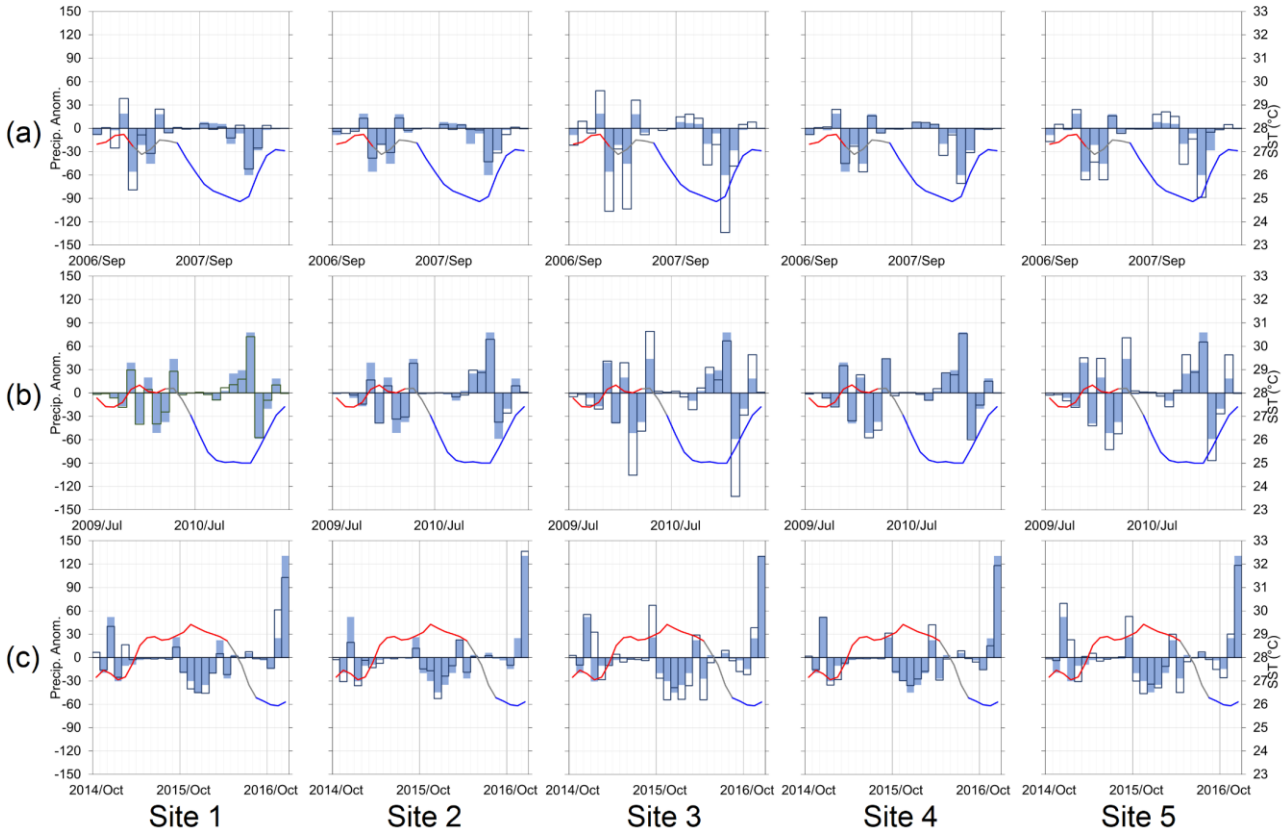


Figure 5. Precipitation anomalies for BBR (solid blue bars) and sites 1 to 5 (hollow bars) and Niño 3.4 SSTs (grey line) for the ENSO periods (with El Niño and La Niña events indicated in red and blue lines, respectively) during (a) September 2006 and June 2008, (b) July 2009 and May 2011, and (c) October 2014 and December 2016.

The highest lagged correlation between FAPAR anomalies and Niño 3.4 generally occurs at some time lag (from 3 to 22 months), though the strongest correlation (0.75) was found at no lag in one particular case (for Site 2 during the first ENSO event). The maximum correlations between monthly FAPAR anomalies and SSTs occur at later lags in sites 3 – 5; approximately 21 and 22 months during the first ENSO period, 16 to 19 months in the second ENSO period, and 14 to 19 months in the third ENSO period. Peak FAPAR correlations for sites 1 – 2 lag the ENSO periods at approximately 7 to 9 months. ENSO-induced correlations for precipitation were most significant during the first ENSO, peaking at 3 months for sites 2, 3 and 5 and 15 months for site 4. No significant precipitation correlations were observed during the second ENSO period, and the maximum correlations observed between precipitation and ENSO during the third period occurred at sites 1, 3 and 5 at no lag.

Table 4. Pearson correlation coefficients (R) between integrated monthly FAPAR and Niño 3.4 (first column in each pair) and between cumulated monthly precipitation amounts and Niño 3.4 (second column in each pair), for the entire BBR region as well as for each of the five individual sites, during the ENSO event between Sep 2006 and Jun 2008, and for the time lags indicated in the leftmost column. The density of the green colour in each Table cell is proportional to its R value, and those that are statistically significant ($p < 0.05$) are set in bold face.

	BBR		Site 1		Site 2		Site 3		Site 4		Site 5	
Lag	FAPAR	Precip.	FAPAR	Precip.	FAPAR	Precip.	FAPAR	Precip.	FAPAR	Precip.	FAPAR	Precip.
No lag	0.395	0.180	0.124	0.112	**0.745**	0.125	0.351	0.231	0.027	0.272	**0.641**	0.161
1 month	**0.471**	0.050	0.165	0.047	**0.673**	0.143	0.274	0.006	0.086	0.024	**0.568**	0.038
2 month	**0.407**	0.280	0.128	0.198	**0.481**	0.364	0.279	0.224	0.025	0.215	**0.484**	0.276
3 month	0.234	**0.467**	0.033	0.327	0.237	**0.487**	0.289	**0.418**	0.177	**0.411**	0.387	**0.487**
4 month	0.059	**0.440**	0.109	0.317	0.042	**0.428**	0.129	0.391	0.361	0.391	0.243	**0.463**
5 month	0.066	0.324	0.317	0.302	0.079	0.315	0.108	0.283	0.389	0.271	0.084	0.307
6 month	0.188	0.078	**0.594**	0.116	0.172	0.089	0.192	0.053	0.330	0.038	0.008	0.038
7 month	0.262	0.063	**0.735**	0.032	0.247	0.049	0.185	0.059	0.190	0.084	0.015	0.113
8 month	0.258	0.168	**0.718**	0.060	0.279	0.158	0.229	0.139	0.025	0.163	0.107	0.220
9 month	0.150	0.274	**0.506**	0.150	0.257	0.293	0.302	0.219	0.282	0.250	0.266	0.290
10 month	0.075	**0.420**	0.110	0.293	0.146	**0.455**	0.397	0.370	**0.527**	0.383	**0.451**	**0.428**
11 month	0.297	**0.447**	0.214	0.354	0.020	**0.470**	**0.429**	**0.409**	**0.661**	0.392	**0.520**	**0.457**
12 month	**0.483**	0.311	**0.452**	0.296	0.145	0.284	**0.454**	0.287	**0.737**	0.246	**0.553**	0.347
13 month	**0.573**	0.044	**0.635**	0.126	0.158	0.023	**0.396**	0.043	**0.720**	0.026	**0.564**	0.095
14 month	**0.516**	0.282	**0.723**	0.125	0.065	0.334	0.283	0.266	**0.539**	0.334	**0.530**	0.227
15 month	0.377	**0.429**	**0.695**	0.223	0.082	**0.439**	0.264	**0.411**	0.253	**0.468**	**0.516**	0.398
16 month	0.237	**0.423**	**0.589**	0.243	0.224	0.387	0.356	**0.414**	0.025	**0.463**	**0.553**	**0.415**
17 month	0.158	0.264	0.333	0.159	0.271	0.223	**0.516**	0.252	0.012	0.302	**0.598**	0.259
18 month	0.164	0.072	0.013	0.062	0.206	0.056	**0.644**	0.055	0.124	0.100	**0.656**	0.028
19 month	0.235	0.063	0.224	0.033	0.105	0.031	**0.701**	0.076	0.330	0.038	**0.701**	0.147
20 month	0.332	0.056	0.168	0.015	0.076	0.018	**0.741**	0.062	**0.531**	0.034	**0.744**	0.186
21 month	0.358	0.032	0.009	0.000	0.153	0.029	**0.738**	0.023	**0.641**	0.002	**0.787**	0.154
22 month	0.281	0.075	0.171	0.063	0.302	0.071	**0.690**	0.037	**0.616**	0.024	**0.793**	0.153
23 month	0.121	0.159	0.275	0.187	**0.473**	0.191	**0.604**	0.105	**0.500**	0.062	**0.770**	0.192
24 month	0.097	0.109	0.279	0.159	**0.592**	0.139	**0.448**	0.051	0.331	0.017	**0.675**	0.136

R
1
0.95
0.9
0.85
0.8
0.75
0.7
0.65
0.6
0.55
0.5
0.45
0.4
0.35
0.3
0.25
0.2
0.15
0.1
0.05
<0.01

Table 5. Pearson correlation coefficients (R) between integrated monthly FAPAR and Niño 3.4 (first column in each pair) and between cumulated monthly precipitation amounts and Niño 3.4 (second column in each pair), for the entire BBR region as well as for each of the five individual sites, during the ENSO event between Jul 2009 and May 2011, and for the time lags indicated in the leftmost column. The density of the green colour in each Table cell is proportional to its R value, and those that are statistically significant ($p < 0.05$) are set in bold face.

	BBR		Site 1		Site 2		Site 3		Site 4		Site 5	
Lag	FAPAR	Precip.	FAPAR	Precip.	FAPAR	Precip.	FAPAR	Precip.	FAPAR	Precip.	FAPAR	Precip.
No lag	0.183	0.227	**0.487**	0.256	0.184	0.318	**0.586**	0.047	**0.569**	0.242	**0.483**	0.114
1 month	0.125	0.258	**0.529**	0.276	0.296	0.349	0.365	0.134	**0.404**	0.276	0.267	0.175
2 month	0.060	0.257	**0.508**	0.276	0.350	0.328	0.119	0.210	0.210	0.271	0.046	0.218
3 month	0.024	0.172	**0.425**	0.201	0.329	0.223	0.092	0.198	0.028	0.177	0.130	0.175
4 month	0.112	0.053	0.327	0.088	0.222	0.091	0.192	0.131	0.069	0.051	0.167	0.093
5 month	0.207	0.086	0.243	0.044	0.052	0.060	0.187	0.009	0.123	0.094	0.097	0.035
6 month	0.349	0.144	0.193	0.111	0.194	0.130	0.115	0.072	0.174	0.159	0.001	0.097
7 month	**0.494**	0.109	0.149	0.096	**0.497**	0.116	0.024	0.064	0.189	0.130	0.119	0.067
8 month	**0.555**	0.070	0.084	0.087	**0.747**	0.094	0.168	0.049	0.148	0.094	0.221	0.026
9 month	**0.491**	0.028	0.037	0.065	**0.866**	0.062	0.282	0.036	0.062	0.054	0.291	0.011
10 month	0.329	0.068	0.206	0.101	**0.822**	0.102	0.342	0.120	0.030	0.093	0.291	0.064
11 month	0.086	0.081	0.341	0.119	**0.559**	0.097	0.319	0.180	0.108	0.092	0.202	0.112
12 month	0.149	0.017	**0.387**	0.059	0.179	0.030	0.188	0.109	0.119	0.007	0.022	0.064
13 month	0.263	0.048	0.332	0.009	0.174	0.029	0.040	0.003	0.011	0.069	0.232	0.006
14 month	0.286	0.108	0.245	0.082	**0.449**	0.082	0.290	0.110	0.147	0.133	**0.474**	0.085
15 month	0.270	0.067	0.158	0.056	**0.669**	0.052	**0.535**	0.135	0.296	0.090	**0.664**	0.076
16 month	0.214	0.013	0.076	0.030	**0.787**	0.012	**0.722**	0.125	**0.409**	0.028	**0.745**	0.037
17 month	0.072	0.114	0.003	0.073	**0.739**	0.099	**0.803**	0.017	**0.515**	0.112	**0.709**	0.082
18 month	0.133	0.174	0.041	0.131	**0.513**	0.149	**0.763**	0.050	**0.584**	0.183	**0.607**	0.132
19 month	0.348	0.182	0.014	0.161	0.083	0.175	**0.619**	0.058	**0.588**	0.201	**0.431**	0.123
20 month	**0.447**	0.158	0.088	0.166	0.364	0.184	**0.382**	0.038	**0.484**	0.188	0.213	0.076
21 month	**0.406**	0.136	0.247	0.159	**0.642**	0.203	0.110	0.036	0.302	0.166	0.004	0.043
22 month	0.282	0.229	**0.389**	0.264	**0.707**	0.300	0.115	0.182	0.110	0.248	0.142	0.158
23 month	0.136	0.214	**0.444**	0.245	**0.613**	0.262	0.247	0.268	0.017	0.221	0.180	0.222
24 month	0.036	0.067	**0.397**	0.107	**0.431**	0.095	0.225	0.183	0.011	0.071	0.097	0.134

R
1
0.95
0.9
0.85
0.8
0.75
0.7
0.65
0.6
0.55
0.5
0.45
0.4
0.35
0.3
0.25
0.2
0.15
0.1
0.05
<0.01

Table 6. Pearson correlation coefficients (R) between integrated monthly FAPAR and Niño 3.4 (first column in each pair) and between cumulated monthly precipitation amounts and Niño 3.4 (second column in each pair), for the entire BBR region as well as for each of the five individual sites, during the ENSO event between Oct 2014 and Dec 2016, and for the time lags indicated in the leftmost column. The density of the green colour in each Table cell is proportional to its R value, and those that are statistically significant ($p < 0.05$) are set in bold face.

	BBR		Site 1		Site 2		Site 3		Site 4		Site 5	
Lag	FAPAR	Precip.	FAPAR	Precip.	FAPAR	Precip.	FAPAR	Precip.	FAPAR	Precip.	FAPAR	Precip.
No lag	0.297	**0.412**	0.293	**0.560**	0.266	0.347	**0.055**	**0.416**	0.273	0.317	0.367	**0.372**
1 month	0.201	**0.399**	0.207	**0.508**	0.138	0.339	0.116	**0.381**	0.235	0.321	0.357	0.347
2 month	0.080	0.316	0.077	**0.403**	0.001	0.263	0.195	0.263	0.170	0.265	0.343	0.239
3 month	0.065	0.195	0.093	0.253	0.155	0.176	0.258	0.099	0.065	0.173	0.250	0.083
4 month	0.242	0.052	0.304	0.077	0.347	0.080	0.300	0.063	0.107	0.062	0.081	0.069
5 month	**0.430**	0.041	**0.500**	0.063	**0.545**	0.028	0.311	0.171	0.298	0.009	0.100	0.155
6 month	**0.599**	0.081	**0.639**	0.152	**0.707**	0.011	0.321	0.219	**0.443**	0.037	0.195	0.181
7 month	**0.726**	0.071	**0.697**	0.175	**0.783**	0.025	0.364	0.214	**0.526**	0.015	0.170	0.168
8 month	**0.783**	0.004	**0.652**	0.133	**0.746**	0.096	**0.426**	0.157	**0.544**	0.052	0.035	0.117
9 month	**0.768**	0.019	**0.547**	0.103	**0.609**	0.119	**0.509**	0.134	**0.548**	0.073	0.134	0.106
10 month	**0.688**	0.045	**0.394**	0.070	**0.404**	0.143	**0.558**	0.099	**0.533**	0.101	0.240	0.091
11 month	**0.541**	0.078	0.181	0.027	0.161	0.187	**0.550**	0.046	**0.484**	0.120	0.290	0.056
12 month	**0.383**	0.123	0.016	0.042	0.064	0.220	**0.569**	0.015	**0.449**	0.147	0.343	0.012
13 month	0.225	0.156	0.190	0.100	0.248	0.233	**0.584**	0.068	**0.381**	0.162	**0.394**	0.019
14 month	0.073	0.156	0.313	0.133	**0.384**	0.220	**0.599**	0.073	0.309	0.145	**0.421**	0.004
15 month	0.048	0.140	0.349	0.147	**0.423**	0.203	**0.546**	0.056	0.251	0.117	0.338	0.025
16 month	0.102	0.066	0.255	0.102	0.330	0.123	**0.431**	0.002	0.232	0.042	0.120	0.067
17 month	0.069	0.010	0.061	0.048	0.112	0.075	0.233	0.050	0.248	0.006	0.207	0.086
18 month	0.056	0.048	0.195	0.015	0.191	0.010	0.043	0.081	0.288	0.063	**0.482**	0.074
19 month	0.235	0.077	**0.458**	0.063	**0.506**	0.037	0.088	0.114	0.315	0.089	**0.603**	0.059
20 month	**0.415**	0.075	**0.658**	0.075	**0.734**	0.065	0.137	0.116	0.296	0.076	**0.519**	0.039
21 month	**0.492**	0.210	**0.747**	0.195	**0.781**	0.220	0.095	0.221	0.257	0.201	0.286	0.144
22 month	**0.428**	0.332	**0.674**	0.352	**0.666**	0.341	0.119	0.312	0.166	0.297	0.121	0.240
23 month	0.273	0.341	**0.453**	**0.403**	**0.449**	0.351	0.235	0.290	0.012	0.291	0.085	0.226
24 month	0.096	0.296	0.172	**0.392**	0.177	0.314	0.264	0.202	0.116	0.236	0.012	0.157

R
1
0.95
0.9
0.85
0.8
0.75
0.7
0.65
0.6
0.55
0.5
0.45
0.4
0.35
0.3
0.25
0.2
0.15
0.1
0.05
<0.01

The logarithmic (base = 2) scatterplots in figure 6 plot for sites 1 – 5, the cumulated precipitation (x-axis) and integrated FAPAR (y-axis) for the months representing the growing (Oct – Mar) and senescing (Apr – Sep) phases of the vegetative season for the El Niño and La Niña during ENSO periods one to three (a – c), and non-event months for the 18 year record, i.e., isolated periods that neither qualify as El Niño nor La Niña according to the ONI classification. Months that were neither El Niño nor La Niña were included to compare how the integrated FAPAR versus accumulated precipitation at the sites were behaving during varying sequences and intensities of El Niño and La Niña with respect to non-event periods. The results show that integrated FAPAR generally increases with accumulated precipitation, with larger integrated FAPAR observed during both the growing and senescing phases of non-event months than either of those events. The El Niño and La Niña regimes were more distinct during periods 1 and 3 than in period 2, and the dependency (slope of the relation) between integrated FAPAR and accumulated precipitation was stronger during the growing than during the senescence phase. This is because the El Niño and La Nina events during periods 1 and 3 represent sharper contrasts in intensity and duration than period 2. In the case of period 3 (period 1), the slope of the relation is strongest during the La Niña (El Niño),

and more subtle during the senescing phases. By contrast, the similar duration and intensities for the El Niño and La Niña events during period 2 compensate each other, and thus have a more subtle slope of relation during event and non-event periods. The findings suggest that the main impact of El Niño and La Niña events is to render the vegetation productivity more dependent on precipitation, when compared to non-event periods. El Niño and La Niña events tend to differentially influence the productivity of vegetation on the various sites during the growing months of the vegetative season, but this relation appears much more dampened during the senescence months.

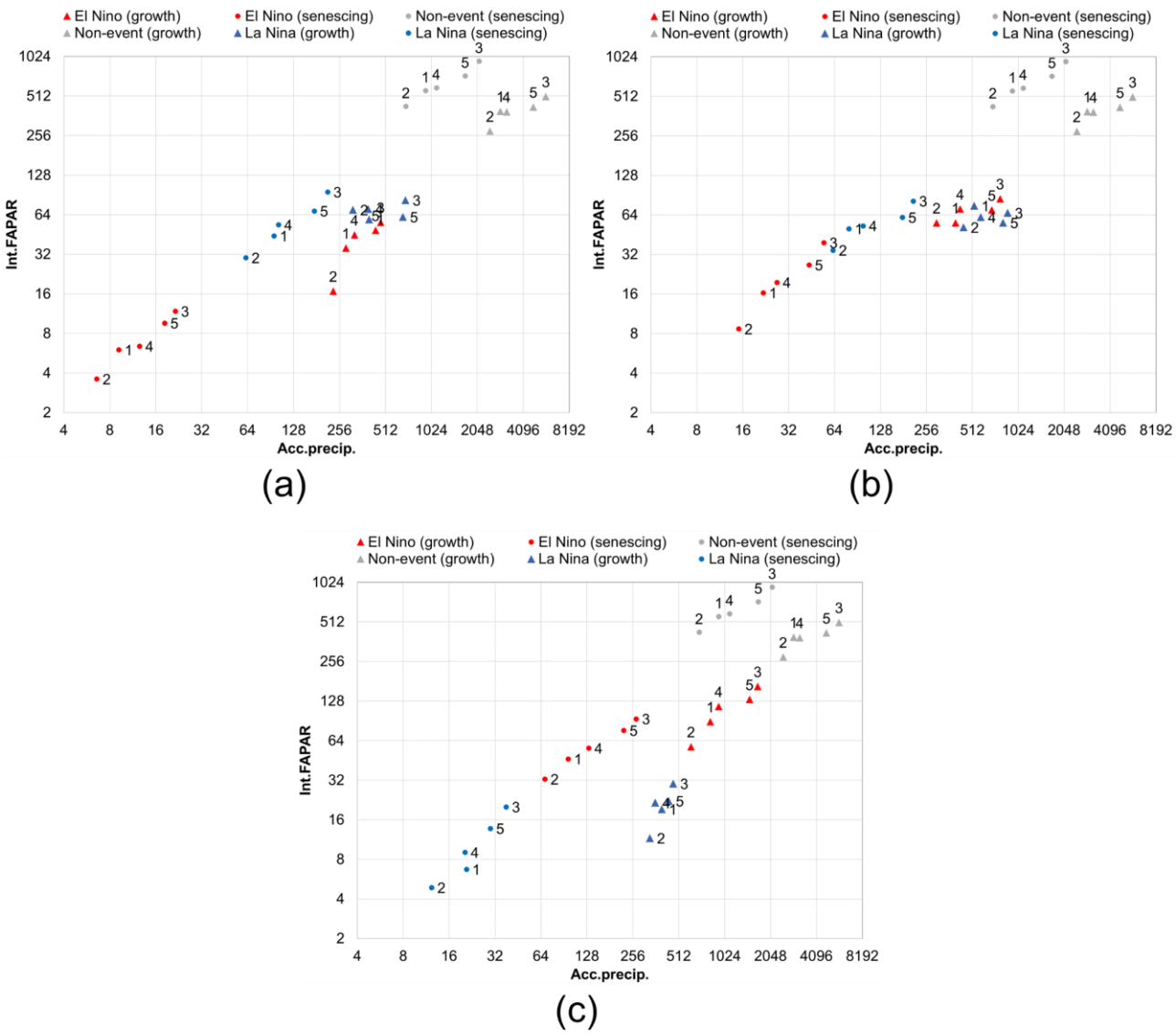


Figure 6. Logarithmic scatterplots (base = 2) of accumulated precipitation (x-axis) and integrated FAPAR (y-axis) for the vegetation sites (points labelled 1 – 5) , plotting ENSO periods one to three (a – c), summed over the growing (Oct – Mar) and senescence months (Apr – Sep) of the El Niño and La Niña events, and non-event months for the 18 year record..

3.2. Magnitude and spatial distribution of FAPAR anomalies during peak ENSO conditions

The maps in Figure 7 show the sum of the FAPAR monthly anomalies, cumulated over the 22 months of ENSO period one (top left panel) and over the 27 months of ENSO period three (top right panel). The contrast between those two panels highlights the differential effect between a weak El Niño followed by a strong La Niña (left) and a strong El Niño followed by a weak La Niña (right). The smaller panels at the bottom of the figure show similar statistics, this time accumulating FAPAR monthly anomalies over the three-month periods centred on the peak of the El Niño and La Niña events within each of those two ENSO periods, respectively.

The 3-monthly cumulated FAPAR anomalies were used to convey the spatial distribution and magnitude of the impacts of peak El Niño and La Niña events on the vegetation during these ENSO periods. The El Niño and La Niña events within period one and three were chosen as they represent a sharp contrast in intensities. Period one includes a weak El Niño followed by a moderate La Niña, while the third period features a very strong El Niño followed by a weak La Niña.

The distribution of randomly sampled pixels (n = 1000) for the 3-monthly cumulated FAPAR anomalies representing peak conditions during the (a) weak El Niño and (b) strong La Niña for period 1, and the (c) strong El Niño and (d) weak La Niña for period 3 are presented in the frequency histograms for sites 1 to 5 in figures 8 to 12, respectively. A bin width of one was used to group the FAPAR anomalies. Positive (negative) anomalies refer to integrated FAPAR values which represent increases (decreases) relative to the long-term record. A random sample of 1000 pixels drawn without replacement was selected for the 3-monthly cumulated FAPAR anomalies at each of the sites. The fixed sample size ensures the frequency statistics are inter-comparable between the sites, and the number of samples chosen was guided by the total number of pixels available at the smallest site, site 5 (n = 1089).

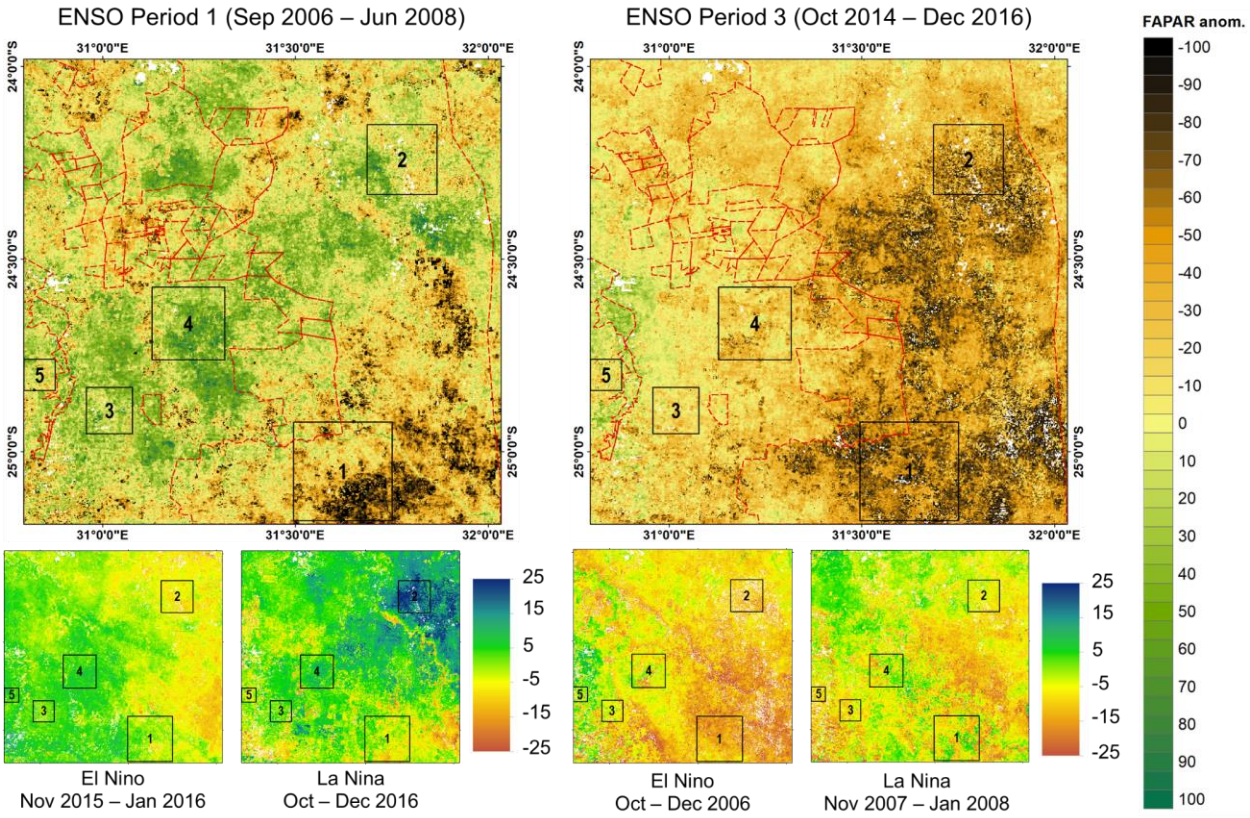


Figure 7. Maps of the sum of the FAPAR monthly anomalies, cumulated over the 22 months of ENSO period one (top left) and over the 27 months of ENSO period three (top right). The bottom panels map cumulated FAPAR monthly anomalies over the three-month periods centred on the peak of the El Niño and La Niña events within each of those two ENSO periods, respectively. The site labels include (1) protected granite Lowveld (PGL), (2) protected basalt Lowveld (PBL), (3) unprotected sour bushveld (USB), (4) unprotected granite Lowveld (UGL), and (5) unprotected Highveld grassland (UHG). White pixel regions represent areas with no data values.

Inspecting the spatial distribution of FAPAR anomalies across the BBR, the peak El Niño conditions experienced during the third ENSO period lead to the most widespread dry conditions as observed by the negative FAPAR anomalies for most of the municipality (-15 to -25). In contrast, negative FAPAR anomalies for the weaker El Niño during the first ENSO period (approximately -5 to -15) were mostly confined to the eastern parts of the municipality in the lower lying areas within the KNP, which is typically drier. Positive FAPAR anomalies during the strong La Niña which followed the weak El Niño within the first period were observed over most of the BBR, concentrating in the north eastern parts (+25). The FAPAR anomalies over the study area remained mostly negative for the weak La Niña that followed the very strong El Niño event during period 3.

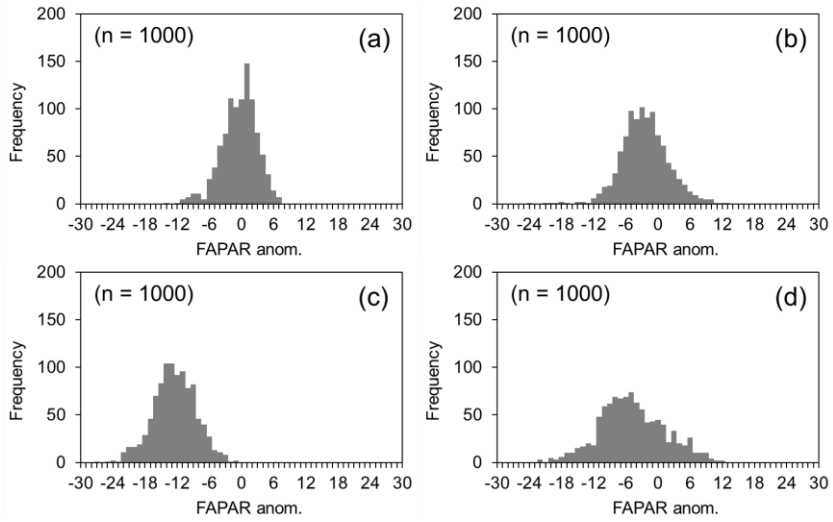


Figure 8. Site 1 frequency histograms of the FAPAR monthly anomalies, cumulated over the three month periods centred on the peak of the (a) weak El Niño and (b) strong La Niña during period 1, and the (c) strong El Niño and (c) weak La Niña during period 3 (bin width = 1).

Site 1 exhibited minor differences between the FAPAR anomalies at peak El Niño and La Niña conditions during the first ENSO period, with a median deviation of about 0 and -3, respectively. At the height of the strong El Niño during the third ENSO period, all of the FAPAR anomalies observed at site 1 were negative, with a median deviation of -13, and at the peak of the weak La Niña, the FAPAR anomalies increased slightly, but remained consistently negative. The biggest departures in cumulative FAPAR anomalies between the El Niño of the two periods was observed at site 1.

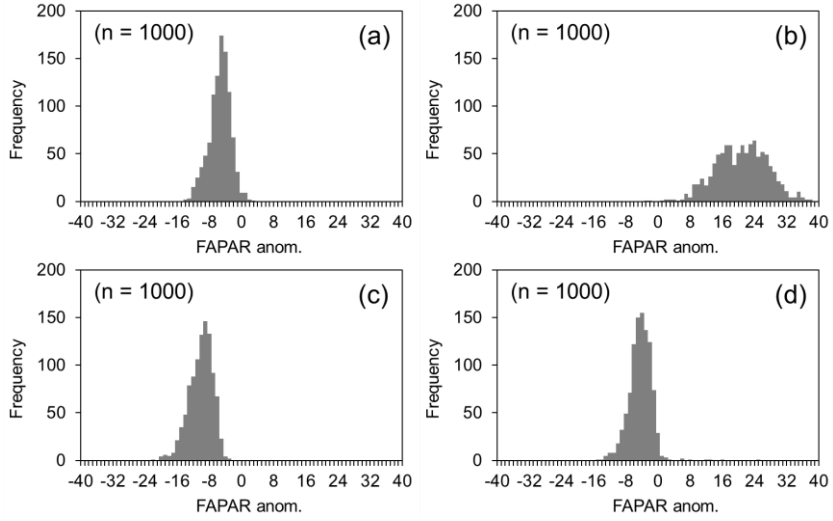


Figure 9. Site 2 frequency histograms of the FAPAR monthly anomalies, cumulated over the three month periods centred on the peak of the (a) weak El Niño and (b) strong La Niña

during period 1, and the (c) strong El Niño and (c) weak La Niña during period 3 (bin width = 1).

At the peak of the weak El Niño during the first ENSO, cumulative FAPAR anomalies were consistently negative throughout most of site 2, with a median deviation of around -6. By contrast, at the peak of the subsequent strong La Niña, cumulative FAPAR anomalies were consistently positive and the most pronounced over that site, with a median deviation of around +20. At the peak of the strong El Niño and weak La Niña during ENSO period 3, site 2 observed mostly negative anomalies, with a median deviation of -10 and -5 respectively.

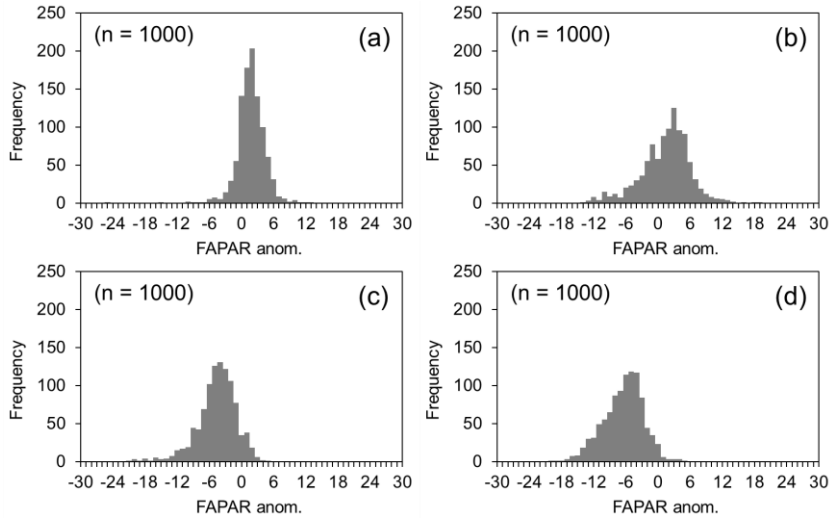


Figure 10. Site 3 frequency histograms of the FAPAR monthly anomalies, cumulated over the three month periods centred on the peak of the (a) weak El Niño and (b) strong La Niña during period 1, and the (c) strong El Niño and (c) weak La Niña during period 3 (bin width = 1).

The FAPAR anomalies at the peak of the weak El Niño and Strong La Niña during the first ENSO period were mostly positive over site 3, with a median deviation of around 2. At the peak of the strong El Niño and weak La Niña during the third ENSO period, the cumulative FAPAR anomalies were mostly negative, with a median deviation of about -5 and -6, respectively. Site 3 observed the biggest differences in the cumulative FAPAR anomalies between the ENSO periods, after site 1, mostly due to the FAPAR departures during the strong El Niño.

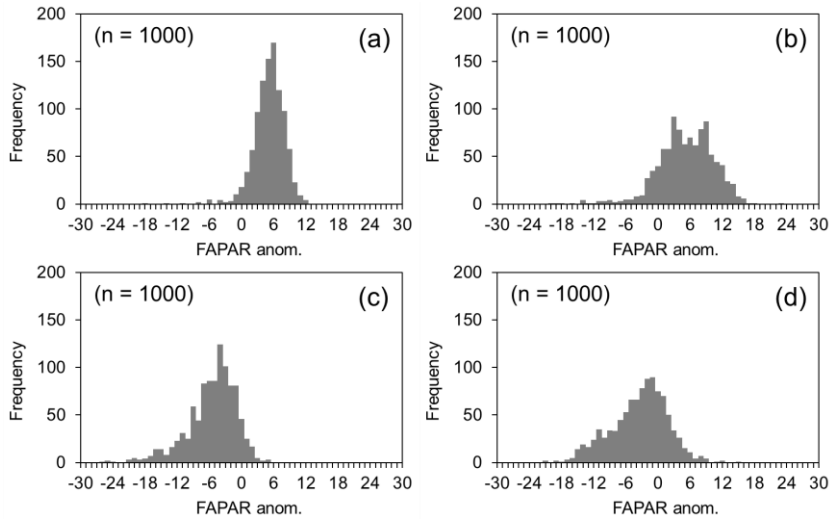


Figure 11. Site 4 frequency histograms of the FAPAR monthly anomalies, cumulated over the three month periods centred on the peak of the (a) weak El Niño and (b) strong La Niña during period 1, and the (c) strong El Niño and (c) weak La Niña during period 3 (bin width = 1).

The cumulative FAPAR anomalies at the peak of the weak El Niño and strong La Niña were consistently positive at site 4, with a median deviation of around 5. The cumulative FAPAR anomalies during the peak of the weak El Niño were the most positive at site four. At the peak of strong El Niño and weak La Niña during ENSO period 3, site 4 observed mostly negative anomalies, with deviations of about -5 and -3, respectively. Departures in the cumulative FAPAR anomalies between the ENSO periods were least pronounced at this site.

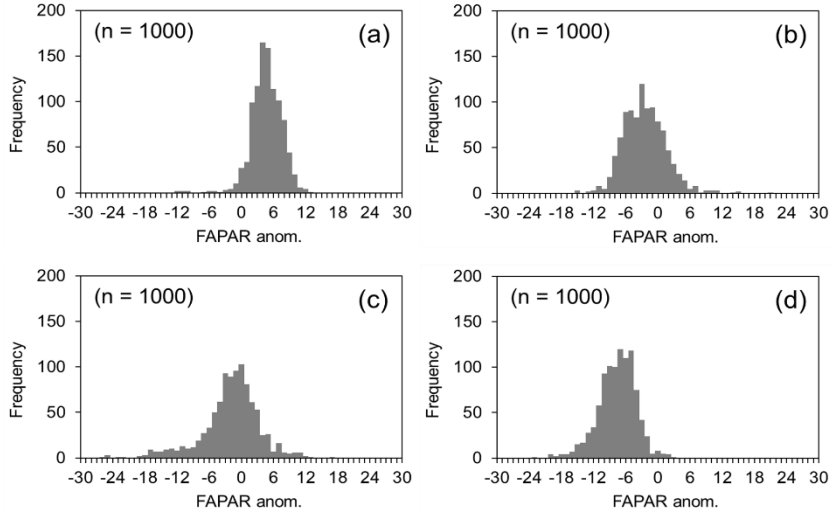


Figure 12. Site 5 frequency histograms of the FAPAR monthly anomalies, cumulated over the three month periods centred on the peak of the (a) weak El Niño and (b) strong La Niña

during period 1, and the (c) strong El Niño and (c) weak La Niña during period 3 (bin width = 1).

At the peak of El Niño during period 1, site 5 observed mostly positive FAPAR anomalies, with a median deviation of 4, and during the La Niña for the same period the cumulative anomalies were mostly negative, with a deviation of -3. By contrast, peak El Niño conditions were consistently negative for ENSO period 3, with a median deviation of -2, and decreased further at the peak of the weak La Niña for the same period, as noted by the median deviation of -8.

3.3. Discussion

The relationships between ENSO, precipitation and FAPAR suggest that the sequence of intensities for peak El Niño and La Niña may be important ecologically. While ENSO is regarded as the major driver of precipitation variability over southern Africa (Pomposi et al., 2018), this study found that the correlations between FAPAR and ENSO are substantially stronger and more significant ($p < 0.05$) than the correlations between precipitation and ENSO. The findings are consistent with regional assessments over southern Africa which show a stronger relationship between NDVI anomalies and Niño 3.4 SSTs than between precipitation anomalies and SSTs (Anyamba et al., 2018). This is likely due to the discontinuous occurrence of precipitation compared with the gradual growth and decay of vegetation over space and time.

There can be delays of multiple months between the occurrence of an ENSO period and the subsequent impact on vegetation, as witnessed by the FAPAR signal, where the lag and the intensity of the effect depend on the site as well as on the severity of ENSO itself. A strong positive relation was observed between integrated FAPAR and accumulated precipitation at all 5 sites, both during the growing and the senescence phases, and for all 3 ENSO periods considered. ENSO appears to differentially influence the productivity of vegetation on the various sites during the growing phase of the vegetative season, but this relation appears much more homogeneous during the senescence phase. The slope of relation for the integrated FAPAR versus accumulated precipitation is highly dependent on the contrast between El Niño and La Niña intensities and duration. Larger integrated FAPAR were observed during both the growing and senescing phases of non-event months than either of those events.

Vegetation decline during El Niño was most pronounced at sites 1 and 2 (protected areas). However, the FAPAR anomalies were consistently lower for site 1 than site 2, even though these sites experienced similar precipitation anomalies for the same periods, and site 2 is

characterised by lower mean annual precipitation. By contrast, the vegetation at site 2 increased the most in response to the strong La Niña event during ENSO period 1, with a correlation of 0.75 observed at no lag between the FAPAR and the SST anomalies.

The differential responses noted between the vegetation productivity of these two sites can be understood through the inverse texture hypothesis of Noy-Meir (1974) who proposed that sandy soils should support higher productivity than finer soils in low rainfall regimes and vice versa. The vegetation at site 2 is characterised by a dense herbaceous layer with few trees occurring over a shallow basalt clay soil (< 2m) which exhibits good growth in response to rainfall events. Site 1 on the other hand, is characterised by granite (sandy) soils with a greater abundance of trees which dilute the response of the grassy understory. By contrast, the granite soils permit better water infiltration, making them less susceptible to evaporation below 10 cm, and their capacity to store water permits vegetation productivity even between years when rainfall may be below average.

Grasses are more advantaged on the water-retaining clay soils which hold water higher in the soil profile after episodic water events, but this also makes them more susceptible to evaporation through the soil's surface. More water is needed to commence vegetation productivity on clay soils than on sandy soils because of the greater initial losses to evaporation and runoff on clay soils (Scholes, 2003). These findings are also consistent with those of Archibald and Scholes (2007) who have modelled leaf green-up rates for semi-arid savanna trees and grasses in the KNP in response to environmental cues, such as soil moisture, concluding that, at a landscape scale, trees have a less variable phenological cycle (within and between years) than grasses. For the most part, a convex relationship exists between grass production and the quantity of trees in these savanna ecosystems, where the grass production declines more steeply per unit increase in tree quantity at low tree cover than at high tree cover (Scholes, 2003). The climate phenomena exhibit more clear relations where the dominant functional plant type is homogenous (e.g., grassland or deciduous forest) than when it is more heterogeneous, as is the case with savannas, which are a mix of trees and grasses. The ecophysiological functionality of plant types appears to be compounded by both infertile (granite) and fertile (basalt) soils.

While sites 1 and 4 both occur on the granite Lowveld, site 4 experienced mostly positive FAPAR anomalies at the peak of El Niño and La Niña events during ENSO period 1. Site 4 also exhibited the smallest difference in cumulative anomalies for El Niño and La Niña between ENSO periods one and three. It is likely that site 4 exhibits less absolute variability in vegetation productivity during El Niño or La Niña events (more stable response) because anthropogenic activities have significantly transformed the vegetation there. By contrast, the

protection offered by the private reserves has contributed considerably to the persistence of unmanaged vegetation in the region, particularly woody vegetation (Coetzer et al., 2010). Site 4 occurs over communal rangelands characterised by homogenous stands which include agricultural fields, plantation forest, and residential areas to name a few. Vegetation structure varies across settlements, but communal land use on the granite substrates has been shown to have a higher impact on the woody cover below 5 m than both elephants and fire (Wessels et al., 2011).

Interestingly, the El Niño and La Niña phases generated opposite effects on Site 5 than on Site 4: in this case, the warming phase of the teleconnection seems to be associated with positive FAPAR anomalies, while cooling phases are generally more associated with negative FAPAR anomalies. Site 5 is located on the northern escarpment (about 1600 m above sea level) over black reef quartzites which overlay dolomite. Some plantation forests (eucalyptus species) occur on the southern extent of the site. These species-rich grasslands receive increased rainfall (MAP 1034 mm) due to enhanced orographic effects. The CHIRPS record may underestimate precipitations due to orographic as it has been shown to depend on the duration of the integration time and to vary with the altitude of the terrain (Belay et al., 2019). Year-round orographic rainfall coupled with above average rainfall during strong La Niña events can cause the soils at this site to oversaturate. When this happens, vegetation productivity can respond negatively, which could explain why negative FAPAR anomalies were observed during the La Niña event of period one.

4. Conclusions

This study explored the sensitivity of vegetation productivity and precipitation to non-periodic and non-seasonal fluctuations as exhibited by ENSO events for five sites over the Bushbuckridge municipality. There is a vast literature concerning these ENSO periods and their impacts on the seasonality of rainfall and vegetation phenology, but the bulk of those publications have been mostly focused on establishing statistical relations at broad spatial scale, typically over oceanic, continental or sub-continental regions (Anyamba and Eastman, 1996; Anyamba et al., 2002; Anyamba et al., 2018; Nicholson and Kim, 1997; Parhi et al., 2016; Philippon et al., 2014; Pomposi et al., 2018). It was found that ecosystems in the BBR study region exhibit significant differential responses to varying sequences and intensities of ENSO, where the relations with the climate phenomena and vegetation are dependent on the dominant functional plant type (e.g., grassland or eastern deciduous forest) and the physical properties of the site (e.g., altitude, soils).

Policy making should not be applied uniformly at municipal or regional scales but should instead consider the response modes of diverse ecosystems at local scales. The findings

demonstrated here are useful for documenting the effects of ENSO events on the ecological responses of different vegetation types in the region. A variety of benefits can be derived from local scale examinations of the magnitude and distribution of FAPAR anomalies during the peak of ENSO events. Understanding vegetation dynamics during historic events such as the 2015/16 El Niño can inform targeted relief efforts and guide conservation management practices.

Two out of four possible classes of ENSO events were examined; namely weak El Niño events followed by strong La Niña events and strong El Niño events followed by weak La Niña events. A potentially useful avenue for further investigations could also examine the response of vegetation when a strong El Niño event is followed by a strong La Niña events and when a weak El Niño event follows a weak La Niña event.

CHAPTER 4 OVERALL DISCUSSION AND CONCLUSION

The purpose of this chapter is to link the findings of the two research chapters (Chapters 2 and 3) with the literature review (Chapter 1) and to highlight the original contributions that this PhD has contributed to the disciplinary area.

Globally, savannas cover about 33 million km^2 or nearly 20% of the Earth's land surface, making them the second largest biome after boreal forest (Scholes and Hall, 1996). Savannas support a fifth of the world's human population and a majority of its rangeland and livestock biomass (Scholes and Archer, 1997). Relations between vegetation properties (such as biomass, leaf area, net primary productivity, etc.) and abiotic factors (like climate, soils, fire, etc.) have long been well established but the four key variables traditionally regarded as the determinants of savanna structure and function are water availability, fire, soils (geology) and herbivory (Anderson et al., 2016; Archibald, 2016; Colgan et al., 2012; Fisher et al., 2009; Gray and Bond, 2015; Kanniah et al. 2010; Le Roux and Bariac 1998; Scholes and Archer 1997; Wessels et al. 2011; Witkowski and O'Connor 1996).

The geographical distribution of savanna on broad spatial and temporal scales is largely constrained by average climate and soil conditions. The widely used Köppen–Geiger climate classification system, originally proposed by Wladmir Köppen in 1884 (subsequently revised by Köppen, notably in 1918 and 1936), and later modified by Rudolf Geiger in 1954 and 1961 categorises climate zones throughout the world based on local vegetation. Under present-day climate and fire regimes, African savannas can assume different stable states, such as tree-dominated or C_4 grass-dominated species, depending on the pre-historical vegetation state of the region (Bond et al., 2005). Present-day Köppen–Geiger climate classification maps (1980-2016) show that savanna in the Lowveld bioregion is prevalent in regions characterised by a hot semi-arid climate in the lower lying parts to the east of South Africa, and by temperate climates in the higher lying areas along the escarpment (Beck et al., 2018). The latest iterations of Köppen-Geiger classification maps are useful for categorising climates based on the distribution of local vegetation, but other approaches are needed to understand the intricate feedbacks between CO_2, trees, C_4 grasses, climate and fire under enhanced anthropogenic forcing (Engelbrecht and Engelbrecht, 2016).

Daily and seasonal fluctuations in water availability and temperature regimes constrain the phenology of vegetation. Mathematically, these fluctuations can be treated as perturbations around a slowly changing mean annual state. Plant species persist in a given environment as long as conditions remain suitable for their growth and reproduction. Farmers have for thousands of years understood and relied on the timing of recurring biological events with

respect to periodic forces. The timing of phenological phases in plants has gained increasing interest as a consequence of climate change; phenology variables are some of the most sensitive data to differences in climate conditions (Menzel, 2006). Non-seasonal or aperiodic perturbations like the El Niño–Southern Oscillation (ENSO) have been studied for decades, but at larger spatial scales and over periods ranging from multiple years to few decades (Lyon and Barnston, 2005; Trenberth, 1997). Also, statistical studies relating vegetation dynamics to ENSO fluctuations have been established for entire biomes, but few detailed investigations, if any, have been conducted at the finer spatial scales of bioregions, especially for African ecosystems (Anyamba et al., 2002; Anyamba et al., 2018; Nicholson and Kim, 1997; Parhi et al., 2016; Philippon et al., 2014).

The Bushbuckridge local municipality (BBR), an area covering about 16,757 km^2 of the Lowveld bioregion, is characterised by savanna vegetation. Savanna vegetation within the Lowveld is critically important in terms of biodiversity and for the sustainable socio-economic development of the region (Grace et al., 2006; Schackleton and Shackleton, 2004; Scholes and Archer, 1997; Twine et al., 2003). Projected impacts of future climate change over southern Africa show a general expansion of woodland in response to increases in CO_2 (Higgins and Scheiter 2012; Moncrieff et al., 2015). Woody plant encroachment in savannas contrasts with deforestation induced by human land use. The gradual proliferation of woody plants in savannas threatens the biodiversity of these ecosystems, and the livelihoods of communities who depend on them (Archer et al., 2017). Woody plant encroachment has the potential to reduce the rangeland carrying capacity of wild and domestic grazers by displacing herbaceous forage in favour of trees and shrubs (Venter et al., 2018). Understanding how this savanna ecosystem responds to increased temperatures, decreased rainfall and more frequent extreme events is crucial for developing adaptation strategies to secure its biodiversity and the environmental services upon which many (mostly rural households) depend. Examining trends in long-term historical data sets can help contextualise and re-frame the narratives about projected future changes by providing a more realistic, empirical lens into the resilience of southern Africa biomes (Hoffman et al., 2019).

This study examined the sensitivity of savanna vegetation productivity and precipitation anomalies, as reported by the Climate Hazards Group InfraRed Precipitations with Stations (CHIRPS), to non-periodic and non-seasonal fluctuations, such as the aperiodic changes of sea surface temperatures (SSTs) in a region of the eastern tropical Pacific Ocean as represented by the ENSO during the first two decades of this century. The FAPAR record was used as a proxy for vegetation productivity and scrutinised alongside the climatic observations to gauge immediate and delayed impacts of peak ENSO events in the BBR

study region. ENSO events occur every 2 to 5 or even 7 years and have been shown to amplify or damp the more regular seasonal or annual variability in environmental constraints mentioned above.

This study includes the monthly Niño 3.4 and Oceanic Niño Index (ONI) climatic records for the period between September 2000 and December 2018. Those records were downloaded from the National Oceanic and Atmospheric Administration (NOAA) National Weather Service Climate Prediction Center (NOAA, 2020a). The Niño 3.4 index, which represents the average sea surface temperature deviation from the long-term mean over the region 5N-5S, 170W-120W of the equatorial tropical Pacific Ocean, arguably constitutes an optimal long-term continuous record to monitor and predict El Niño and La Niña events (Trenberth, 1997; Trenberth, 2001).

The spatial and temporal distribution of precipitations over the study region were characterised using the CHIRPS precipitation record for the period between 2000 and 2018 (Funk et al., 2014; Funk et al., 2015). This data set offers a gridded precipitation record for continental areas between 50°S–50°N and 180°E–180°W, at a spatial resolution of 0.05°; it was downloaded from the Famine Early Warning Systems Network (FEWS NET, 2020). While the CHIRPS record is a suitable source of spatial and temporal information on precipitation, it is based on a limited number of weather stations available in the region and is known to underestimate precipitations due to orographic effects. An independent study by Belay et al. (2019), showed that the reliability of the CHIRPS data set depends on the duration of the integration time and varies with the altitude of the terrain.

Long-term records (2000 – 2018) of the Fraction of Absorbed Photosynthetically Active Radiation (FAPAR) derived from the Multi-angle Imaging SpectroRadiometer (MISR) instrument were used to characterise the land surface phenology in the environment of the Bushbuckridge local municipality (BBR). The study area falls within the overlap of two MISR Paths (168 and 169) giving a staggered revisit period every 7 and 9 days over the period 2000 – 2018. The FAPAR is closely related to vegetation productivity and biomass yield, and has been identified as an Essential Climate Variable (Bojinski et al., 2014; Gobron and Verstraete, 2009). The algorithms implemented in the MISR-HR processing system that generated the FAPAR product used in this study have been extensively evaluated (D'Odorico et al., 2014; Gobron et al., 2019; Kaminski et al 2017; Pinty et al., 2011c) and take advantage of state of the art radiation transfer models as well as cutting edge optimisation techniques (Clerici et al., 2010; Lavergne et al., 2007; Pinty et al., 2011a and b).

The property describing the difference in surface reflectance measurements when observing the same target but from different directions or under different illumination conditions is

referred to as anisotropy. Anisotropy is usually regarded as a source of noise when analysing remote sensing data from mono-angular spectral instruments but constitutes a definite advantage when analysing measurements from multi-angular instruments. Spectral measurements acquired by mono-angular instruments take anisotropy for granted and usually assume that the measurements are attributed to changes in the geophysical media. Surface reflectance measurements of plant canopies captured by satellite instruments are not only dependent on their structural and physical properties but also the angles at which they are illuminated by the Sun and the direction at which they are observed. The MISR-HR FAPAR used in this study offers an improved characterization of atmospheric and terrestrial environments because capturing quasi-simultaneous multi-angular measurements of a target permits an accurate, quantitative decoupling of the distinct spectral and directional signatures of those geophysical media. While it is possible to characterise the anisotropy of a given target using mono-angular measurements acquired under different geometries of illumination over longer periods of time, as is the case with MODIS reflectance anisotropy products (Schaaf et al., 2010), that approach does not account for physical changes that may occur in the target over those periods.

The main limitation of biogeophysical variables retrieved from satellite remote sensing techniques in the solar spectral range is the inability to observe the planetary surface when clouds (or optically thick aerosols) are present in the atmosphere, which is typically the case between October and March in the study region. This constraint can generate a systematic bias in the record because clouds occur most often during the rainy season, when plants grow and develop, i.e., when those measurements are most needed. Nevertheless, the scientific basis for the interpretation of those measurements, the progressive, continuous nature of plant phenology, and the opportunity to repeatedly observe the same targets in time offer ample opportunities to document the seasonal growth and senescence of the vegetation. Data can also be occasionally missing due to technical problems with the instrument or the platform, but that is generally a minor issue.

The key contributions based on the findings in chapters 2 and 3 are discussed in sections 1 and 2, respectively.

1. Evaluating and enhancing vegetation phenology in historical FAPAR records

Chapter 2 was primarily focused on developing a key methodological element of the study. It also included simulating reliable estimates of the seasonal phenology of the plant canopy despite the presence of missing data and noise in the FAPAR records, which are mostly attributed to clouds during the rainy season. Most land surface phenology studies have tended to focus on agricultural regions in the Northern Hemisphere. In contrast, phenology

studies of African terrestrial environments are comparatively less well studied, and many locations appear to exhibit larger fluctuations than crops (Cho et al., 2017; Cho and Ramoelo, 2019; Wessels et al., 2004). Mathematical models, such as the logistic curve have typically been used to model the land surface phenology of those environments even though similar mathematical models (e.g., hyperbolic tangent and sine) are effective too (Beck et al., 2006; Zhang et al., 2003; Zhang et al., 2006). This research quantified, for the first time, the phenology of the vegetation around the Skukuza Eddy covariance (EC) flux tower using long-term MISR-HR FAPAR, and confronted the results of multiple models to *in situ* GPP measurements derived from the flux tower.

The suitability of four different parametric double S-shaped models (Gaussian, Hyperbolic Tangent, Logistic, and Sine) to represent the seasonal variability of the productivity of plant canopies despite the presence of missing observations in the MISR-HR FAPAR record was assessed by evaluating their numerical efficiency. The MISR-HR FAPAR and in *situ* GPP for savanna vegetation around the Skukuza EC flux tower were integrated over the course of vegetative seasons to provide a more representative characterisation of biomass accumulation.

The MISR-HR FAPAR derived from optical multi-angular measurements acquired in space provides quasi instantaneous estimates at the time of the satellite overpass while the GPP measurements derived from the Skukuza EC flux tower refer to integrated values throughout the day (expressed in units of gC m^{-2} d^{-1}), which exhibit a very high day-to-day variability, as a result of fluctuations in local conditions, including turbulence. Investigating relations between GPP or biomass accumulation of the same environment from spaceborne and ground-based sensors is complex, but provides a unique opportunity to benchmark phenology models from independent sources of information.

All four parametric models were capable of simulating vegetative seasons, especially when the FAPAR record was well distributed in time. However, differences were noted in the models' efficiency and effectiveness with respect to gaps in the data. The hyperbolic tangent and logistic models were found to generate essentially equivalent traces, as expected since their parameters can be adjusted to match those models exactly. Nevertheless, the former model (which is computationally more expensive) was found to be somewhat less sensitive to the temporal distribution of FAPAR observations during the vegetative season. The Sine model simulated the phenology with the smallest cost function (smallest mismatch between the model and the observed data), but was most sensitive to temporal gaps in the vegetative seasons. Longer gaps in the FAPAR records, especially during the growth phase of the vegetative season, presented the biggest challenge especially for the purpose of

investigating more meaningful comparisons between the model fits and the GPP measurements. However, a general non-linear relation between modelled FAPAR and GPP, as measured by the Skukuza EC flux tower was found. Correlation coefficients between the Skukuza EC flux tower GPP and the estimates were equal to or larger than 0.69 where the inversion models were amply constrained by well-spaced FAPAR records. Other studies have reported similar relations between modelled FAPAR and EC flux tower GPP measurements, but for crop fields (Cheng et al., 2014; Zhang et al., 2014). It was also shown that integrated FAPAR adequately tracks GPP in this environment as long as the latter varies in the range from 0 to 5 gC m^{-2} d^{-1}. However, beyond this upper threshold, the relation between FAPAR and GPP tends to saturate.

In chapter 3, the model inversion procedure was expanded to select, for successive vegetative seasons, the parametric double S-shaped model which yields the smallest mismatch between the model and the observed data. The flexibility of selecting the optimal parametric double S-shaped function delivers a greater number of successful inversions for the vegetative seasons. This line of investigation could be extended by:

- Comparing simulated FAPAR to the GPP estimates derived at other Eddy Covariance flux towers across South Africa to compare biomass accumulation and carbon exchanges between different bioregions (e.g., Malopeni, Agincourt, and Vuwani eddy covariance flux towers).
- Exploring to what extent spatial correlations could be exploited to estimate missing data values (e.g., by kriging) to buttress the temporal modelling approach.

2. Examining the influence of ENSO on the phenology of Lowveld vegetation

Variations in precipitation between years, which influence variations in the amount of green leaf area, seasonal patterns, and soil water availability are regarded as the main drivers of Net Ecosystem Exchange in southern African savannas (Archibald et al., 2009). Progressive climate change poses a threat to these ecosystems. Global climate-carbon model simulations for the African continent under the IPCC SRES-A_2 socio-economic CO_2 emission scenario found that warming over African ecosystems induces a reduction of net ecosystem productivity, which would contribute 38% to the global climate-carbon cycle positive feedback by the end of the 21st century (Friedlingstein et al., 2010). In some regions, fewer but more intense rainfall events are expected with longer intervening dry periods (IPCC, 2007), which would result in significant impacts on vegetation dynamics in savannas, such

as an increase in trees and shrubs in previously open savannas, and limited tree growth in wetter savannas (D'Onofrio et al., 2018; D'Onofrio et al., 2019).

Early investigations in this study examined whether or not linear trends in response to progressive climate change could be observed in the MISR-HR FAPAR, but statistically significant tendencies were not established. This is likely because 20 years' worth of observations may still be insufficient to document the presence of definite trends, but also because large inter-annual fluctuations may mask such trends. The study then shifted to focus on aperiodic climatic fluctuations such as the ENSO which usually occur every 2 to 5 years. ENSO plays a major role in climate and affects different regions differently. The relationship between ENSO and precipitation variability over southern Africa is complex, given internal atmospheric variations and modulations with other irregular oscillations, such as the Indian Ocean Dipole (IOD) (Pomposi et al., 2018). But despite this, the strong relationship between precipitation and El Niño events (ENSO warming phase) over southern Africa during austral summer have been shown to be the leading cause of severe droughts which are detrimental to food security over the region (Yuan et al., 2014).

The influence of ENSO teleconnections on the phenology of southern African ecosystems is understudied even though it has been shown to be the major driver of precipitation variability over the sub-continent on an interannual timescale (Janowiak, 1988, Jury et al., 2004; Philippon et al., 2014). Investigations of the impacts of ENSO periods on the seasonality of rainfall and vegetation phenology have mostly focused on establishing relations at broad spatial scale, typically over oceanic, continental or sub-continental regions (Anyamba and Eastman, 1996; Anyamba et al., 2002; Anyamba et al., 2018; Nicholson and Kim, 1997; Parhi et al., 2016; Philippon et al., 2014; Pomposi et al., 2018).

This study explored the sensitivity of vegetation productivity and precipitation to historical ENSO periods occurring within the last two decades for five sites over the area encompassing the Bushbuckridge local municipality (23°58'52.46" S to 25°11'14.63" S and 30°47'42.14" E to 32°02'00.92" E). The locations of those sites were selected to include various combinations of vegetation and soil units, within both the Kruger National Park (KNP) and the communal rangelands, to gauge the differences between unmanaged and transformed vegetation during ENSO periods. The vegetation units were identified using the national vegetation map published by the South African National Biodiversity Institute (SANBI 2006-2012). The vegetation sites under National Parks management include sites 1 and 2 on granite and basalt Lowveld, respectively. Sampled sites falling outside of National Parks management included site 3 on Legogote sour bushveld, site 4 on granite Lowveld

over communal rangelands, and site 5 on Highveld grassland in the south western corner of the study region, between the northern escarpment and the Lowveld.

To facilitate comparisons with ENSO anomalies, the FAPAR and CHIRPS records were cumulatively aggregated into monthly values. The long-term average was removed from these records to yield departures relative to the typical range of seasonal variability during this period. Regression analyses were performed between the FAPAR/precipitation anomalies and SSTs anomalies as exhibited by the Niño 3.4 index. Lagged correlations revealed when ENSO exerts maximum influence, where the lag and the intensity of the effect were dependent on the site as well as on the severity of ENSO itself. Cumulated FAPAR anomalies were used to examine the impacts of El Niño and La Niña events at each site during different intensities.

Three pairs of sites were found to exhibit aspects with common and differing spatial characteristics. These included site 1 versus site 2, site 1 versus site 4, and site 4 versus site 5. The findings did not include evidence through field campaigns. Tentative ecological explanations were offered, which could prompt further research to confirm the current conjecture.

Site 1 versus Site 2:
Sites 1 and 2 both occur in the Kruger National Park (KNP), but site 1 occurs over granite Lowveld and site 2 occurs over basalt Lowveld. The ENSO phases were found to differentially influence productivity of vegetation occurring in basalt Lowveld and granite Lowveld within the KNP. These two sites exhibited different responses especially during strong La Niña. The inverse texture hypothesis offers a plausible ecological explanation for the differences noted (Noy-Meir, 1974). Site 1 is characterised by sandy soils, which allow water to penetrate to deeper soil layers accessible to tree roots only, and experience less loss of soil moisture to evaporation. Site 2 on the other hand is dominated by a dense herbaceous layer which benefits from the water-retaining properties of the clay soil, but loses more moisture to evaporation (Scholes, 2003). Site 1 yielded fewer increases (decreases) in productivity during La Niña (El Niño) events in comparison, owing to the sandy granite soil which is characterised by more trees. The sharp departures noted in the FAPAR anomalies during peak El Niño and La Niña events support the tree-grass characteristics documented for the basalt and granite soils (Scholes and Archer, 1997). Thus, the impact of ENSO on the productivity of vegetation depends not only on the intensity of the event but also on soil properties such as particle size, density and water holding capacity. These findings also agree with Archibald and Scholes (2007) who demonstrate at a landscape scale how trees have a less variable phenological cycle (within and between years) than grasses.

Site 1 versus Site 4:

Sites 1 and 4 both occur on granite Lowveld, but site 1 is located within the KNP and site 4 over adjacent communal areas. Comparisons between protected and unprotected sites showed that areas whose vegetation is significantly utilised for anthropogenic activities respond quite differently during ENSO phases. In the case of site 4, which included homogenous stands of agricultural fields, plantation forest, and residential areas in communal rangelands, departures in vegetation productivity was less variable during ENSO phases. Comparison of the communal rangelands with adjacent protected areas has shown that the transformed communal areas, whilst characterised by lower height vegetation and more bare ground, can show patterns of higher plant species richness and beta diversity (Shackleton, 2000). The less variable FAPAR anomalies noted at site 4 could be due to cultivated plant species that may be more drought-resistant than the unmanaged vegetation observed in the adjacent protected areas or irrigation practices that complement or compensate for available precipitations.

Site 4 versus Site 5:

Sites 4 and 5 both occur in areas outside of National Parks management, but differ by land use and altitude. Site 5 occurs on the northern escarpment at an altitude of about 1600 m above sea level (Highveld) and contains a mix of grassland and plantation forest whereas site 4 occurs over communal rangelands in the central Lowveld. At site 5, the impacts of El Niño and La Niña phases were opposite to what was observed in Site 2: here, the warming phase of the teleconnection seems to be associated with positive FAPAR anomalies, while cooling phases are generally more associated with negative FAPAR anomalies. Site 5 has a higher mean annual precipitation than site 4 (about 1034 mm and 800 mm, respectively). The orography of site 5, which is located on the escarpment bordering the Lowveld leads to enhanced rainfall. The CHIRPS record may underestimate rainfall amounts at site 5 as it has been previously shown to be sensitive to rainfall induced by orographic lifting. Thus, the negative FAPAR anomalies noted at site 5 during the La Niña phases could indicate oversaturated soils conditions, which would lead to a decline in the vegetation productivity of that site.

The relationships between ENSO, precipitation and FAPAR suggest that the sequence of intensities for peak El Niño and La Niña events may be important ecologically, with the FAPAR exhibiting a substantially stronger and more significant ($p < 0.05$) relationship with ENSO than precipitation. Broad scale studies have characterised the effects that ENSO has on vegetation productivity over southern Africa. But, the findings offered here show that such intricate connections between climate fluctuations and vegetation dynamics are observable at much more local scales. The findings complement those which observe a substantially

stronger relationship between ENSO and vegetation productivity than between ENSO and precipitation over the southern African region (Anyamba et al., 2018), with the exception that continental scale investigations have used the NDVI as a proxy for vegetation productivity whereas the FAPAR was used in this instance, and at a much more local scale.

A strong positive relation was observed between the integrated FAPAR and accumulated precipitation at all 5 sites, both during the growing and the senescence phases, and for the three ENSO periods considered. ENSO appears to differentially influence the productivity of vegetation on the various sites during the growing phase of the vegetative season, but this relation appears much more homogeneous during the senescence phase. A continental-scale phenological analysis of Africa suggests that the rainy season onset precedes and is an effective predictor of the growing season onset for grass species, but woody species generally green-up before the onset of the rainy season and have a variable delayed senescence period after the rainy season likely due to potential groundwater use by relatively deep roots or stem-water reserve (Guan et al., 2014).

3. Overall conclusion

The relation between temporally-integrated MISR-HR FAPAR and GPP, as measured from the Skukuza EC flux tower, appears to be promising for monitoring plant canopy productivity in environments over the Lowveld. FAPAR is better correlated with ENSO than the CHIRPS precipitations. The influence of ENSO on vegetation was shown to be quite variable spatially, with opposite effects on different ecosystems within the study region. These ecosystems are not only sensitive to the particular sequence and relative strengths of the El Niño and La Niña phases, but the severity of the impact appears to be dependent on the physical properties of the site (soils, altitude and land use), and the relations appear more distinguished when ecophysiological properties are attributed to a dominant functional plant type than a mix of functional plant types (e.g., herbaceous versus woody vegetation). While ENSO fluctuations are themselves not currently predictable, they may nevertheless offer some degree of predictability regarding their subsequent effects, since their impact on the productivity of vegetation tends to be delayed by weeks to months after those events.

The relations offered here may not be extremely strong, or corroborated by field campaigns, but hint that monitoring ENSO could lead to some degree of useful early warning for agricultural production systems within a properly understood statistical framework. Effective policymaking in the Bushbuckridge local municipality should not be applied uniformly at municipal or regional scales but should instead consider the response modes of the diverse ecosystems at local scales and consider the protection status of areas. Future efforts should direct the findings to a more practical setting where it can be established if this information

can benefit policymakers in environmental management. These could be but are not limited to improving targeted relief efforts during droughts or flooding that occur after extreme ENSO conditions, and guiding risk mitigation and conservation strategies.

COMBINED REFERENCES

Acocks, J.P.H. (1988) Veld types of South Africa. (Third edition) Memoirs of the Botanical Survey of South Africa. No. *57*, pp.1-146,

Adole, T., Dash, J., and Atkinson, P.M. (2016) A systematic review of vegetation phenology in Africa. Ecological Informatics, no. 34, pp.117–128. doi:10.1016/j.ecoinf.2016.05.004.

Adole, T., Dash, J., Rodriguez-Galiano, V. and Atkinson, P.M. (2019) Photoperiod controls vegetation phenology across Africa. Communications Biology, vol. 2, no. 1, pp.1-13, doi: 10.1038/s42003-019-0636-7.

Alessandri, A., Catalano, F., De Felice, M., Van Den Hurk, B., Reyes, F.D., Boussetta, S., Balsamo, G. and Miller, P.A. (2017). Multi-scale enhancement of climate prediction over land by increasing the model sensitivity to vegetation variability in EC-Earth. Climate Dynamics, vol, 49, no.4, pp. 1215-1237. doi: 10.1007/s00382-016-3372-4.

Anav, A., Friedlingstein, P., Beer, C., Ciais, P., Harper, A., Jones, C., Murray-Tortarolo, G., Papale, D., Parazoo, N.C., Peylin, P. and Piao, S. (2015) Spatiotemporal patterns of terrestrial gross primary production: A review. Reviews of Geophysics, vol. 53, no. 3, pp.785-818, doi: 10.1002/2015RG000483.

Anderson, K., Ryan, B., Sonntag, W., Kavvada, A. and Friedl, L. (2017) Earth observation in service of the 2030 Agenda for Sustainable Development. Geo-spatial Information Science, vol. 20, no. 2, pp.77-96. doi: 10.1080/10095020.2017.1333230.

Anderson, T.M., White, S., Davis, B., Erhardt, R., Palmer, M., Swanson, A., Kosmala, M. and Packer, C. (2016) The spatial distribution of African savannah herbivores: species associations and habitat occupancy in a landscape context. Philosophical Transactions of the Royal Society B: Biological Sciences, vol. 371, no.1703, p.20150314. doi: 10.1098/rstb.2015.0314.

Annegarn, H.J., Otter, L., Swap, R.J. and Scholes, R.J. (2002) Southern Africa's ecosystem in a test-tube: a perspective on the Southern African Regional Science Initiative (SAFARI 2000): commentary. South African Journal of Science, vol. 98, no. 3-4, pp.111-113, available from: https://hdl.handle.net/10520/EJC97462.

Anyamba, A. and Eastman, J.R. (1996) Interannual variability of NDVI over Africa and its relation to El Niño/Southern Oscillation. Remote Sensing, vol. 17, no. 13, pp. 2533-2548. doi: 10.1080/01431169608949091.

Anyamba, A., Glennie, E. and Small, J. (2018). Teleconnections and interannual transitions as observed in African vegetation: 2015–2017. Remote Sensing, vol.10, no. 7, p.1038. doi: 10.3390/rs10071038.

Anyamba, A., Tucker, C.J. and Mahoney, R. (2002). From El Niño to La Niña: Vegetation response patterns over east and southern Africa during the 1997–2000 period. Journal of Climate, vol. 15, no. 21, pp. 3096-3103. doi: 10.1175/1520-0442(2002)015<3096:FENOTL>2.0.CO;2

Archer, E., Engelbrecht, F., Hänsler, A., Landman, W., Tadross, M. and Helmschrot, J. (2018). Seasonal prediction and regional climate projections for southern Africa In: Climate change and adaptive land management in southern Africa - assessments, changes, challenges, and solutions (ed. by Revermann, R., Krewenka, KM, Schmiedel, U., Olwoch, JM, Helmschrot, J. and Jürgens, N.), pp. 14-21, Biodiversity & Ecology , 6 , Göttingen: Klaus Hess Publishers. doi: 10.7809 / be.00296

Archer, S.R., Andersen, E.M., Predick, K.I., Schwinning, S., Steidl, R.J. and Woods, S.R., (2017) Woody plant encroachment: causes and consequences. In: Briske D. (Eds.) Rangeland Systems. Springer Series on Environmental Management. Cham: Springer. doi: 10.1007/978-3-319-46709-2_2.

Archibald, S. (2016) Managing the human component of fire regimes: lessons from Africa. Philosophical Transactions of the Royal Society B: Biological Sciences, vol. 371, no. 1696, pp. 1 – 11, doi: 10.1098/rstb.2015.0346.

Archibald, S. and Scholes, R.J. (2007) Leaf green-up in a semi-arid African savanna - separating tree and grass responses to environmental cues. Journal of Vegetation Science, Vol. 18, pp. 583-594, doi: 10.1111/j.1654-1103.2007.tb02572.x.

Archibald, S., Bond, W.J., Stock, W.D. and Fairbanks, D.H.K. (2005) Shaping the landscape: fire–grazer interactions in an African savanna. Ecological Applications, vol. 15, no.1, pp. 96-109. doi: 10.1890/03-5210.

Archibald, S., Nickless, A., Govender, N., Scholes, R.J. and Lehsten, V. (2010) Climate and the inter-annual variability of fire in southern Africa: a meta-analysis using long-term field data and satellite-derived burnt area data. Global Ecology and Biogeography, vol. 19, no. 6, pp. 794-809.

Archibald, S., Roy, D.P., van Wilgen, B.W. and Scholes, R.J. (2009) What limits fire? An examination of drivers of burnt area in Southern Africa. Global Change Biology, vol. 15, no. 3, pp. 613-630. doi: 10.1111/j.1365-2486.2008.01754.x

Archibald, S., Staver, A.C. and Levin, S.A. (2012) Evolution of human-driven fire regimes in Africa. Proceedings of the National Academy of Sciences, vol. 109, no. 3, pp. 847-852. doi: 10.1073/pnas.1118648109

Asner, G P. (2000) Contribution of multi-view angle remote sensing to land-surface and biogeochemical research. Remote Sensing Reviews, no. 18. pp.137–165.

Baldocchi, D.D. (2003) Assessing the eddy covariance technique for evaluating carbon dioxide exchange rates of ecosystems: past, present and future. Global Change Biology, no. 9, pp. 479–492. doi: 10.1046/j.1365-2486.2003.00629.x.

Baldocchi, D.D. (2008) 'Breathing' of the terrestrial biosphere: lessons learned from a global network of carbon dioxide flux measurement systems. Australian Journal of Botany, no. 56, pp.1–26. doi: 10.1071/BT07151.49.

Baldwin, D. G., and Coakley, J. A. (1991) Consistency of Earth Radiation Budget Experiment bidirectional models and the observed anisotropy of reflected sunlight, Journal of Geophysical Research, vol. 96, no. D3, pp. 5195–5207. doi: 10.1029/90JD02414.

Barkstrom, B. R., and Smith, G. L. (1986) The Earth Radiation Budget Experiment: Science and implementation, Rev. Geophys., vol. 24, no. 2, pp. 379– 390. doi:10.1029/RG024i002p00379.

Beck, H.E., McVicar, T.R., van Dijk, A.I., Schellekens, J., de Jeu, R.A. and Bruijnzeel, L.A. (2011) Global evaluation of four AVHRR–NDVI data sets: Intercomparison and assessment against Landsat imagery. Remote Sensing of Environment, vol. 115, no. 10, pp. 2547-2563. doi: 10.1016/j.rse.2011.05.012.

Beck, H.E., Zimmermann, N.E., McVicar, T.R., Vergopolan, N., Berg, A. and Wood, E.F. (2018) Present and future Köppen-Geiger climate classification maps at 1-km resolution. Scientific Data, vol. 5, no. 1, pp.1-12. doi: 10.1038/sdata.2018.214.

Beck, P.S., Atzberger, C., Høgda, K.A., Johansen, B. and Skidmore, A.K. (2006) Improved monitoring of vegetation dynamics at very high latitudes: A new method using MODIS NDVI. Remote Sensing of Environment, vol. 100, no. 3, pp. 321-334. doi: 10.1016/j.rse.2005.10.021

Béland, M. and Fournier, R. (2008, July.)Extracting Savanna Tree Structure Parameters from Multi-Angular Remote Sensing. In IGARSS 2008-2008 IEEE International Geoscience and Remote Sensing Symposium. Vol. 3, pp. III-306. IEEE. doi:10.1109/IGARSS.2008.4779344

Belay, A.S., Fenta, A.A., Yenehun, A., Nigate, F., Tilahun, S.A., Moges, M.M., Dessie, M., Adgo, E., Nyssen, J., Chen, M. and Griensven, A.V. (2019) Evaluation and Application of Multi-Source Satellite Rainfall Product CHIRPS to Assess Spatio-Temporal Rainfall Variability on Data-Sparse Western Margins of Ethiopian Highlands. Remote Sensing vol. 11, no. 22, pp. 2688. doi: 10.3390/rs11222688

Bojinski, S., M. M. Verstraete, T. C. Peterson, Richter, C., Simmons, A., and Zemp, M. (2014) The concept of Essential Climate Variables in support of climate research, applications, and policy, Bulletin of the American Meteorological Society, vol. 95, pp.1431–1443, doi: 10.1175/BAMS-D-13-00047.1.

Bonan, G.B. (1997) Effects of Land Use on the Climate of the United States. Climatic Change, vol. 37, pp. 449–486. doi:10.1023/A:1005305708775

Bond, W. J., and Midgley, G. F. (2012) Carbon dioxide and the uneasy interactions of trees and savannah grasses. Philosophical Transactions of the Royal Society of London. Series B, Biological Sciences, vol. 367, no. 1588, pp. 601–612. doi:10.1098/rstb.2011.0182

Bond, W.J. (2008) What limits trees in C_4 grasslands and savannas? Annual Review of Ecology, Evolution, and Systematics, vol. 39, pp. 641-659.

Bond, W.J., Woodward, F.I. and Midgley, G.F. (2005) The global distribution of ecosystems in a world without fire. New Phytologist, vol. 165, no. 2, pp. 525-538. doi: 10.1111/j.1469-8137.2004.01252.x

Bounoua, L., Cooatz, G. J., Los, S. O., Sellers, P. J., Dazlich, D. A., Tucker, C. J., and Randall, D. A. (2000). Sensitivity of climate to changes in NDVI. Journal of Climate, vol. 13, pp. 2277–2292.

Bounoua, L., DeFries, R., Collatz, G.J., Sellers, P. and Khan, H. (2002) Effects of land cover conversion on surface climate. Climatic Change, vol. 52, no. 1-2, pp. 29-64. doi:10.1023/A:1013051420309

Buitenwerf, R., Bond, W.J., Stevens, N. and Trollope, W.S.W. (2012) Increased tree densities in South African savannas: >50 years of data suggests CO_2 as a driver. Global Change Biology, vol. 18, no.2, pp. 675-684. doi: 10.1111/j.1365-2486.2011.02561.x

Caparros-Santiago, J.A., Rodriguez-Galiano, V. and Dash, J. (2021) Land surface phenology as indicator of global terrestrial ecosystem dynamics: A systematic review. ISPRS Journal of Photogrammetry and Remote Sensing, vol. 171, pp.330-347, doi: 10.1016/j.isprsjprs.2020.11.019.

Chandrasekhar, S. (1960) Radiative Transfer. New York: Dover.

Cheng, Y.B., Zhang, Q., Lyapustin, A.I., Wang, Y. and Middleton, E.M. (2014) Impacts of light use efficiency and fPAR parameterization on gross primary production modeling. Agricultural and Forest Meteorology, vol.189, pp.187-197. doi: 10.1016/j.agrformet.2014.01.006

Chernetskiy, M., Gómez-Dans, J., Gobron, N., Morgan, O., Lewis, P., Truckenbrodt, S., and Schmullius, C. (2017) Estimation of FAPAR over Croplands Using MISR Data and the Earth Observation Land Data Assimilation System (EO-LDAS). Remote Sensing, vol. 9, pp.1–30. doi: 10.3390/rs9070656.

Cho, M.A. and Ramoelo, A. (2019) Optimal dates for assessing long-term changes in tree-cover in the semi-arid biomes of South Africa using MODIS NDVI time series (2001–2018). International Journal of Applied Earth Observation and Geoinformation, vol. 81, pp. 27-36. doi: 10.1016/j.jag.2019.05.014.

Cho, M.A., Mathieu, R., Asner, G.P., Naidoo, L., van Aardt, J., Ramoelo, A., Debba, P., Wessels, K., Main, R., Smit, I.P.J., and Erasmus, B. (2012) Mapping tree species composition in South African savannas using an integrated airborne spectral and LiDAR system. Remote Sensing of Environment, vol. 125, pp. 214–226. doi:10.1016/j.rse.2012.07.010.

Cho, M.A., Ramoelo, A. and Dziba, L. (2017) Response of land surface phenology to variation in tree cover during green-up and senescence periods in the semi-arid savanna of Southern Africa. Remote Sensing, vol. 9, no. 7, pp. 689. doi: 10.3390/rs9070689.

Chopping, M., North, M., Chen, J., Schaaf, C.B., Blair, J.B., Martonchik, J.V. and Bull, M.A. (2012) Forest canopy cover and height from MISR in topographically complex southwestern US landscapes assessed with high quality reference data. IEEE Journal of Selected Topics in Applied Earth Observations and Remote Sensing, vol. 5, no. 1, pp. 44-58. doi: 10.1109/JSTARS.2012.2184270.

Clerici, M., Vossbeck, M., Pinty, B., Kaminski, T., Taberner, M., Lavergne, T., and Andredakis, I. (2010) Consolidating the Two-Stream Inversion Package (JRC-TIP) to Retrieve Land Surface Parameters From Albedo Products. IEEE Journal of Selected Topics in Applied Earth Observations and Remote Sensing, vol. 3, pp. 286–295. doi:10.1109/JSTARS.2010.2046626.

Coetzer, K.L., Erasmus, B.F.N., Witkowski, E.T.F., and Bachoo, A.K. (2010) Land-cover change in the Kruger to Canyons Biosphere Reserve (1993–2006): A first step towards creating a conservation plan for the subregion. South African Journal of Science, vol. 106, pp. 1–10. doi: 10.4102/sajs.v106i7/8.221.

Coetzer, K.L., Erasmus, B.F.N., Witkowski, E.T.F., and Reyers, B. (2013) The Race for Space: Tracking Land-Cover Transformation in a Socio-ecological Landscape, South Africa. Environmental Management, vol. 52, pp. 595–611. doi: 10.1007/s00267-013-0094-9.

Colgan, M.S., Asner, G.P., Levick, S.R., Martin, R.E. and Chadwick, O.A. (2012) Topo-edaphic controls over woody plant biomass in South African savannas. Biogeosciences, vol. 9, pp.1809-1821. doi: 10.5194/bg-9-1809-2012.

D'Odorico, P., Gonsamo, A., Pinty, B., Gobron, N., Coops, N., Mendez, E., and Schaepman, M.E. (2014) Intercomparison of fraction of absorbed photosynthetically active radiation products derived from satellite data over Europe. Remote Sensing of Environment, vol. 142, pp.142–154. doi: 10.1016/j.rse.2013.12.005.

D'Onofrio, D., Sweeney, L., von Hardenberg, J. et al. (2019) Grass and tree cover responses to intra-seasonal rainfall variability vary along a rainfall gradient in African tropical grassy biomes. Scientific Reports, vol. 9, pp. 2334. doi: 10.1038/s41598-019-38933-9.

Danaher, T. J. (2002, September). An empirical BRDF correction for Landsat TM and ETM+ imagery. Proceedings of the 11th Australasian Remote Sensing and Photogrammetry Conference, Brisbane, Australia.

Dash, J. and Curran, P. J. (2004) The MERIS Terrestrial Chlorophyll Index. International Journal of Remote Sensing, vol. 25, pp. 5003-5013, doi: 10.1080/0143116042000274015.

De Lemos, H., Verstraete, M.M. and Scholes, M. (2020) Parametric Models to Characterize the Phenology of the Lowveld Savanna at Skukuza, South Africa. Remote Sensing, vol. 12, no. 23, pp. 3927. doi: 10.3390/rs12233927.

Dickinson, R.E. and Henderson-Sellers, A. (1988) Modelling tropical deforestation: A study of GCM land-surface parametrizations. Q.J.R. Meteorol. Soc., vol. 114, pp.439-462. doi:10.1002/qj.49711448009.

Dieppois, B., Rouault, M. and New, M. (2015) The impact of ENSO on Southern African rainfall in CMIP5 ocean atmosphere coupled climate models. Climate Dynamics, vol. 45, no.9, pp. 2425-2442. doi: 10.1007/s00382-015-2480-x.

Diner, D.J., Asner, G.P., Davies, R., Knyazikhin, Y., Muller, J.P., Nolin, A.W., Pinty, B., Schaaf, C.B., and Stroeve, J., 1999. New Directions in Earth Observing: Scientific Applications of Multiangle Remote Sensing. Bulletin of the American Meteorological Society, no. 80, pp.2209–2228. doi: 10.1175/1520-0477(1999)080<2209:NDIEOS>2.0.CO;2.

D'Onofrio, D, von Hardenberg, J, and Baudena, M. (2018) Not only trees: Grasses determine African tropical biome distributions via water limitation and fire. Global Ecol Biogeogr, vol. 27. pp. 714– 725. doi:10.1111/geb.12735.

Dovie, D.B., Witkowski, E.T.F. and Shackleton, C.M. (2004) The fuelwood crisis in southern Africa—relating fuelwood use to livelihoods in a rural village. GeoJournal, vol. 60, no. 2, pp.123-133. doi: 10.1023/B:GEJO.0000033597.34013.9f.

Dzerefos, C.M., Witkowski, E.T.F. and Shackleton, C.M. (2003) Host-preference and density of woodrose-forming mistletoes (Loranthaceae) on savanna vegetation, South Africa. Plant Ecology, vol. 167, no. 1, pp.163-177. doi: 10.1023/A:1023991514968.

Engelbrecht, C.J. and Engelbrecht, F.A. (2016) Shifts in Köppen-Geiger climate zones over southern Africa in relation to key global temperature goals. Theoretical and Applied Climatology, vol. 123, no. 1-2, pp. 247-261. doi: 10.1007/s00704-014-1354-1.

Engelbrecht, F., Adegoke, J., Bopape, M.J., Naidoo, M., Garland, R., Thatcher, M., McGregor, J., Katzfey, J., Werner, M., Ichoku, C. and Gatebe, C. (2015) Projections of rapidly rising surface temperatures over Africa under low mitigation. Environmental Research Letters, vol. 10, no. 8, pp. 1-12. doi:10.1088/1748-9326/10/8/085004.

Engelsen, O., Pinty, B., Verstraete, M.M., and Martonchik, J.V. (1996) Parametric Bidirectional Reflectance Factor Models: Evaluation, Improvements and Applications. Technical Report EUR 16426 EN, Ispra: EC Joint Research Centre.

Erasmus, B.F.N., Coetzer, K., Mambo, J., Archer, E.R.M., Fisher, J.T., and Asner, G.P. (2011) Environmental change in Bushbuckridge. In Observation on Environmental Change in South Africa. Stellenbosch: SunMedia Publishing, pp. 1–5.

Fairbairn, M.B. (2005) Planetary photometry: The Lommel-Seeliger law. Journal of the Royal Astronomical Society of Canada, vol. 99, no. 3, pp. 92.

Fensholt, R., Langanke, T., Rasmussen, K., Reenberg, A., Prince, S.D., Tucker, C., Scholes, R.J., Le, Q.B., Bondeau, A., Eastman, R. and Epstein, H. (2012) Greenness in semi-arid areas across the globe 1981–2007—an Earth Observing Satellite based analysis of trends and drivers. Remote Sensing of Environment, vol.121, pp.144-158. doi: 10.1016/j.rse.2012.01.017.

Fensholt, R., Sandholt, I. and Rasmussen, M.S. (2004) Evaluation of MODIS LAI, fAPAR and the relation between fAPAR and NDVI in a semi-arid environment using in situ measurements. Remote Sensing of Environment, vol. 91, no. 3-4, pp. 490-507. doi: 10.1016/j.rse.2004.04.009.

FEWS NET (Famine Early Warning Systems Network), 2020. Data Library, acquired from https://earlywarning.usgs.gov/fews/datadownloads/Global/CHIRPS/., last accessed on 21 December, 2020.

Fisher, J., Erasmus, B.F.N., Witkowski, E.T.F., Van Aardt, J., Asner, G., Kennedy-Bowdoin, T., Knapp, D., Mathieu, R. and Wessels, K. (2009) Three-dimensional woody vegetation structure across different land-use types and land-use intensities in a semi-arid savanna, In: International Geoscience and Remote Sensing Symposium (IGARSS), July 2009, Cape Town. Vol. 2, pp. 198-201. doi: 10.1109/IGARSS.2009.5418040.

Fisher, J.T., Witkowski, E.T.F., Erasmus, B.F.N., Mograbi, P.J., Asner, G.P.; van Aardt, J.A.N., Wessels, K.J., and Mathieu, R. (2015). What lies beneath: detecting sub-canopy changes in savanna woodlands using a three-dimensional classification method. Applied Vegetation Science, vol. 18, pp. 528–540. doi: 10.1111/avsc.12160.

Fisher, J.T., Witkowski, E.T.F., Erasmus, B.F.N., van Aardt, J.A.N., Asner, G.P., Wessels, K.J., and Mathieu, R. (2012) Human-modified landscapes: patterns of fine-scale woody vegetation structure in communal savannah rangelands. Environmental Conservation, vol. 39, pp.72–82. doi:10.1017/S0376892911000592.

Friedlingstein, P., Cadule, P., Piao, S.L., Ciais, P. and Sitch, S. (2010) The African contribution to the global climate-carbon cycle feedback of the 21st century. Biogeosciences, vol. 7, no. 2, pp. 513–519. doi: 10.5194/bg-7-513-2010.

Friend, A.D., Arneth, A., Kiang, N.Y., Lomas, M., Ogée, J., Rödenbeck, C., Running, S.W., Santaren, J.D., Sitch, S., Viovy, N., Woodward, F.I., and Zaehle, S. (2007) FLUXNET and modelling the global carbon cycle. Global Change Biology, vol. 13, pp. 610–633. doi:10.1111/j.1365-2486.2006.01223.x.

Fritz S. (2014) Global Earth Observation System of Systems (GEOSS). In: Njoku E.G. (Eds.) Encyclopedia of Remote Sensing. Encyclopedia of Earth Sciences Series. Springer, New York, NY. doi:10.1007/978-0-387-36699-9_57.

Funk, C., Peterson, P., Landsfeld, M., Pedreros, D., Verdin, J., Shukla, S., Husak, G., Rowland, J., Harrison, L., Hoell, A. and Michaelsen, J. (2015) The climate hazards infrared precipitation with stations—a new environmental record for monitoring extremes. Scientific Data, vol. 2, no. 1, pp.1-21. doi: 10.1038/sdata.2015.66.

Funk, C.C., Peterson, P.J., Landsfeld, M.F., Pedreros, D.H., Verdin, J.P., Rowland, J.D., Romero, B.E., Husak, G.J., Michaelsen, J.C. and Verdin, A.P. (2014) A quasi-global precipitation time series for drought monitoring. US Geological Survey Data Series, vol. 832, no. 4, pp.1-12. doi: 10.3133/ds832.

GEO community., n.d. Group on Earth Observations, accessed 12 September 2017, < https://www.earthobservations.org/geo_community.php>.

Gerstl, S.A.W. and Simmer, C. (1986) Radiation physics and modelling for off-nadir satellite-sensing of non-Lambertian surfaces. Remote Sensing of Environment, vol. 20, no. 1, pp.1-29. doi: 10.1016/0034-4257(86)90011-8.

Gobron, N. and Verstraete, M.M. (2009) Fraction of Absorbed Photosynthetically Active Radiation (FAPAR); Technical Report T10–GTOS 65; Global Terrestrial Observing System (GTOS): Rome, Italy, 2009.

Gobron, N., Marioni, M., Robustelli, M. and Vermote, E. (2019) Can We Use the QA4ECV Black-sky Fraction of Absorbed Photosynthetically Active Radiation (FAPAR) using AVHRR Surface Reflectance to Assess Terrestrial Global Change? Remote Sensing, vol. 11, no. 24, pp. 3055. doi: 10.3390/rs11243055.

Gobron, N., Pinty, B., Aussedat, O., Chen, J.M., Cohen, W.B., Fensholt, R., Gond, V., Huemmrich, K.F., Lavergne, T., Mélin, F. and Privette, J.L. (2006) Evaluation of fraction of absorbed photosynthetically active radiation products for different canopy radiation transfer regimes: Methodology and results using Joint Research Center products derived from SeaWiFS against ground-based estimations. Journal of Geophysical Research: Atmospheres, vol. 111, no. D13. doi:10.1029/2005JD006511.

Gobron, N., Pinty, B., Mélin, F., Taberner, M., Verstraete, M.M., Robustelli, M. and Widlowski, J.L. (2007) Evaluation of the MERIS/ENVISAT FAPAR product. Advances in Space Research, vol. 39, no. 1, pp.105-115. doi: 10.1016/j.asr.2006.02.048.

Gobron, N., Pinty, B., Verstraete, M.M., Widlowski, J.L., and Diner, D.J. (2002) Uniqueness of Multiangular Measurements—Part II: Joint Retrieval of Vegetation Structure and Photosynthetic Activity From MISR. IEEE Transactions on Geoscience and Remote Sensing, vol. 40, pp.1574–1592. doi:10.1109/TGRS.2002.801147.

Goddard, L. and Dilley, M. (2005) El Niño: catastrophe or opportunity. Journal of Climate, vol. 18, no. 5, pp. 651-665. doi: 10.7916/D8X34XDH.

Good, S.P. and Caylor, K.K. (2011) Climatological determinants of woody cover in Africa. Proceedings of the National Academy of Sciences, vol. 108, no. 12, pp. 4902-4907. doi: 10.1073/pnas.1013100108.

Gough, C. M. (2011) Terrestrial Primary Production: Fuel for Life. Nature Education Knowledge, vol. 3, no. 10, pp. 28.

Govender, N, Trollope, W.S.W, Wilgen, B.R. (2006) The effect of fire season, fire frequency, rainfall and management on fire intensity in savanna vegetation in South Africa. Journal of Applied Ecology, vol. 43, pp.748-758. doi: 10.1111/j.1365-2664.2006.01184.x

Grace, J., José, J.S., Meir, P., Miranda, H.S. and Montes, R.A. (2006) Productivity and carbon fluxes of tropical savannas. Journal of Biogeography, vol. 33, no. 3, pp. 387-400. doi: 10.1111/j.1365-2699.2005.01448.x.

Gray, E.F. and Bond, W.J., 2015. Soil nutrients in an African forest/savanna mosaic: drivers or driven?. South African Journal of Botany, vol. 101, pp.66-72. doi: 10.1016/j.sajb.2015.06.003.

Guan, K., Wood, E.F., Medvigy, D., Kimball, J., Pan, M., Caylor, K.K., Sheffield, J., Xu, X. and Jones, M.O. (2014) Terrestrial hydrological controls on land surface phenology of African savannas and woodlands. Journal of Geophysical Research: Biogeosciences, vol. 119, no. 8, pp.1652-1669. doi: 10.3390/rs9070689.

Hapke, B. (1981) Bidirectional reflectance spectroscopy: 1. Theory. Journal of Geophysical Research: Solid Earth, vol. 86, no. B4, pp. 3039-3054. doi: 10.1029/JB086iB04p03039.

Helm, C.V. and Witkowski, E.T.F. (2012) Characterising wide spatial variation in population size structure of a keystone African savanna tree. Forest Ecology and Management, vol. 263, pp.175-188. doi: 10.1016/j.foreco.2011.09.024.

Hester, A.J., Scogings, P.F. and Trollope, W.S. (2006) Long-term impacts of goat browsing on bush-clump dynamics in a semi-arid subtropical savanna. Plant Ecology, vol. 183, no. 2, pp. 277-290. doi: 10.1007/s11258-005-9039-6.

Higgins, S.I. and Scheiter, S. (2012) Atmospheric CO_2 forces abrupt vegetation shifts locally, but not globally. Nature, vol. 488, no. 7410, pp. 209-212. doi: 10.1038/nature11238.

Higgins, S.I., Bond, W.J. and Trollope, W.S. (2000) Fire, resprouting and variability: a recipe for grass–tree coexistence in savanna. Journal of Ecology, vol. 88, no. 2, pp. 213-229. doi: 10.1046/j.1365-2745.2000.00435.x.

Higgins, S.I., Shackleton, C.M. and Robinson, E.R. (1999) Changes in woody community structure and composition under contrasting land use systems in a semi-arid savanna, South Africa. Journal of Biogeography, vol. 26, no. 3, pp.619-627. doi: 10.1046/j.1365-2699.1999.t01-1-00317.x.

Hoegh-Guldberg, O., D. Taylor, J.M., Bindi, M., Brown, S., Camilloni, I., Diedhiou, A., Djalante, R., Ebi, K.L., Engelbrecht, F., Guiot, J., Hijioka, Y., Mehrotra, S., Payne, A., Seneviratne, S.L., Thomas, A., Warren, R. and Zhou, G. (2018) Impacts of 1.5ºC Global Warming on Natural and Human Systems. In: Global Warming of 1.5°C. An IPCC Special Report on the impacts of global warming of 1.5°C above pre-industrial levels and related global greenhouse gas emission pathways, in the context of strengthening the global response to the threat of climate change, sustainable development, and efforts to eradicate poverty [Masson-Delmotte, V., P. et al. (Eds.)]. In Press.

Hoek van Dijke, A.J., Mallick, K., Schlerf, M., Machwitz, M., Herold, M. and Teuling, A.J. (2020) Examining the link between vegetation leaf area and land–atmosphere exchange of water, energy, and carbon fluxes using FLUXNET data. Biogeosciences, vol. 17, no. 17, pp. 4443-4457. doi: 10.5194/bg-2020-50.

Hoffman, M.T., Rohde, R.F. and Gillson, L. (2019) Rethinking catastrophe? Historical trajectories and modelled future vegetation change in southern Africa. Anthropocene, vol. 25, pp.100189. doi: 10.1016/j.ancene.2018.12.003

Huang, B., Thorne, P.W., Banzon, V.F., Boyer, T., Chepurin, G., Lawrimore, J.H., Menne, M.J., Smith, T.M., Vose, R.S. and Zhang, H.M. (2017) Extended reconstructed sea surface temperature, version 5 (ERSSTv5): upgrades, validations, and intercomparisons. Journal of Climate, vol. 30, no. 20, pp. 8179-8205. doi: 10.1175/JCLI-D-16-0836.1.

Huber, S., Koetz, B., Psomas, A., Kneubuehler, M., and Schopfer, J.T. (2010) Impact of multiangular information on empirical models to estimate canopy nitrogen concentration in mixed forest. Journal of Applied Remote Sensing, vol. 4, no. 1, pp. 043530. doi: 10.1117/1.3435334.

Huete, A., Didan, K., Miura, T., Rodriguez, E.P., Gao, X. and Ferreira, L.G. (2002) Overview of the radiometric and biophysical performance of the MODIS vegetation indices. Remote Sensing of Environment, vol. 83, no. 1-2, pp.195-213, doi: 10.1016/S0034-4257(02)00096-2.

Huete, A.R. (1988) A soil-adjusted vegetation index (SAVI). Remote Sensing of Environment, vol. 25, no. 3, pp.295-309, doi: 10.1016/0034-4257(88)90106-X.

Huffman, G.J., Adler, R.F., Bolvin, D.T. and Nelkin, E.J. (2010) The TRMM Multi-Satellite Precipitation Analysis (TMPA). In: Gebremichael M., Hossain F. (Eds.) Satellite Rainfall Applications for Surface Hydrology. Dordrecht: Springer. doi: 10.1007/978-90-481-2915-7_1.

Huffman, G.J., Bolvin, D.T., Nelkin, E.J., Wolff, D.B., Adler, R.F., Gu, G., Hong, Y., Bowman, K.P. and Stocker, E.F. (2007) The TRMM Multisatellite Precipitation Analysis (TMPA): Quasi-global, multiyear, combined-sensor precipitation estimates at fine scales. Journal of Hydrometeorology, vol. 8, no. 1, pp. 38-55. doi: 10.1175/JHM560.1.

Intergovernmental Panel on Climate Change (IPCC) (2007) Climate Change 2007: The Physical Science Basis. Summary for Policymakers. New York: Cambridge University Press.

Jacobowitz, H., Soule, H. V., Kyle, H. L., and House, F. B. (1984) The Earth Radiation Budget (ERB) Experiment: An overview, Journal of Geophysical Research, vol. 89, no. D4, pp. 5021– 5038, doi: 10.1029/JD089iD04p05021.

Janowiak, J.E. (1988) An investigation of interannual rainfall variability in Africa. Journal of Climate, vol. 1, no. 3, pp. 240-255. doi: 10.1175/1520-0442(1988)001<0240:aioirv>2.0.co;2.

Janowiak, J.E., Joyce, R.J. and Yarosh, Y. (2001) A real-time global half-hourly pixel-resolution infrared dataset and its applications. Bulletin of the American Meteorological Society, vol. 82, no. 2, pp. 205-218. doi: 10.1175/1520-0477(2001)082<0205:ARTGHH>2.3.CO;2.

Janssens, I.A., Freibauer, A., Ciais, P., Smith, P., Nabuurs, G.J., Folberth, G., Schlamadinger, B., Hutjes, R.W., Ceulemans, R., Schulze, E.D. and Valentini, R. (2003) Europe's terrestrial biosphere absorbs 7 to 12% of European anthropogenic CO2 emissions. Science, vol.300, pp.1538-1542, doi: 10.1126/science.1083592.

Joiner, J., Yoshida, Y., Zhang, Y., Duveiller, G., Jung, M., Lyapustin, A., Wang, Y. and Tucker, C.J. (2018) Estimation of terrestrial global gross primary production (GPP) with satellite data-driven models and eddy covariance flux data. Remote Sensing, vol. 10, no. 9, p.1346, doi: 10.3390/rs10091346.

Jones, P. D., Lister, D. H., Osborn, T. J., Harpham, C., Salmon, M., and Morice, C. P. (2012) Hemispheric and large-scale land-surface air temperature variations: An extensive revision and an update to 2010, J. Geophys. Res., vol. 117, no. D05127, doi:10.1029/2011JD017139.Jupp, D.L. and Walker, J. (1997) Detecting structural and growth changes in woodlands and forests: The challenge for remote sensing and the role of geometric-optical modelling. In The Use of Remote Sensing in the Modeling of Forest Productivity (pp. 75-108). Dordrecht: Springer.

Jury, M.R., White, W.B. and Reason, C.J. (2004) Modelling the dominant climate signals around southern Africa. Climate Dynamics, vol. 23, no. 7-8, pp. 717-726.

Kalema, V.N. and Witkowski, E.T.F. (2012) Land-use impacts on woody plant density and diversity in an African savanna charcoal production region. International Journal of Biodiversity Science, Ecosystem Services and Management, vol. 8, pp. 231–247. doi:10.1080/21513732.2012.681070.

Kalisa, W., Igbawua, T., Henchiri, M., Ali, S., Zhang, S., Bai, Y. and Zhang, J. (2019) Assessment of climate impact on vegetation dynamics over East Africa from 1982 to 2015. Scientific Reports, vol. 9, no. 1, pp.1-20. doi: 10.1038/s41598-019-53150-0.

Kaminski, T., Pinty, B., Voßbeck, M., Lopatka, M., Gobron, N. and Robustelli, M. (2017) Consistent retrieval of land surface radiation products from EO, including traceable uncertainty estimates. Biogeosciences, vol. 14, no. 9, pp. 2527-2541. doi: 10.5194/bg-14-2527-2017.

Kanniah, K.D., Beringer, J. and Hutley, L.B. (2010) The comparative role of key environmental factors in determining savanna productivity and carbon fluxes: A review, with special reference to northern Australia. Progress in Physical Geography, vol. 34, pp. 459-490, doi: 10.1177/0309133310364933.

Kaufman, Y.J. and Tanre, D. (1992) Atmospherically resistant vegetation index (ARVI) for EOS-MODIS. IEEE Transactions on Geoscience and Remote Sensing, vol. 30, no. 2, pp. 261-270.

Kaufmann, R. K., Zhou, L., Myneni, R. B., Tucker, C. J., Slayback, D., Shabanov, N. V., and Pinzon, J. (2003) The effect of vegetation on surface temperature: A statistical analysis of NDVI and climate data, Geophys. Res. Lett., vol. 30, no. 2147, doi:10.1029/2003GL018251, 22.

Knapp, K.R., Ansari, S., Bain, C.L., Bourassa, M.A., Dickinson, M.J., Funk, C., Helms, C.N., Hennon, C.C., Holmes, C.D., Huffman, G.J. and Kossin, J.P. (2011) Globally gridded satellite observations for climate studies. Bulletin of the American Meteorological Society, vol. 92, no. 7, pp. 893-907. doi: 10.1175/2011BAMS3039.1.

Knorr, W., Kaminski, T., Scholze, M., Gobron, N., Pinty, B., Giering, R., and Mathieu, P.-P. (2010) Carbon cycle data assimilation with a generic phenology model, Journal of Geophysical Research, vol. 115, no. G04017, doi: 10.1029/2009JG001119.

Knyazikhin, Yu, Martonchik, J.V., Diner, D.J., Myneni, R.B., Verstraete, M., Pinty, B. and Gobron, N. (1998) Estimation of vegetation canopy leaf area index and fraction of absorbed photosynthetically active radiation from atmosphere-corrected MISR data. Journal of Geophysical Research: Atmospheres, vol. 103, no. D24. pp. 32239-32256. doi: 10.1029/98JD02461.

Köppen, W. (1884) Die Wärmezonen der Erde, nach der Dauer der heissen, gemässigten und kalten Zeit und nach der Wirkung der Wärme auf die organische Welt betrachtet. Meteorologische Zeitschrift, vol. 1, no. 21, pp. 5-226.

Koppen, W. (1918) Klassifikation der Klima nach Temperatur, Niederschlag und Jahreslauf. Petermanns Mitt, vol.64.

Köppen, W. and Geiger, R. (1936) Handbuch der klimatologie, vol. 1, pp. 1-44, Berlin: Gebrüder Borntraeger.

Kutsch, W.L., Hanan, N., Scholes, B., McHugh, I., Kubheka, W., Eckhardt, H. and Williams, C. (2008) Response of carbon fluxes to water relations in a savanna ecosystem in South Africa. Biogeosciences, vol. 5, no. 6, pp.1797-1808. doi: 10.5194/bg-5-1797-2008.

Kutsch, W.L., Hanan, N., Scholes, R.J., McHugh, I., Kubheka, W., Eckhardt, H. and Williams, C. (2008) Response of carbon fluxes to water relations in a savanna ecosystem in South Africa. Biogeosciences Discussions, European Geosciences Union, vol. 5, no. 3, pp. 2197-2235. HAL Id: hal-00298009.

Lakhraj-Govender, R. and Grab, S.W. (2019) Assessing the impact of El Niño–Southern Oscillation on South African temperatures during austral summer. International Journal of Climatology, vol. 39, no. 1, pp.143-156. doi: 10.1002/joc.5791.

Laurent, V.C., Verhoef, W., Clevers, J.G. and Schaepman, M.E. (2011) Inversion of a coupled canopy–atmosphere model using multi-angular top-of-atmosphere radiance data: A forest case study. Remote Sensing of Environment, vol. 115, no. 10, pp. 2603-2612. doi: 10.1016/j.rse.2011.05.016.

Lavergne, T., Kaminski, T., Pinty, B., Taberner, M., Gobron, N., Verstraete, M.M., Vossbeck, M., Widlowski, J.L. and Giering, R. (2007) Application to MISR land products of an RPV model inversion package using adjoint and Hessian codes. Remote Sensing of Environment, vol. 107, no. 1-2, pp. 362-375. doi: 10.1016/j.rse.2006.05.021.

Le Roux, X and Bariac, T. (1998) Seasonal Variations in Soil, Grass and Shrub Water Status in a West African Humid Savanna. Oecologia, vol. 113, pp. 456-466. doi: 10.1007/s004420050398.

Liang, S. (2001) Narrowband to broadband conversions of land surface albedo I: Algorithms. Remote Sensing of Environment, vol. 76, no. 2, pp. 213-238. doi: 10.1016/S0034-4257(00)00205-4.

Liu, H.Q. and Huete, A. (1995) A feedback based modification of the NDVI to minimize canopy background and atmospheric noise. IEEE Transactions on Geoscience and Remote Sensing, vol. 33, no. 2, pp.457-465, doi: 10.1109/TGRS.1995.8746027.

Lloyd, J., Bird, M.I., Vellen, L., Miranda, A.C., Veenendaal, E.M., Djagbletey, G., Miranda, H.S., Cook, G. and Farquhar, G.D. (2008) Contributions of woody and herbaceous vegetation to tropical savanna ecosystem productivity: a quasi-global estimate. Tree Physiology, vol. 28, no. 3, pp. 451-468. doi: 10.1093/treephys/28.3.451.

Lyon, B. and Barnston, A.G. (2005) ENSO and the spatial extent of interannual precipitation extremes in tropical land areas. Journal of Climate, 18(23), pp.5095-5109. doi: 10.1175/JCLI3598.1.

MacBean, N., Maignan, F., Peylin, P., Bacour, C., Bréon, F.M. and Ciais, P. (2015) Using satellite data to improve the leaf phenology of a global Terrestrial Biosphere Model. Biogeosciences Discussions, vol. 12, no. 16. doi: 10.5194/bg-12-7185-2015.

Madonsela, S., Cho, M.A., Ramoelo, A., Mutanga, O. (2017) Remote sensing of species diversity using Landsat 8 spectral variables. ISPRS Journal of Photogrammetry and Remote Sensing, vol. 133, pp.116–127. doi:10.1016/j.isprsjprs.2017.10.008.

Mahlangu, P., Mathieu, R., Wessels, K., Naidoo, L., Verstraete, M.M., Asner, G., and Main, R. (2018) Indirect Estimation of Structural Parameters in South African Forests Using MISR-HR and LiDAR Remote Sensing Data. Remote Sensing, vol. 10, pp.1–31. doi:10.3390/rs10101537.

Main, R., Mathieu, R., Kleynhans, W., Wessels, K., Naidoo, L. and Asner, G.P. (2016) Hyper-temporal C-band SAR for baseline woody structural assessments in deciduous savannas. Remote Sensing, vol. 8, no. 661, pp.1-19. doi: 10.3390/rs8080661.

Martens, C., Hickler, T., Davis-Reddy, C., Engelbrecht, F., Higgins, S.I., von Maltitz, G.P., Midgley, G.F., Pfeiffer, M. and Scheiter, S. (2020) Large uncertainties in future biome changes in Africa call for flexible climate adaptation strategies. Global Change Biology, vol. 00, pp.1– 19. doi:10.1111/gcb.15390.

Martínez, B. and Gilabert, M.A. (2009) Vegetation dynamics from NDVI time series analysis using the wavelet transform. Remote Sensing of Environment, vol. 113, no. 9, pp.1823-1842. doi: 10.1016/j.rse.2009.04.016.

Martínez, B., Camacho, F., Verger, A., García-Haro, F.J. and Gilabert, M.A. (2013) Intercomparison and quality assessment of MERIS, MODIS and SEVIRI FAPAR products over the Iberian Peninsula. International Journal of Applied Earth Observation and Geoinformation, vol. 21, pp. 463-476. doi: 10.1016/j.jag.2012.06.010.

Martonchik, J.V., Bruegge, C.J. and Strahler, A.H. (2000) A review of reflectance nomenclature used in remote sensing. Remote Sensing Reviews, vol. 19, no. 1-4, pp. 9-20. doi: 10.1080/02757250009532407.

Matsika, R., Erasmus, B.F.N., and Twine, W.C. (2013) Double jeopardy: The dichotomy of fuelwood use in rural South Africa. Energy Policy, vol. 52, pp. 716–725. doi:10.1016/j.enpol.2012.10.030.

McPhaden, M.J., Zebiak, S.E. and Glantz, M.H. (2006) ENSO as an integrating concept in earth science. Science, vol. 314, no. 5806, pp.1740-1745. doi: 10.1126/science.1132588.

Menzel, A., Sparks, T.H., Estrella, N. and Roy, D.B. (2006) Altered geographic and temporal variability in phenology in response to climate change. Global Ecology and Biogeography, vol. 15, no.5, pp.498-504, doi: 10.1111/j.1466-822X.2006.00247.x.

Meyer, D., Verstraete, M.M. and Pinty, B, (1995) The effect of surface anisotropy and viewing geometry on the estimation of NDVI from AVHRR, Remote Sensing Reviews, vol. 12, No. 1-2, 3–27; doi: 10.1080/02757259509532272.

Midgley, G., and Bond, W. (2015) Future of African terrestrial biodiversity and ecosystems under anthropogenic climate change. Nature Climate Change vol. 5, pp. 823–829. doi:10.1038/nclimate2753.

Minnaert, M. (1941) The reciprocity principle in lunar photometry. Astrophysical Journal, vol. 93, pp.403-410. doi:10.1086/144279.

Mograbi, P.J., Asner, G.P., Witkowski, E.T., Erasmus, B.F., Wessels, K.J., Mathieu, R. and Vaughn, N.R. (2017) Humans and elephants as treefall drivers in African savannas. Ecography, vol. 40, no. 11, pp.1274-1284. doi: 10.1111/ecog.02549.

Mograbi, P.J., Erasmus, B.F., Witkowski, E.T.F., Asner, G.P., Wessels, K.J., Mathieu, R., Knapp, D.E., Martin, R.E. and Main, R. (2015) Biomass increases go under cover: woody vegetation dynamics in South African rangelands. PLoS One, vol. 10, no. 5, pp. e0127093. doi: 10.1371/journal.pone.0127093.

Mograbi, P.J., Witkowski, E.T., Erasmus, B.F., Asner, G.P., Fisher, J.T., Mathieu, R. and Wessels, K.J. (2019) Fuelwood extraction intensity drives compensatory regrowth in African savanna communal lands. Land Degradation & Development, vol, 30, no. 2, pp.190-201. doi: 10.1002/ldr.3210.

Moncrieff, G.R., Scheiter, S., Bond, W.J. and Higgins, S.I. (2014) Increasing atmospheric CO 2 overrides the historical legacy of multiple stable biome states in Africa. New Phytologist, vol. 201, no. 3, pp. 908-915. doi: 10.1111/nph.12551.

Moncrieff, G.R., Scheiter, S., Slingsby, J.A. and Higgins, S.I. (2015) Understanding global change impacts on South African biomes using Dynamic Vegetation Models. South African Journal of Botany, vol. 101, pp.16-23. doi: 10.1016/j.sajb.2015.02.004.

Monteith, J.L. (1972) Solar radiation and productivity in tropical ecosystems. Journal of Applied Ecology, vol. 9, no. 3, pp.747-766. doi: 10.2307/2401901.

Monteith, J.L. (1977) Climate and the efficiency of crop production in Britain. Philosophical Transactions of the Royal Society of London. B, Biological Sciences, vol. 281, no. 980, pp. 277-294. doi: 10.1098/rstb.1977.0140.

Mucina, L. and Rutherford, M.C. (2006) The vegetation of South Africa, Lesotho and Swaziland. Strelitzia vol. 19, (South African National Biodiversity Institute: Pretoria, South Africa). Memoirs of the Botanical Survey of South Africa.

Myneni, R.B. and Williams, D.L. (1994) On the relationship between FAPAR and NDVI. Remote Sensing of Environment, vol. 49, no. 3, pp. 200-211. doi: 10.1016/0034-4257(94)90016-7.

Naidoo, L., Cho, M.A., Mathieu, R., and Asner, G. (2012) Classification of savanna tree species, in the Greater Kruger National Park region, by integrating hyperspectral and LiDAR data in a Random Forest data mining environment. ISPRS Journal of Photogrammetry and Remote Sensing, vol. 69, pp.167–179. doi:10.1016/j.isprsjprs.2012.03.005.

Niang, I., Ruppel, O.C., Abdrabo, M.A., Essel, A., Lennard, C., Padgham, J. and Urquhart, P. (2014) Africa. Climate Change 2014: Impacts, Adaptation, and Vulnerability. Part B: Regional Aspects. Contribution of Working Group II to the Fifth Assessment Report of the Intergovernmental Panel on Climate Change (ed. by V.R. Barros, et al.), pp. 1199–1265. Cambridge: Cambridge University Press.

Nicholson, S.E. and Kim, J. (1997) The relationship of the El Niño–Southern oscillation to African rainfall. International Journal of Climatology: A Journal of the Royal Meteorological Society, vol. 17, no. 2, pp.117-135. doi: 10.1002/(SICI)1097-0088(199702)17:2<117::AID-JOC84>3.0.CO;2-O.

Nickless, A., Archibald, S.A., Van der Merwe, M.R., Scholes, R.J., Williams, C.A. and Hanan, N. (2011) Estimation of net ecosystem exchange at the Skukuza flux site, Kruger National Park, South Africa. Available from: http://hdl.handle.net/10204/5135

Nicodemus, F. E. (1977) Geometrical considerations and nomenclature for reflectance. Washington, DC: National Bureau of Standards, US Department of Commerce. Available from: http://physics.nist.gov/Divisions/Div844/facilities/specphoto/pdf/geoConsid.pdf

NOAA (National Oceanic and Atmospheric Administration). (2020a) Climatic Indices. https://www.cpc.ncep.noaa.gov/data/indices/ last accessed on 4 January 2021.

NOAA (National Oceanic and Atmospheric Administration). (2020b) Cold and warm episodes by season. https://origin.cpc.ncep.noaa.gov/products/analysis_monitoring/ensostuff/ONI_v5.php. Accessed 1 Jan 2021.

Noy-Meir, I. (1974) Desert ecosystems: higher trophic levels. Annual Review of Ecology and Systematics, vol. 5, no. 1, pp.195-214.

O'Connor, T.G., Puttick, J.R. and Hoffman, M.T. (2014) Bush encroachment in southern Africa: changes and causes. African Journal of Range & Forage Science, vol. 31, no. 2, pp. 67-88. doi: 10.2989/10220119.2014.939996.

Osborne, C.P., Charles-Dominique, T., Stevens, N., Bond, W.J., Midgley, G. and Lehmann, C.E.R. (2018) Human impacts in African savannas are mediated by plant functional traits. New Phytologist, vol. 220, pp.10-24. doi:10.1111/nph.15236.

Otter, L.B., Scholes, R.J., Dowty, P., Privette, J., Caylor, K., Ringrose, S., Mukelabai, M., Frost, P., Hanan, N., Totolo, O. and Veenendaal, E.M. (2002) The Southern African regional science initiative (SAFARI 2000): wet season campaigns. South African Journal of Science, vol. 98, no. 3, pp.131-137, available from: https://hdl.handle.net/10520/EJC97438.

Parhi, P., Giannini, A., Gentine, P. and Lall, U. (2016) Resolving contrasting regional rainfall responses to El Niño over tropical Africa. Journal of Climate, vol. 29, no. 4, pp.1461-1476. doi: 10.1175/JCLI-D-15-0071.1.

Parsons, D.A.B., Shackleton, C.M. & Scholes, R.J. (1997) Changes in herbaceous layer condition under contrasting land uses systems in the semi-arid Lowveld, South Africa. Journal of Arid Environments, vol. 37, pp. 319-329. doi: 10.1006/jare.1997.0283.

Philippon, N., Martiny, N., Camberlin, P., Hoffman, M.T. and Gond, V. (2014) Timing and patterns of the ENSO signal in Africa over the last 30 years: Insights from normalized difference vegetation index data. Journal of Climate, vol. 27, no. 7, pp. 2509-2532. doi: 10.1175/JCLI-D-13-00365.1.

Piao, S., Tan, J., Chen, A., Fu, Y.H., Ciais, P., Liu, Q., Janssens, I.A., Vicca, S., Zeng, Z., Jeong, S.J. and Li, Y. (2015) Leaf onset in the northern hemisphere triggered by daytime temperature. Nature Communications, vol. 6, no. 1, pp.1-8, doi: 10.1038/ncomms7911.

Pinty, B. and Verstraete, M.M. (1998) Modeling the scattering of light by homogeneous vegetation in optical remote sensing. Journal of the Atmospheric Sciences, vol. 55, no. 2, pp.137-150. doi: 10.1175/1520-0469(1998)055<0137:MTSOLB>2.0.CO;2

Pinty, B., Andredakis, I., Clerici, M., Kaminski, T., Taberner, M., Verstraete, M.M., Gobron, N., Plummer, S. and Widlowski, J.L. (2011a). Exploiting the MODIS albedos with the Two-stream Inversion Package (JRC-TIP): 1. Effective leaf area index, vegetation, and soil properties. Journal of Geophysical Research: Atmospheres, vol. 116, no. D9. doi: 10.1029/2010JD015372.

Pinty, B., Clerici, M., Andredakis, I., Kaminski, T., Taberner, M., Verstraete, M.M., Gobron, N., Plummer, S. and Widlowski, J.L. (2011b) Exploiting the MODIS albedos with the Two-stream Inversion Package (JRC-TIP): 2. Fractions of transmitted and absorbed fluxes in the vegetation and soil layers. Journal of Geophysical Research: Atmospheres, vol. 116, no. D9. doi: 10.1029/2010JD015373.

Pinty, B., Jung, M., Kaminski, T., Lavergne, T., Mund, M., Plummer, S., Thomas, E. and Widlowski, J.L.(2011c) Evaluation of the JRC-TIP 0.01 products over a mid-latitude deciduous forest site. Remote Sensing of Environment, vol. 115, no. 12, pp. 3567-3581. doi: 10.1016/j.rse.2011.08.018.

Pinty, B., Lavergne, T., Voßbeck, M., Kaminski, T., Aussedat, O., Giering, R., Gobron, N., Taberner, M., Verstraete, M.M. and Widlowski, J.L. (2007) Retrieving surface parameters for climate models from Moderate Resolution Imaging Spectroradiometer (MODIS)-Multiangle Imaging Spectroradiometer (MISR) albedo products. Journal of Geophysical Research: Atmospheres, vol. 112, no. D10. doi: 10.1029/2006JD008105.

Pinty, B., Verstraete, M. M., and Dickinson, R. E. (1990) A physical model of the bidirectional reflectance of vegetation canopies: 2. Inversion and validation, Journal of Geophysical Research, vol. 95, no. D8, pp.11767–11775, doi: 10.1029/JD095iD08p11767.

Pinty, B., Widlowski, J.L., Gobron, N., Verstraete, M.M., Diner, D.J. (2002) Uniqueness of Multiangular Measurements—Part I: An Indicator of Subpixel Surface Heterogeneity From MISR. IEEE Transactions on Geoscience and Remote Sensing, vol. 40, pp.1560–1573. doi: 10.1109/TGRS.2002.801148.

Pinzon, J.E. and Tucker, C.J. (2014) A non-stationary 1981–2012 AVHRR NDVI3g time series. Remote Sensing, vol. 6, no. 8, pp. 6929-6960. doi: 10.3390/rs6086929.

Pitman, A.J. (2003) The evolution of, and revolution in, land surface schemes designed for climate models. International Journal of Climatology, vol. 23, pp. 479-510. doi: 10.1002/joc.893.

Pomposi, C., Funk, C., Shukla, S., Harrison, L. and Magadzire, T. (2018) Distinguishing southern Africa precipitation response by strength of El Niño events and implications for decision-making. Environmental Research Letters, vol. 13, no. 7, pp. 074015. doi: 10.1088/1748-9326/aacc4c.

Rahman, H., Pinty, B., Verstraete, M.M. (1993) Coupled Surface-Atmosphere Reflectance (CSAR) Model. 2. Semiempirical Surface Model Usable With NOAA Advanced Very High Resolution Radiometer Data. Journal of Geophysical Research, vol. 98. pp. 20,791–20,801. doi:10.1029/93JD02072.

Rasmusson, E.M. and Carpenter, T.H. (1982) Variations in tropical sea surface temperature and surface wind fields associated with the Southern Oscillation/El Niño. Monthly Weather Review, vol. 110, no. 5, pp. 354-384. doi: 10.1175/1520-0493(1982)110<0354:VITSST>2.0.CO;2.

Rayleigh, L. (1903. XXI) On the spectrum of an irregular disturbance. The London, Edinburgh, and Dublin Philosophical Magazine and Journal of Science, vol. 5, no. 26, pp. 238-243.

Reichmann, L.G. and Sala, O.E. (2014) Differential sensitivities of grassland structural components to changes in precipitation mediate productivity response in a desert ecosystem. Functional Ecology, vol. 28, no. 5, pp.1292-1298, doi: 10.1111/1365-2435.12265.

Richardson, A.D., Hufkens, K., Milliman, T. and Frolking, S. (2018) Intercomparison of phenological transition dates derived from the PhenoCam Dataset V1. 0 and MODIS satellite remote sensing. Scientific Reports, vol. 8, no. 1, pp.1-12. doi: 10.1038/s41598-018-23804-6.

Richardson, A.D., Keenan, T.F., Migliavacca, M., Ryu, Y., Sonnentag, O. and Toomey, M. (2013) Climate change, phenology, and phenological control of vegetation feedbacks to the climate system. Agricultural and Forest Meteorology, vol. 169, pp.156-173. doi: 10.1016/j.agrformet.2012.09.012.

Richardson, A.J. and Wiegand, C.L. (1977) Distinguishing vegetation from soil background information. Photogrammetric Engineering and Remote Sensing, vol. 43, no. 12, pp.1541-1552.

Roques, K.G., O'connor, T.G. and Watkinson, A.R. (2001) Dynamics of shrub encroachment in an African savanna: relative influences of fire, herbivory, rainfall and density dependence. Journal of Applied Ecology, vol. 38, no. 2, pp. 268-280. doi: 10.1046/j.1365-2664.2001.00567.x.

Ross, J. (1981) The radiation regime and architecture of plant stands. The Hague: Dr. W. Junk Publishers.

Rouse, J.W., Haas, R.H., Schell, J.A., and Deering, D.W. (1973) Monitoring vegetation systems in the Great Plains with ERTS. In: Proceedings of the 3rd ERTS Symposium (1), Greenbelt, MD. : Goddard Space Flight Center, pp. 309–317.

Sage, R.F., Kubien, D.S. (2003) Quo vadis C_4? An ecophysiological perspective on global change and the future of C_4 plants. Photosynthesis Research, vol. 77, pp. 209–225. doi:10.1023/A:1025882003661.

Saha, S., Moorthi, S., Wu, X., Wang, J., Nadiga, S., Tripp, P., Behringer, D., Hou, Y.T., Chuang, H.Y., Iredell, M. and Ek, M. (2014) The NCEP climate forecast system version 2. Journal of Climate, vol. 27, no. 6, pp. 2185-2208. doi: 10.1175/JCLI-D-12-00823.1.

Sala, O.E., Gherardi, L.A., Reichmann, L., Jobbagy, E. and Peters, D. (2012) Legacies of precipitation fluctuations on primary production: theory and data synthesis. Philosophical Transactions of the Royal Society B: Biological Sciences, vol. 367, no. 1606, pp.3135-3144, doi: 10.1098/rstb.2011.0347.

SANBI (South African National Biodiversity Institute), 2006-2012. The Vegetation Map of South Africa, Lesotho and Swaziland, Mucina, L., Rutherford, M.C. and Powrie, L.W. (Editors), Online, http://bgis.sanbi.org/SpatialDataset/Detail/18, Version 2012., last accessed on 12 June, 2020.

Sankaran, M. & Ratnam, J. (2013) African and Asian Savannas. In Encyclopedia of Biodiversity, 2nd Edition. Simon Levin (Editor-in-Chief). Dordrecht: Elsevier Press.

Sankaran, M., Ratnam, J. and Hanan, N. (2008) Woody cover in African savannas: the role of resources, fire and herbivory. Global Ecology and Biogeography, vol. 17, no. 2, pp. 236-245. doi: 10.1111/j.1466-8238.2007.00360.x.

Sankaran, M., Ratnam, J. and Hanan, N.P. (2004) Tree–grass coexistence in savannas revisited–insights from an examination of assumptions and mechanisms invoked in existing models. Ecology Letters, vol. 7, no. 6, pp. 480-490. doi: 10.1111/j.1461-0248.2004.00596.x.

Schaaf, C.B., Liu, J., Gao, F. and Strahler, A.H. (2010) Aqua and Terra MODIS albedo and reflectance anisotropy products. In Land Remote Sensing and Global Environmental Change, pp. 549-561, Springer, New York, NY.

Schaepman-Strub, G., Schaepman, M.E., Painter, T.H., Dangel, S. and Martonchik, J.V. (2006) Reflectance quantities in optical remote sensing—Definitions and case studies. Remote Sensing of Environment, vol. 103, no.1, pp. 27-42. doi:10.1016/j.rse.2006.03.002.

Scheiter, S. and Higgins, S.I. (2007) Partitioning of root and shoot competition and the stability of savannas. The American Naturalist, vol. 170, no. 4, pp.587-601. doi: 10.1086/521317.

Scheiter, S. and Higgins, S.I. (2009) Impacts of climate change on the vegetation of Africa: an adaptive dynamic vegetation modelling approach. Global Change Biology, vol. 15, no. 9, pp. 2224-2246. doi: 10.1111/j.1365-2486.2008.01838.x.

Scheiter, S., Moncrieff, G.R., Pfeiffer, M. and Higgins, S.I. (2020) African biomes are most sensitive to changes in CO 2 under recent and near-future CO 2 conditions. Biogeosciences, vol. 17, no. 4, pp.1147-1167. doi: 10.5194/bg-17-1147-2020.

Scholes, M.C., Matrai, P.A., Andreae, M.O., Smith, K.A., Manning, M.R., Artaxo, P., Barrie, L.A., Bates, T.S., Butler, J.H., Ciccioli, P. and Cieslik, S.A. (2003) Biosphere-atmosphere interactions. In Atmospheric Chemistry in a Changing World, pp. 19-71, Springer, Berlin, Heidelberg.

Scholes, R.J. (1990) The influence of soil fertility on the ecology of African savannas. Journal of Biogeography, vol. 17, pp. 417-419.

Scholes, R.J. (2003) Convex relationships in ecosystems containing mixtures of trees and grass. Environmental and Resource Economics, vol. 26, no. 4, pp. 559-574.

Scholes, R.J. (2009) Syndromes of dryland degradation in southern Africa. African Journal of Range & Forage Science, vol. 26, no. 3, pp.113-125. doi: 10.2989/AJRF.2009.26.3.2.947.

Scholes, R.J. and Archer, S.R. (1997) Tree-grass interactions in savannas. Annual Review of Ecology and Systematics, vol. 28, no. 1, pp. 517-544. doi: 10.1146/annurev.ecolsys.28.1.517.

Scholes, R.J. and Hall, D.O. (1996) The carbon budget of tropical savannas, woodlands and grasslands. In Modelling Terrestrial Ecosystems: Breymeyer, A., Hall, D., Melillo, J. and Agren, G. (Eds.), Chichester: Wiley.

Scholes, R.J. and Walker, B.H. (1993) An African savanna: synthesis of the Nylsvley Study. Cambridge: Cambridge University Press. doi: 10.1017/CBO9780511565472.

Scholes, R.J., Gureja, N., Giannecchinni, M., Dovie, D., Wilson, B., Davidson, N., Piggott, K., McLoughlin, C., Van der Velde, K., Freeman, A. and Bradley, S. (2001) The environment and vegetation of the flux measurement site near Skukuza, Kruger National Park. Koedoe, vol. 44, no. 1, pp. 73-83, doi: 10.4102/koedoe.v44i1.187.

Sellers, P.J. (1987) Canopy reflectance, photosynthesis, and transpiration, II. The role of biophysics in the linearity of their interdependence. Remote sensing of Environment, vol. 21, no.2, pp.143-183, doi: 10.1016/0034-4257(87)90051-4.

Sellers, P.J., Dickinson, R.E., Randall, D.A., Betts, A.K., Hall, F.G., Berry, J.A., Collatz, G.J., Denning, A.S., Mooney, H.A., Nobre, C.A. and Sato, N. (1997) Modeling the exchanges of energy, water, and carbon between continents and the atmosphere. Science, vol. 275, no. 5299, pp. 502-509. doi: 10.1126/science.275.5299.502.

Shackleton, C.M, and Shackleton, S. (2004) The importance of non-timber forest products in rural livelihood security and as safety nets: a review of evidence from South Africa. South African Journal of Science, vol. 100, no. 11, pp. 658-664.

Shackleton, C.M. (2000) Comparison of plant diversity in protected and communal lands in the Bushbuckridge lowveld savanna, South Africa. Biological Conservation, vol. 94, no. 3, pp. 273-285.

Shackleton, C.M. (2001) Managing regrowth of an indigenous savanna tree species (Terminalia sericea) for fuelwood: the influence of stump dimensions and post-harvest coppice pruning. Biomass and Energy, vol. 20, pp. 261 –270.

Shackleton, C.M. and Shackleton, S.E. (2000) Direct use values of secondary resources harvested from communal savannas in the Bushbuckridge lowveld, South Africa. Journal of Tropical Forest Products, vol. 6, no. 1, pp. 28-47.

Shackleton, C.M., Griffin, N.J., Banks, D.I., Mavrandonis, J.M. and Shackleton, S.E. (1994) Community structure and species composition along a disturbance gradient in a communally managed South African savanna. Vegetation, vol. 115, no. 2, pp.157-167. doi: 10.1007/BF00044870.

Shackleton, C.M., Guthrie, G. and Main, R. (2005) Estimating the potential role of commercial over-harvesting in resource viability: a case study of five useful tree species in South Africa. Land Degradation & Development, vol. 16, no. 3, pp. 273-286. doi: 10.1002/ldr.652.

Shackleton, S. (2004) Livelihood benefits from the local level commercialization of savanna resources: a case study of the new and expanding trade in marula (Sclerocarya birrea) beer in Bushbuckridge, South Africa. South African Journal of Science, vol. 100, no. 11, pp. 651-657.

Shackleton, S.E., Shackleton, C.M., Netshiluvhi, T.R., Geach, B.S., Ballance, A. and Fairbanks, D.H.K. (2002) Use patterns and value of savanna resources in three rural villages in South Africa. Economic Botany, vol. 56, no. 2, pp.130-146. doi: 10.1663/0013-0001(2002)056[0130:UPAVOS]2.0.CO;2.

Shultis, J.K. and Myneni, R.B. (1988) Radiative transfer in vegetation canopies with anisotropic scattering. Journal of Quantitative Spectroscopy and Radiative Transfer, vol. 39, no. 2, pp.115-129. doi: 0022-4073(88)90079-9.

Snyder, W.C. (2002) Definition and invariance properties of structured surface BRDF. IEEE Transactions on Geoscience and Remote Sensing, vol. 40, no. 5, pp.1032-1037. doi: 10.1109/TGRS.2002.1010890.

Specht, R.L. and Specht, A. (1999) Australian plant communities: Dynamics of structure, growth and biodiversity. Australian Plant Communities: Dynamics of Structure, Growth and Biodiversity, Oxford University Press, Melbourne.

Stevens, N., Bond, W., Hoffman, M.T., Midgley, G. (2015) Change Is in the Air: Ecological Trends and Their Drivers in South Africa. South African Environmental Observation Network (SAEON), Pretoria. Available from: http://www.saeon.ac.za/Change%20is%20in%20the%20air_WEB%20VERSION.pdf.

Stevens, N., Lehmann, C.E.R., Murphy, B.P. and Durigan, G. (2017) Savanna woody encroachment is widespread across three continents. Global Change Biology, vol. 23. pp. 235-244. doi:10.1111/gcb.13409.

Swinbank, W.C. (1951) The measurement of vertical transfer of heat and water vapor by eddies in the lower atmosphere. Journal of Meteorology, vol. 8, no. 3, pp.135-145. doi: 10.1175/1520-0469(1951)008<0135:TMOVTO>2.0.CO;2.

Tang, J., Körner, C., Muraoka, H., Piao, S., Shen, M., Thackeray, S.J. and Yang, X. (2016) Emerging opportunities and challenges in phenology: a review. Ecosphere, vol. 7, no. 8, pp. 1-17, doi: 10.1002/ecs2.1436.

Thornton, R. (2002) Environment and Land in Bushbuckridge, South Africa. In Human Rights & the Environment: Conflicts and Norms in a Globalizing World: Lyuba, Z. (Eds.), pp.219-240, London: Taylor and Francis, doi: 10.4324/9781849771634.

Trenberth, K.E. (1997) The definition of El Niño. Bulletin of the American Meteorological Society, vol. 78, no. 12, pp. 2771-2778.

Trenberth, K.E. and Stepaniak, D.P. (2001) Indices of El Niño evolution. Journal of Climate, vol. 14, no. 8, pp.1697-1701.

Tucker, C.J. (1979) Red and photographic infrared linear combinations for monitoring vegetation. Remote sensing of Environment, vol. 8, no. 2, pp.127-150, doi: 10.1016/0034-4257(79)90013-0.

Twine, W., Moshe, D., Netshiluvhi, T. and Siphugu, V. (2003) Consumption and direct-use values of savanna bio-resources used by rural households in Mametja, a semi-arid area of Limpopo province, South Africa. South African Journal of Science, vol. 99, no. 9, pp. 467-473.

Twine, W.C. (2005) Socio-economic transitions influence vegetation change in the communal rangelands of the South African Lowveld. African Journal of Range and Forage Science, vol. 22, no. 2, pp. 93-99. doi: 10.2989/10220110509485866.

United Nations. (2017) World population prospects. New York, NY, USA: United Nations.

van Langevelde, F., Van De Vijver, C.A., Kumar, L., Van De Koppel, J., De Ridder, N., Van Andel, J., Skidmore, A.K., Hearne, J.W., Stroosnijder, L., Bond, W.J. and Prins, H.H. (2003) Effects of fire and herbivory on the stability of savanna ecosystems. Ecology, vol. 84, no. 2, pp. 337-350.

Van Wijk, M.T. and Rodriguez-Iturbe, I. (2002) Tree-grass competition in space and time: Insights from a simple cellular automata model based on ecohydrological dynamics. Water Resources Research, vol. 38, no. 9, pp.1-14. doi: 10.1029/2001WR000768.

Venter, F.J., Scholes, R.J. and Eckhardt, H.C. (2003) The abiotic template and its associated vegetation pattern. In The Kruger Experience: Ecology and Management of Savanna Heterogeneity; du Toit, J.T., Rogers, K.H., Biggs, H.C., (Eds.), Washington, DC.: Island Press, pp. 83–129.

Venter, Z.S., Cramer, M.D. and Hawkins, H.J. (2018) Drivers of woody plant encroachment over Africa. Nature Communications, vol. 9, no. 1, pp.1-7, doi: 10.1038/s41467-018-04616-8.

Verbesselt, J., Somers, B., Lhermitte, S., Jonckheere, I., Van Aardt, J., Coppin, P. (2007) Monitoring herbaceous fuel moisture content with SPOT VEGETATION time-series for fire risk prediction in savanna ecosystems. Remote Sensing of Environment, vol. 108, pp. 357–368. doi:10.1016/j.rse.2006.11.019.

Verger, A., Filella, I., Baret, F. and Peñuelas, J. (2016) Vegetation baseline phenology from kilometric global LAI satellite products. Remote Sensing of Environment, vol. 178, pp.1-14, doi: 10.1016/j.rse.2016.02.057.

Verstraete, M. M. and B. Pinty (1996) Designing optimal spectral indices for remote sensing applications, IEEE Transactions on Geoscience and Remote Sensing, vol. 34, pp. 1254–1265; doi:10.1109/36.536541.

Verstraete, M. M. and B. Pinty (2001) Introduction to special section: Modeling, measurement and exploitation of anisotropy in the radiation field, Journal of Geophysical Research, vol. 106, no. 11, pp. 903-11,907, doi: 10.1029/2000JD900759.

Verstraete, M. M., Pinty, B., and Dickinson, R. E. (1990) A physical model of the bidirectional reflectance of vegetation canopies: 1. Theory, Journal of Geophysical Research, vol. 95, no. D8, pp.11755– 11765, doi: 10.1029/JD095iD08p11755.

Verstraete, M.M. (1987) Radiation transfer in plant canopies: Transmission of direct solar radiation and the role of leaf orientation. Journal of Geophysical Research: Atmospheres, vol. 92, no. D9, pp.10985-10995. doi: 10.1029/JD092iD09p10985.

Verstraete, M.M. (1988) Radiation transfer in plant canopies: Scattering of solar radiation and canopy reflectance. Journal of Geophysical Research: Atmospheres, vol. 93, no. D8, pp. 9483-9494. doi: 10.1029/JD093iD08p09483.

Verstraete, M.M., Hunt, L.A., Scholes, R.J., Clerici, M., Pinty, B. and Nelson, D.L. (2012) Generating 275-m resolution land surface products from the Multi-Angle Imaging Spectroradiometer data. IEEE Transactions on Geoscience and Remote Sensing, vol. 50, no. 10, pp. 3980-3990. doi: 10.1109/TGRS.2012.2189575.

Vilà, M., Espinar, J.L., Hejda, M., Hulme, P.E., Jarošík, V., Maron, J.L., Pergl, J., Schaffner, U., Sun, Y. and Pyšek, P. (2011) Ecological impacts of invasive alien plants: a meta-analysis of their effects on species, communities and ecosystems. Ecology Letters, vol. 14, no. 7, pp. 702-708. doi: 10.1111/j.1461-0248.2011.01628.x.

Von Helmholtz, H. (1924) Helmholtz's treatise on physiological optics (Vol. 2). Washington, DC.: Optical Society of America.

Walker B.H., Noy-Meir I. (1982) Aspects of the Stability and Resilience of Savanna Ecosystems. In: Huntley B.J., Walker B.H. (Eds.) Ecology of Tropical Savannas. Ecological Studies (Analysis and Synthesis), vol 42. Berlin: Springer. doi: 10.1007/978-3-642-68786-0_26

Walker, B.H., Ludwig, D., Holling, C.S. and Peterman, R.M. (1981) Stability of semi-arid savanna grazing systems. The Journal of Ecology, vol. 69, pp. 473-498. doi: doi.org/10.2307/2259679.

Walter, H. (1971) Ecology of Tropical and Subtropical Vegetation. Edinburgh: Oliver

Wang, J., Wu, C., Wang, X. and Zhang, X. (2019) A new algorithm for the estimation of leaf unfolding date using MODIS data over China's terrestrial ecosystems. ISPRS Journal of Photogrammetry and Remote Sensing, vol. 149, pp.77-90. doi: 10.1016/j.isprsjprs.2019.01.017.

Wang, R., Chen, J.M., Liu, Z. and Arain, A. (2017) Evaluation of seasonal variations of remotely sensed leaf area index over five evergreen coniferous forests. ISPRS Journal of Photogrammetry and Remote Sensing, vol. 130, pp.187-201, doi: 10.1016/j.isprsjprs.2017.05.017.

Wessels, K.J., Colgan, M.S., Erasmus, B.F.N., Asner, G.P., Twine, W.C., Mathieu, R., Van Aardt, J.A.N., Fisher, J.T. and Smit, I.P.J. (2013) Unsustainable fuelwood extraction from South African savannas. Environmental Research Letters, vol. 8, no. 1, pp. 014007.

Wessels, K.J., Mathieu, R., Erasmus, B.F.N., Asner, G.P., Smit, I.P.J., van Aardt, J., Main, R., Fisher, J., Marais, W., Kennedy-Bowdoin, T., Knapp, D.E., Emerson, R. & Jacobson, J. (2011) Impact of contrasting land use on woody vegetation structure in the Lowveld savannas of South Africa. Forest Ecology and Management, vol. 261, pp.19-29. doi: 10.1016/j.foreco.2010.09.012.

Wessels, K.J., Mathieu, R., Erasmus, B.F.N., Asner, G.P., Smit, I.P.J., van Aardt, J., Main, R., Fisher, J., Marais, W., Kennedy-Bowdoin, T., Knapp, D.E., Emerson, R. and Jacobson, J. (2011) Impact of contrasting land use on woody vegetation structure in the Lowveld savannas of South Africa. Forest Ecology and Management, vol. 261, pp.19-29. doi: 10.1016/j.foreco.2010.09.012.

Wessels, K.J., Prince, S.D., Frost, P.E. and Van Zyl, D. (2004) Assessing the effects of human-induced land degradation in the former homelands of northern South Africa with a 1 km AVHRR NDVI time-series. Remote Sensing of Environment, vol. 91, no. 1, pp. 47-67. doi: 10.1016/j.rse.2004.02.005.

Widlowski, J.L., Pinty, B., Gobron, N., Verstraete, M.M., Diner, D.J. and Davis, A.B. (2004) Canopy structure parameters derived from multi-angular remote sensing data for terrestrial carbon studies. Climatic Change, vol. 67, no. 2-3, pp. 403-415. doi: 10.1007/s10584-004-3566-3.

Wigley, B.J., Bond, W.J. and Hoffman, M.T. (2010) Thicket expansion in a South African savanna under divergent land use: local vs. global drivers? Global Change Biology, vol. 16, no. 3, pp. 964-976. doi: 10.1111/j.1365-2486.2009.02030.x.

Williams, A. and Shackleton, C.M. (2002) Fuel wood use in South Africa: Where to in the 21st Century? Southern African Forestry Journal, vol. 196, no. 1, pp. 1-7, doi: 10.1080/20702620.2002.10434611.

Williams, R.J., Duff, G.A., Bowman, D.M.J.S. and Cook, G.D. (1996) Variation in the composition and structure of tropical savannas as a function of rainfall and soil texture along a large-scale climatic gradient in the Northern Territory, Australia. Journal of Biogeography, vol. 23, no. 6, pp. 747-756. doi: 10.1111/j.1365-2699.1996.tb00036.x.

Witkowski, E.T.F., O'Connor, T.G. (1996) Topo-edaphic, floristic and physiognomic gradients of woody plants in a semi-arid African savanna woodland. Vegetation, vol. 124, pp. 9–23. doi: 10.1007/BF00045140.

Wolter, K. and Timlin, M.S. (2011) El Niño/Southern Oscillation behaviour since 1871 as diagnosed in an extended multivariate ENSO index (MEI. ext). International Journal of Climatology, vol. 31, no. 7, pp.1074-1087. doi: 10.1002/joc.2336.

Xiao, X., Zhang, Q., Braswell, B., Urbanski, S., Boles, S., Wofsy, S., Moore III, B. and Ojima, D. (2004) Modeling gross primary production of temperate deciduous broadleaf forest using satellite images and climate data. Remote Sensing of Environment, vol. 91, no. 2, pp.256-270, doi: 10.1016/j.rse.2004.03.010.

Yuan, C., Tozuka, T., Landman, W.A. and Yamagata, T. (2014) Dynamical seasonal prediction of Southern African summer precipitation. Climate Dynamics, vol. 42, no. 11-12, pp.3357-3374, doi: 10.1007/s00382-013-1923-5.

Yuan, W., Liu, S., Zhou, G., Zhou, G., Tieszen, L.L., Baldocchi, D., Bernhofer, C., Gholz, H., Goldstein, A.H., Goulden, M.L. and Hollinger, D.Y. (2007) Deriving a light use efficiency model from eddy covariance flux data for predicting daily gross primary production across biomes. Agricultural and Forest Meteorology, vol. 143, no. 3-4, pp.189-207, doi: 10.1016/j.agrformet.2006.12.001.

Zhang, Q., Cheng, Y.B., Lyapustin, A.I., Wang, Y., Gao, F., Suyker, A., Verma, S. and Middleton, E.M. (2014) Estimation of crop gross primary production (GPP): fAPARchl versus MOD15A2 FPAR. Remote Sensing of Environment, vol. 153, pp.1-6. doi: 10.1016/j.rse.2014.07.012.

Zhang, X., Friedl, M.A. and Schaaf, C.B. (2006) Global vegetation phenology from Moderate Resolution Imaging Spectroradiometer (MODIS): Evaluation of global patterns and comparison with in situ measurements. Journal of Geophysical Research: Biogeosciences, vol. 111, no. G4. doi: 10.1029/2006JG000217.

Zhang, X., Friedl, M.A., Schaaf, C.B., Strahler, A.H., Hodges, J.C., Gao, F., Reed, B.C. and Huete, A. (2003) Monitoring vegetation phenology using MODIS. Remote sensing Sensing of environmentEnvironment, vol. 84, no. 3, pp. 471-475. doi: 10.1016/S0034-4257(02)00135-9.

Zhang, X., Liu, L. and Henebry, G.M. (2019) Impacts of land cover and land use change on long-term trend of land surface phenology: a case study in agricultural ecosystems. Environmental Research Letters, vol. 14, no. 4, pp. 044020. doi:10.1088/1748-9326/ab04d2.

Zhang, Y., Xiao, X., Wu, X., Zhou, S., Zhang, G., Qin, Y. and Dong, J. (2017) A global moderate resolution dataset of gross primary production of vegetation for 2000–2016. Scientific Data, vol. 4, no. 1, pp.1-13, doi: 10.1038/sdata.2017.165.Zhu, Z., S. Piao, Y. Xu, A. Bastos, P. Ciais, and Peng, S. (2017) The effects of teleconnections on carbon fluxes of global terrestrial ecosystems, Geophysical Research Letters, vol. 44, pp. 3209–3218, doi:10.1002/ 2016GL071743.